Design and Optimization of Magnetorquer Coil for a 2U CubeSat

a project presented to
The Faculty of the Department of Aerospace Engineering
San José State University

in partial fulfillment of the requirements for the degree
Master of Science in Aerospace Engineering

by

Utku Karhan

May 2026

approved by

Ali Guarneros Luna
Faculty Advisor

San José State
UNIVERSITY

© 2026
Utku Karhan
ALL RIGHTS RESERVED

ABSTRACT

Design and Optimization of Magnetorquer Coil for a 2U CubeSat

Utku Karhan

This report presents the design, modeling, simulation, and experimental validation of optimized magnetorquer coils for the SpartanSAT 2U CubeSat, with the goal of providing reliable attitude control in Low Earth Orbit. Traditional control systems struggle to obtain accurate data of the crescent moon due to severe illumination gradients. Thus, this work investigates a magnetorquer based Attitude Determination Control System as an alternative approach for spacecraft orientation and cislunar navigation support. The study develops multiple coil configurations and evaluates their performance using MATLAB orbital simulations, and International Geomagnetic Reference Field geomagnetic characterization. Control algorithms, including B-dot detumbling logic, are designed and optimized to balance magnetic dipole output, power consumption, and current limits. Coils in simulation undergo verification and calibration to validate analytical and simulation results. The findings provide a complete design workflow for magnetorquer systems on small satellites and demonstrate an optimized magnetic actuation approach capable of supporting the mission's unique lunar-observation requirements.

ACKNOWLEDGEMENTS

I would like to express my utmost gratitude to:

- First and foremost, my father, Senior Maritime Pilot Atilla Karhan (*dec.*), for providing me with the passion for aerospace in the little time we had to spend together.
- My family, Şadiye Karhan, Eyüp Sabri Yarmalı (*dec.*), Hasan Özgür Yarmalı, Neşe Yarmalı, Yiğit Yarmalı, İrem Yarmalı, Yüksel Savaşçı (*dec.*), Bülent Savaşçı (*dec.*) and Serdar Savaşçı for their unconditional love, support, and trust in everything I have done. I wouldn't have made it this far and achieved this much without them by my side.
- My advisor Professor Ali Guarneros Luna for her instructions throughout the completion of this report. Her guidance and expertise played a key role in keeping the project on track and bringing the project work to completion.
- Dr. Mourtos for his constant support that made it possible for me to complete this report in a timely manner.
- And finally, my friends, Kerim Şişmanoğlu, Hüseyin Kağan Kil, Yusuf Bora Gökçeler, Gökmen Mehmet Dilek, Mahmut Kargılı, Neil Walter Arnett, Edward Choi, and Nattapon Oonlamom for being my closest friends, and for being there for me during my hardest moments. I owe much of my success to them.

Table Of Contents

List of Figures vii
List of Tables xi
Symbols xii
1. Introduction **1**
1.1 Motivation 1
1.2 Literature Review 1
1.2.1 Background 1
1.2.2 Fundamentals of Magnetorquer Functionality 3
1.2.3 Different Types of Magnetorquers 4
1.3 Project Proposal 12
1.4 Methodology 13
2. Modeling **15**
2.1 Modeling Setup 15
2.2 Magnetorquer Design and Optimization 15
2.3 Simulation and Control Algorithm Development 15
2.4 Reference Frames 16
2.4.1 Geocentric Inertial Frame 16
2.4.2 Earth Fixed Frame 17
2.4.3 Polar Coordinate Frame 17
2.4.4 Orbital Frame 18
2.4.5 Vehicle Frame 19
2.5 Evaluation and Implementation 20
3. Testing **21**
4. Simulation **22**
4.1 Simulation Setup 22
4.1.1 Further Assumptions 26
4.2 Uncontrolled Tumbling Response 27
4.3 Open-loop Response 32
4.4 B-dot Controller Case Study 37
4.4.1 Number of Turns Sweep 38
4.4.2 Coil Area Sweep 57
4.4.3 Current Limit Sweep 72

4.4.4 Orbit Sensitivity Study 87
5. Discussion **101**
6. Conclusion and Future Work **102**
References 104
Appendix A: MATLAB Code **107**

List of Figures

Figure 1.1 – Components of attitude determination control system [2] 2
Figure 1.2 – Magnetorquers [5] 3
Figure 1.3 – Loops in a magnetorquer 4
Figure 1.4 – Inner, W_1, and outer, W_0, dimensions of printed magnetorquer [1] 5
Figure 1.5 – Plot of trace width against torque, torque to power ratio, power and current [1] 6
Figure 1.6 – Plot of W_1/W_0 against torque, torque to power ratio and power consumption [1] 7
Figure 1.7 – Magnetic torque rod [6] 7
Figure 1.8 – Torque vs current [6] 8
Figure 1.9 – Torque vs voltage [6] 9
Figure 1.10 – Air core magnetorquer design [8] 9
Figure 2.1 – Geocentric inertial reference frame [17] 17
Figure 2.2 – Earth fixed frame and polar coordinate frame [17] 18
Figure 2.3 – Orbital reference frame [17] 19
Figure 2.4 – Vehicle frame [17] 20
Figure 3.1 – Schematic illustration of a B-dot probe [20] 21
Figure 4.1 – Orbit and axis assumption 27
Figure 4.2 – Angular velocity components uncontrolled tumbling response 28
Figure 4.3 – Angular velocity magnitude uncontrolled tumbling response 29
Figure 4.4 – Rotational kinetic energy uncontrolled tumbling response 29
Figure 4.5 – Commanded vs actual dipole moment uncontrolled tumbling response 30
Figure 4.6 – Coil current uncontrolled tumbling response 30
Figure 4.7 – Coil voltage uncontrolled tumbling response 31
Figure 4.8 – Coil power uncontrolled tumbling response 31
Figure 4.9 – Total coil power consumption uncontrolled tumbling response 32
Figure 4.10 – Commanded vs actual dipole error uncontrolled tumbling response 32
Figure 4.11 – Angular velocity components open loop response 33
Figure 4.12 – Angular velocity magnitude open loop response 34
Figure 4.13 – Rotational kinetic energy open loop response 34
Figure 4.14 – Commanded vs actual dipole moment open loop response 35
Figure 4.15 – Coil current open loop response 35
Figure 4.16 – Coil voltage open loop response 36
Figure 4.17 – Coil power open loop response 36
Figure 4.18 – Total coil power consumption open loop response 37
Figure 4.19 – Commanded vs actual dipole error open loop response 37
Figure 4.20 – Angular velocity components N = 100 38
Figure 4.21 – Angular velocity magnitude N = 100 39
Figure 4.22 – Rotational kinetic energy N = 100 39
Figure 4.23 – Commanded vs actual dipole moment N = 100 40
Figure 4.24 – Coil current N = 100 40
Figure 4.25 – Coil voltage N = 100 41
Figure 4.26 – Coil power N = 100 41
Figure 4.27 – Total coil power consumption N = 100 42
Figure 4.28 – Commanded vs actual dipole error N = 100 42

Figure 4.29 – Angular velocity components N = 200 43
Figure 4.30 – Angular velocity magnitude N = 200 43
Figure 4.31 – Rotational kinetic energy N = 200 44
Figure 4.32 – Commanded vs actual dipole moment N = 200 44
Figure 4.33 – Coil current N = 200 45
Figure 4.34 – Coil voltage N = 200 45
Figure 4.35 – Coil power N = 200 46
Figure 4.36 – Total coil power consumption N = 200 46
Figure 4.37 – Commanded vs actual dipole error N = 200 47
Figure 4.38 – Angular velocity components N = 400 47
Figure 4.39 – Angular velocity magnitude N = 400 48
Figure 4.40 – Rotational kinetic energy N = 400 48
Figure 4.41 – Commanded vs actual dipole moment N = 400 49
Figure 4.42 – Coil current N = 400 49
Figure 4.43 – Coil voltage N = 400 50
Figure 4.44 – Coil power N = 400 50
Figure 4.45 – Total coil power consumption N = 400 51
Figure 4.46 – Commanded vs actual dipole error N = 400 51
Figure 4.47 – Angular velocity components N = 800 52
Figure 4.48 – Angular velocity magnitude N = 800 52
Figure 4.49 – Rotational kinetic energy N = 800 53
Figure 4.50 – Commanded vs actual dipole moment N = 800 53
Figure 4.51 – Coil current N = 800 54
Figure 4.52 – Coil voltage N = 800 54
Figure 4.53 – Coil power N = 800 55
Figure 4.54 – Total coil power consumption N = 800 55
Figure 4.55 – Commanded vs actual dipole error N = 800 56
Figure 4.56 – Angular velocity components coil area = 0.004 m² 57
Figure 4.57 – Angular velocity magnitude coil area = 0.004 m² 58
Figure 4.58 – Commanded vs actual dipole moment coil area = 0.004 m² 58
Figure 4.59 – Coil current coil area = 0.004 m² 59
Figure 4.60 – Coil voltage coil area = 0.004 m² 59
Figure 4.61 – Total coil power consumption coil area = 0.004 m² 60
Figure 4.62 – Commanded vs actual dipole error coil area = 0.004 m² 60
Figure 4.63 – Angular velocity components coil area = 0.006 m² 61
Figure 4.64 – Angular velocity magnitude coil area = 0.006 m² 61
Figure 4.65 – Commanded vs actual dipole moment coil area = 0.006 m² 62
Figure 4.66 – Coil current coil area = 0.006 m² 62
Figure 4.67 – Coil voltage coil area = 0.006 m² 63
Figure 4.68 – Total coil power consumption coil area = 0.006 m² 63
Figure 4.69 – Commanded vs actual dipole error coil area = 0.006 m² 64
Figure 4.70 – Angular velocity components coil area = 0.008 m² 64
Figure 4.71 – Angular velocity magnitude coil area = 0.008 m² 65
Figure 4.72 – Commanded vs actual dipole moment coil area = 0.008 m² 65
Figure 4.73 – Coil current coil area = 0.008 m² 66
Figure 4.74 – Coil voltage coil area = 0.008 m² 66

Figure 4.75 – Total coil power consumption coil area = 0.008 m² 67
Figure 4.76 – Commanded vs actual dipole error coil area = 0.008 m² 67
Figure 4.77 – Angular velocity components coil area = 0.01 m² 68
Figure 4.78 – Angular velocity magnitude coil area = 0.01 m² 68
Figure 4.79 – Commanded vs actual dipole moment coil area = 0.01 m² 69
Figure 4.80 – Coil current coil area = 0.01 m² 69
Figure 4.81 – Coil voltage coil area = 0.01 m² 70
Figure 4.82 – Total coil power consumption coil area = 0.01 m² 70
Figure 4.83 – Commanded vs actual dipole error coil area = 0.01 m² 71
Figure 4.84 – Angular velocity components max current = 0.02 Amps 72
Figure 4.85 – Angular velocity magnitude max current = 0.02 Amps 73
Figure 4.86 – Commanded vs actual dipole moment max current = 0.02 Amps 73
Figure 4.87 – Coil current max current = 0.02 Amps 74
Figure 4.88 – Coil voltage max current = 0.02 Amps 74
Figure 4.89 – Coil power consumption max current = 0.02 Amps 75
Figure 4.90 – Commanded vs actual dipole error max current = 0.02 Amps 75
Figure 4.91 – Angular velocity components max current = 0.05 Amps 76
Figure 4.92 – Angular velocity magnitude max current = 0.05 Amps 76
Figure 4.93 – Commanded vs actual dipole moment max current = 0.05 Amps 77
Figure 4.94 – Coil current max current = 0.05 Amps 77
Figure 4.95 – Coil voltage max current = 0.05 Amps 78
Figure 4.96 – Coil power consumption max current = 0.05 Amps 78
Figure 4.97 – Commanded vs actual dipole error max current = 0.05 Amps 79
Figure 4.98 – Angular velocity components max current = 0.1 Amps 79
Figure 4.99 – Angular velocity magnitude max current = 0.1 Amps 80
Figure 4.100 – Commanded vs actual dipole moment max current = 0.1 Amps 80
Figure 4.101 – Coil current max current = 0.1 Amps 81
Figure 4.102 – Coil voltage max current = 0.1 Amps 81
Figure 4.103 – Coil power consumption max current = 0.1 Amps 82
Figure 4.104 – Commanded vs actual dipole error max current = 0.1 Amps 82
Figure 4.105 – Angular velocity components max current = 0.15 Amps 83
Figure 4.106 – Angular velocity magnitude max current = 0.15 Amps 83
Figure 4.107 – Commanded vs actual dipole moment max current = 0.15 Amps 84
Figure 4.108 – Coil current max current = 0.15 Amps 84
Figure 4.109 – Coil voltage max current = 0.15 Amps 85
Figure 4.110 – Coil power consumption max current = 0.15 Amps 85
Figure 4.111 – Commanded vs actual dipole error max current = 0.15 Amps 86
Figure 4.112 – Angular velocity components current mission 88
Figure 4.113 – Commanded vs actual dipole moment current mission 88
Figure 4.114 – Coil current current mission 89
Figure 4.115 – Coil voltage current mission 89
Figure 4.116 – Coil power current mission 90
Figure 4.117 – Total coil power consumption current mission 90
Figure 4.118 – Angular velocity components low LEO 91
Figure 4.119 – Commanded vs actual dipole moment low LEO 91
Figure 4.120 – Coil current low LEO 92

Figure 4.121 – Coil voltage low LEO 92
Figure 4.122 – Coil power low LEO 93
Figure 4.123 – Total coil power consumption low LEO 93
Figure 4.124 – Angular velocity components mid LEO 94
Figure 4.125 – Commanded vs actual dipole moment mid LEO 94
Figure 4.126 – Coil current mid LEO 95
Figure 4.127 – Coil voltage mid LEO 95
Figure 4.128 – Coil power mid LEO 96
Figure 4.129 – Total coil power consumption mid LEO 96
Figure 4.130 – Angular velocity components high LEO 97
Figure 4.131 – Commanded vs actual dipole moment high LEO 97
Figure 4.132 – Coil current high LEO 98
Figure 4.133 – Coil voltage high LEO 98
Figure 4.134 – Coil power high LEO 99
Figure 4.135 – Total coil power consumption high LEO 99

List of Tables

Table 1.1 – Summary of pros & cons of magnetorquers integration ways 12
Table 1.2 – Gantt chart for AE295 13
Table 2.1 – Designated reference frames 16
Table 4.1 – Fixed parameters for uncontrolled tumbling response 28
Table 4.2 – Fixed parameters for open-loop response 33
Table 4.3 – Fixed parameters for number of turns sweep 38
Table 4.4 – Quantitative numerical results of number of turns sweep case study 56
Table 4.5 – Fixed parameters for coil area sweep 57
Table 4.6 – Quantitative numerical results of coil area sweep case study 71
Table 4.7 – Fixed parameters for current limit sweep 72
Table 4.8 – Quantitative numerical results of current limit sweep case study 86
Table 4.9 – Perigee and apogee values for orbit sensitivity study 87
Table 4.10 – Fixed parameters for orbit sensitivity study 87
Table 4.11 – Quantitative numerical results of orbit sensitivity case study 99

Symbols

Symbol	Definition	Units (SI)
$\vec{T}$	Torque Output	N-m
T_{body}	Body-frame output torque	N-m
$\vec{M}_{dipole}$	Dipole Moment	A-m^2
M_{cmd}	Commanded Dipole moment	A-m^2
M_{actual}	Actual Dipole moment	A-m^2
$\vec{B}$	Magnetic Flux Density of Earth	Tesla
B	Magnetic Field	Tesla
$\dot{B}$	Rate of change of Magnetic Field	Tesla/s
B_{body}	SpartanSAT body frame	Tesla
N	Current number of loops	-----
I	Current flow through the loop	Amps
I_{req}	Current needed in the coil to generate designed dipole moment	Amps
I_{cmd}	Commanded current	Amps
A	Area of the loop (coil)	m^2
W	Weight	N
w	Width	m/cm
h	Height	m/cm
d	Depth	m/cm
t	Thickness	m/cm
t	Time	s
W_1	Inner Width	m/cm
W_0	Outer Width	m/cm
r	The distance from the magnetorquer center to the magnetorquer	m
k	B-dot Controller Gain	-----
q	Quaternion state matrix	-----
q_0	Quaternion initial attitude state matrix	-----
$\dot{q}$	Quaternion derivative	-----
x	SpartanSAT state matrix	-----
x_f	SpartanSAT full state matrix	-----
$\boldsymbol{m}$	SpartanSAT mass	kg
J	Inertia Matrix	kg-m^2
J_x, J_y, J_z	Principle moments of Inertia	kg-m^2
$\boldsymbol{Q}(\omega)$	Quaternion propagated angular velocity matrix	deg/s
μ	Earth gravitational parameter	m^3/s^2
R_E	Radius of Earth	km
h_p	Height of the satellite above the Earth's surface at its closest point	km
h_a	Height of the satellite above the Earth's surface at its highest point	km
r_p	Perigee Altitude	km
r_a	Apogee Altitude	km
a	Semi-major Axis	km

e	Eccentricity	-----
p	Semi-latus rectum	km
n	Mean motion	rad/s
M	Mean anomaly	rad
E	Eccentric anomaly	rad
v	True anomaly	rad
r_{pf}	Perifocal position	km
V	Voltage	V
V_{max}	Maximum voltage	V
R	Resistance	Ohms
P	Coil power	Watt
KE	Kinetic energy	J
X,Y,Z	Base Vectors	-----
Greek Symbols		
λ	Geocentric Longitude	deg
ρ	Geocentric Latitude	deg
Ω_E	Ascension	deg
Θ	Geocentric Colatitude	deg
Ω	Angle in the equatorial plane between the vernal equinox and the ascending node	deg
I	Orbital Inclination	deg
η	Angle locating the vehicle in orbit measured from the ascending node	deg
μ_0	Magnetorquer Permeability	H/m
ω	Angular velocity	deg/s
ω_0	Initial angular velocity	deg/s
$\dot{\omega}$	Angular acceleration	deg/s^2
κ	Wire Packing Factor	-----
Subscripts		
$( )_I$	Geocentric Inertial Reference Frame	-----
$( )_E$	Earth Fixed Frame	-----
$( )_B$	Polar Coordinate Frame	-----
$( )_F$	Orbital Frame	-----
$( )_S$	Vehicle Frame	-----
Acronyms		
ADCS	Attitude Determination Control System	-----
LEO	Low Earth Orbit	-----
PCB	Printed Circuit Board	-----
VR	Virtual Reality	-----
HIL	Hardware In the Loop	-----
IGRF	International Geomagnetic Reference Field	-----
ECI	Earth Centered Inertial	-----

1. Introduction

1.1 Motivation

Satellites require precise attitude control to fulfill mission objectives, such as maintaining orientation for imaging, communication and navigation. Traditional attitude control systems rely on attitude determination control system (ADCS) mechanisms such as reaction wheels or thrusters, which present challenges in terms of mass, complexity, and resource consumption.

Magnetorquers are devices that generate magnetic components by running current through coils. They offer a lightweight and sustainable alternative, using the Earth's geomagnetic field to produce torque. Particularly in small satellite missions, magnetorquers have become attractive for their simplicity and reliability. However, their effectiveness is limited by the strength of the available geomagnetic field and coil design parameters. Main weaknesses of magnetorquers, such as not being able to generate enough torque in all directions simultaneously, will be highly evaluated for optimal performance parameters.

This project will focus on the development and optimization of magnetic coils tailored for a 2U satellite orientation control, in LEO (Low Earth Orbit), investigating design, and control algorithms that maximize performance while minimizing resource consumption to gain accurate data of the crescent moon. Since current star trackers experience moon interference in their field of view, an alternative method involving a magnetorquer based ADCS is to be developed to prevent the saturated background that appears on star trackers which result in no start being able to be tracked. The magnetorquer design will then be integrated into the SpartanSAT, the 2U satellite mentioned above.

1.2 Literature Review

To assess the feasibility of a magnetorquer based control system, it is necessary to review the current state, and previous use, of technology across multiple areas. It is also crucial to understand why magnetorquers are in use and their historical use with scientific reasoning and their place in an attitude control system.

1.2.1 Background

Over the years, the satellites' sizes have been reducing while their expected functionality is increasing. Due to their affordability, mass and size, CubeSats and nano satellites have become popular options for various research agencies, space institutions, and universities. While affordability is a key factor in this popularity, the radically reduced sizes of these satellites bring

in challenges, especially about the available space to fit all the subsystems and components of the design. One of these crucial subsystems is the ADCS consisting of various components that can be seen below in Figure 1. This subsystem oversees de-tumbling, controlling, and orienting the satellite after initial deployment and during the satellite operations [1].

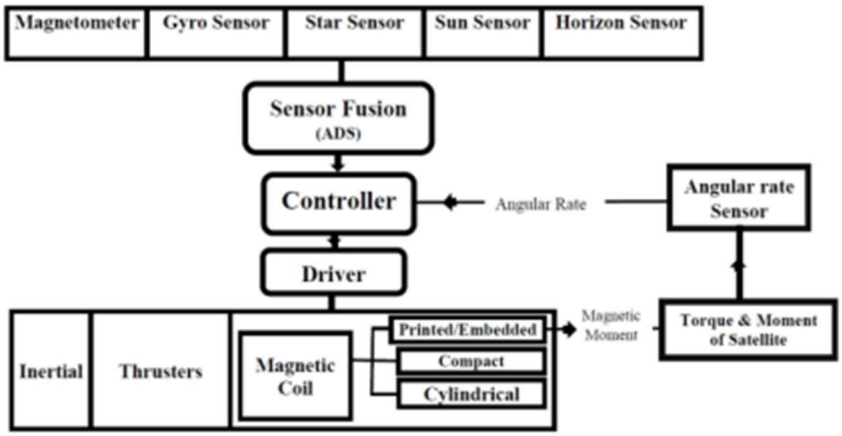


Figure 1.1 - Components of attitude determination control system [2]

Evaluating the ADCS could be done in multiple ways, but one of the categorizations is based on whether they are passive or active. Passive ones are more gravity gradient based while active ones are significantly less affordable and have a permanent magnetics approach.

To ensure the necessary pointing accuracy, active control systems are used more often, compared to passive systems in the industry [3]. But to reduce the costs, there is a popular component that is used: A magnetorquer.

Magnetorquers are core magnetic attitude control actuators. They use the local (earth) magnetic field to generate the torque, which is used to rotate the satellite [1]. To generate torque, they utilize earth's magnetic field with their magnetic dipole due to conductivity caused by compact and cylindrical rods, by creating the required rotation, to ensure satellites are precisely aligned, oriented and stabilized [2,4, 5]. This generated magnetic dipole interacts with the local external magnetic field, generating a torque perpendicular to the dipole and field. Magnetorquers by themselves cannot generate the control desired for the mission but can be used as a key element. Most of the satellites today use a system consisting of thrusters, momentum & reaction wheels, and magnetorquer coils.



Figure 1.2 - Magnetorquers [5]

1.2.2 Fundamentals of Magnetorquer Functionality

There are different types of magnetorquers based on the way they are integrated into the satellites and the ADCS itself. But there is a generalized and applicable mathematical approach that could be followed when making necessary design decisions and constraints.

The generated magnetic dipole moment interacts with Earth's magnetic field resulting in a magnetic torque on the spacecraft. This generation could be expressed as:

$$\vec{T} = \vec{M}_{dipole} \times \vec{B} \tag{1.1}$$

Where $\vec{T}$ is the output torque in N-m and $\vec{M}_{dipole}$ is the dipole moment in A-m^2 generated by the magnetorquer and $\vec{B}$ is the magnetic flux density of Earth in Tesla. Considering the magnetic flux density of Earth increases as the altitude increases, it is possible to conclude that in lower altitudes there will be more output torque generated via a magnetorquer involving ADCS. Therefore, it makes more sense to utilize magnetorquer in LEO operations rather than higher altitude missions. Thus, one of the mission requirements to consider involving a magnetorquer in the ADCS is the altitude requirement of spacecraft.

To define the magnetic dipole moment, the number of current loops is an important factor.



Figure 1.3 - Loops in a magnetorquer

The mathematical expression of the magnetic dipole moment can be expressed as:

$$\vec{M}_{dipole} = N \cdot I \cdot A \tag{1.2}$$

Where N is the number of current loops, I is the current flowing through the loop in Amps and A is the area of the loop (coil) in m^2. The resultant moment will be generated normal to the planar area with direction based on the right-hand rule.

1.2.3 Different Types of Magnetorquers

- PCB (Printed Circuit Board) Printed

  A PCB printed magnetorquer is a flat actuator in which conductive traces embedded on a printed circuit board produce a magnetic dipole when current flows. The generated dipole interacts with Earth's magnetic field to generate the control moment [4].

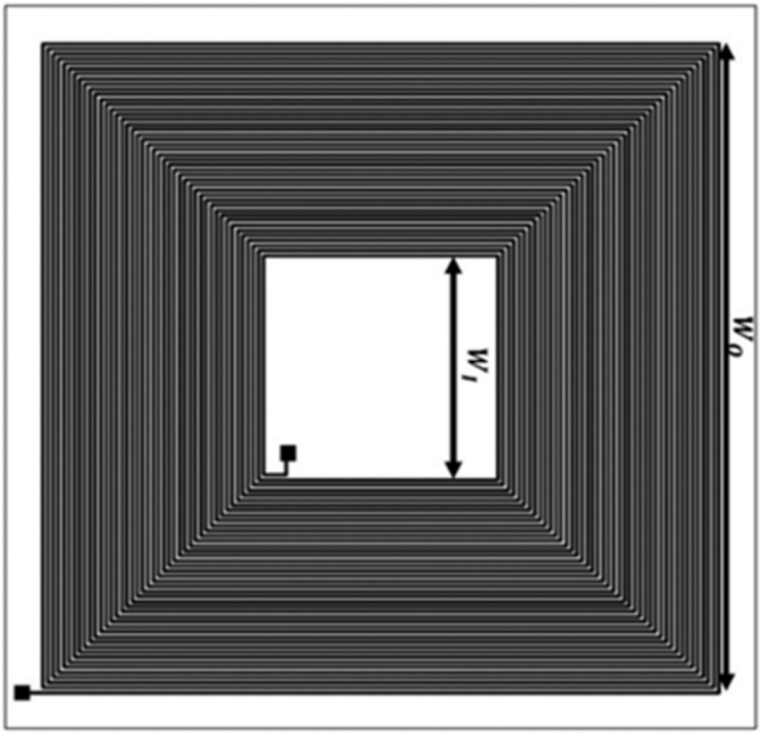


Figure 1.4 - Inner, W_1, and outer, W_0, dimensions of printed magnetorquer [1]

Compared to the other magnetorquer types, in this report, the PCB printed magnetorquers are unique with their inner and outer geometric widths. To better understand the theoretical relation, research was done about torque output optimization of PCB printed magnetorquer and the results are shown in Figures 1.5 - 1.7 below.

The first plot shows the generated torque, torque to power ratio, power consumption and current flow against variations in trace widths that could be referenced back to Fig. 1.4.

It is seen, from Figure 1.5, that increasing the trace width, the torque to power ratio decreases for any selected applied voltage. Due to the torque generated increasing with the increase in trace width, power consumption also increases in large proportions, thus causing a decrease in torque to power ratio. The analysis has been performed for two selected voltages which were 3.3V and 5V. As the selected trace width increases, there is significant increase in the torque but at the expense of consumed power, causing an upper limit on selection of torque to power ratio [1].

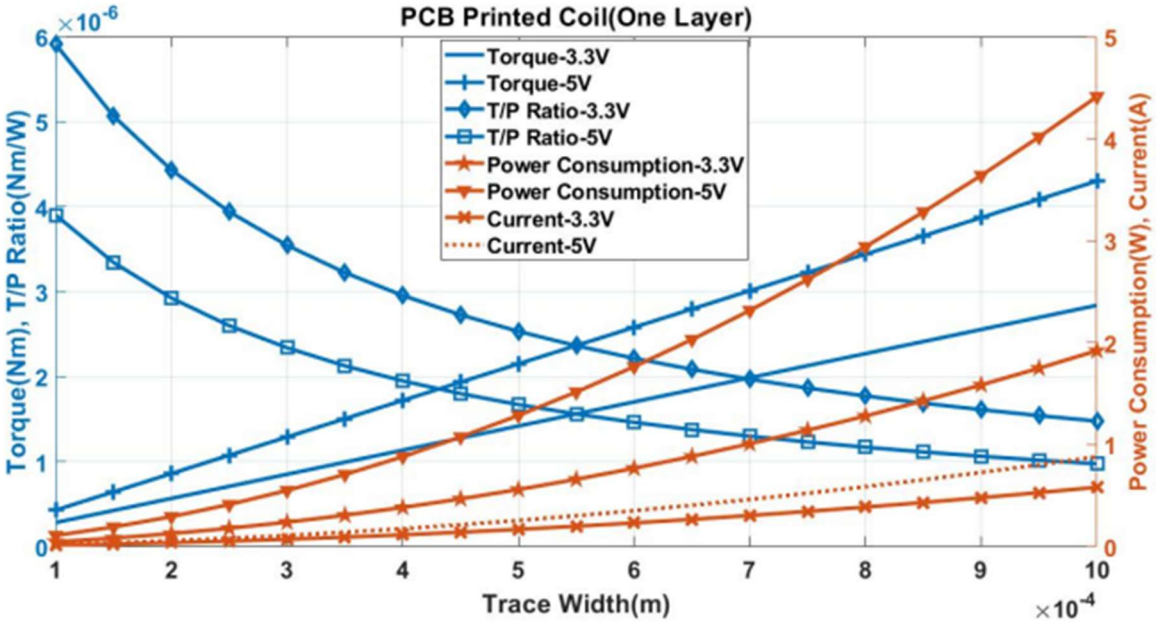


Figure 1.5 - Plot of trace width against torque, torque to power ratio, power and current [1]

On Figure 1.6, The selection of outermost and innermost dimensions is specified to see the delta of the effects. The study has been conducted by varying the ratio of inner and outer dimensions of the printed traces, W_1, and W_0. The resultant torque and torque to power ratio for two operating voltages (3.3V and 5V) is plotted. As the magnetorquer encompasses more area of the printed circuit board, directly proportional with W_1, and W_0, the generated torque and torque to power ratio increases. The total length of coil also increases by increasing the outer dimensions which causes the resistance to increase effectively permitting less current to flow in the magnetorquer. It is possible to state, from the graph, that for a fixed inner dimension, if the outer dimension increases, there is an increase in torque to power ratio. As a design rule, the outer dimension should be larger in magnetorquer, if permitted by the board. Contrarily, for a fixed outer dimension, increasing the inner dimension causes a decrease in the encompassed area of the magnetorquer, resulting in limiting the number of traces [1].

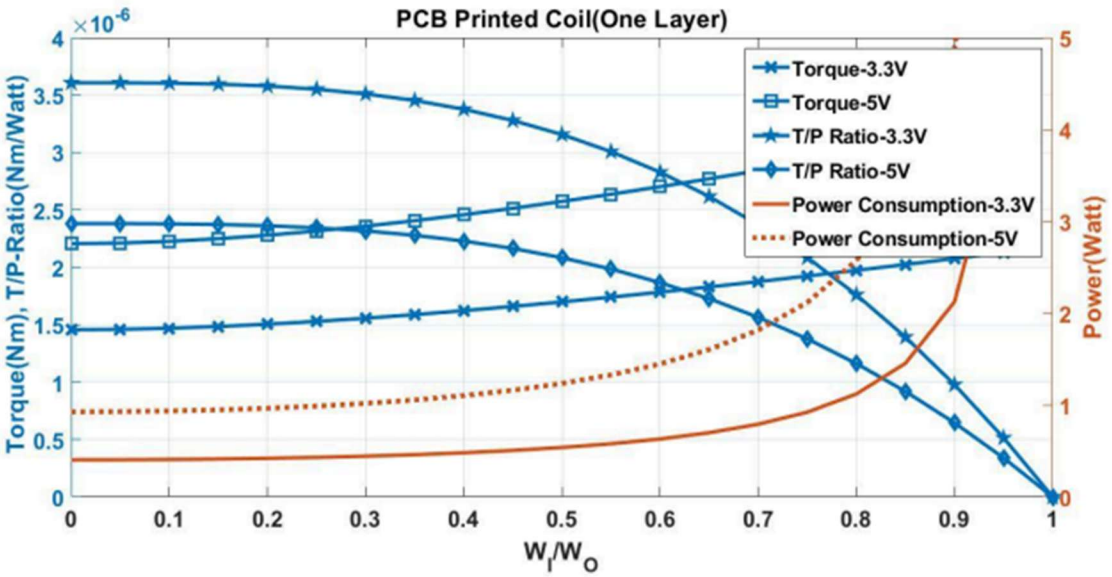


Figure 1.6 - Plot of W_1/W_0 against torque, torque to power ratio and power consumption [1]

- Torque Rods

A magnetic torque rod is an actuator used for satellite attitude control. The approach is to generate a controllable magnetic moment that interacts with the Earth's magnetic field to produce a resultant torque and adjust the satellite's position accordingly [6].

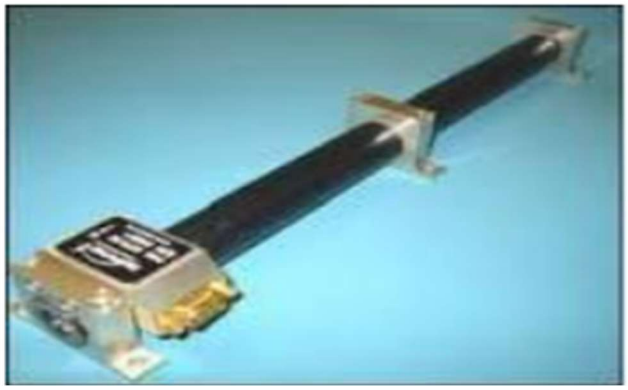


Figure 1.7 - Magnetic torque rod [6]

To better understand the theoretical relation, research was made about torque output optimization of torque rode magnetorquers and the results are shown in Figures 1.8 - 1.9 below.

On Figure 1.8, it is seen that different variations were configured on a torque rode magnetorquer to see resultant torque impact vs current. Comparing the same number of coils in series and parallel, the parallel one is capable of producing more torque, 1417 N - m, with more provided current while the one in series has a limitation and cannot generate more than 354.2 N - m. Single coil approach has a constant increase as parallel coils do but also experiences the

limitation the coils in series and the hybrid combination do. Depending on the resultant torque requirement and current availability, these configurations offer different approaches and availability with variety.

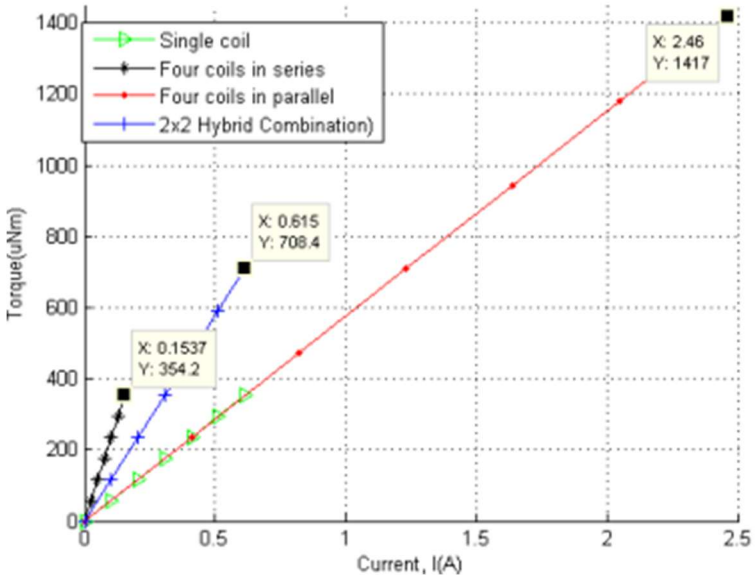


Figure 1.8 - Torque vs current [6]

On Figure 1.9, it is seen that different variations were configured on a torque rode magnetorquer to see resultant torque impact vs voltage. For the torques generated comparison, each configuration required the same amount of voltage, 18V. Comparing the same number of coils in series and parallel, the coils in parallel can generate more torque, 1417 N - m vs the coils in series, 354.2 N - m. While the single coil and 4 coils in series produced the same amount of torque, meaning multiple coils in series do not have impact regarding resultant torque vs voltage consumed, the hybrid approach produced 708.4 N - m resultant torque. Thus, regarding voltage consumption, using multiple coils in parallel will result in more torque.

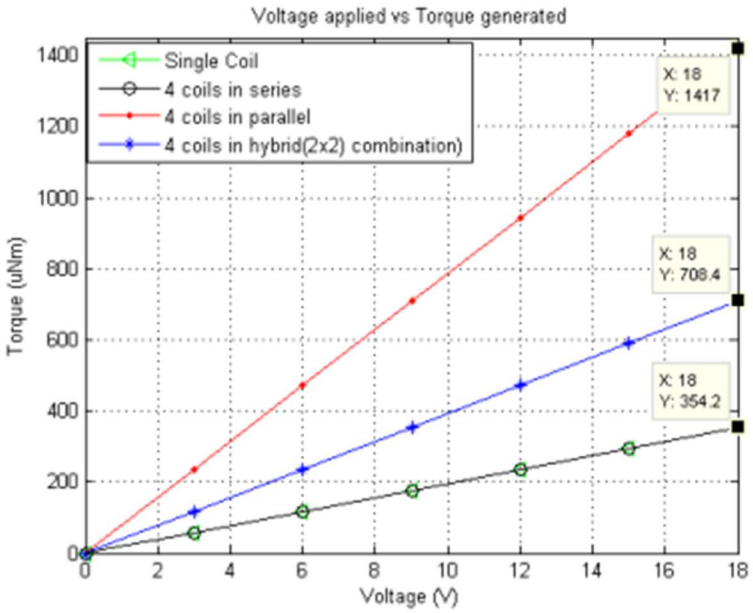


Figure 1.9 - Torque vs voltage [6]

- Air Core

An air-core magnetorquer consists of wire coils wound around a non-magnetic core and generates a magnetic moment linearly proportional to current: this dipole moment interacts with Earth's magnetic field to provide attitude control torque, avoiding ferromagnetic hysteresis and core losses [7]. An air core magnetorquer design is provided with w (width), h (height), d (depth), t (thickness) dimensions in Figure 1.10, below.

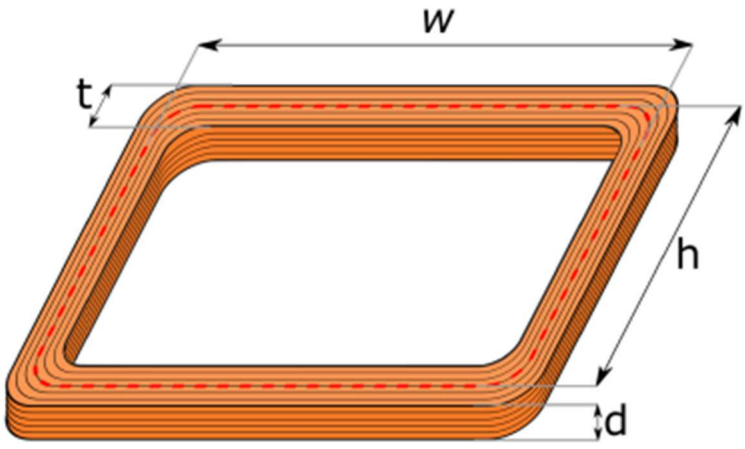


Figure 1.10 - Air core magnetorquer design [8]

The unique side of the air core magnetorquer for this report is that the number of current loops, N, is calculated by multiplying the thickness by the depth and the wire packing factor, κ describing the number of turns of wire for a unit of area [8].

$$N = \kappa \cdot t \cdot d \tag{1.3}$$

Therefore, from a theoretical standpoint, increasing the depth, packing factor or the thickness of the air core magnetorquer will lead to more dipole moment created referring to eq. 1.2, thus more torque generated, referring to eq. 1.1.

Integration of magnetorquer involves various approaches. The main integration ways involve PCB Printed magnetorquers, air core magnetorquers and torque rode magnetorquers. Multiple factors are considered to make the necessary integration choice:

- Magnetic dipole moment capability
    - The generated magnetic dipole determines how much torque the device can provide given the ambient magnetic field.
    - For torque rods with ferromagnetic core, the dipole obtained is higher per coil size compared with air-core coils.
    - PCB-integrated coils have lower dipole moments because of trace thickness and limited number of turns [9].
- Mass, volume, structural integration
    - A PCB-printed coil has advantages in terms of minimal volume since it can be integrated into existing board or structure, saving space [10].
    - Torque rods have a ferromagnetic core and are heavier, occupy a discrete volume, and require structural mounting [9].
    - Air-core coils can be lighter than rod cores, but may need larger area to achieve comparable moments, which can increase volume or power [11].
- Power consumption and driver electronics
    - Achieving a given magnetic moment with a smaller coil area or fewer turns means higher current or voltage needed, which impacts power budget and driver design. For example, PCB coils may need higher current because of limited area [10].
    - Torque rods with ferromagnetic cores can achieve higher moments for given current because the core amplifies the field [9].
    - Air-core coils require more windings and/or larger area for the same moment, so they may consume more power (or have larger volume) [11].
- Residual magnetism / disturbance effects
    - A known drawback of using ferromagnetic cores in torque rods is that the core material can retain some magnetization when powered off, which may disturb sensitive instruments such as magnetometers or create unwanted bias [11].
    - Air-core and PCB-based coils, without ferrous core, generally have negligible residual magnetization when turned off, so less risk of leftover fields.
- Manufacturing and structural complexity / integration risk

    - PCB-integrated magnetorquers offer efficient packaging but designing them requires careful coil design in terms of trace widths, layers, thermal/structural considerations [10].
    - Torque rods are more "standard" actuator form-factors (wire wound around ferrous core) and may have more commercial heritage, but need structural mounting, possible demagnetization cycles, and may impose mounting constraints [12].
    - Air-core coils might need custom winding or location on spacecraft structure, and their geometry may be constrained by available area.
- Thermal / environmental / magnetic environment
    - The local ambient magnetic field strength influences actuator effectiveness [11].
    - Thermal, vibration, structure, and stray fields must be considered such as how the coil heat affects the board, how vibrations affect winding integrity. PCB traces may have thermal current limits. PCB magnetorquer design specifically studied trace width, number of turns, and thermal dissipation [10].
    - Thermal behavior of embedded coil designs introduces a constraint that operates in parallel with magnetic performance. Through detailed thermal modeling of reconfigurable PCB integrated magnetorquers, coils arranged in series produce the lowest power dissipation for a given dipole moment while compact single coil configurations generate the highest temperature rise among configurations studied [13].
- Mission functionality / control objectives
    - Is the magnetorquer used for momentum dumping, coarse detumbling, or fine pointing? The torque levels and bandwidth requirements vary significantly. For high agility or rapid detumble, more torque margin might be needed. For small residual corrections, PCB or air-core may suffice [9].
    - Magnetorquers can only exert torque perpendicular to the ambient magnetic field. They cannot generate arbitrary 3-axis torque at any given instant. Thus, the actuator must be sized accordingly and used along with other actuators if needed [12].
    - Magnetometers can be used as the sole sensor for effective B-dot detumbling with use of algorithms that estimate angular rate via magnetometer data, removing the dependence on gyroscopes or sun sensors [14].

While different types of magnetorquers have their advantages and disadvantages, a fundamental limitation shared across all magnetorquer configurations is the inherent under

actuation of the generated force. Because the interaction of a magnetic dipole with the geomagnetic field always produces a torque perpendicular to the local field vector, no control authority exists along that direction at any given instant. Lovera and Astolfi demonstrated that full three axis attitude stabilization remains achievable over a complete orbit by exploiting the time varying nature of the geomagnetic field, provided the control law is designed accordingly [15]. In practice, this means the coil must be sized for worst case field geometry along the orbit, and the control system must accumulate unsatisfied torque demands until favorable field orientations are encountered.

Table 1.1 - Summary of pros & cons of magnetorquers integration ways

Integration Way	Pros	Cons
PCB Printed	● Compact ● Minimal added mass/volume ● Integrates into structure or board ● Good for small satellites where packaging is tight [10].	● Lower magnetic moment for given size/current ● May need higher current/voltage ● Trace width, layer count, thermal limits are design constraints
Torque Rode	● High torque per current/volume ● Efficient power usage for given moment [9]	● Requires structural mounting ● Residual magnetization risk which may complicate structural layout
Air Rode	● Simpler construction ● No residual magnetization [12] ● Flexible layout	● Larger coil area or more turns needed per torque generated ● May consume more power or need more board/panel space.

1.3 Project Proposal

This project will design, test. simulate, and assess the performance of a magnetorquer in ADCS capable of providing continuous positioning, navigation, and orientation to a 2U satellite with the mission goal of demonstrating a functional VR (Virtual Reality) experiment in LEO that involves a novel cislunar navigation payload with a software defined radio. The unique side of

the project will be that the SpartanSAT will be specifically designed to obtain accurate data of the crescent moon with the magnetorquer design case study parameters that will be obtained by the research executed in this report. The current control systems, in the industry, can't process the crescent moon due to the radical visualization differences between the two sides of the moon.

The following research questions will guide this investigation:

- What is the optimal way to design a magnetorquer that will interact with the rest of the ADCS?
- What type of magnetorquer should be used to maximize the generated torque and orientation capabilities?
- What types of control algorithms should be used to prevent communication & data latency?
- How can the coil geometry (number of sweep turns, area) be optimized to maximize magnetic dipole strength while maintaining component integrity?
- What trade-offs exist between power consumption, torque output, and altitude for different coil configurations?
- How do orbital altitude and inclination influence magnetorquer efficiency, and can adaptive control strategies be implemented to compensate for variations in Earth's magnetic field?

This research investigation aims to fulfill the current control systems with insufficient star tracker capabilities and bring a new approach by creating a magnetorquer based ADCS that will be able to track accurate data of the moon.

1.4 Methodology

This project will be started by sophisticated academic research on satellite(s) / satellite constellations, in LEO that have utilized magnetorquers in their ADCS and additionally, preferably, copper coils. The literature review will be then followed by identifying existing design methodologies, control strategies, and performance trade-offs to establish realistic design parameters and performance benchmarks for this project. The next step will be modeling and simulation of the magnetorquer design. Creating control algorithms, determination of reference frames, design & optimization, and SpartanSAT mission specific validation will be part of modeling and simulation.

Table 1.2 – Gantt chart for AE295

Objective	**08/25**	**09/25**	**10/25**	**11/25**	**12/25**	**01/26**	**02/26**	**03/26**	**04/26**
Literature Review	✓	✓	✓	✓					

Methodology	✓	✓	✓	✓	✓				
Modeling				✓	✓	✓	✓	✓	✓
Simulation					✓	✓	✓	✓	✓
Software Testing						✓	✓	✓	✓
Discussion									✓
Future Work / Conclusion									✓

2. Modeling

2.1 Modeling Setup

SpartanSAT's attitude dynamics and its interaction with Earth's magnetic field will be modeled. The IGRF (International Geomagnetic Reference Field) will serve as the baseline geomagnetic model to simulate the time-varying magnetic environment. Simulations will be conducted in MATLAB/Simulink to model the spacecraft dynamics and control behavior with corresponding orbital conditions and environmental parameters.

2.2 Magnetorquer Design and Optimization

Multiple magnetorquer coil designs will be developed, each varying by:

- Wire gauge
- Number of turns
- Coil geometry (e.g. thickness) and cross-sectional area
- Mounting orientation
- Magnetorquer cross-sectional area

2.3 Simulation and Control Algorithm Development

Each design variant will be simulated in MATLAB to predict:

- Torque output under various geomagnetic conditions
- Power consumption and efficiency
- Response time and detumbling performance

Attitude control algorithms will be implemented to command coil currents in response to body-frame magnetic field variation and angular velocity. The control parameters will be tuned to achieve stable and responsive behavior within operational constraints. Comparative analysis will be performed to identify the optimal coil configuration and control law combination. The performance optimization goal revolves around the parameters of the magnetic moment, power consumption, and mass while varying the rod geometry, number of turns, and the current.

The algorithm will be constructed by the necessary input geometry to calculate geometrical parameters, and the associated demagnetizing factor strongly influences the achievable magnetic dipole moment. After inputting the geometry parameters, the algorithm will go through a range of current values and calculate magnetic moments to analyze the relation between current values and turns.

The algorithm will then progress into evaluating practical constraints by determining the maximum allowable current for the chosen geometry and computing the resulting power consumption to understand limitations in terms of electrical power availability further plotting the consumed power vs coil configuration as part of the geometry.

Additionally, a feedback loop will check whether the power requirement and number of turns are realistic, reflecting the iterative nature of magnetorquer design.

Lastly, the feedback loop will be designed though a B-dot controller. This type of controller was chosen because its control law is the most widely adopted control algorithm for initial detumbling of magnetically actuated small satellites [16]. The method commands a dipole moment proportional to the measured rate of change of the body frame magnetic field, producing a dampening torque that opposes the spacecraft angular velocity. Avanzini and Guilietti provided a rigorous proof of global asymptotic convergence from arbitrary initial tumbling conditions and proposed a quasi-optimal gain criterion scaled to the orbital rate, requiring only a three-axis magnetometer with no additional rate sensors [16]. Detumbling time and final residual angular rate remain dependent on the achievable dipole moment and orbital inclination, both of which must be considered also during coil sizing.

2.4 Reference Frames

While algorithm development is a crucial factor in simulation, another critical point is the determination of the necessary reference frame. For the most optimal results amongst the available reference frames, geocentric inertial frame, earth fixed frame, polar coordinate frame, orbital frame, and the vehicle frame, earth fixed frame will be observed to ensure the integrity of the simulation.

Table 2.1 - Designated reference frames

Reference Frame	Base Vectors
Geocentric Inertial Frame	$\mathbf{X}_I, \mathbf{Y}_I, \mathbf{Z}_I$
Earth Fixed Frame	$\mathbf{X}_E, \mathbf{Y}_E, \mathbf{Z}_E$
Polar Coordinate Frame	$\mathbf{X}_B, \mathbf{Y}_B, \mathbf{Z}_B$
Orbital Frame	$\mathbf{X}_F, \mathbf{Y}_F, \mathbf{Z}_F$
Vehicle Frame	$\mathbf{X}_S, \mathbf{Y}_S, \mathbf{Z}_S$

2.4.1 Geocentric Inertial Frame

Geocentric Inertial Frame is a nonrotating, Earth referenced frame with its origin located in the center of the Earth. The $\mathbf{Z}_I$-axis is directed along the Earth's mean rotational axis, positive north. The $\mathbf{X}_I$- axis is directed toward the mean vernal equinox. The $\mathbf{Y}_I$-axis completes a standard right-handed system [17].

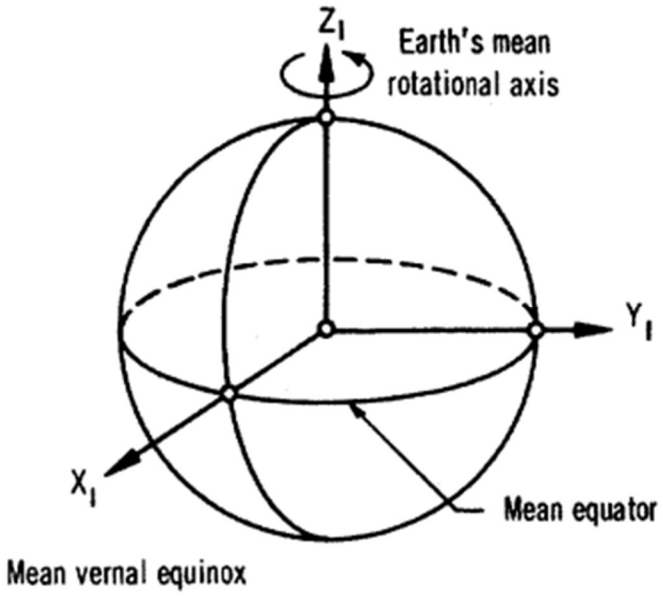


Figure 2.1 - Geocentric inertial reference frame [17]

2.4.2 Earth Fixed Frame

Earth Fixed Frame is a rotating, Earth referenced frame with its origin located in the center of the Earth. The $\mathbf{Z}_E$-axis is directed along the Earth's mean rotational axis, positive north. The $\mathbf{X}_E$-axis is positively directed through the Earth's Equator at the meridian of Greenwich. The $\mathbf{Y}_E$-axis completes a standard right-handed system [17].

2.4.3 Polar Coordinate Frame

Polar Coordinate Frame is a rotating, Earth referenced frame with its origin located in a random point in space, P. The $\mathbf{Z}_B$-axis is directed along the radius connecting point P to the Earth's center positive outward. The $\mathbf{X}_B$-axis is directed along the local meridian toward increasing theta. The $\mathbf{Y}_B$-axis completes a standard right-handed system [17].

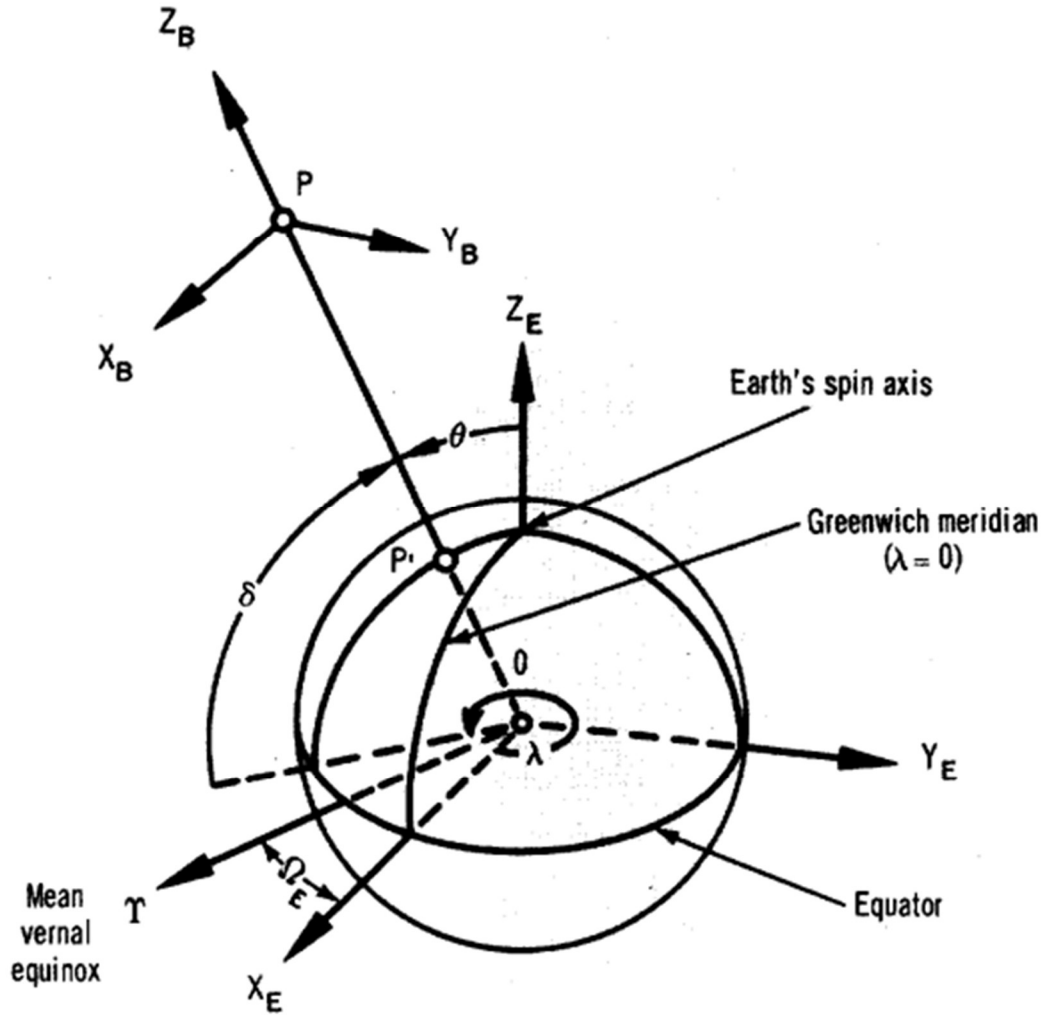


Figure 2.2 - Earth fixed frame and polar coordinate frame [17]

In Figure 9, above, P' is the point on the Earth's surface on the line joining O and P. R is the distance from Earth's center to P. R_e is the distance from Earth's center P'. Ω_E is the right ascension of the Greenwich meridian measure positive eastward. λ is the geocentric longitude, measured positive eastward from the Greenwich meridian to the meridian containing P'. δ is the geocentric latitude. θ is the geocentric colatitude ($90^o - \delta$) [17].

2.4.4 Orbital Frame

Orbital Frame is a rotating, Earth referenced frame with its origin located in the vehicle center of mass. The $\mathbf{Z}_F$-axis is along a line joining the Earth's center and the vehicle's center of mass, positive toward the Earth. The $\mathbf{X}_F$-axis is in the orbital plane normal to $\mathbf{Z}_F$ and positive in the sense of forward motion along the orbit. The $\mathbf{Y}_F$-axis completes a standard right-handed system [17].

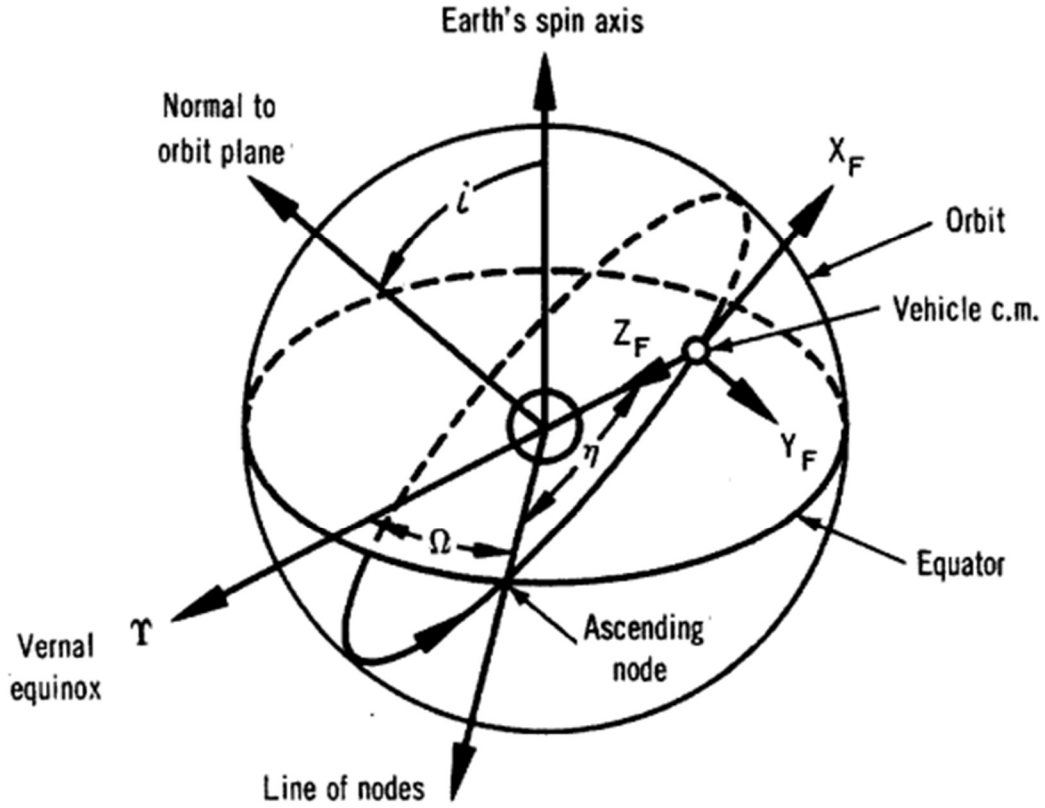


Figure 2.3 - Orbital reference frame [17]

In Figure 10, above, Ω is the angle in the equatorial plane between the vernal equinox and the ascending node. *i* is the orbital inclination which is the angle between the equatorial plane and the orbital plane. η is the angle locating the vehicle in orbit measured from the ascending node [17].

2.4.5 Vehicle Frame

Vehicle Frame is a rotating, vehicle referenced frame with its origin located in the vehicle center of mass. The $\mathbf{X}_S$-axis is along the vehicle longitudinal axis of symmetry. The $\mathbf{Y}_S$-axis is a principal axis of inertia. The $\mathbf{Z}_S$-axis is a principal axis of inertia orthogonal to the $\mathbf{X}_S$ and $\mathbf{Y}_S$ planes [17].

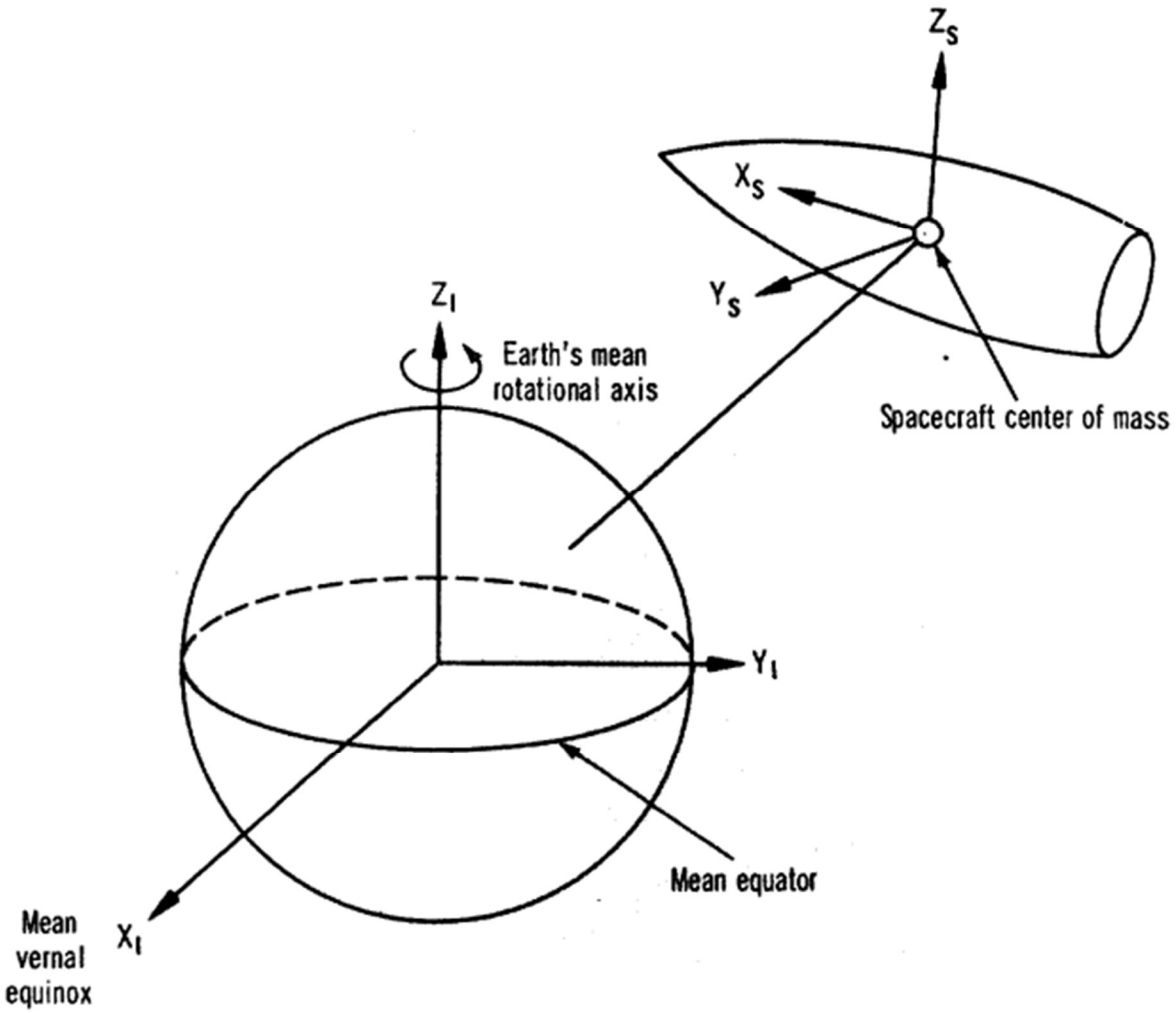


Figure 2.4 - Vehicle frame [17]

2.5 Evaluation and Implementation

The performance of the final design and control strategy will be quantitatively evaluated using key performance metrics such as:

- Generated magnetic dipole moment
- Torque output
- Power-to-torque efficiency
- Attitude stabilization accuracy and settling time

3. Testing

Testing is one of the crucial parts to validate the functionality of the magnetorquer that will be designed. In the testing phase the following aspects will be evaluated:

- Verify that the magnetorquer produces the required magnetic dipole moment per design.
- Confirm that the magnetorquer actuates correctly under command signals.
- Validate that the attitude control system using the magnetorquer produces the desired attitude/orientation changes under realistic magnetic field conditions.
- Ensure reliability under various orbit altitudes.

The accurate measurement of the magnetic moment generated by the magnetorquer will be accomplished in a controlled magnetic software test environment, if possible, to null out ambient magnetic fields, then apply current and measure the field produced [18].

The magnetorquer will be commanded in various cases to verify that current flows correctly, coil resistance and voltage & current draw are within expected limits. This will be useful to detect incorrect coil parameters [19].

The testing will be carried out in a full software phase. This report is solely focused on software design and algorithm development.

The testing concept will be based on a B-dot software test approach. B-dot probes, also known as inductive magnetic field probes, are beneficial to conduct performance measurements in electric space thrusters where a time-varying magnetic field is present [20].

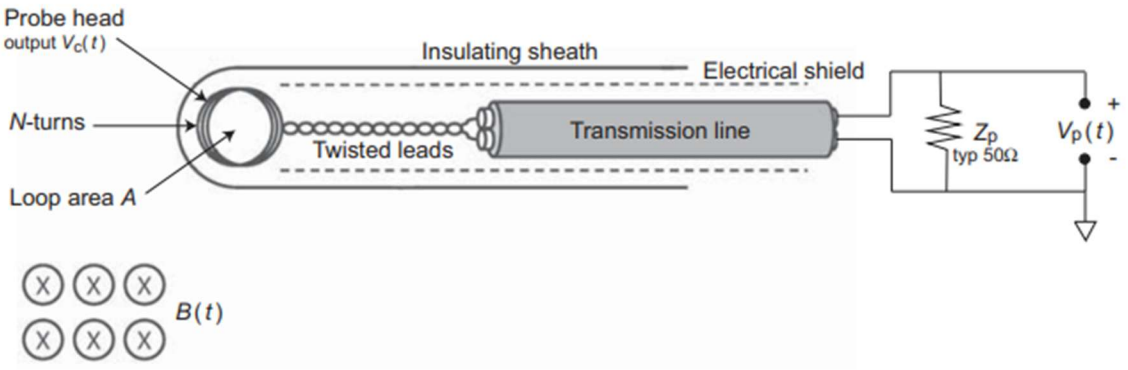


Figure 3.1 - Schematic illustration of a B-dot probe [20]

4. Simulation

To find and optimize the magnetorquer design a MATLAB simulation was developed and run based on various coil geometric features, SpartanSAT mission specific parameters and satellite geometry. In this simulation, spacecraft rigid-body attitude dynamics, orbit propagation, Earth magnetic field modeling using IGRF, quaternion-based frame transformation, B-dot, detumbling control, magnetorquer coil actuator limits and power, voltage, current, dipole performance tracking were taken into account to provide real-life-mission specific outcome data to follow a realistic software based approach further translating into hardware component design in the future.

4.1 Simulation Setup

The simulation starts off by the definition of the state vectors. The SpartanSAT state, x, quaternion attitude state, q, body frame angular velocity, ω, and the full state, x_f vectors are defined by:

$$x = \begin{bmatrix} q \\ w \end{bmatrix}, q = \begin{bmatrix} q_0 \\ q_1 \\ q_2 \\ q_3 \end{bmatrix}, \omega = \begin{bmatrix} \omega_x \\ \omega_y \\ \omega_z \end{bmatrix}, x_f = \begin{bmatrix} q_0 \\ q_1 \\ q_2 \\ q_3 \\ \omega_x \\ \omega_y \\ \omega_z \end{bmatrix} \tag{4.1}$$

The inertia matrix, J, represents the SpartanSAT's resistance to angular acceleration about its body axes. The principal moments of inertia J_x, J_y, J_z, are calculated via spacecraft dimensions in the **x**, **y**, **z** axis and its mass $\boldsymbol{m}$ = 2.66 kg. For the calculation of the inertia matrix, it was assumed that the SpartanSAT's mass is uniformly distributed and the principal axes align with the body axes.

$$J = \begin{bmatrix} J_x & 0 & 0 \\ 0 & J_y & 0 \\ 0 & 0 & J_z \end{bmatrix} \tag{4.2}$$

$$J_x = \frac{1}{12}\boldsymbol{m}(y^2 + z^2)\ ,\ J_y = \frac{1}{12}\boldsymbol{m}(x^2 + z^2),\ \ J_z = \frac{1}{12}\boldsymbol{m}(x^2 + y^2) \tag{4.3}$$

Initial quaternion attitude, q_0, was assumed that SpartanSAT initially starts aligned with the inertial reference frame. The initial attitude is taken as identity to isolate the detumbling behavior. For B-dot detumbling, the main variable of interest, for this simulation, is angular velocity, not precise initial pointing.

$$q_0 = \begin{bmatrix} 1 \\ 0 \\ 0 \\ 0 \end{bmatrix} \tag{4.4}$$

The initial angular velocity, ω_0, was a value determined by analyzing multiple research papers working on similar projects. Per a CubeSat attitude stabilization project with a B-dot controller and similar mission specs in University of Blida 1 [21], the values 0.45 rad/s (25.8 deg/s), 0.35 rad/s (20.1 deg/s), and 0.40 rad/s (22.9 deg/s) for **x**, **y**, **z** axis were utilized respectively with the resultant magnitude of 39.9 deg/s. Per another similar study about satellite life cycles in Aalborg University Department of Control Engineering [22], an angular velocity of 0.1 rad/s (5.7 deg/s) for each axis with the resultant magnitude of 9.9 deg/s. The satellite structure in the study at Aalborg University consisted of a high-definition camera. Since one of the mission goals of SpartanSAT is to contribute to cislunar navigation, it will contain a camera in the satellite body, too. Therefore, initial angular velocity selection was made closer to 9.9 deg/s rather than 39.9 deg/s. It is important to note that depending on the delta in the mission specs, the source code in Appendix A can easily be modified since this angular velocity value below is a representative post-deployment tumbling case, not a measured SpartanSAT value.

$$\omega_0 = \begin{bmatrix} 8 \\ -6 \\ 5 \end{bmatrix} \frac{deg}{s}, |\omega_0| = \sqrt{8^2 + (-6)^2 + 5^2} = 11.2 \frac{deg}{s} \tag{4.5}$$

To capture the nonlinear rigid-body coupling between axes, the simulation is solving for the angular acceleration, $\dot{\omega}$, based on core rotational dynamics using Euler's rigid body equations. For the calculation of torque output, T, equation (1.1) is utilized. For more information in magnetorquer physics about dipole moments in this simulation, refer to equation (1.2).

$$J\dot{\omega} + \omega \times (J\omega) = T \leftrightarrow \dot{\omega} = J^{-1}[T - \omega \times (J\omega)] \tag{4.6}$$

The quaternion derivative is modeled below to indicate how fast the spin motion is, where the vehicle is pointing, and how the spinning motion changes where the vehicle is pointing.

$$\dot{q} = \frac{1}{2}\boldsymbol{Q}(\omega)q \quad , \quad \boldsymbol{Q}(\omega) = \begin{bmatrix} 0 & -\omega_x & -\omega_y & -\omega_z \\ \omega_x & 0 & \omega_z & -\omega_y \\ \omega_y & -\omega_z & 0 & \omega_x \\ \omega_z & \omega_y & -\omega_x & 0 \end{bmatrix} \tag{4.7}$$

For orbit propagation, Earth gravitational parameter, $\mu = 3.986004418 \times 10^{14} \frac{m^3}{s^2}$ value was used with radius of Earth, $R_E = 6371$ km.

The following orbital parameters were computed in the simulation:

- Perigee altitude in terms of h_p, height of the satellite above the Earth's surface at its closest point,

$$r_p = R_E + h_p \tag{4.8}$$

- Apogee altitude in terms of h_a, height of the satellite above the Earth's surface at its highest point,

$$r_a = R_E + h_a \tag{4.9}$$

- Semi-major axis,

$$a = \frac{r_a + r_p}{2} \tag{4.10}$$

- Eccentricity,

$$e = \frac{r_a - r_p}{r_a + r_p} \tag{4.11}$$

- Semi-latus rectum,

$$p = a(1 - e^2) \tag{4.12}$$

- Mean motion,

$$n = \sqrt{\frac{\mu}{a^3}} \tag{4.13}$$

- Mean anomaly,

$$M = nt \tag{4.14}$$

- Kepler's equation in terms of eccentric anomaly, E,

$$M = E - esin(E) \tag{4.15}$$

- True anomaly,

$$v = 2\arctan\left(\frac{sin\left(\frac{E}{2}\right)\sqrt{1+e}}{cos\left(\frac{E}{2}\right)\sqrt{1-e}}\right) \tag{4.16}$$

- Perifocal position,

$$r_{pf} = \frac{p}{1+ecos(v)}\begin{bmatrix}\cos(v)\\ \sin(v)\\ 0\end{bmatrix} \tag{4.17}$$

The simulation uses an IGRF-based geomagnetic model. It takes the spacecraft position in ECI (Earth-Centered Inertial axis) and simulation time, converts the position to geodetic latitude, longitude, and altitude, evaluates the IGRF model, and rotates the magnetic field back into ECI. This frame is centered at the Earth's center of mass and remains fixed relative to inertial space, allowing the application of Newton's laws without additional rotational terms.

The B-dot controller logic was established by the magnetic field expressed in the SpartanSAT body frame, B_{body}, since the magnetorquer coils are body-fixed with the commanded dipole moment, M_{cmd}. B_{body} was obtained by the ECI-to-Body magnetic field transformation through inertial to body frame in Appendix A, "spacecraft_dynamics.m" utilizing quaternion computation of direction cosine matrix. Controller logic is as below where k is the controller gain:

$$M_{cmd} = -k\dot{B}\ , \qquad \frac{dB_{body}}{dt} \approx -\omega \times B_{body} \tag{4.18}$$

Re-arranging,

$$M_{cmd} = -k\left(-\omega \times B_{body}\right) = \omega \times B_{body} \tag{4.19}$$

Based on specified initial resistance, voltage, and current, simulation is calculating the commanded and actual values for them based on M_{cmd}. First, the current needed in the coil to generate designed dipole moment, I_{req}, is calculated where A is the coil area.

$$I_{req} = \frac{M_{cmd}}{N * A} \tag{4.20}$$

Then the corresponding voltage, V, values were calculated using Ohm's law for the commanded current, I_{cmd}, obtained by the iteration for maximum and minimum current values where R corresponds to resistance.

$$V = I_{cmd}R \tag{4.21}$$

If the required voltage exceeds the bus voltage, initial set design value, the current is reduced:

$$I = \frac{V_{max}}{R} \tag{4.22}$$

The actual generated dipole moment, M_{actual}, and coil power, P, are generated as follows:

$$M_{actual} = N * A * I_{cmd} \tag{4.23}$$

$$P = {I_{req}}^2 R \tag{4.24}$$

Finally, after the actuator produces M_{actual}, the body-frame output torque, T_{body} is evaluated, and further applied directly into Euler's rotational equation while checking for kinetic energy, KE.

$$T_{body} = M_{actual} \times B_{body} \tag{4.25}$$

$$\dot{\omega} = J^{-1}\left[T_{body} - \omega \times (J\omega)\right] \tag{4.26}$$

$$KE = \frac{1}{2}\omega^T J\omega \tag{4.27}$$

4.1.1 Further Assumptions

Throughout the simulation, there were many assumptions made to ensure mission specific conditions. The assumptions vary amongst orbital mechanics, coil geometry, and detumbling fine pointing:

- Simulation assumes:
    - Two-body orbit propagation
    - No drag

    - No atmospheric decay
    - Circular or near-circular orbits are used for sensitivity studies, e = 0 or e ≈ 0.
- Coil design assumes:
    - Three identical orthogonal coils
    - Each coil has the same number of turns
    - Each coil has the same area
    - Each coil has the same resistance
    - Current and voltage limits are symmetric in positive and negative directions
    - Inductance and current rise time are neglected
- The range for detumbling and fine pointing is determined as $|\omega| < 0.5 \frac{deg}{s}$
- The spacecraft orbit and rotation were assumed and modeled as Figure 4.1 below.

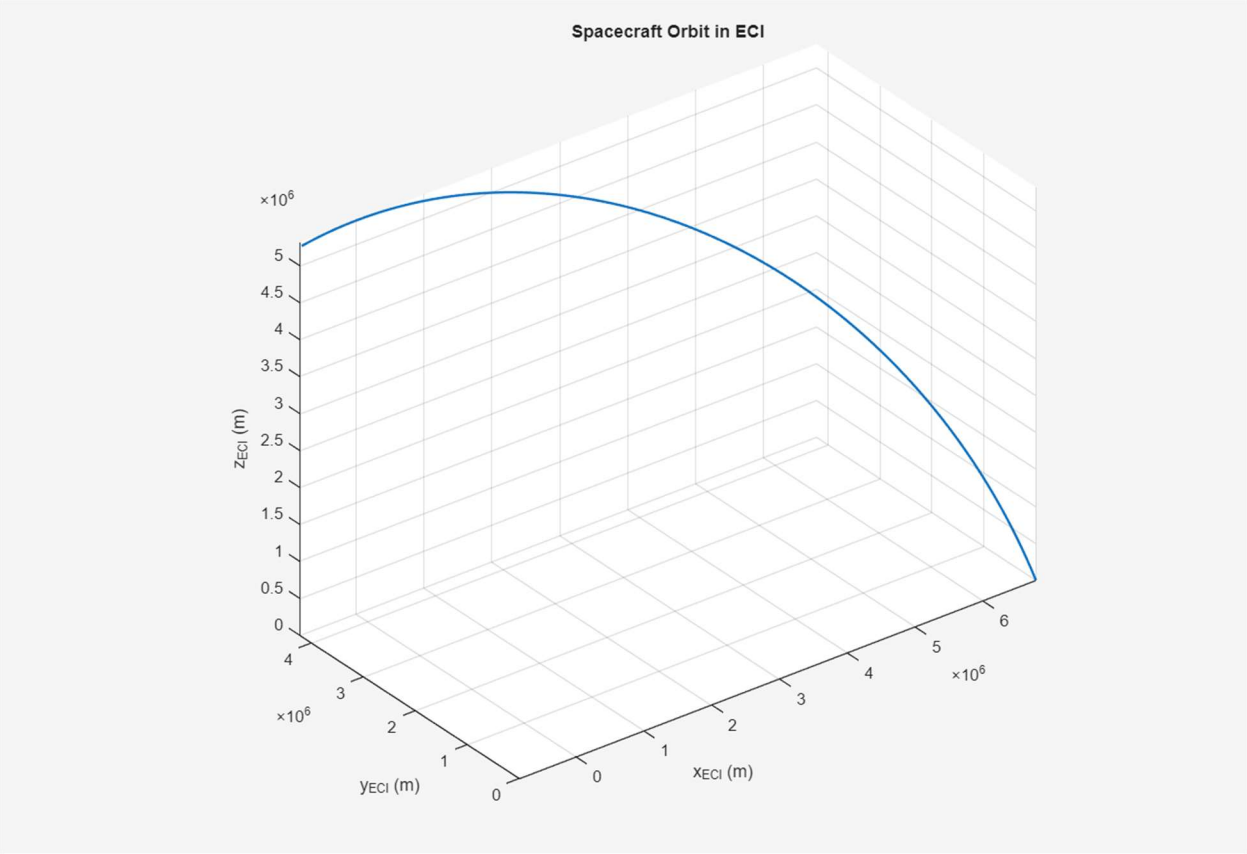


Figure 4.1 - Orbit and axis assumption

4.2 Uncontrolled Tumbling Response

The uncontrolled tumbling response was analyzed by setting the control gain, k, to zero, effectively disabling the magnetorquer system and resulting in zero commanded dipole moment.

Under these conditions, the spacecraft dynamics reduce to pure torque-free rigid-body motion governed by Euler's equations.

Coil parameters that were fixed for uncontrolled tumbling response:

Table 4.1 – Fixed parameters for uncontrolled tumbling response

N turns	B-dot controller gain, k	Coil area, (m^2)	Coil resistance (Ohms)	Coil max current (A)	Coil max voltage (V)
200	0	0.01	4.4	0.15	12

The simulation generates plots for angular velocity magnitude and its components, kinetic energy, commanded vs actual dipole moment, coil current, voltage and power, and finally the error for generated dipole moment.

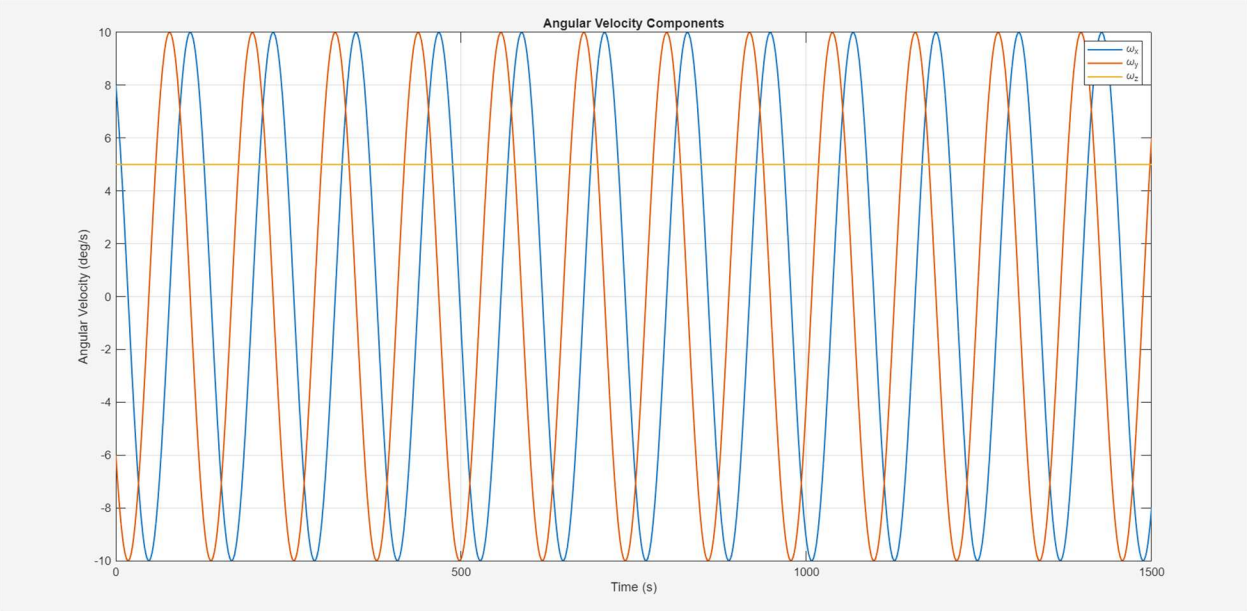


Figure 4.2 – Angular velocity components uncontrolled tumbling response

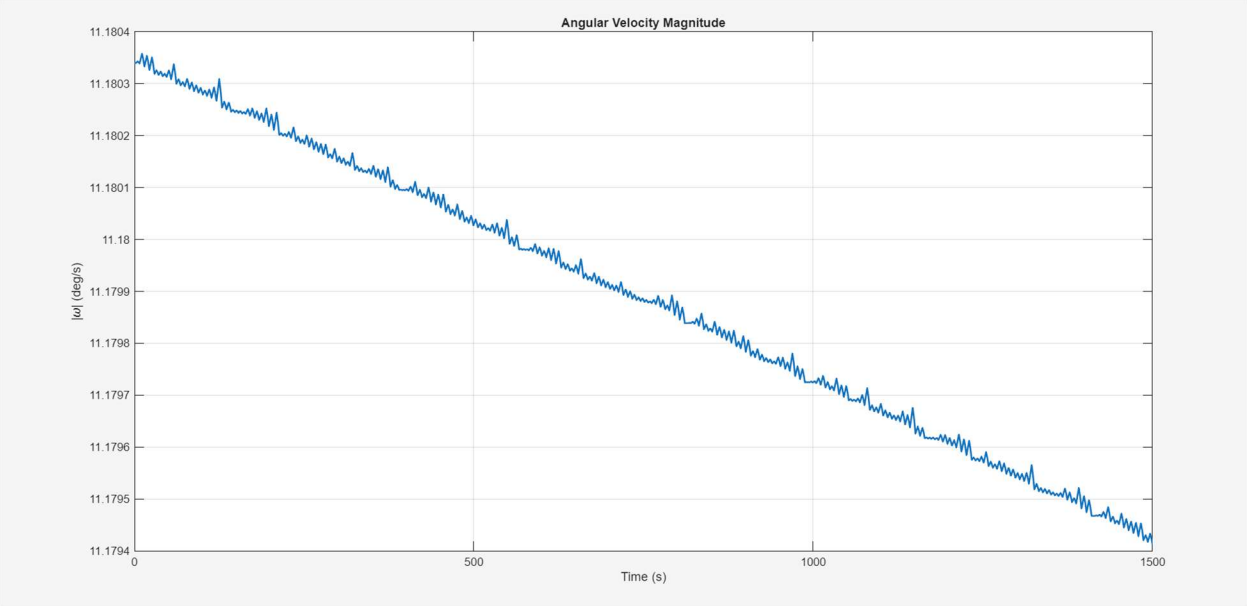


Figure 4.3 – Angular velocity magnitude uncontrolled tumbling response

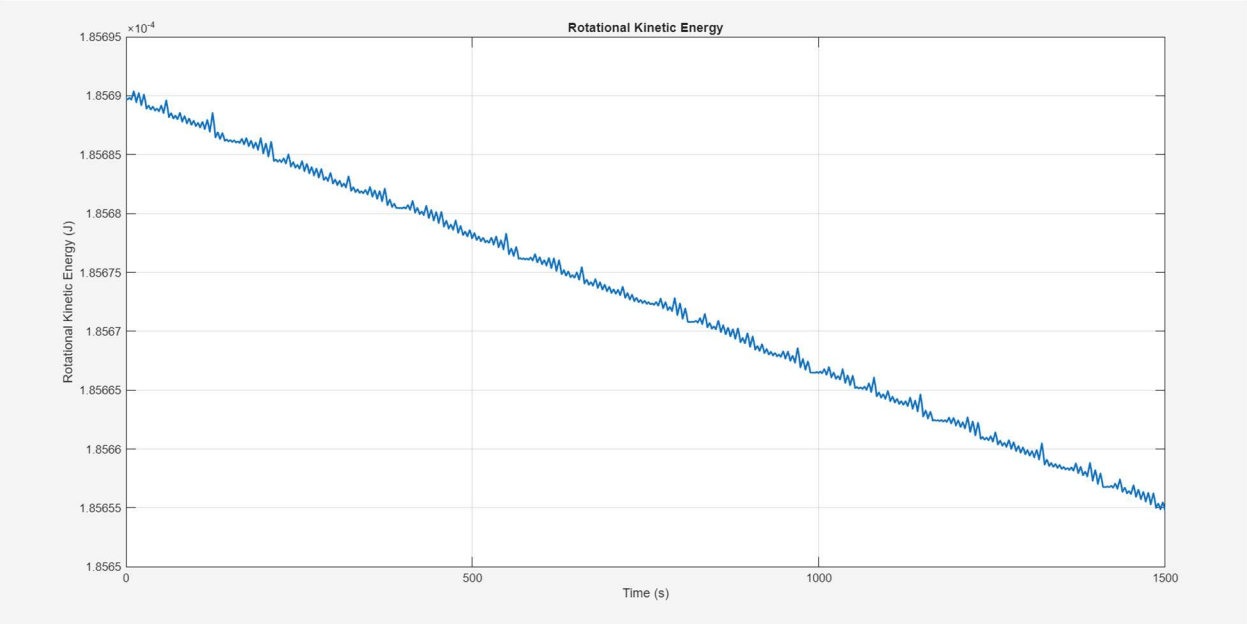


Figure 4.4 – Rotational kinetic energy uncontrolled tumbling response

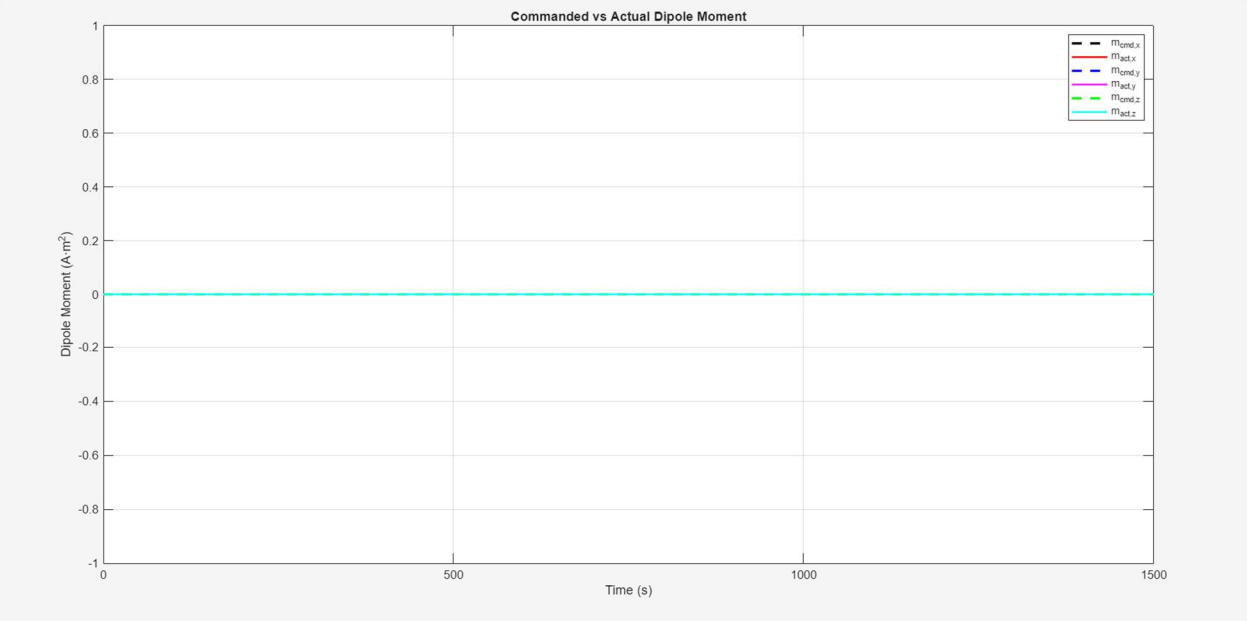


Figure 4.5 – Commanded vs actual dipole moment uncontrolled tumbling response

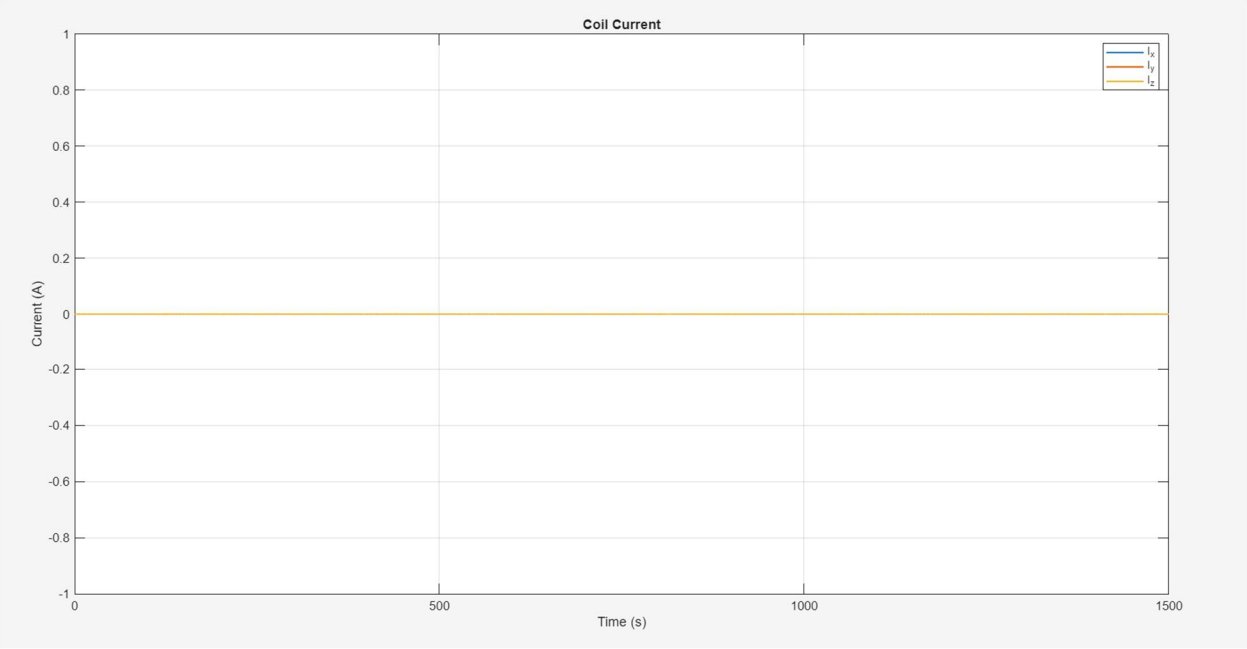


Figure 4.6 – Coil current uncontrolled tumbling response

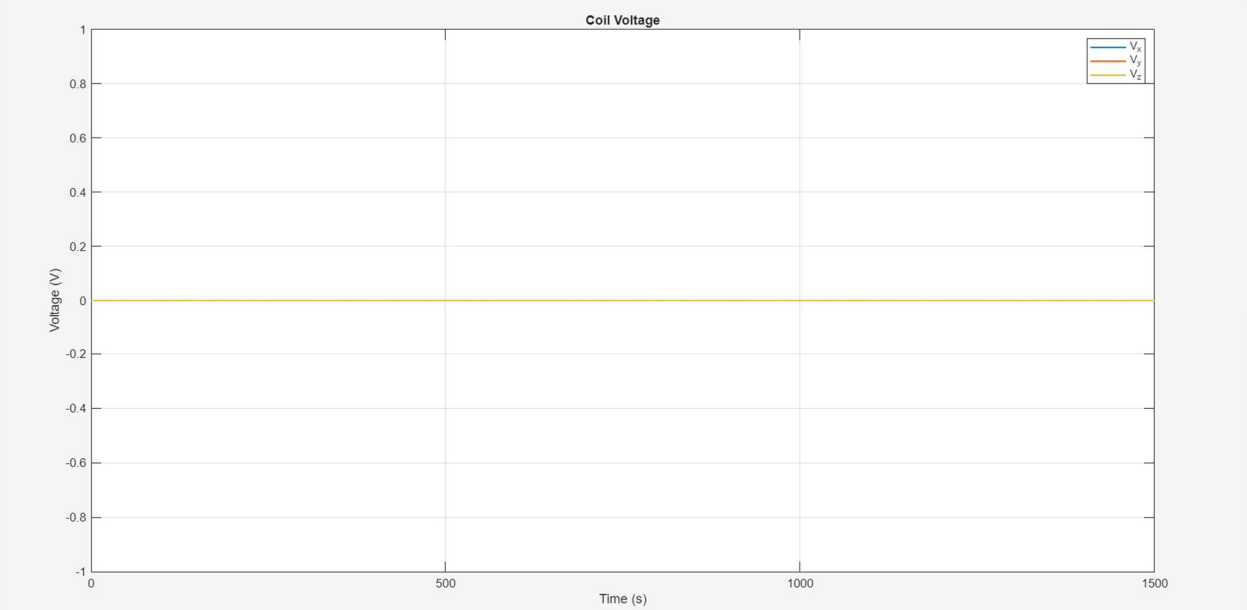


Figure 4.7 – Coil voltage uncontrolled tumbling response

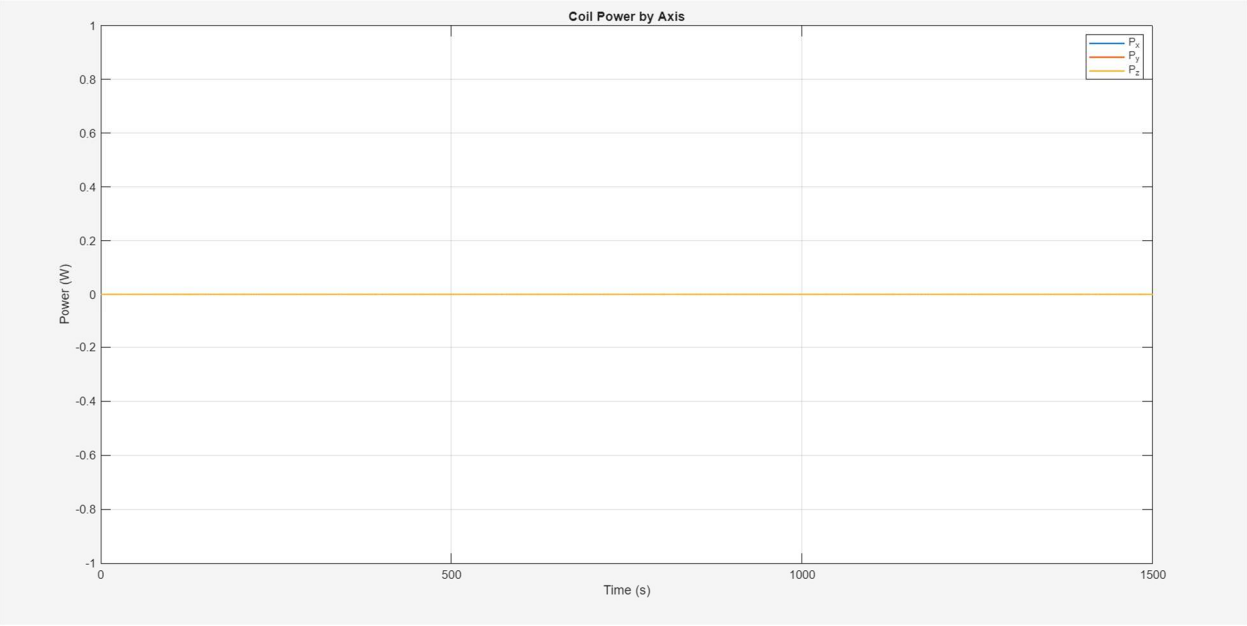


Figure 4.8 – Coil power uncontrolled tumbling response

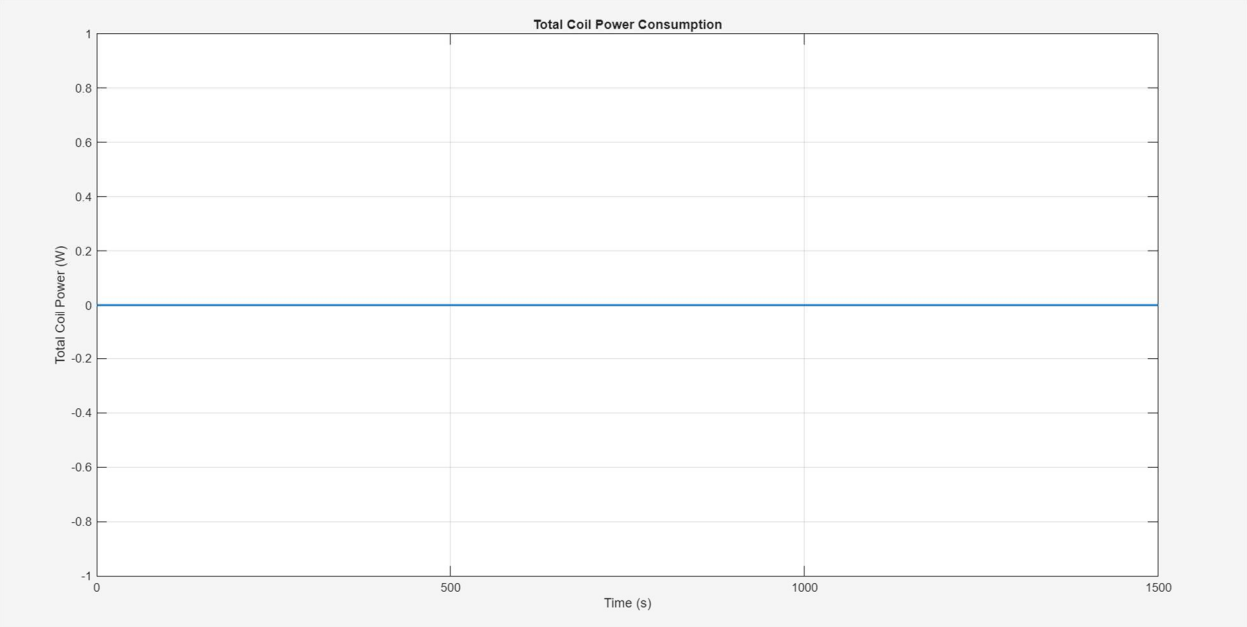


Figure 4.9 – Total coil power consumption uncontrolled tumbling response

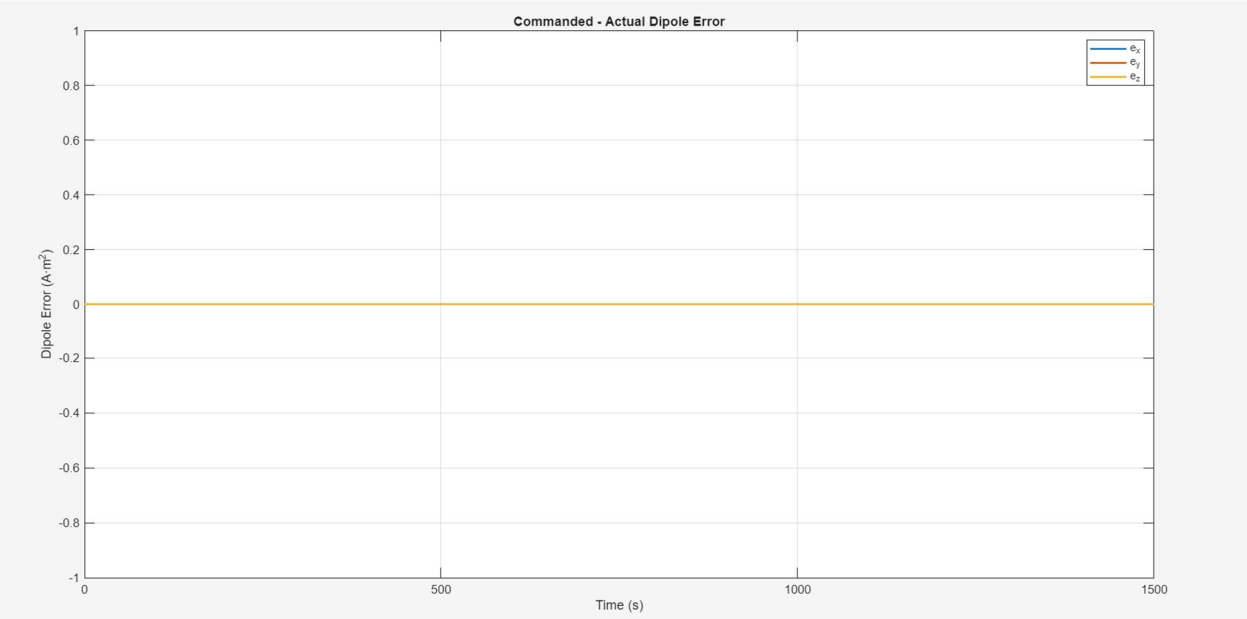


Figure 4.10 – Commanded vs actual dipole error uncontrolled tumbling response

4.3 Open-loop Response

The open-loop response was evaluated by applying a constant magnetic dipole moment without feedback from the spacecraft state making the B-dot controller gain unimpactful. In this configuration, the magnetorquer generates a fixed torque based on the interaction between the constant dipole and the time-varying Earth magnetic field.

Coil parameters that were fixed for open-loop response:

Table 4.2 – Fixed parameters for open-loop response

N turns	B-dot controller gain, k	Coil area, (m^2)	Coil resistance (Ohms)	Coil max current (A)	Coil max voltage (V)
200	-	0.01	4.4	0.15	12

The simulation generates plots for angular velocity magnitude and its components, kinetic energy, commanded vs actual dipole moment, coil current, voltage and power, and finally the error for generated dipole moment.

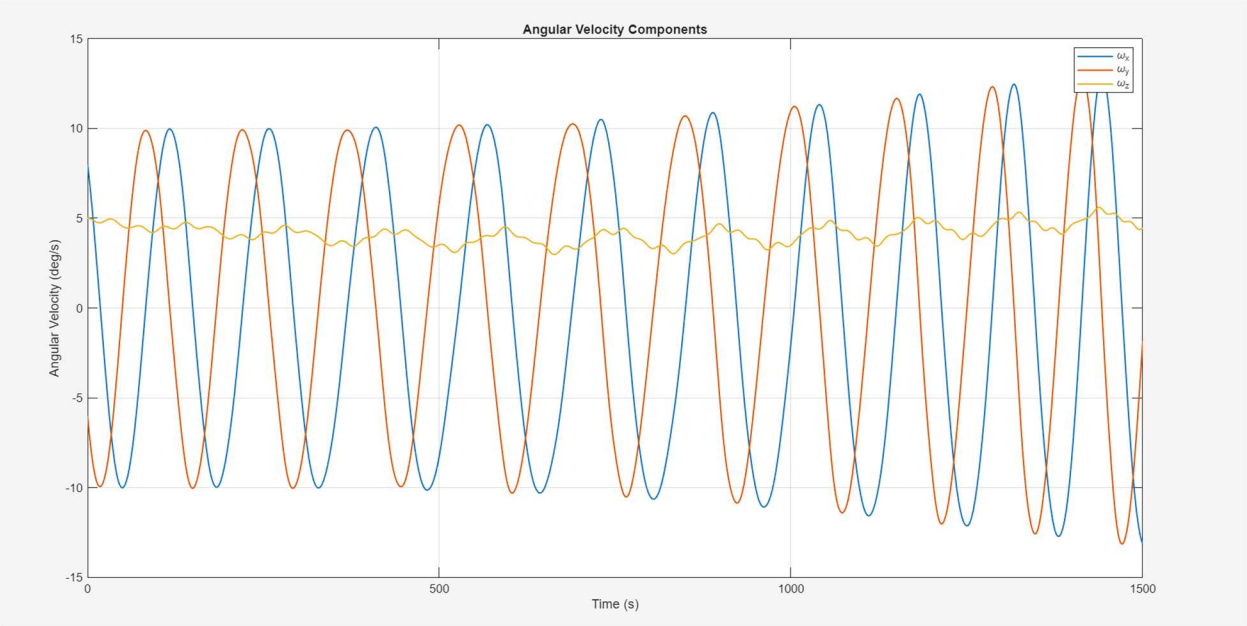


Figure 4.11 – Angular velocity components open loop response

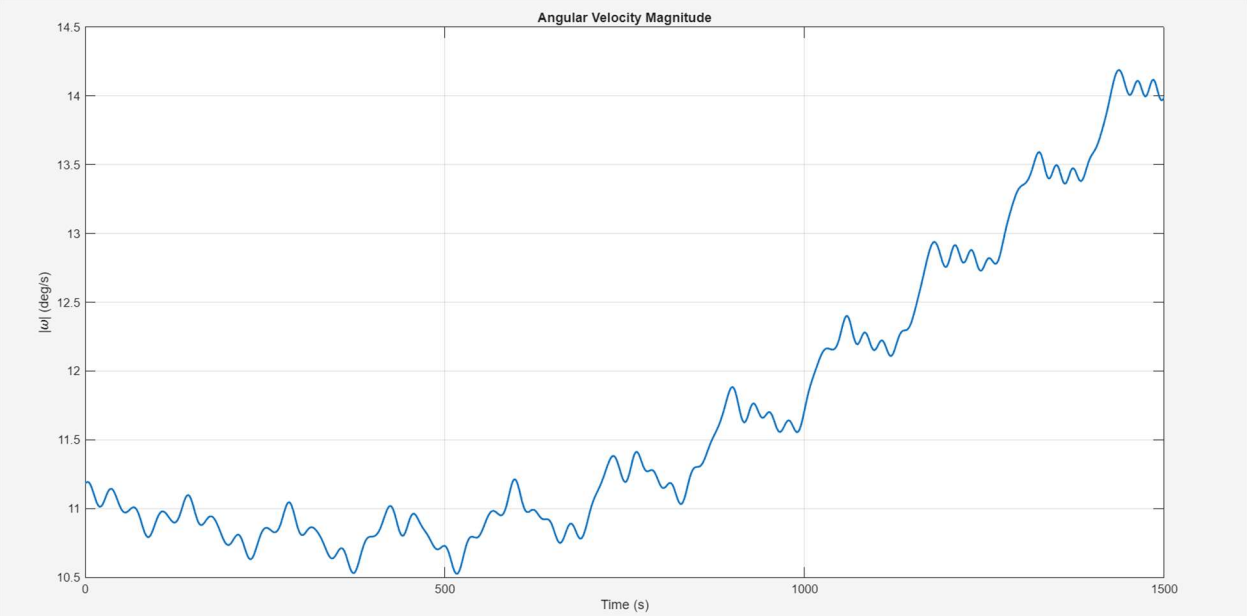


Figure 4.12 – Angular velocity magnitude open loop response

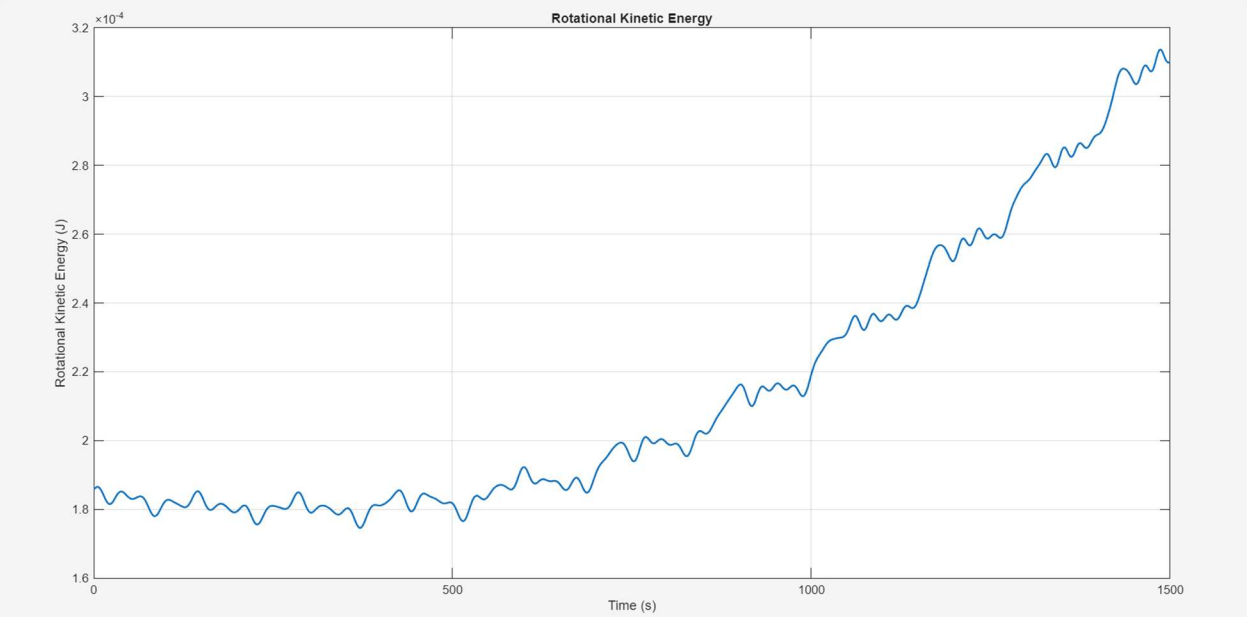


Figure 4.13 – Rotational kinetic energy open loop response

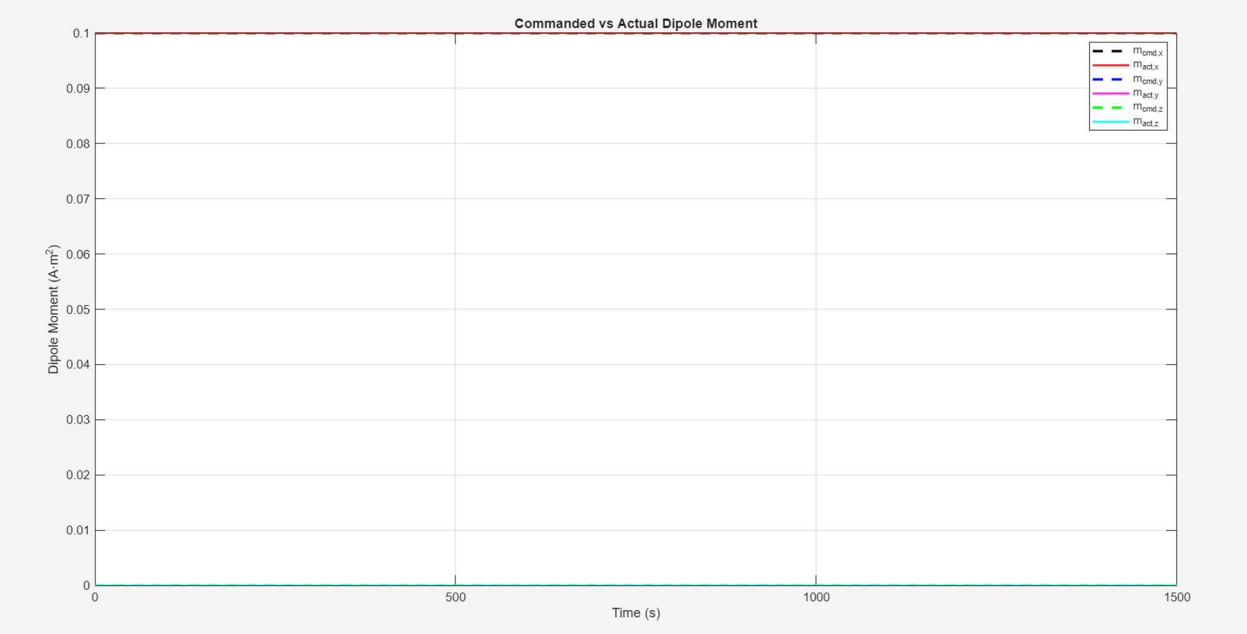


Figure 4.14 – Commanded vs actual dipole moment open loop response

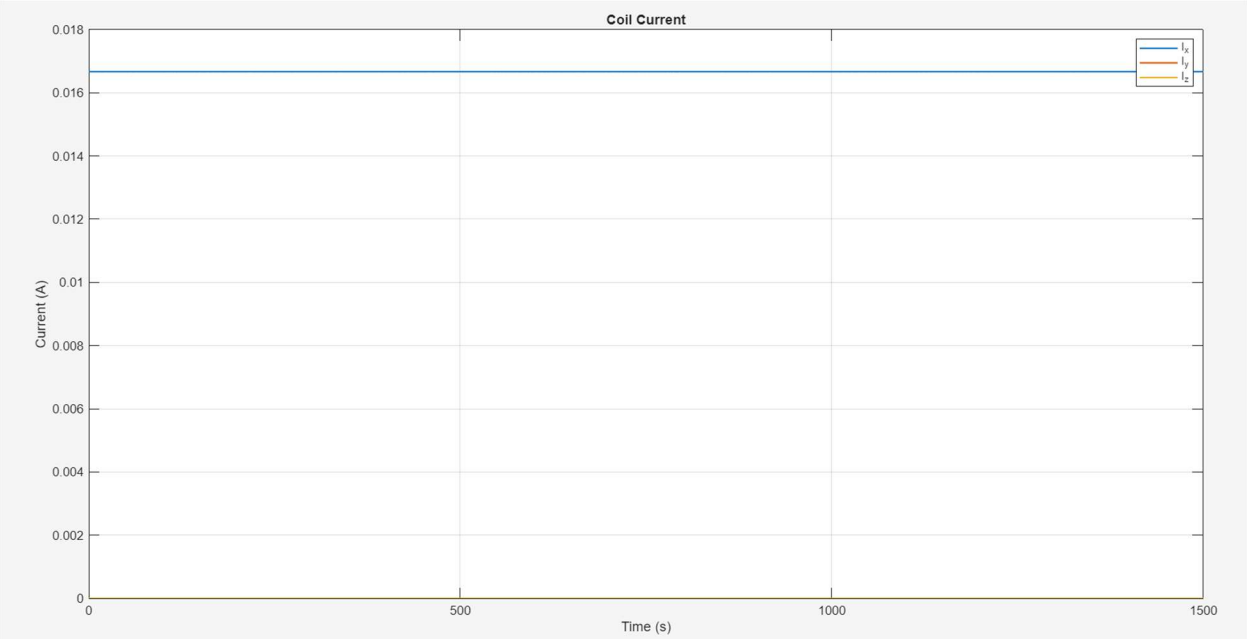


Figure 4.15 – Coil current open loop response

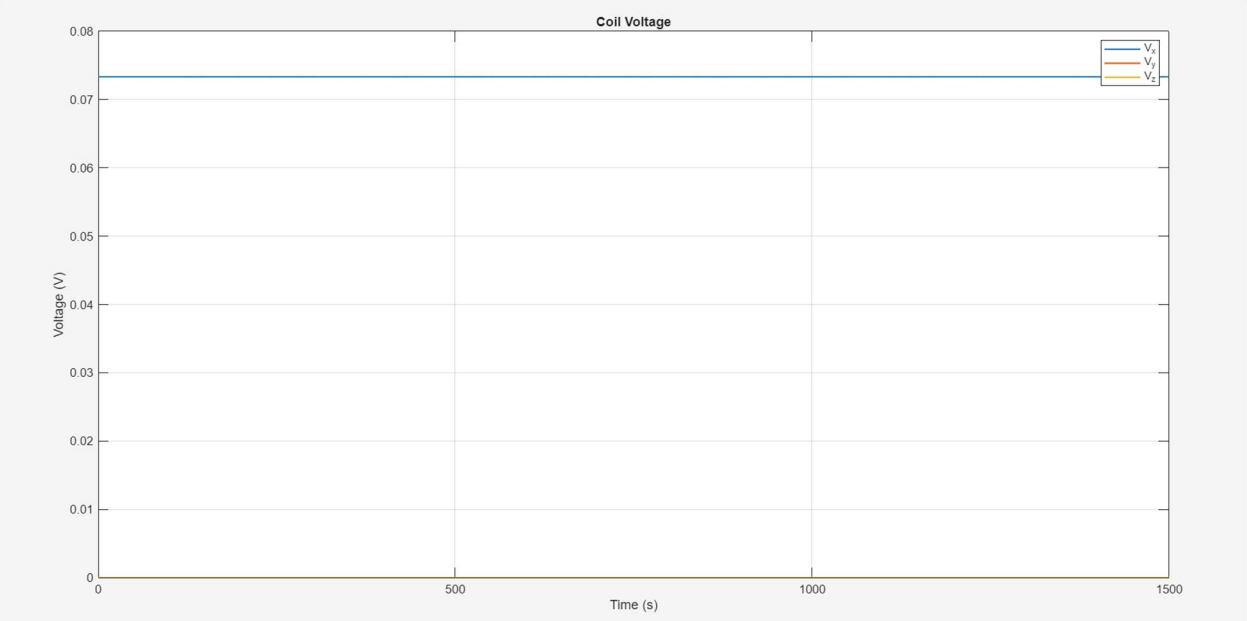


Figure 4.16 – Coil voltage open loop response

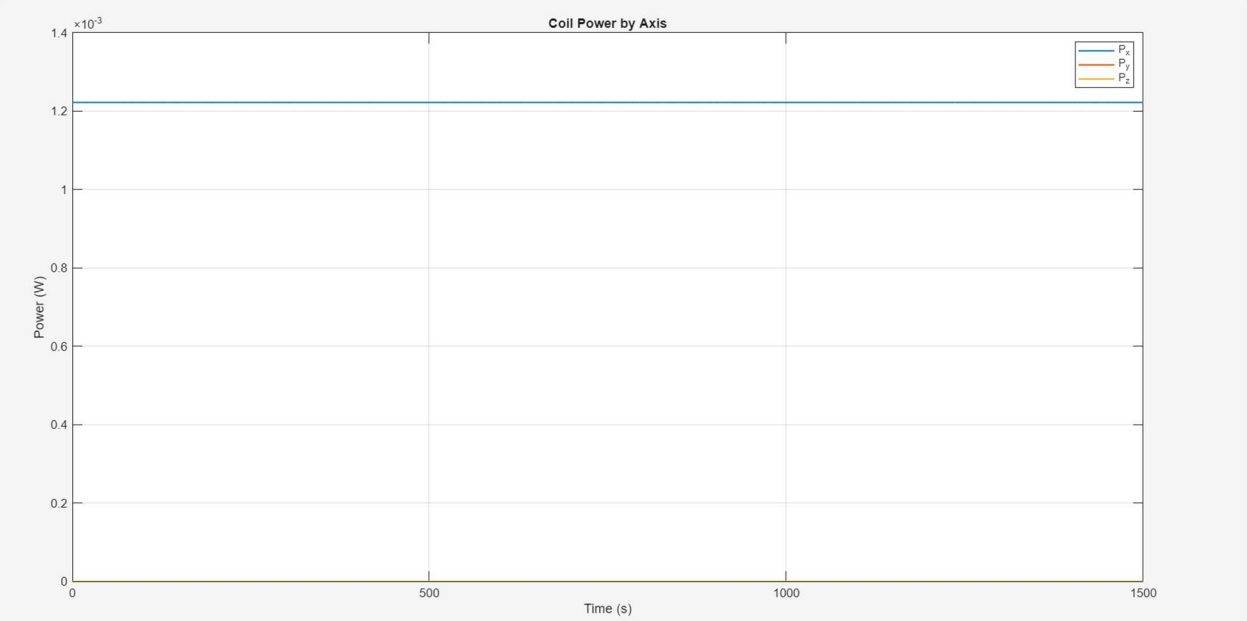


Figure 4.17 – Coil power open loop response

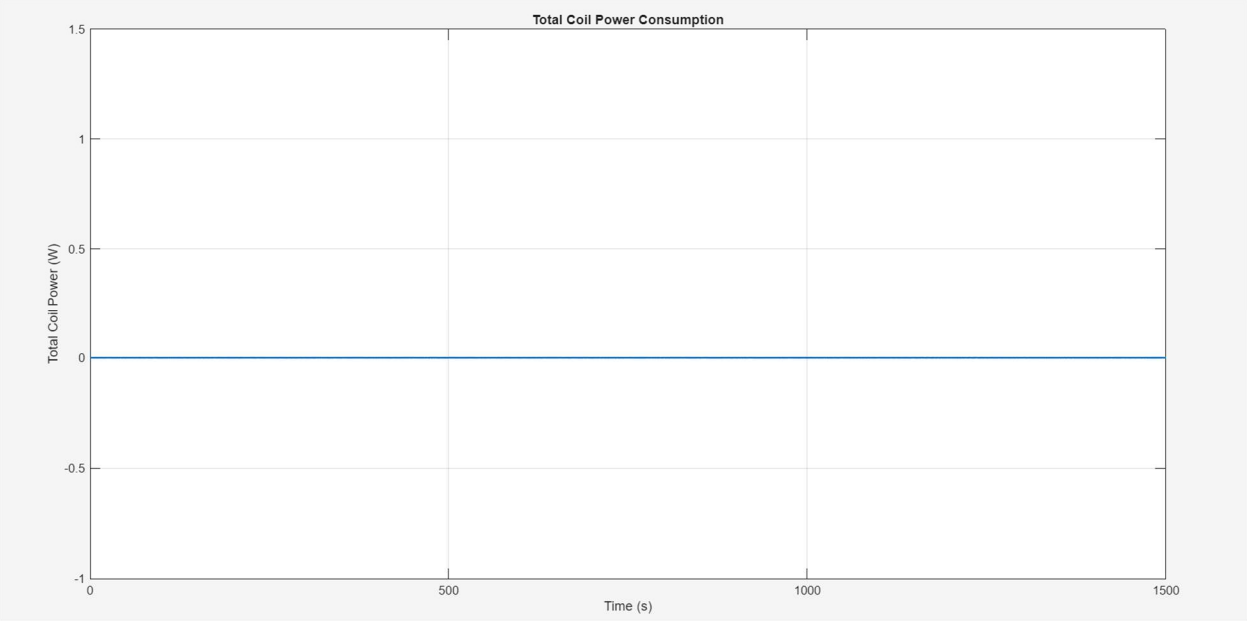


Figure 4.18 – Total coil power consumption open loop response

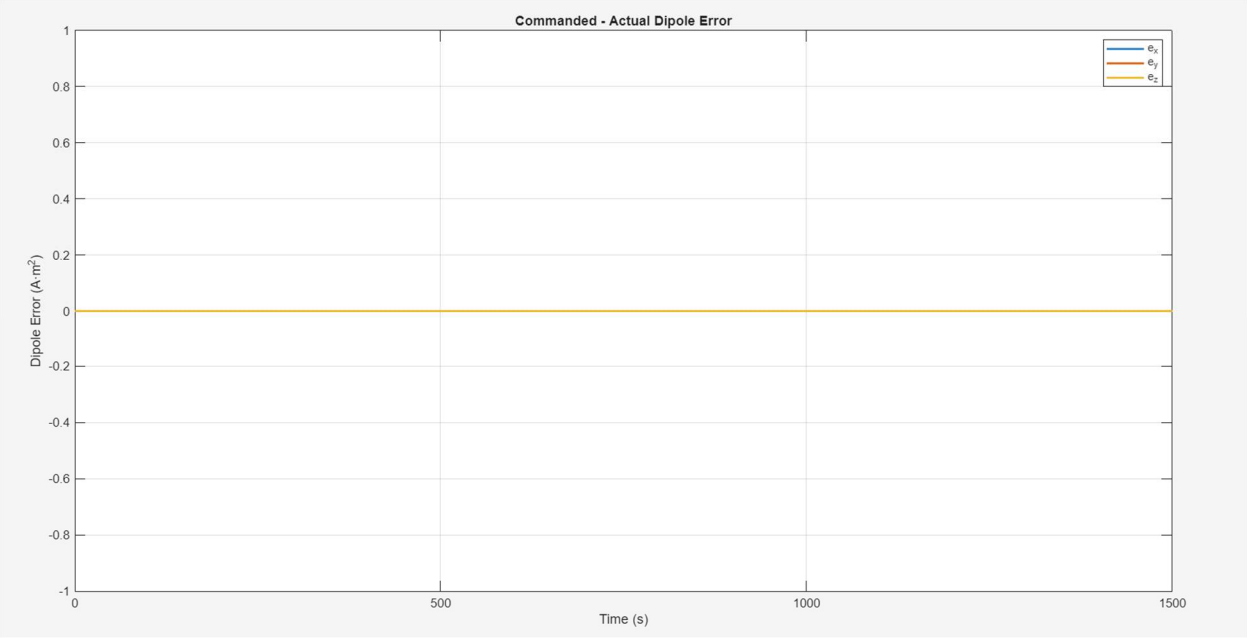


Figure 4.19 – Commanded vs actual dipole error open loop response

4.4 B-dot Controller Case Study

The closed-loop response was implemented using a B-dot control law, where the commanded magnetic dipole is proportional to the cross product of the spacecraft angular velocity and the body-frame magnetic field. This approach provides a passive damping mechanism that opposes rotational motion by extracting kinetic energy through magnetic interaction with Earth's field.

The case study consists of four different variants based on orbit sensitivity, number of turns sweep in the coil, coil area sweep, and current limit sweep.

4.4.1 Number of Turns Sweep

In this sub-study, the simulation was run for number of turns in the coil, N = 100, 200, 400, 800. Below are the set parameters for the plot results.

Table 4.3 – Fixed parameters for number of turns sweep

B-dot controller gain, k	Coil area, (m^2)	Coil resistance (Ohms)	Coil max current (A)	Coil max voltage (V)
5e4	0.01	4.4	0.15	3.3

- **N = 100**

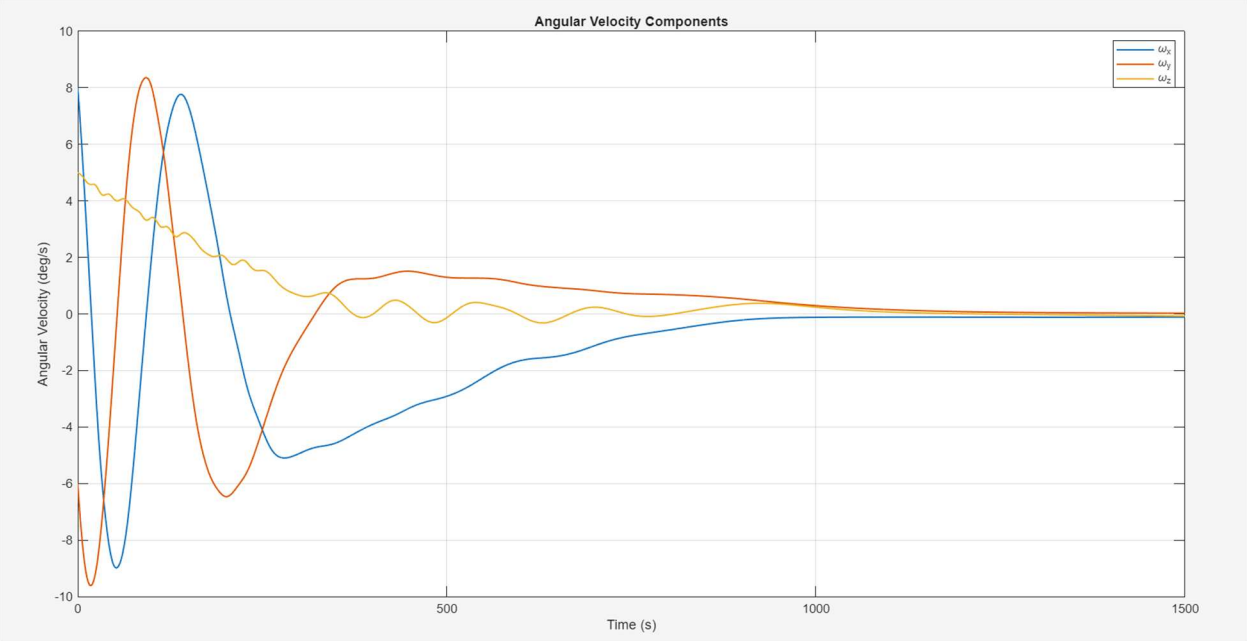


Figure 4.20 – Angular velocity components N = 100

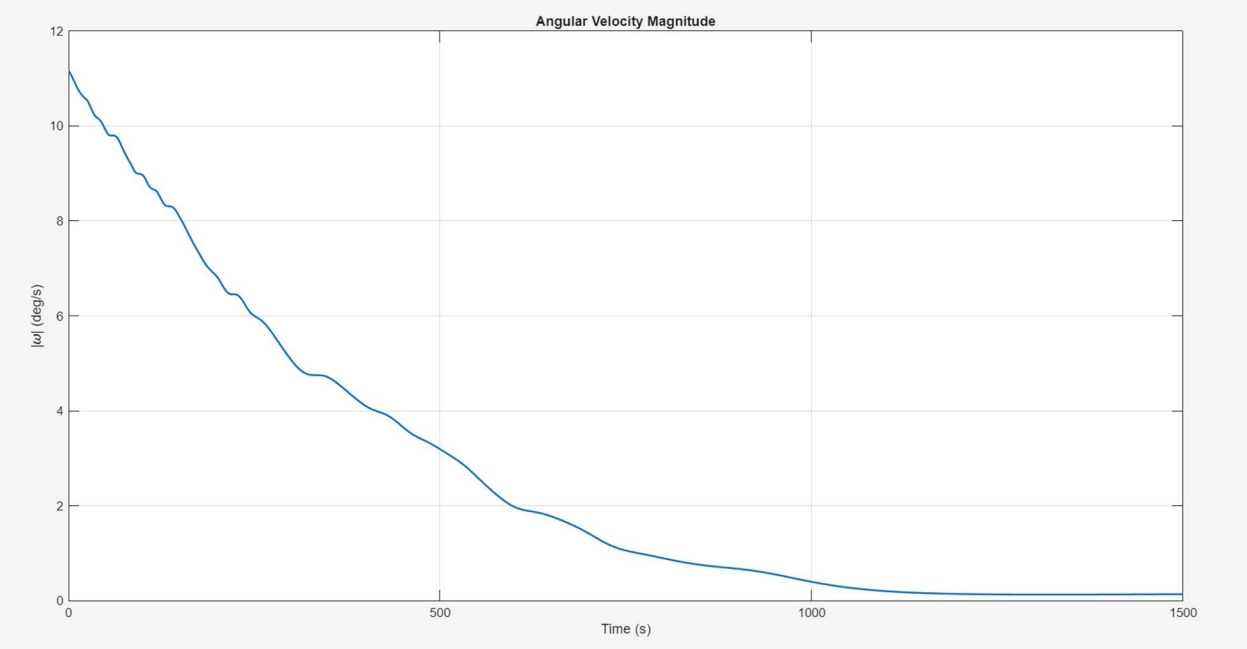


Figure 4.21 – Angular velocity magnitude N = 100

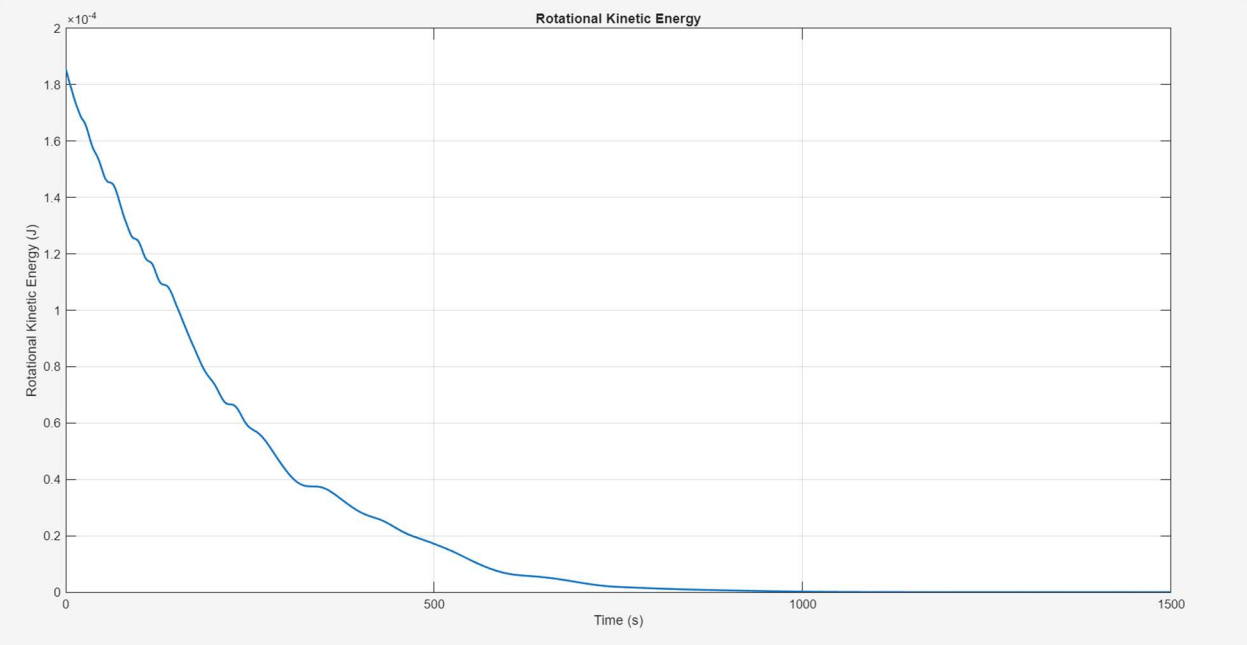


Figure 4.22 – Rotational kinetic energy N = 100

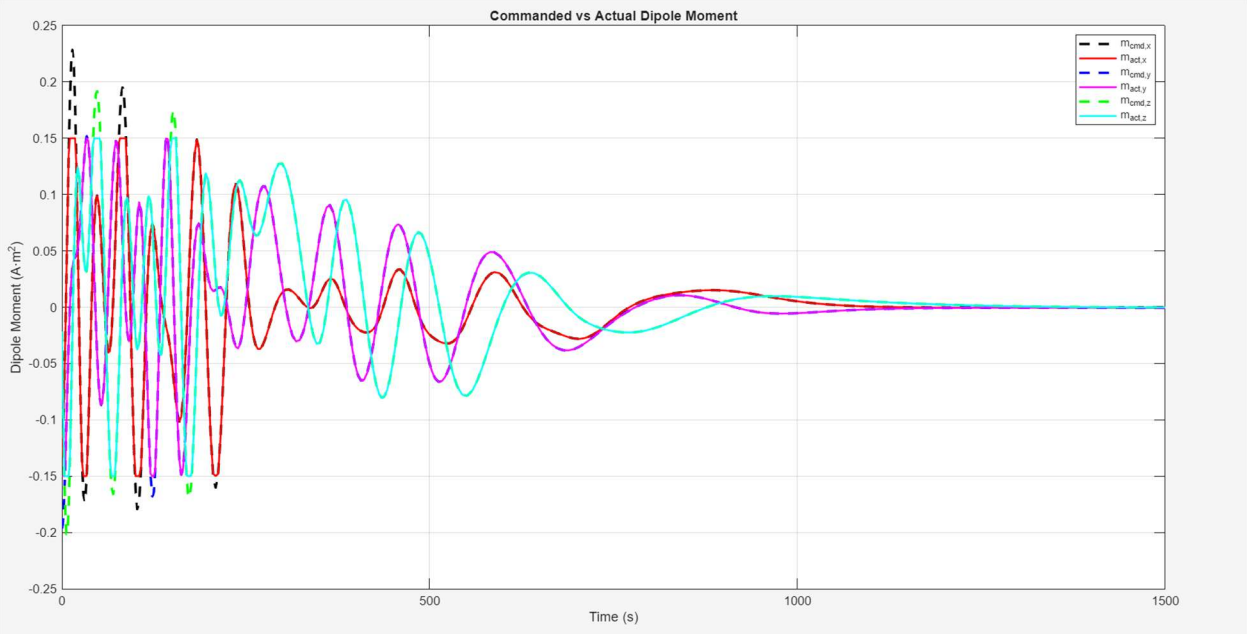


Figure 4.23 – Commanded vs actual dipole moment N = 100

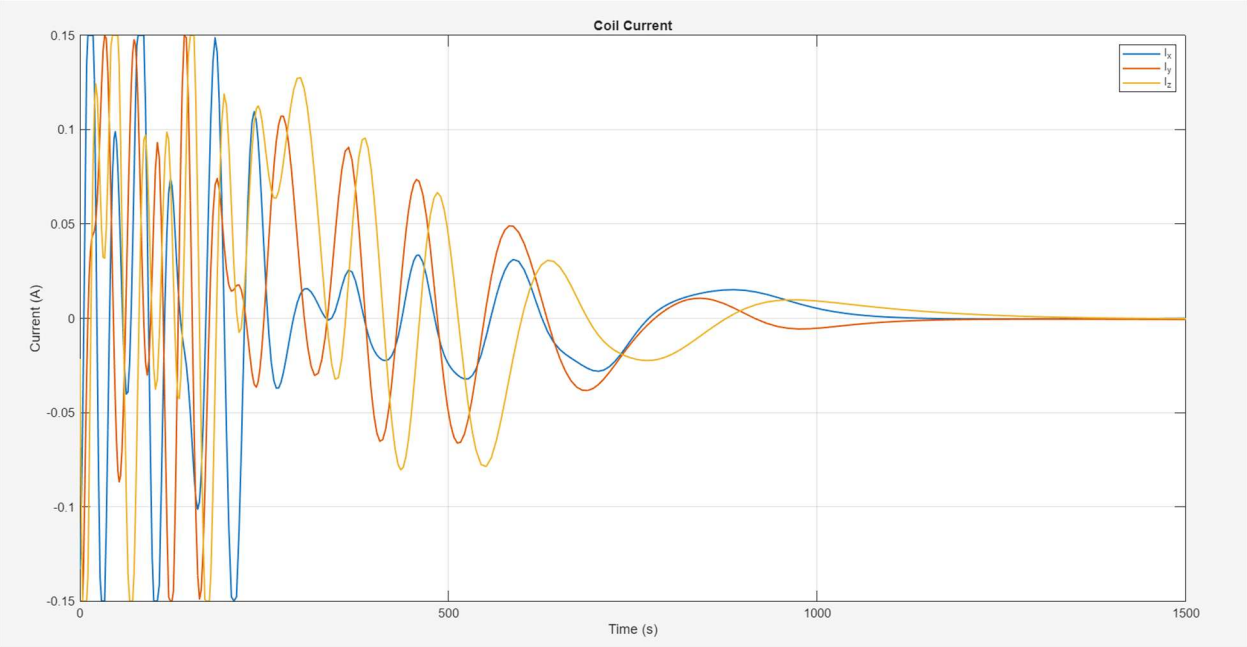


Figure 4.24 – Coil current N = 100

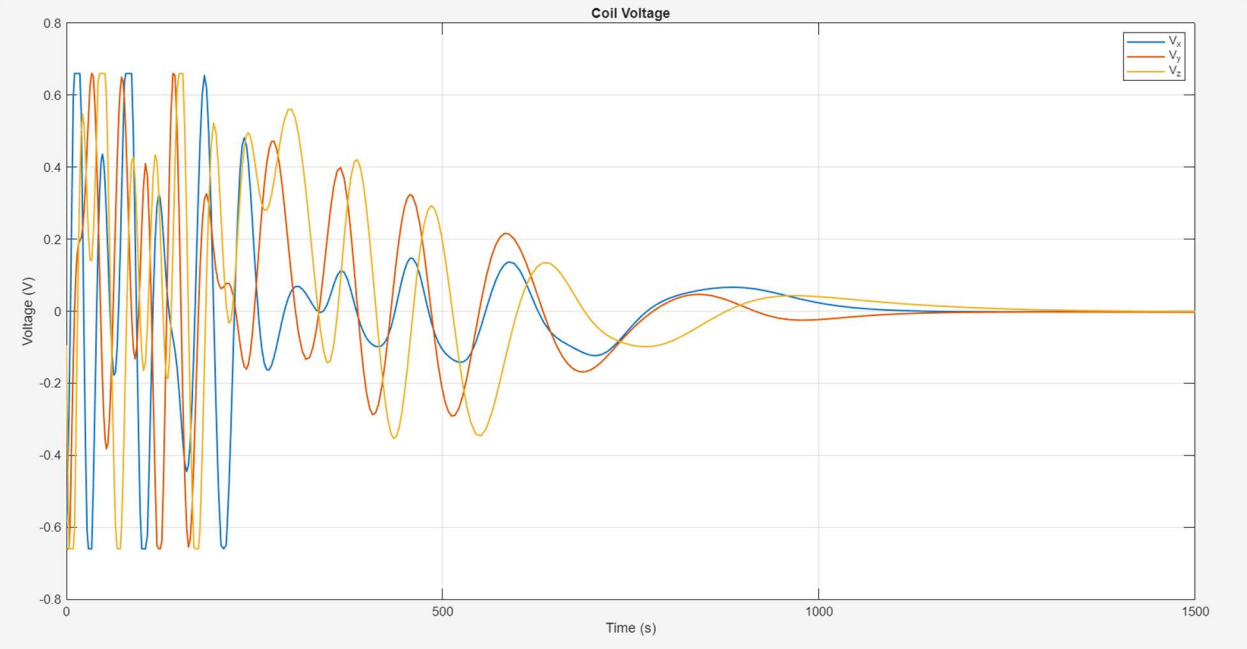


Figure 4.25 – Coil voltage N = 100

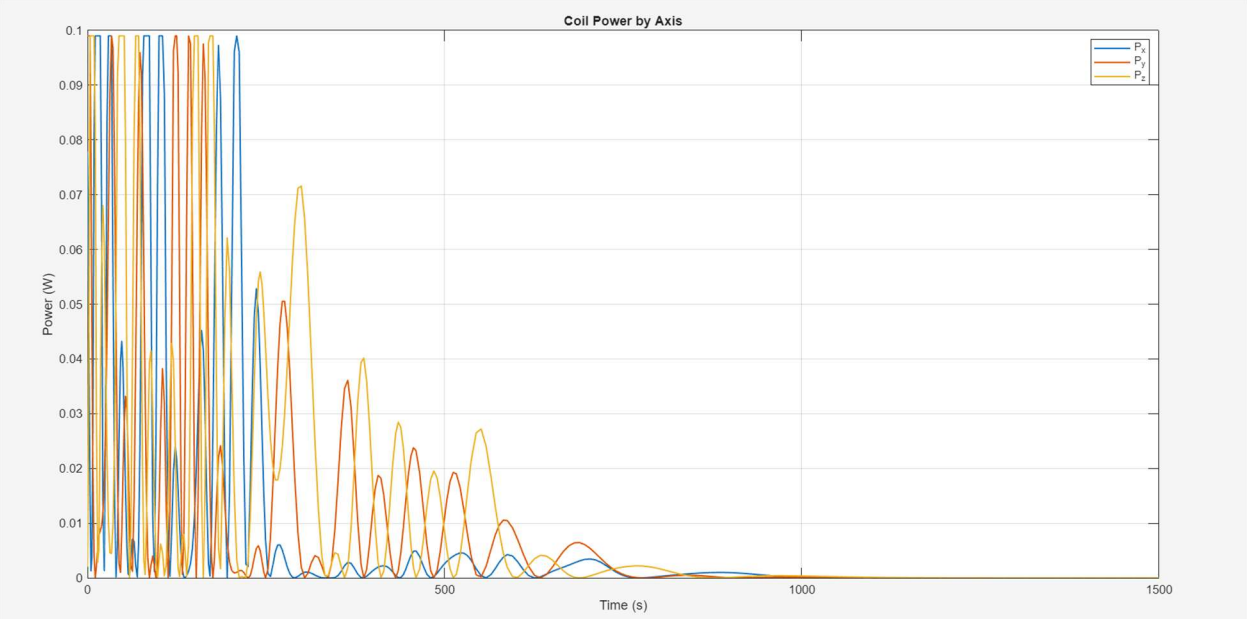


Figure 4.26 – Coil power N = 100

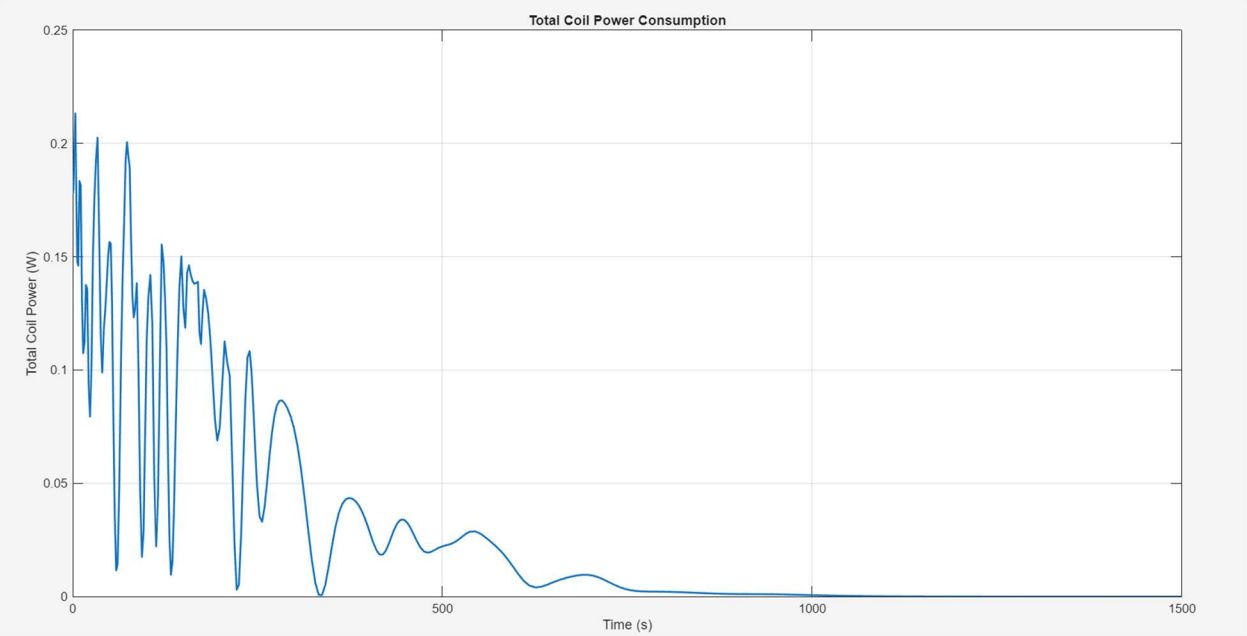


Figure 4.27 – Total coil power consumption N = 100

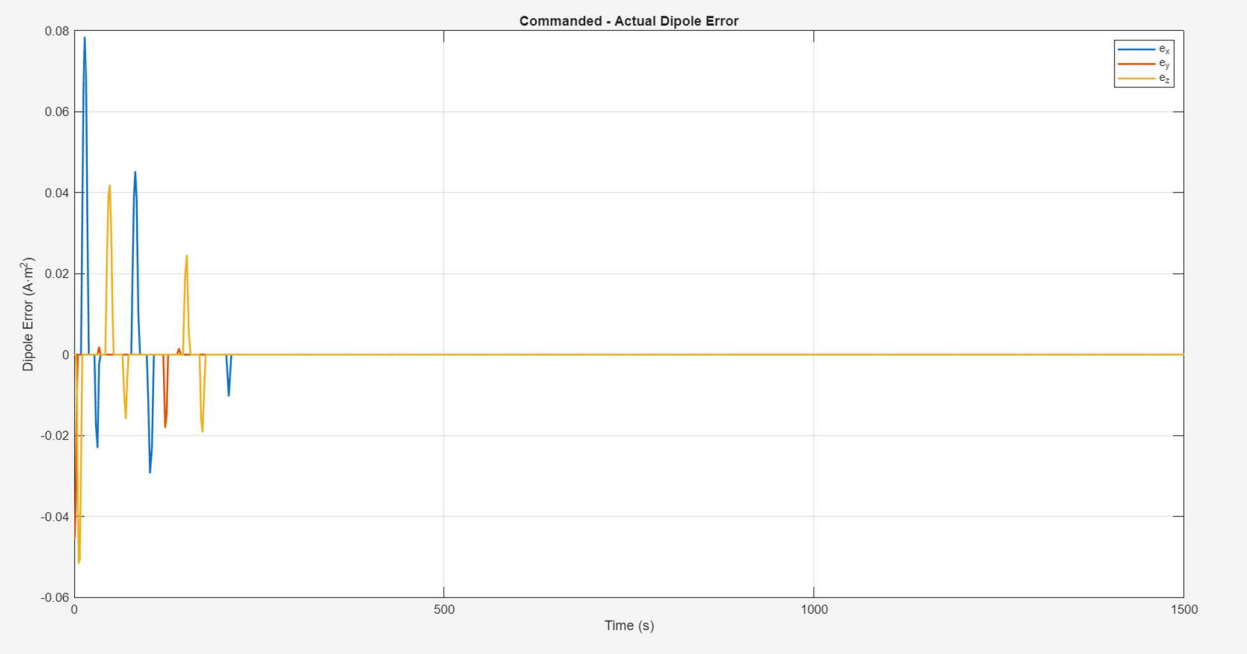


Figure 4.28 – Commanded vs actual dipole error N = 100

- **N = 200**

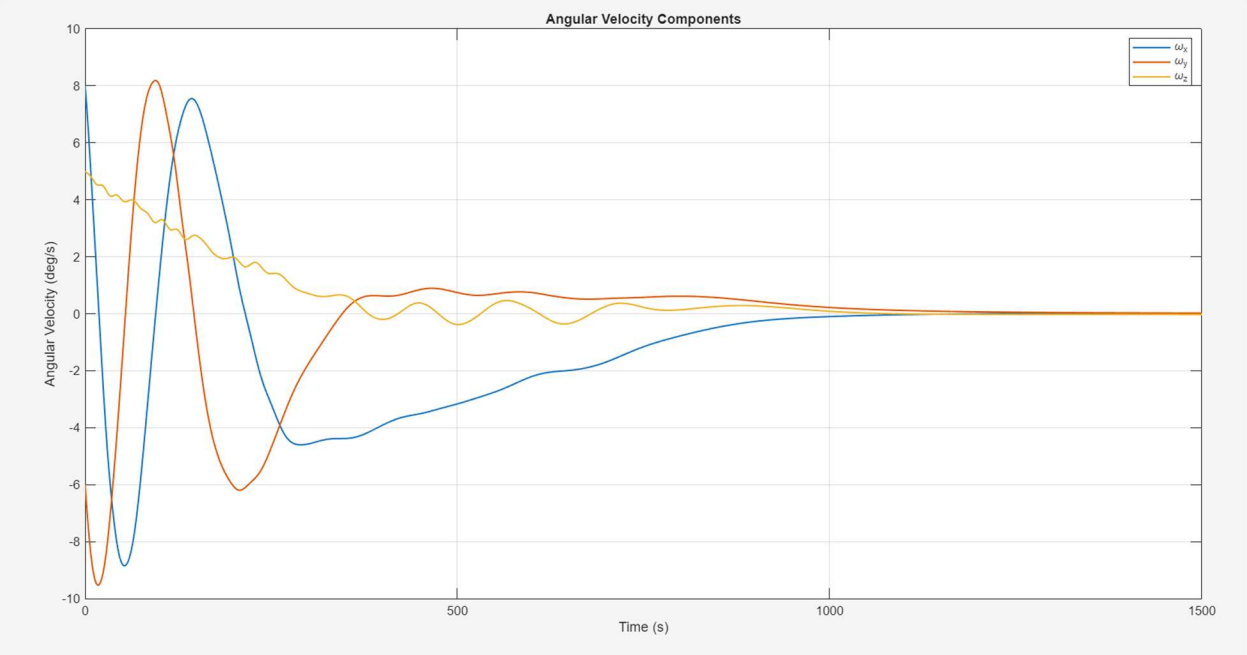


Figure 4.29 – Angular velocity components N = 200

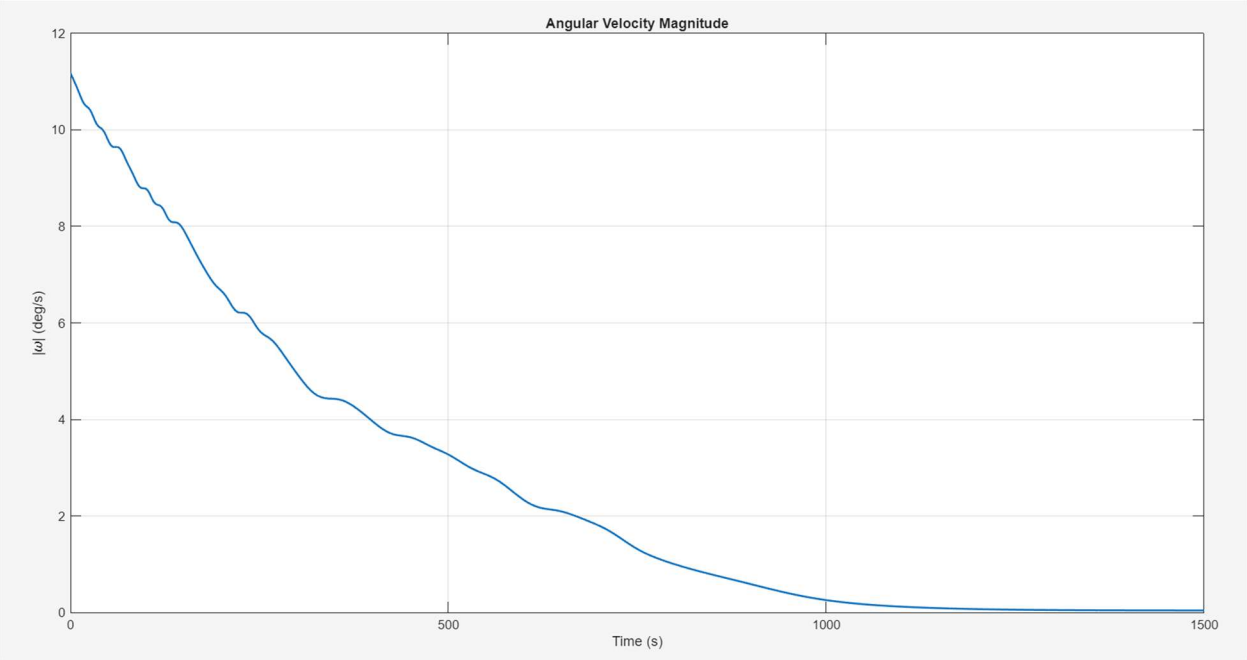


Figure 4.30 – Angular velocity magnitude N = 200

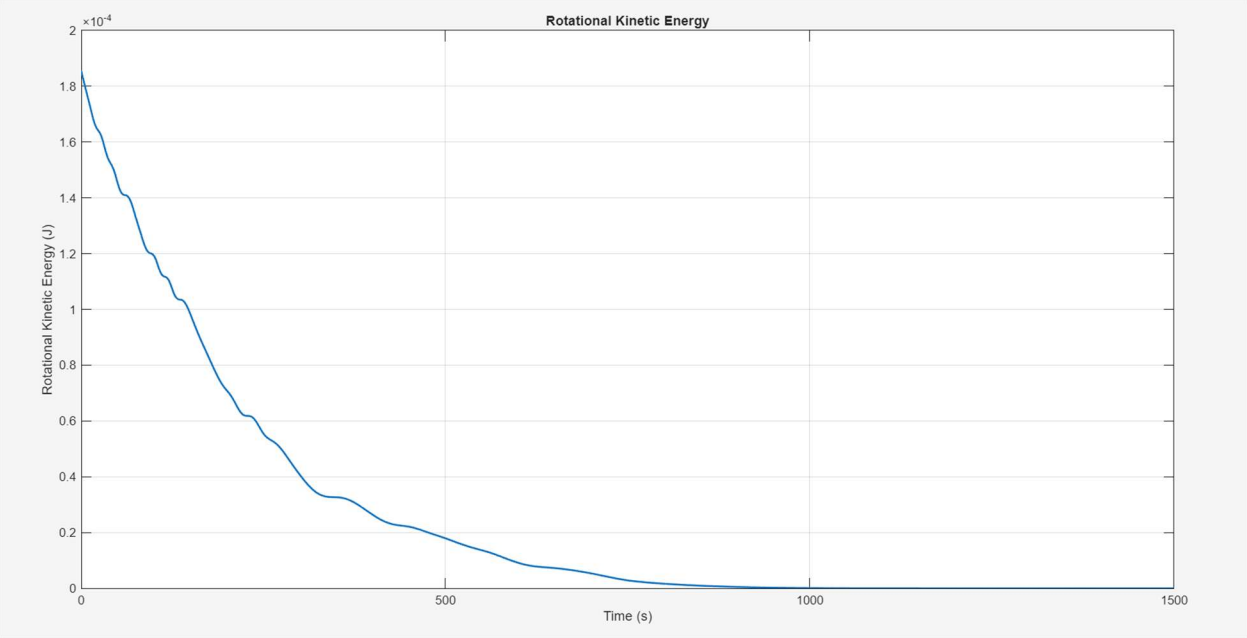


Figure 4.31 – Rotational kinetic energy N = 200

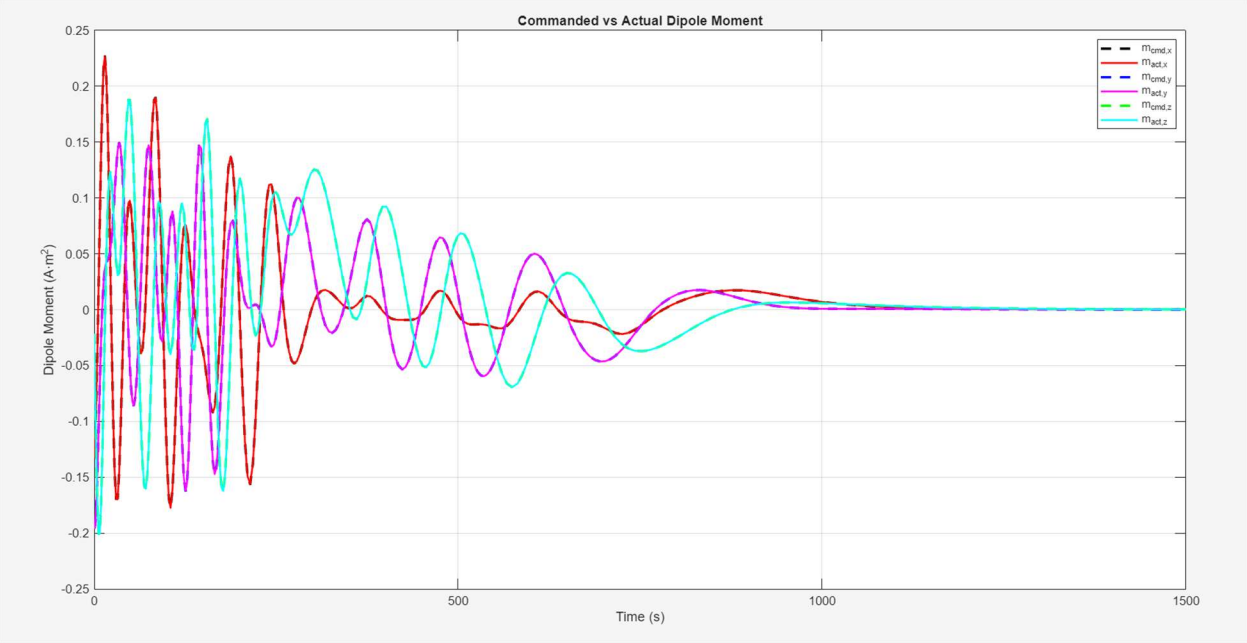


Figure 4.32 – Commanded vs actual dipole moment N = 200

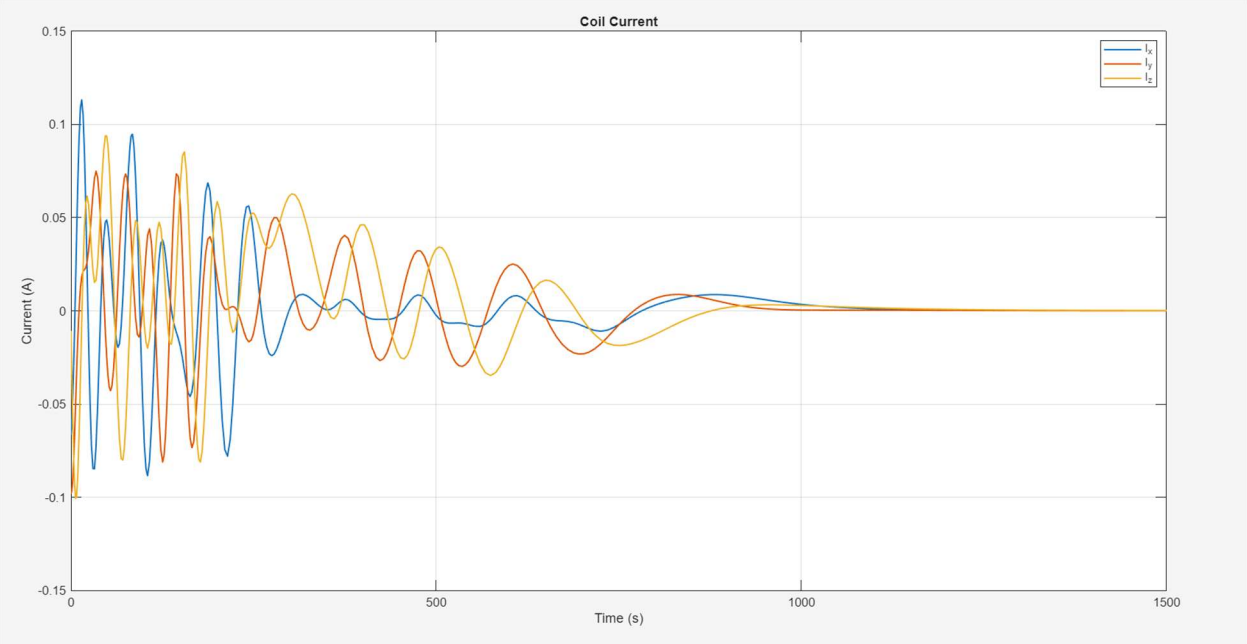


Figure 4.33 – Coil current N = 200

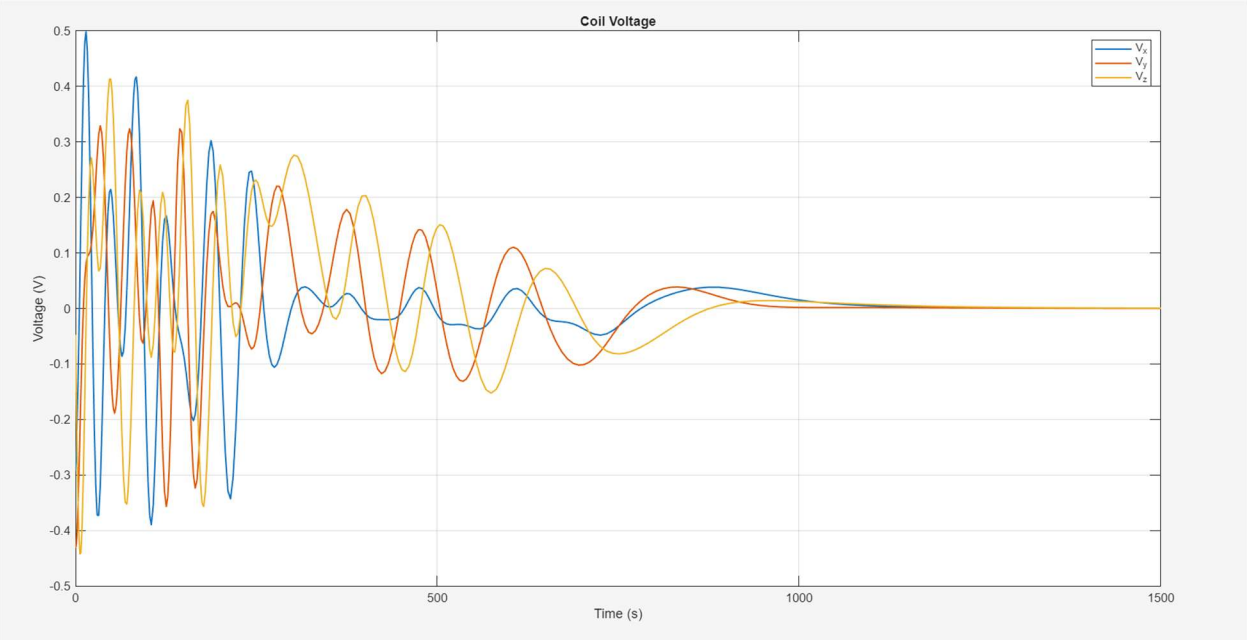


Figure 4.34 – Coil voltage N = 200

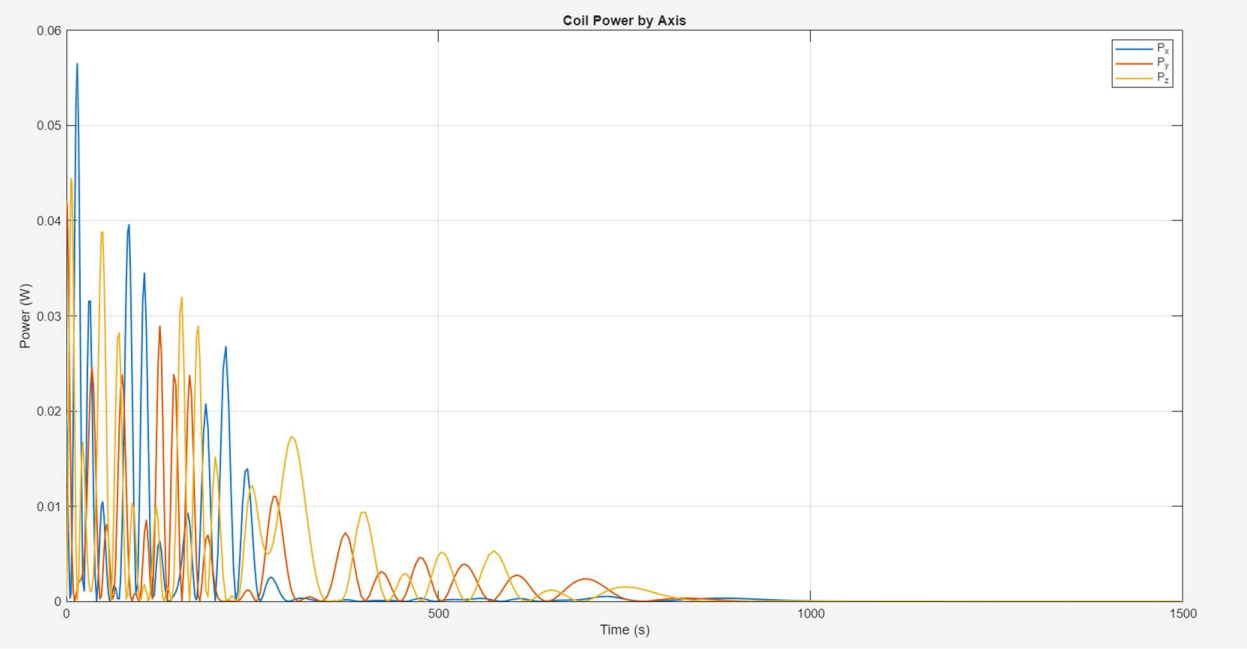


Figure 4.35 – Coil power N = 200

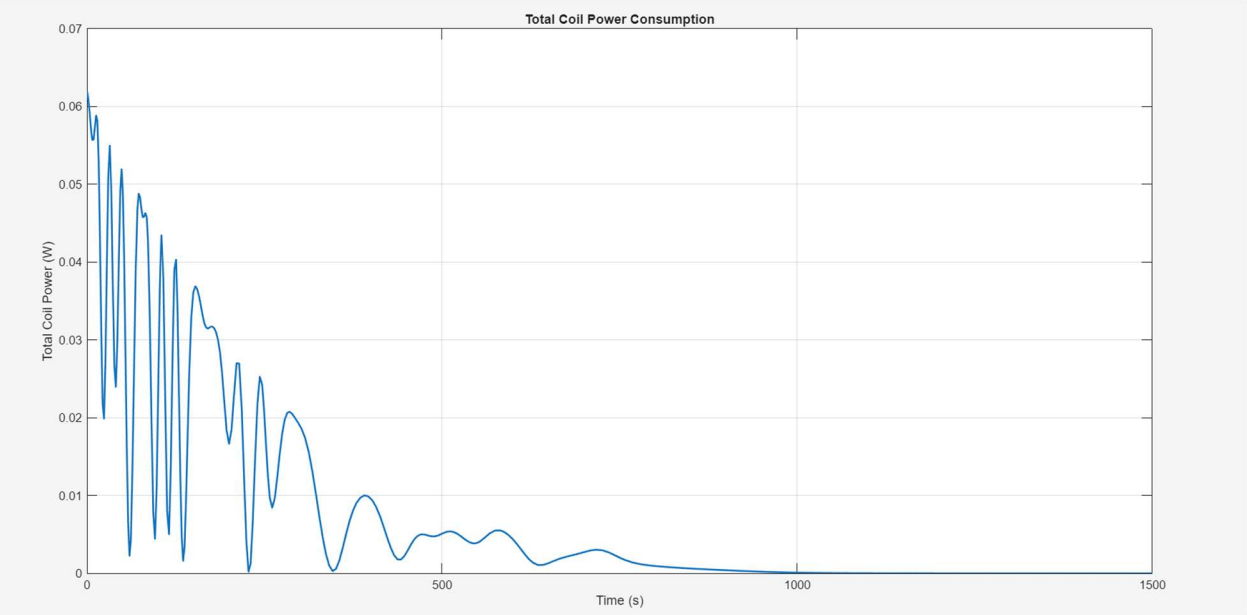


Figure 4.36 – Total coil power consumption N = 200

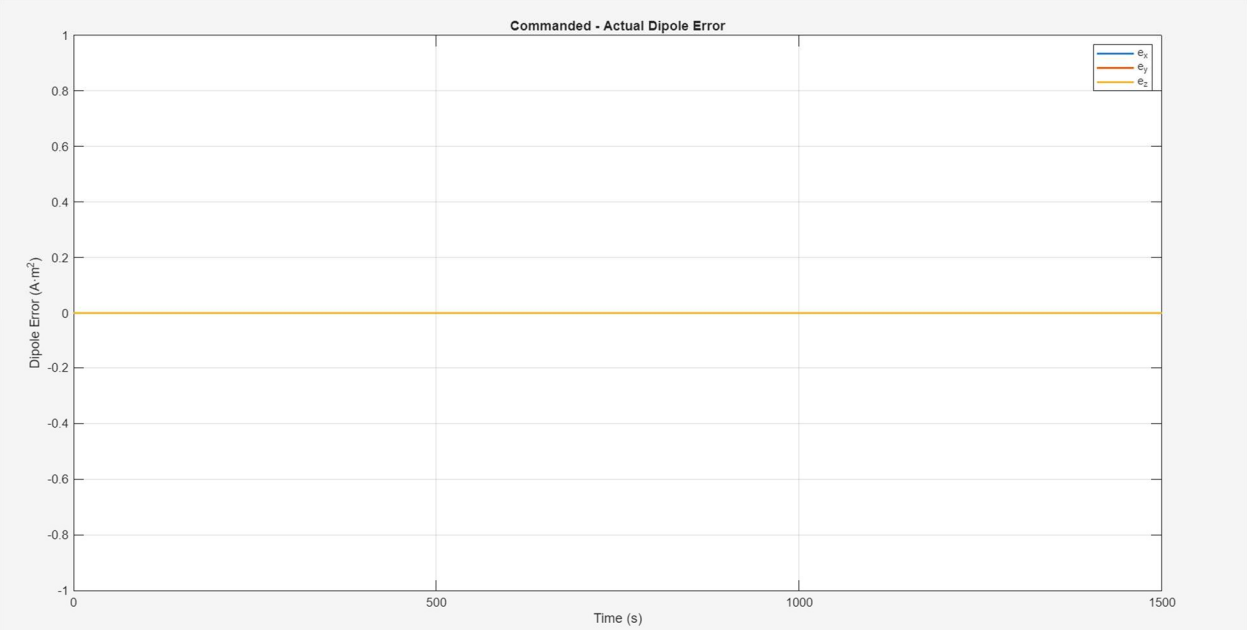


Figure 4.37 – Commanded vs actual dipole error N = 200

- **N = 400**

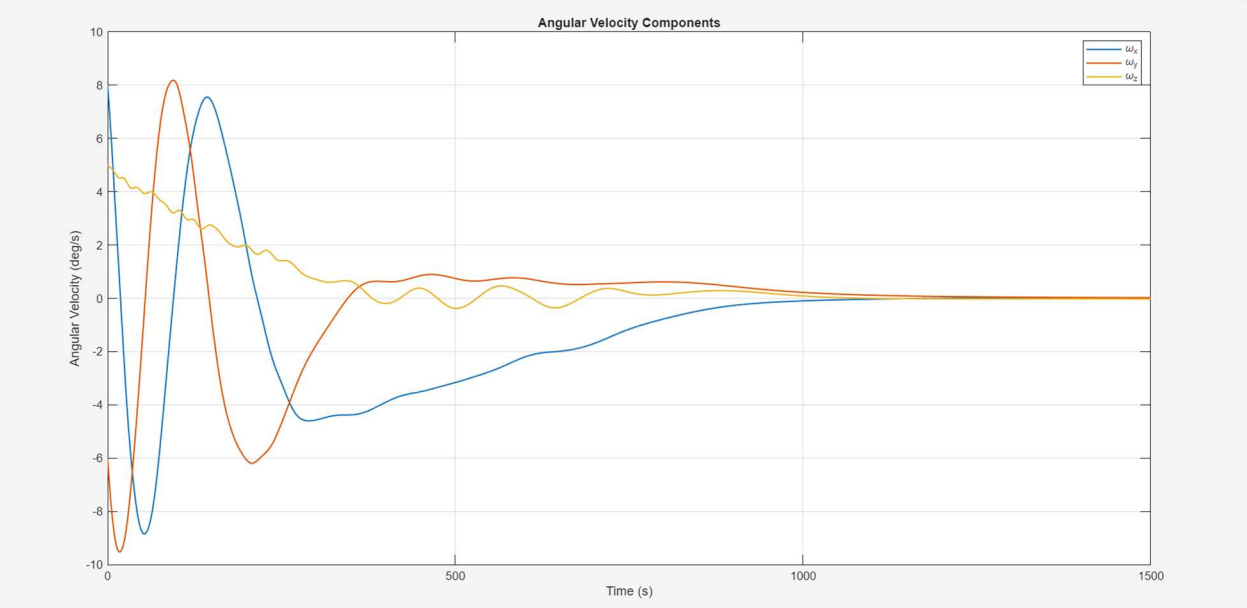


Figure 4.38 – Angular velocity components N = 400

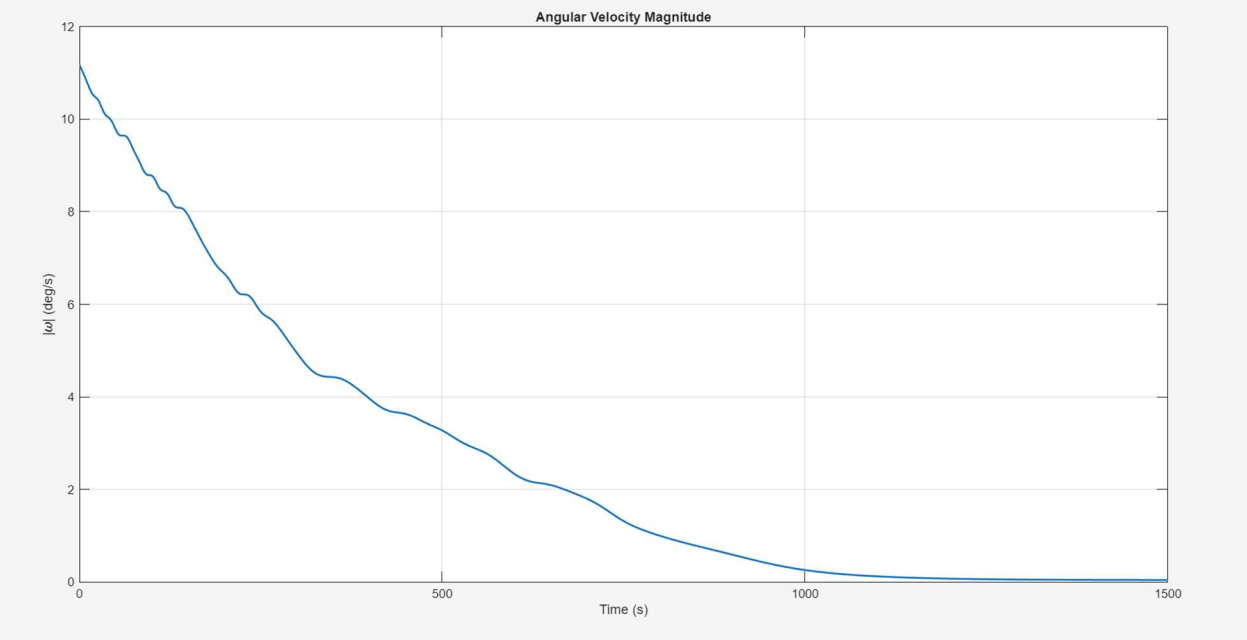


Figure 4.39 – Angular velocity magnitude N = 400

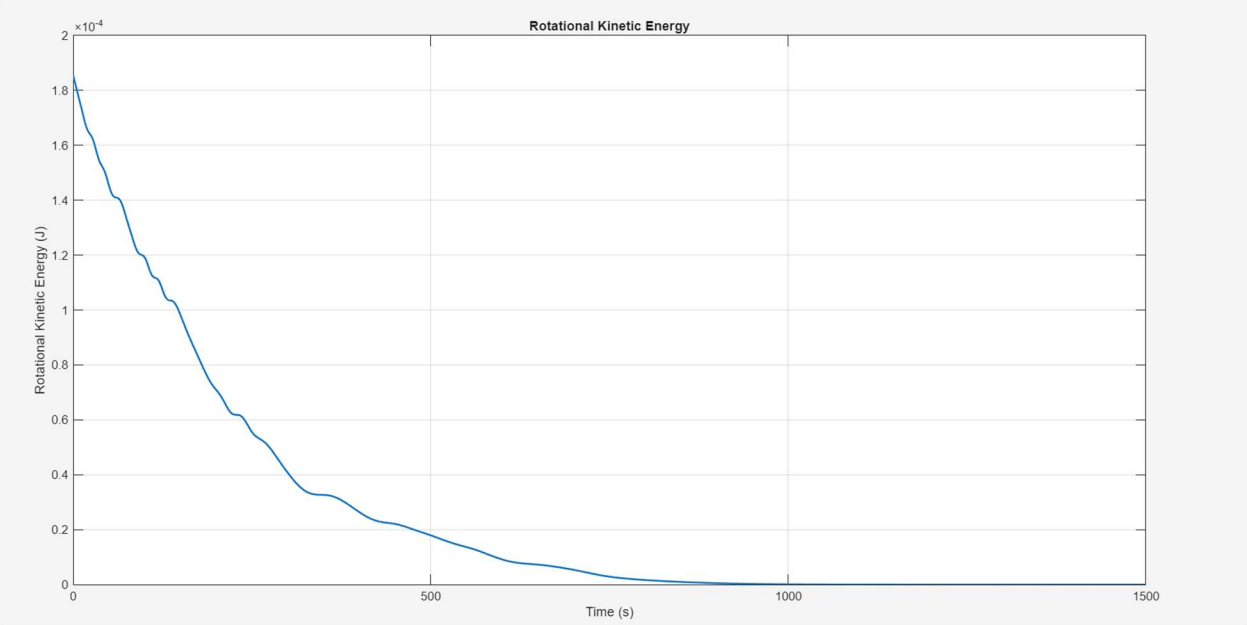


Figure 4.40 – Rotational kinetic energy N = 400

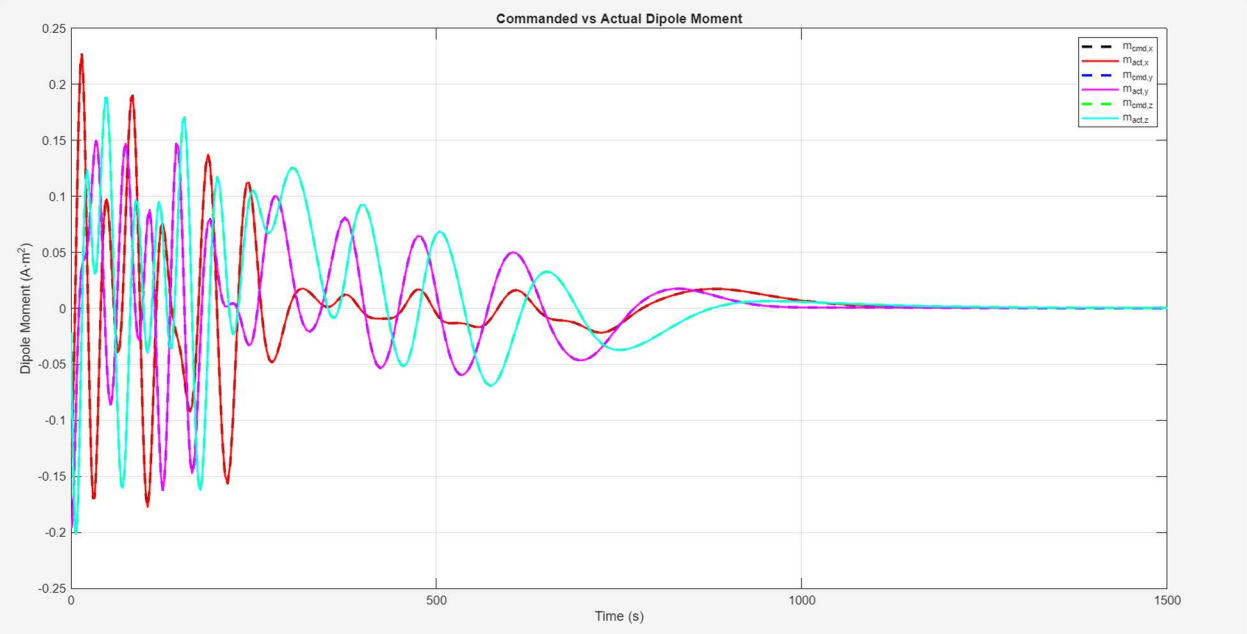


Figure 4.41 – Commanded vs actual dipole moment N = 400

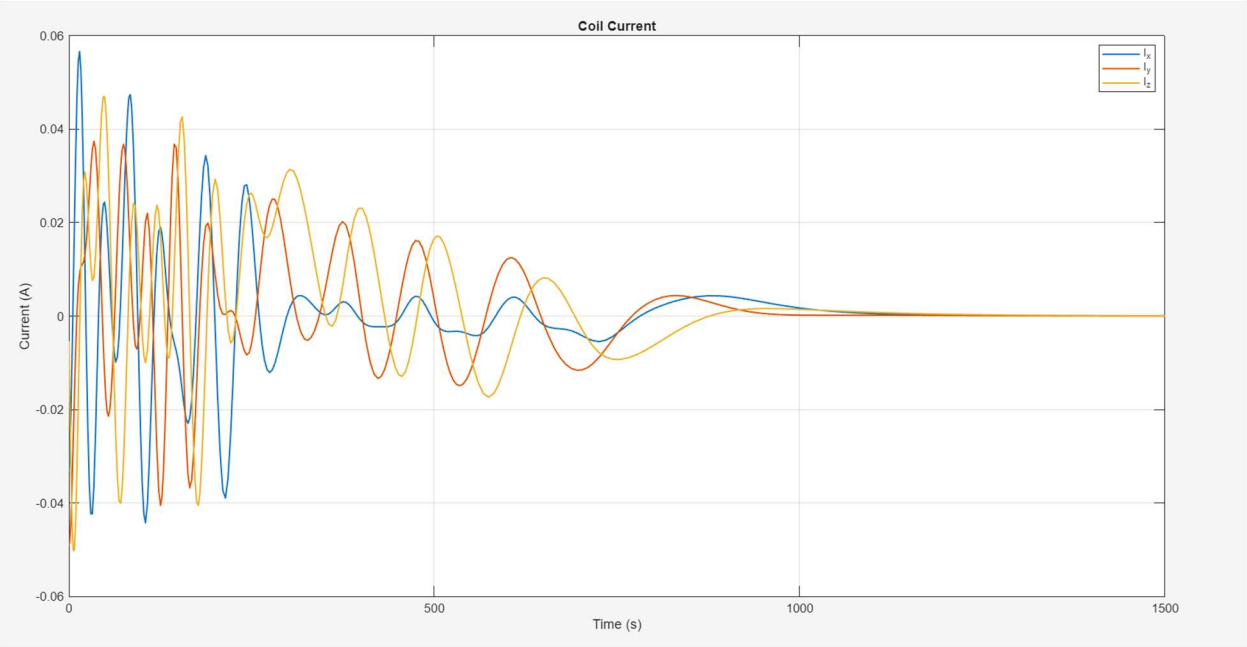


Figure 4.42 – Coil current N = 400

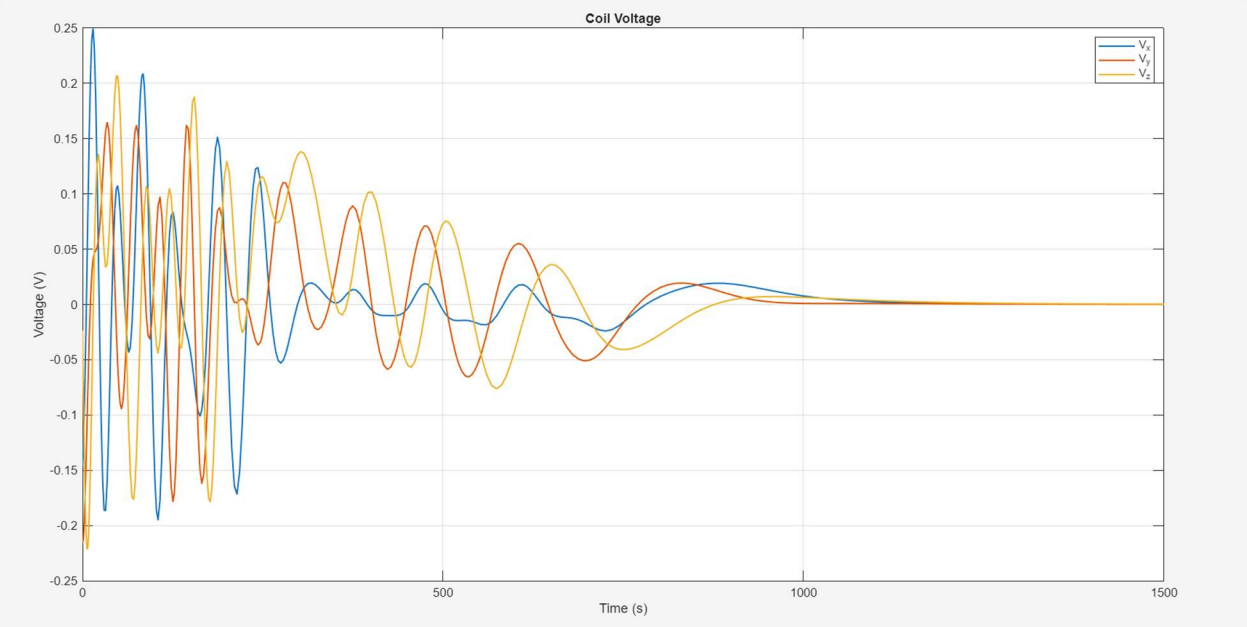


Figure 4.43 – Coil voltage N = 400

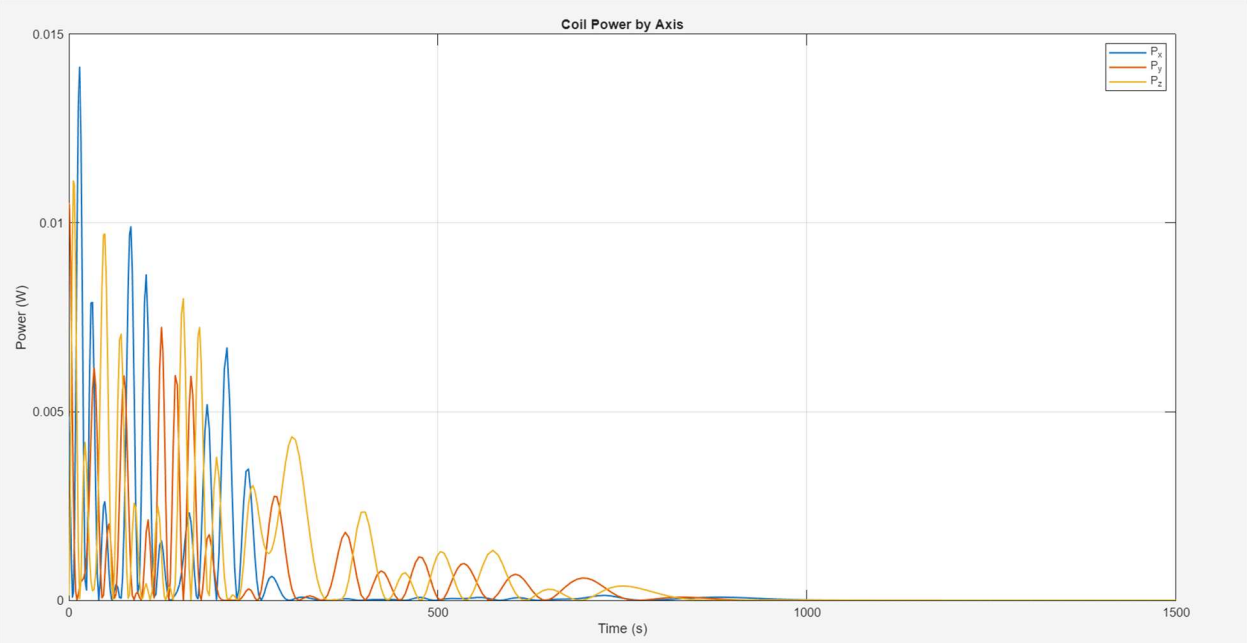


Figure 4.44 – Coil power N = 400

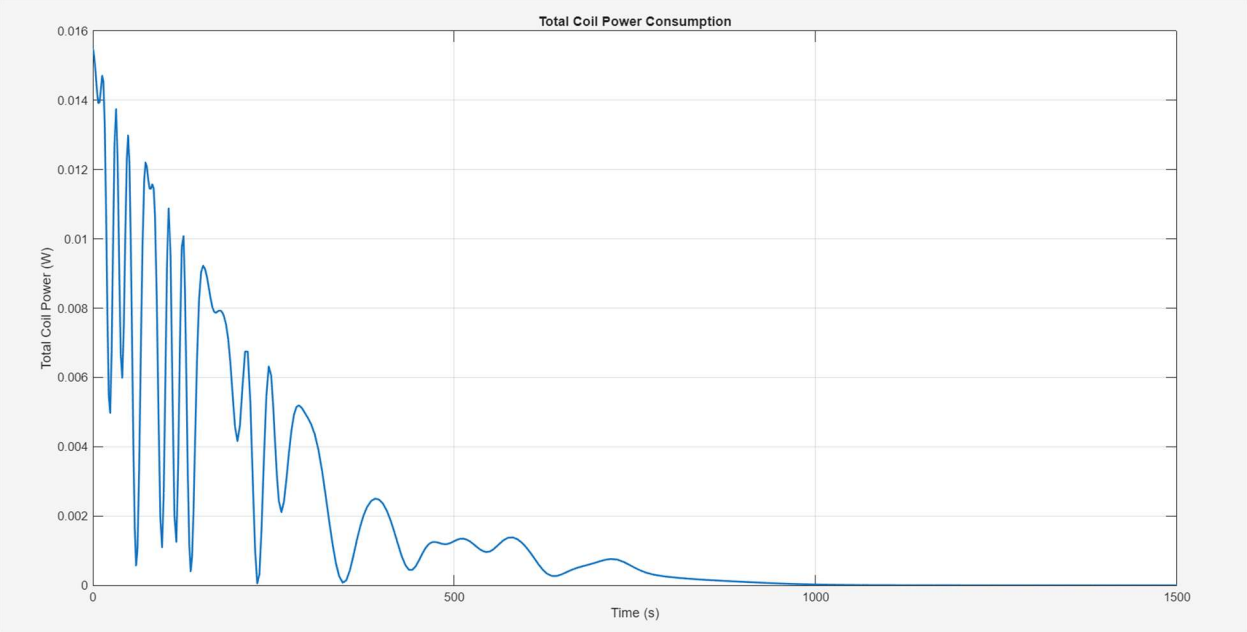


Figure 4.45 – Total coil power consumption N = 400

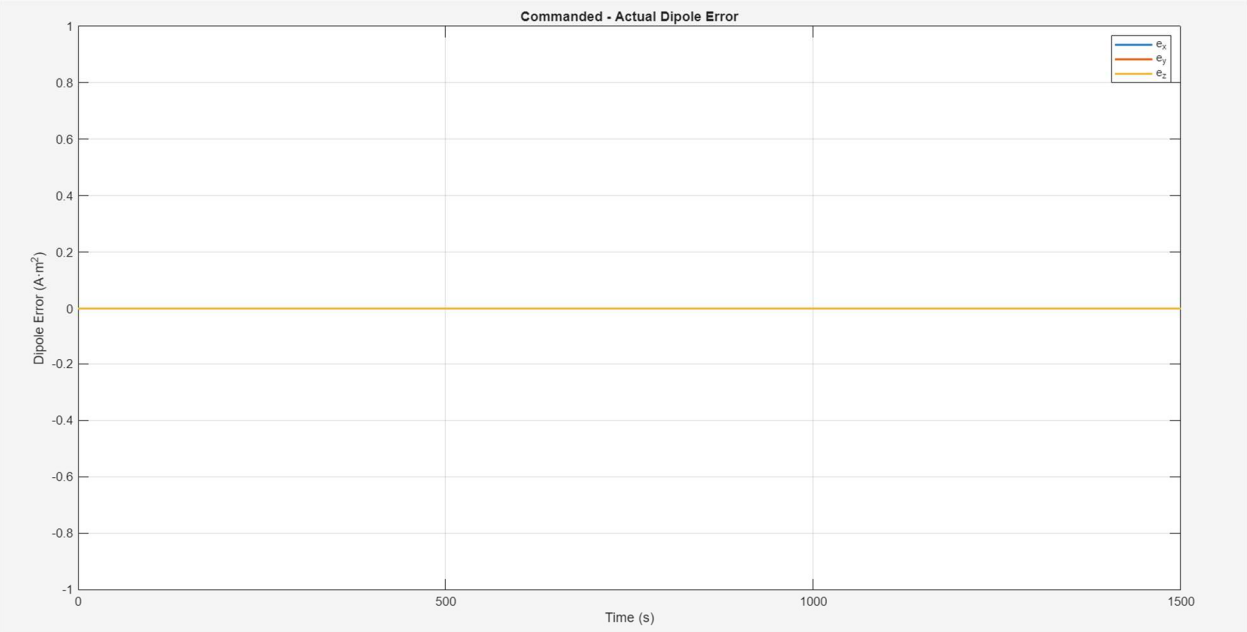


Figure 4.46 – Commanded vs actual dipole error N = 400

- **N = 800**

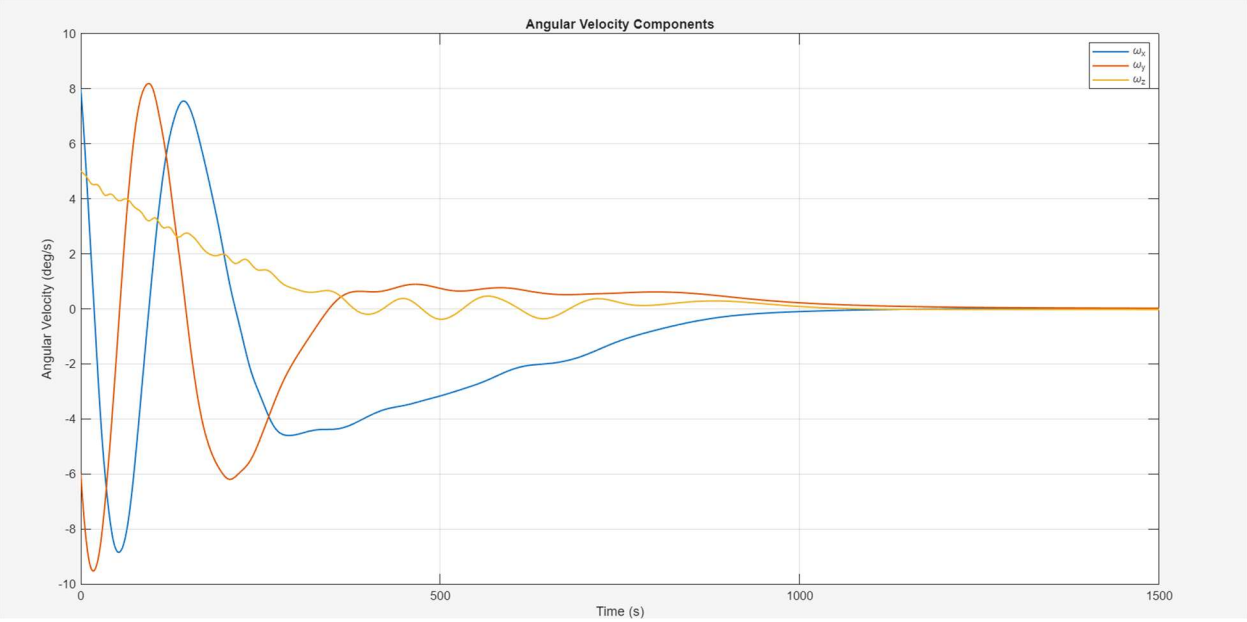


Figure 4.47 – Angular velocity components N = 800

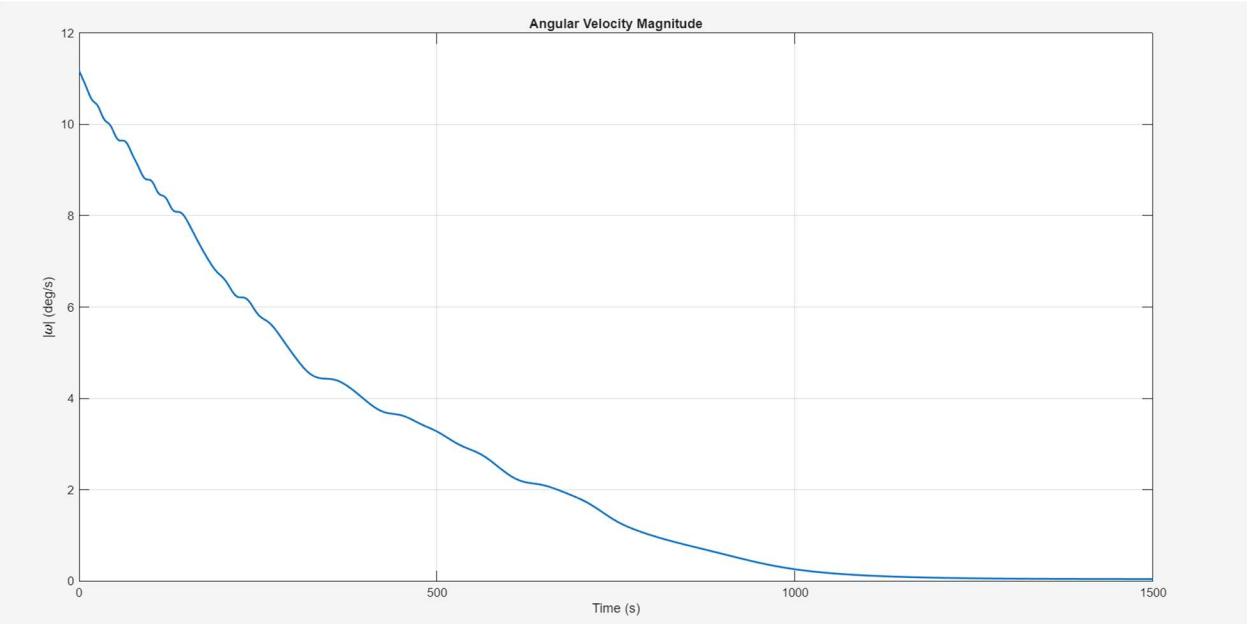


Figure 4.48 – Angular velocity magnitude N = 800

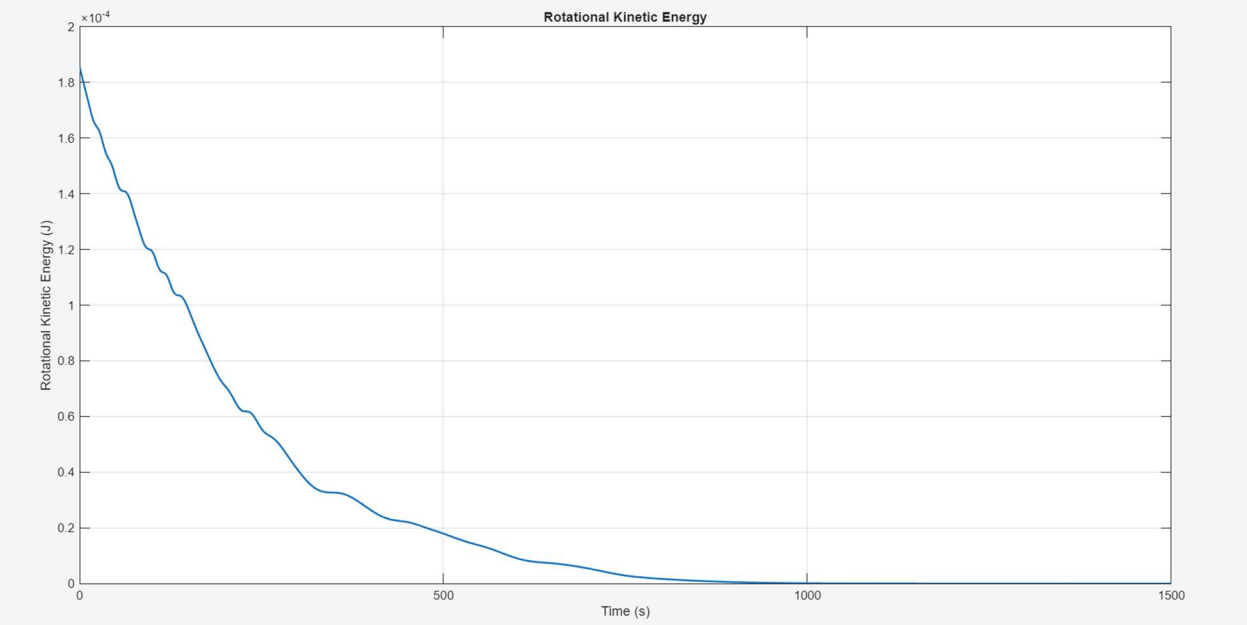


Figure 4.49 – Rotational kinetic energy N = 800

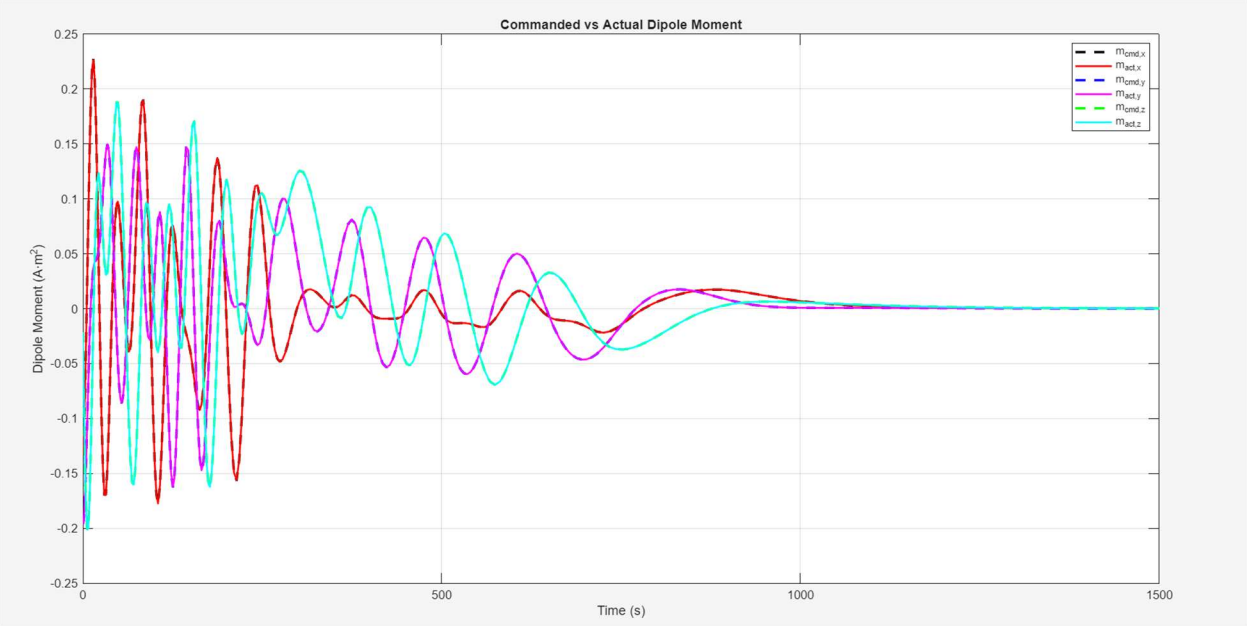


Figure 4.50 – Commanded vs actual dipole moment N = 800

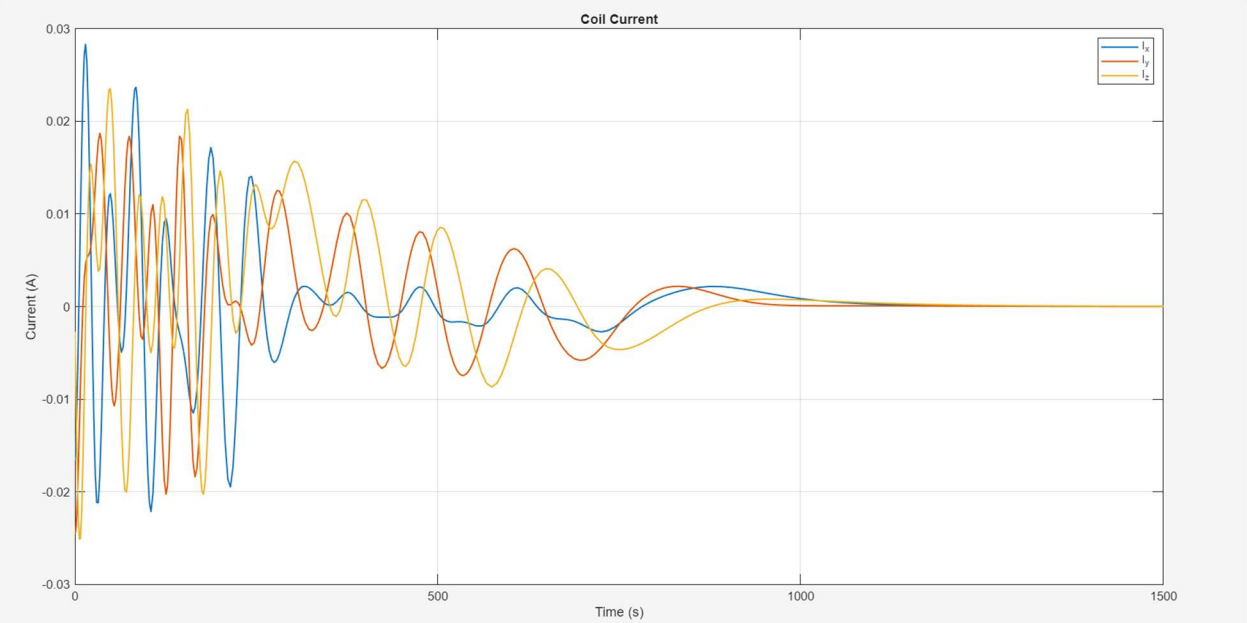


Figure 4.51 – Coil current N = 800

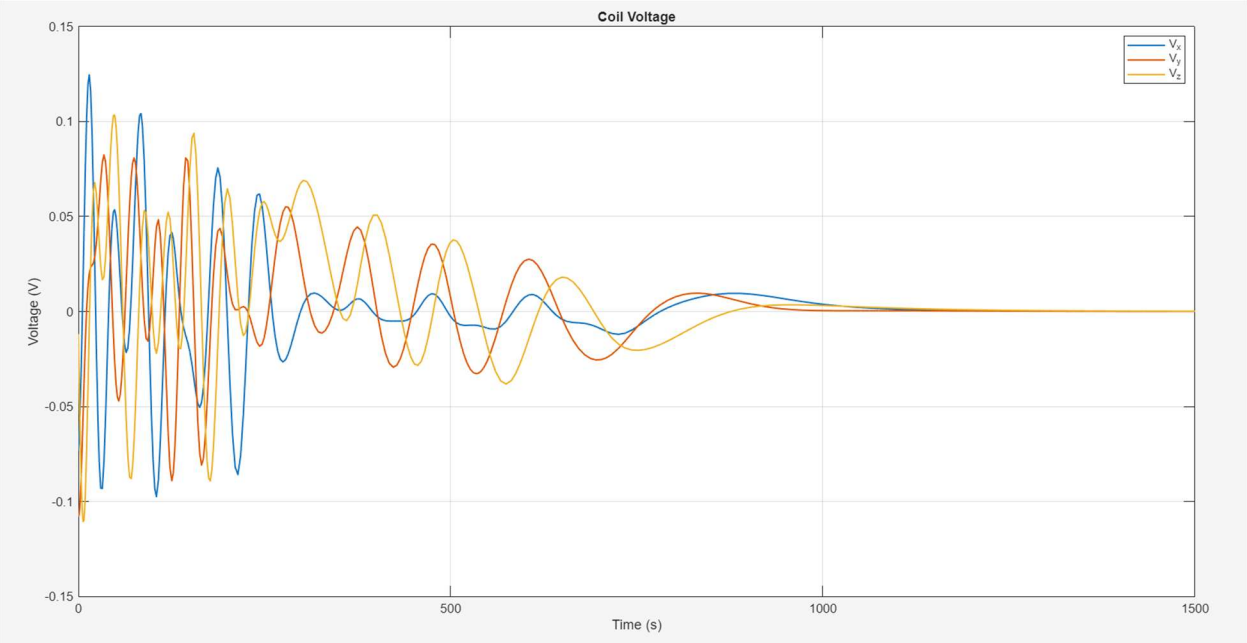


Figure 4.52 – Coil voltage N = 800

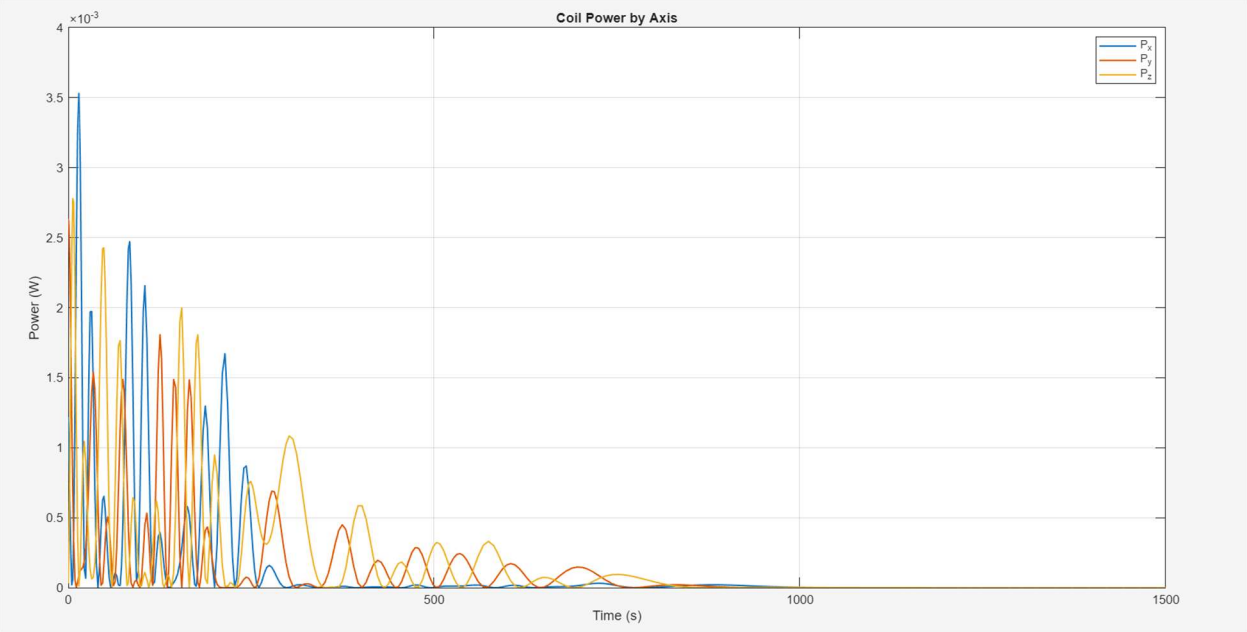


Figure 4.53 – Coil power N = 800

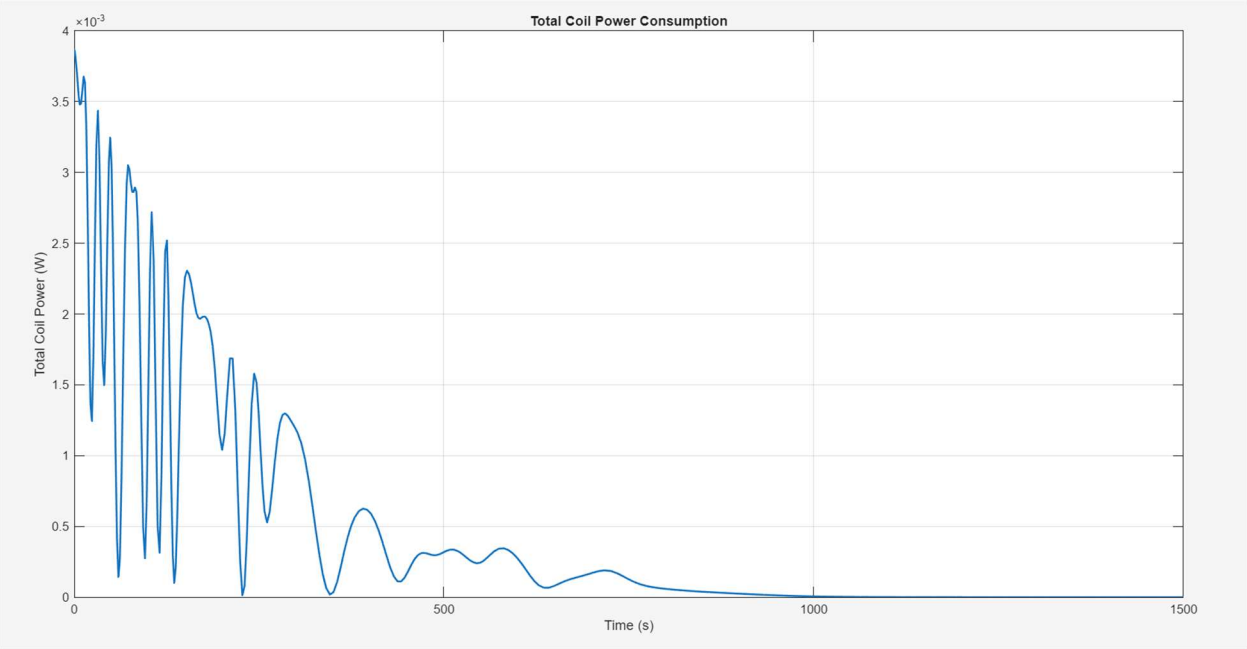


Figure 4.54 – Total coil power consumption N = 800

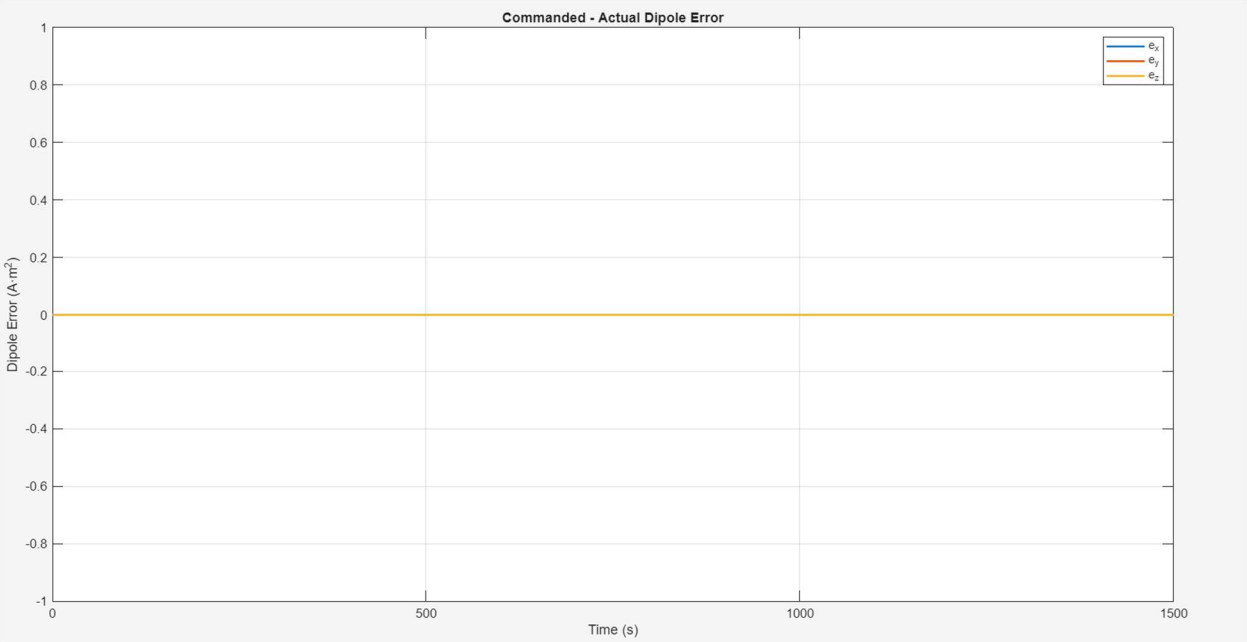


Figure 4.55 – Commanded vs actual dipole error N = 800

Quantitative numerical results are provided below for number of turns sweep case study:

Table 4.4 – Quantitative numerical results of number of turns sweep case study

N turns	Detumble time to 0.50 deg/s (s)	Peak power (W)	Peak current (A)	Peak dipole (A·m²)	Peak Voltage (V)	Final $\|\omega\|$ (deg/s)
100	975.045	0.2133	[0.1500 0.1500 0.1500]	[0.1500 0.1500 0.1500]	[0.6600 0.6600 0.6600]	0.135
200	933.137	0.0620	[0.1133 0.0978 0.1005]	[0.2267 0.1956 0.2010]	[0.4987 0.4303 0.4423]	0.042
400	933.137	0.0155	[0.0567 0.0489 0.0503]	[0.2267 0.1956 0.2010]	[0.2493 0.2152 0.2212]	0.042
800	933.137	0.0039	[0.0283 0.0244 0.0251]	[0.2267 0.1956 0.2010]	[0.1247 0.1076 0.1106]	0.042

4.4.2 Coil Area Sweep

In this sub-study, the simulation was run for coil area, A = 0.004, 0.006, 0.008, 0.01 m^2. Below are the set parameters for the plot results.

Table 4.5 – Fixed parameters for coil area sweep

B-dot controller gain, k	N turns	Coil resistance (Ohms)	Coil max current (A)	Coil max voltage (V)
5e4	200	4.4	0.15	5

- **Coil Area = 0.004 m^2**

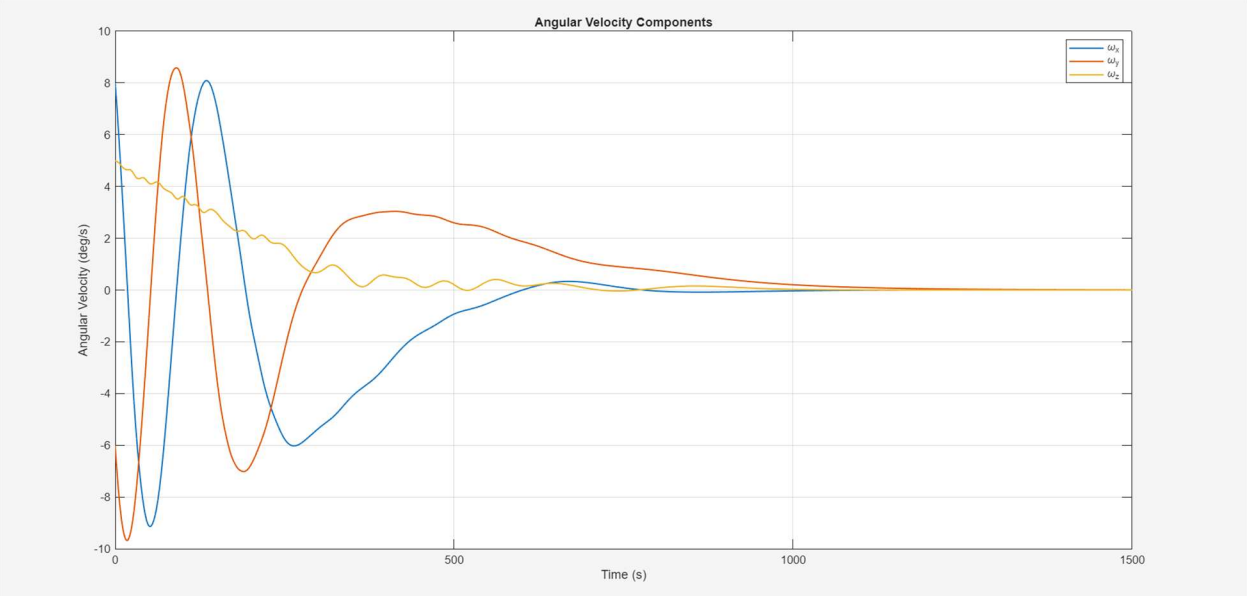


Figure 4.56 – Angular velocity components coil area = 0.004 m^2

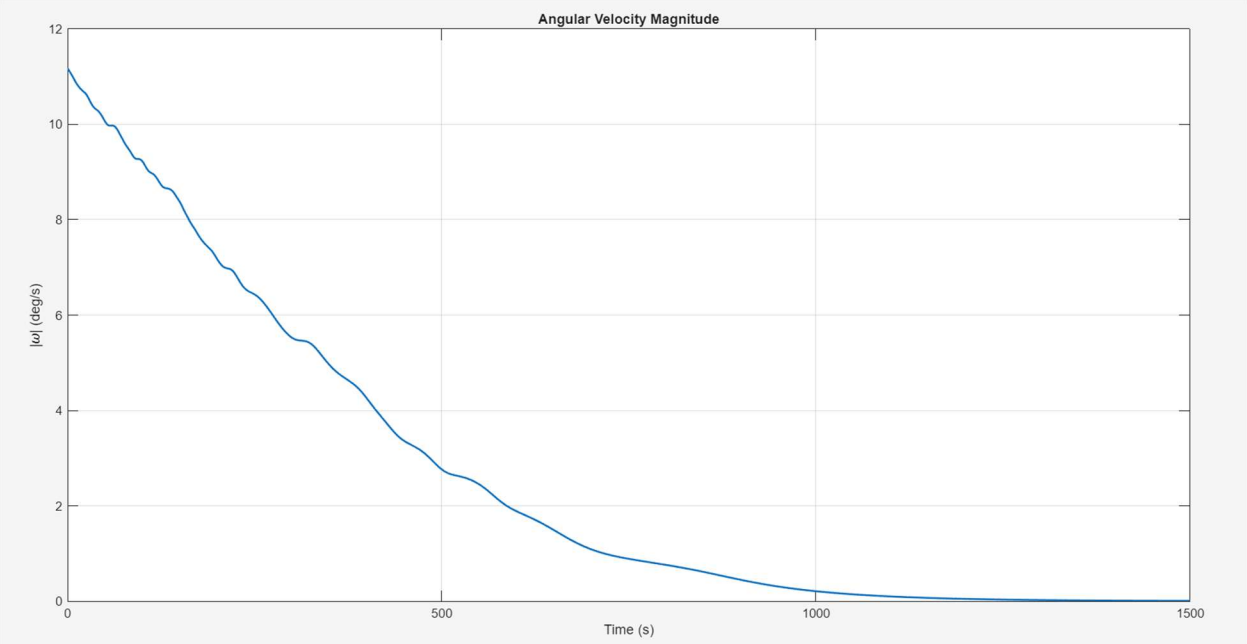


Figure 4.57 – Angular velocity magnitude coil area = 0.004 m^2

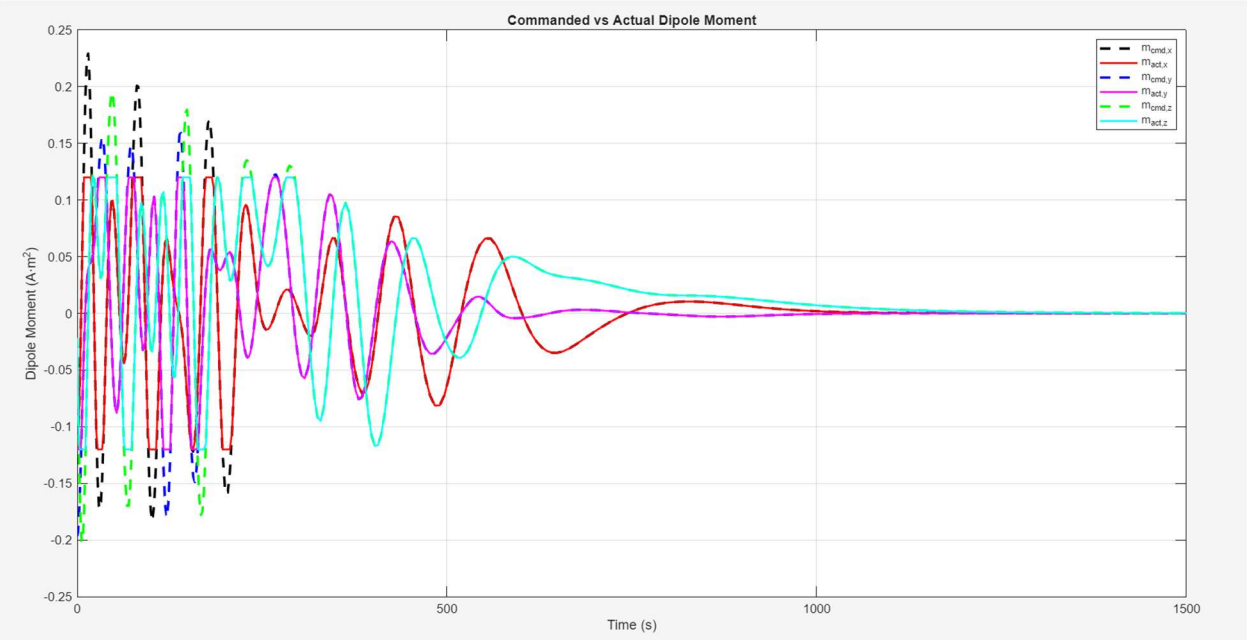


Figure 4.58 – Commanded vs actual dipole moment coil area = 0.004 m^2

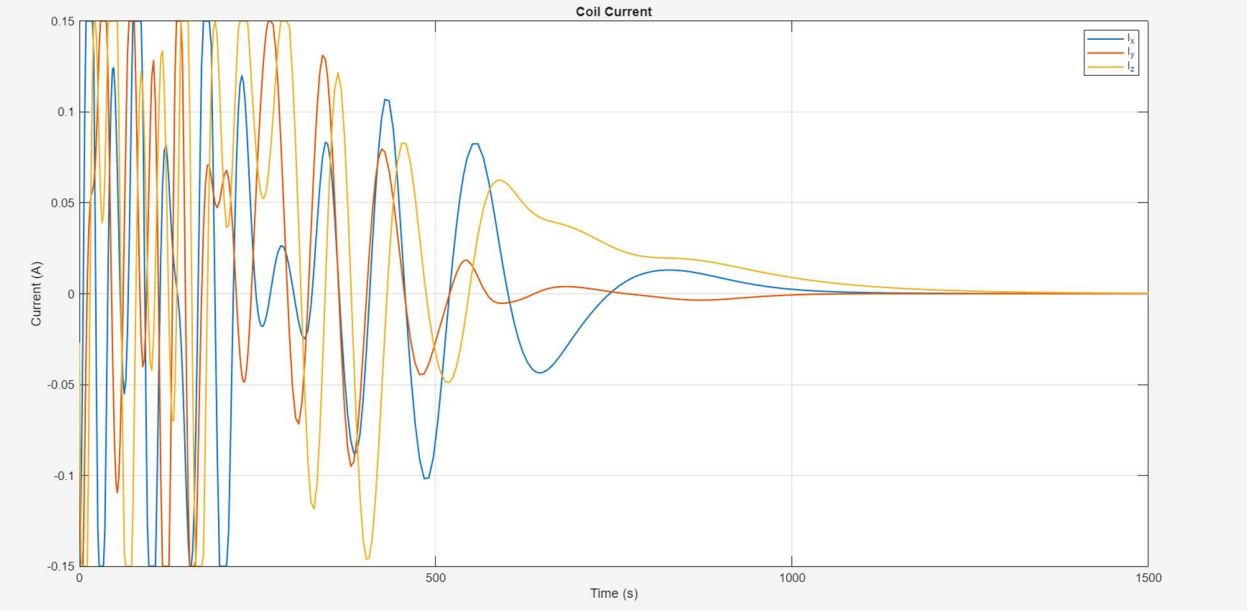


Figure 4.59 – Coil current coil area = 0.004 m^2

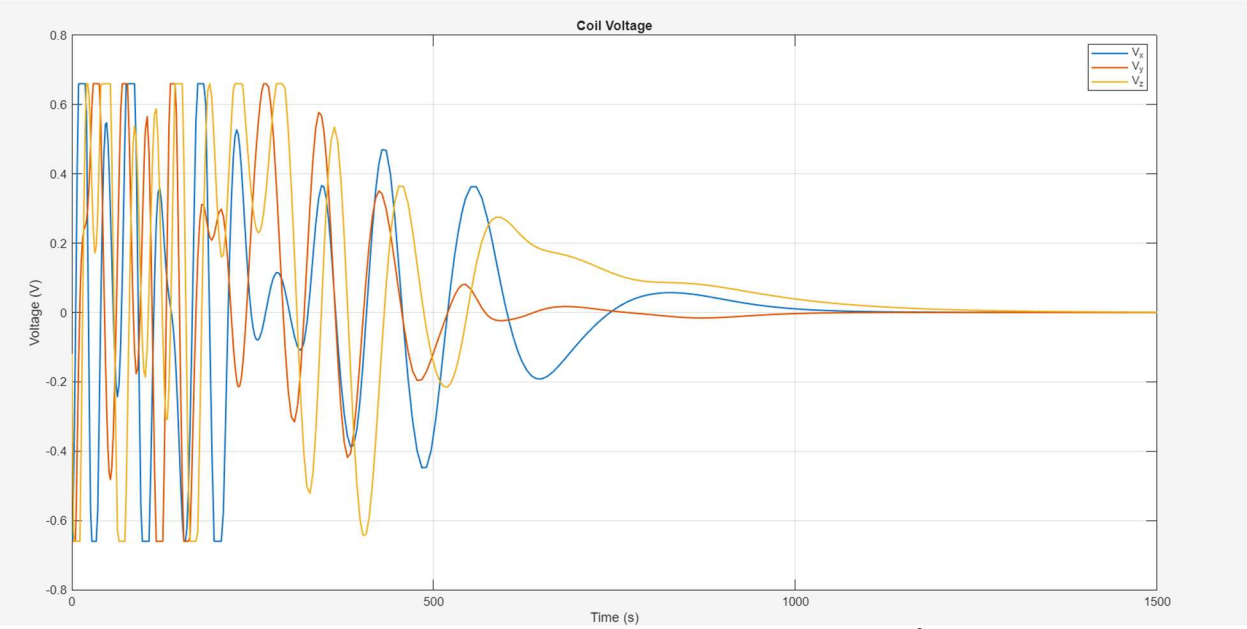


Figure 4.60 – Coil voltage coil area = 0.004 m^2

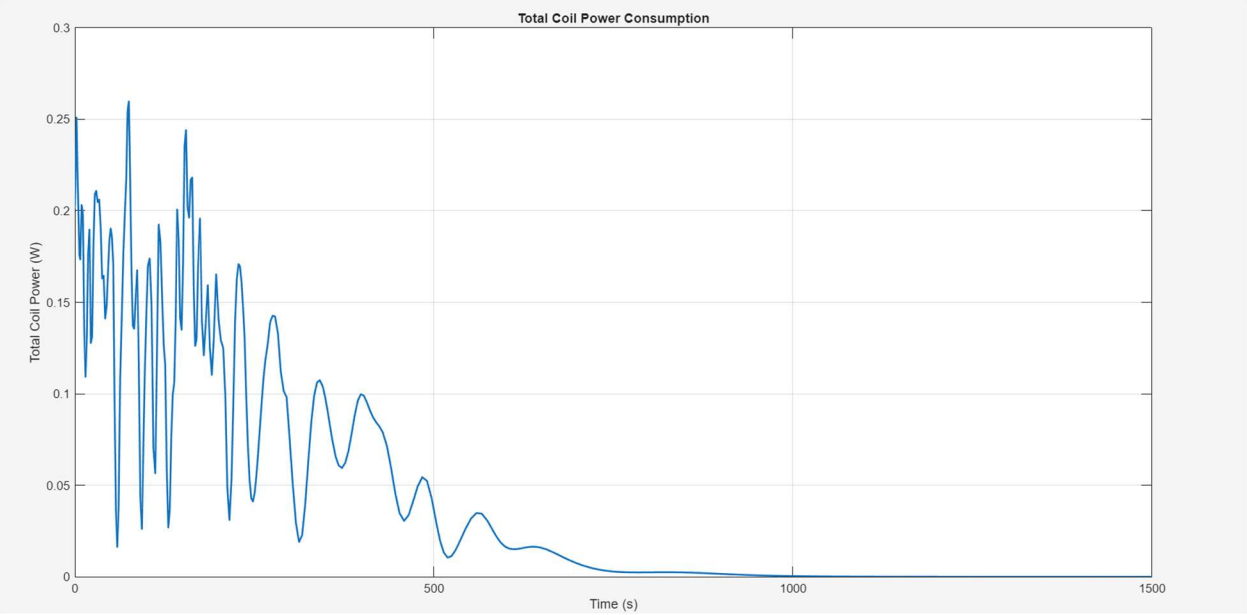


Figure 4.61 – Total coil power consumption coil area = 0.004 m^2

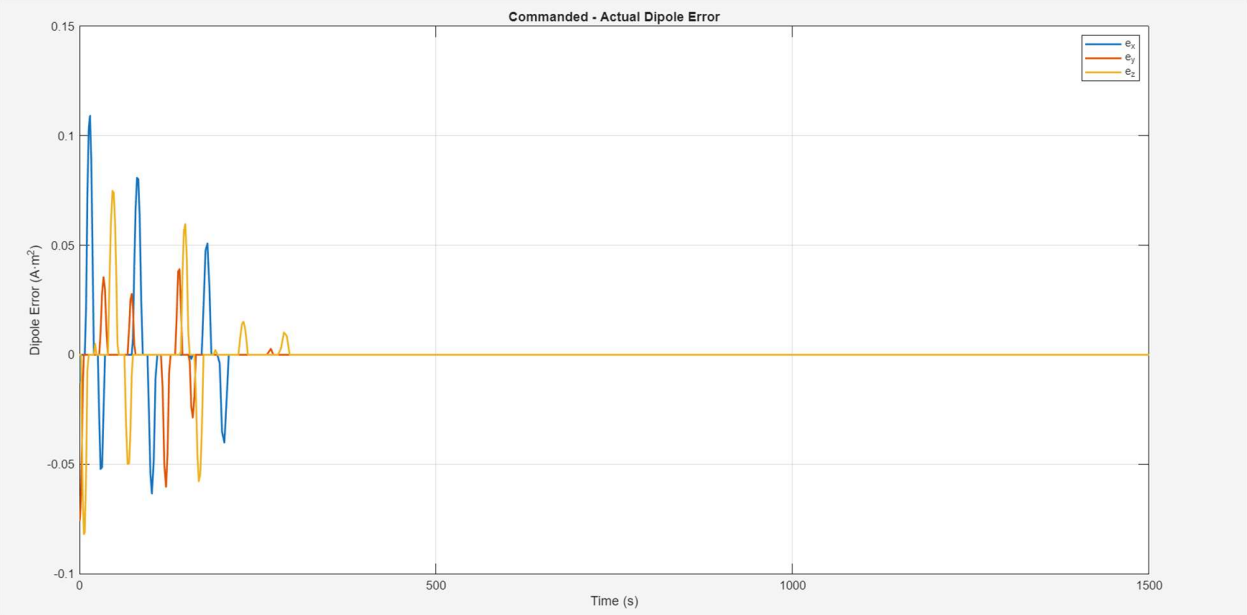


Figure 4.62 – Commanded vs actual dipole error coil area = 0.004 m^2

- **Coil Area = 0.006 m^2**

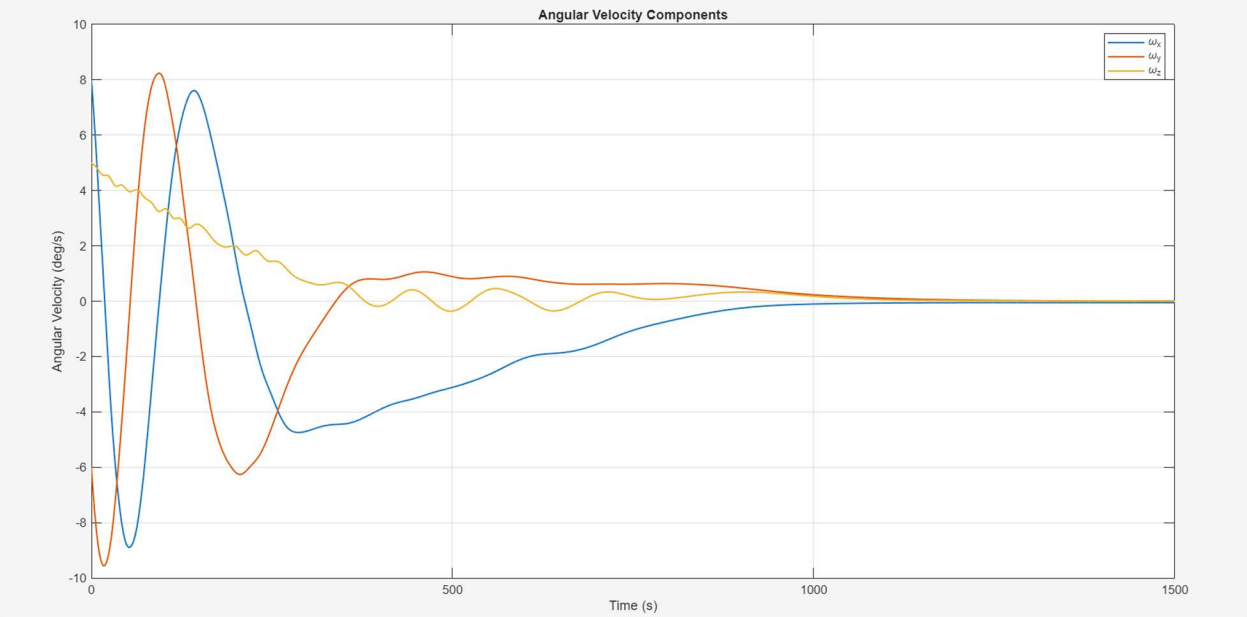


Figure 4.63 – Angular velocity components coil area = 0.006 m^2

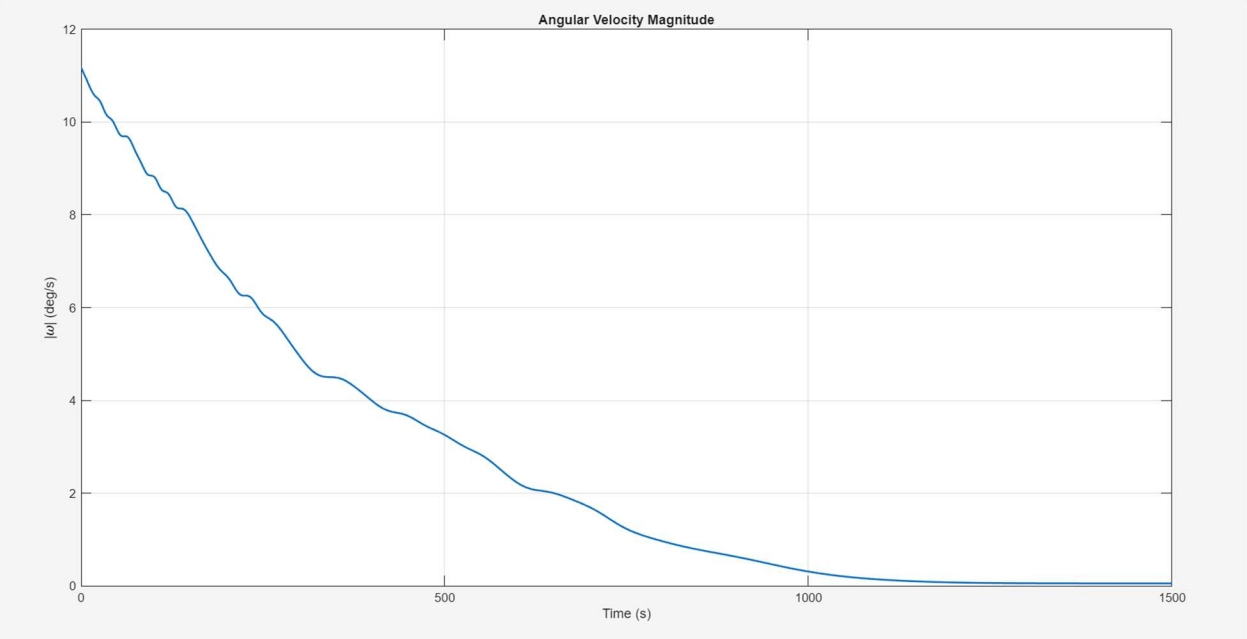


Figure 4.64 – Angular velocity magnitude coil area = 0.006 m^2

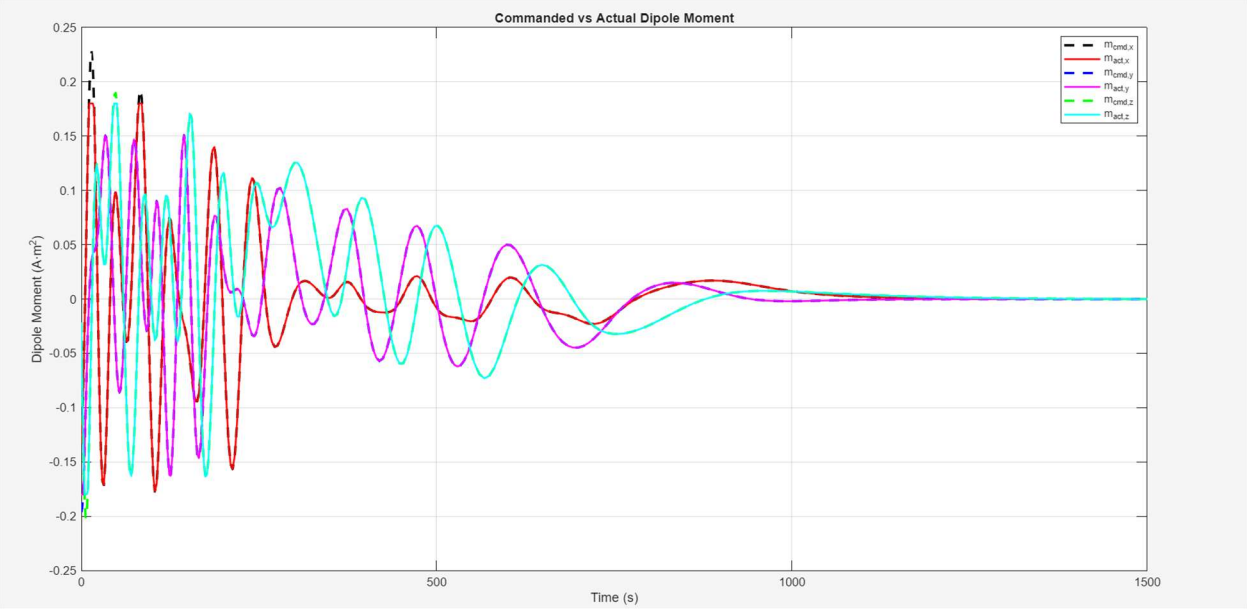


Figure 4.65 – Commanded vs actual dipole moment coil area = 0.006 m^2

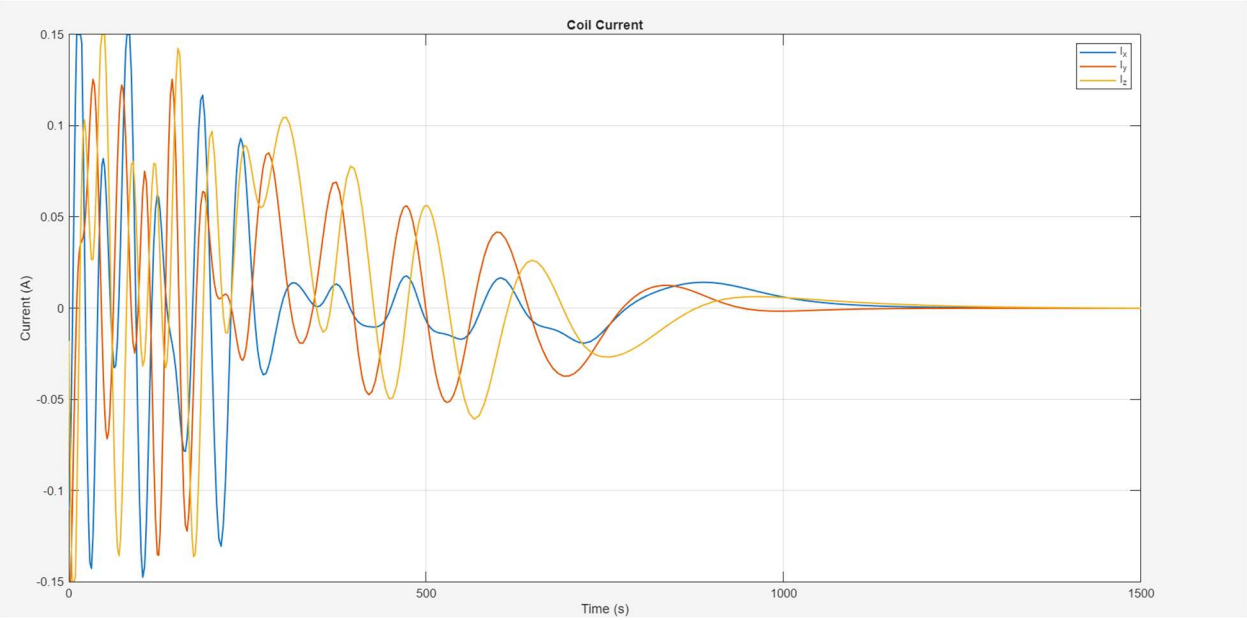


Figure 4.66 – Coil current coil area = 0.006 m^2

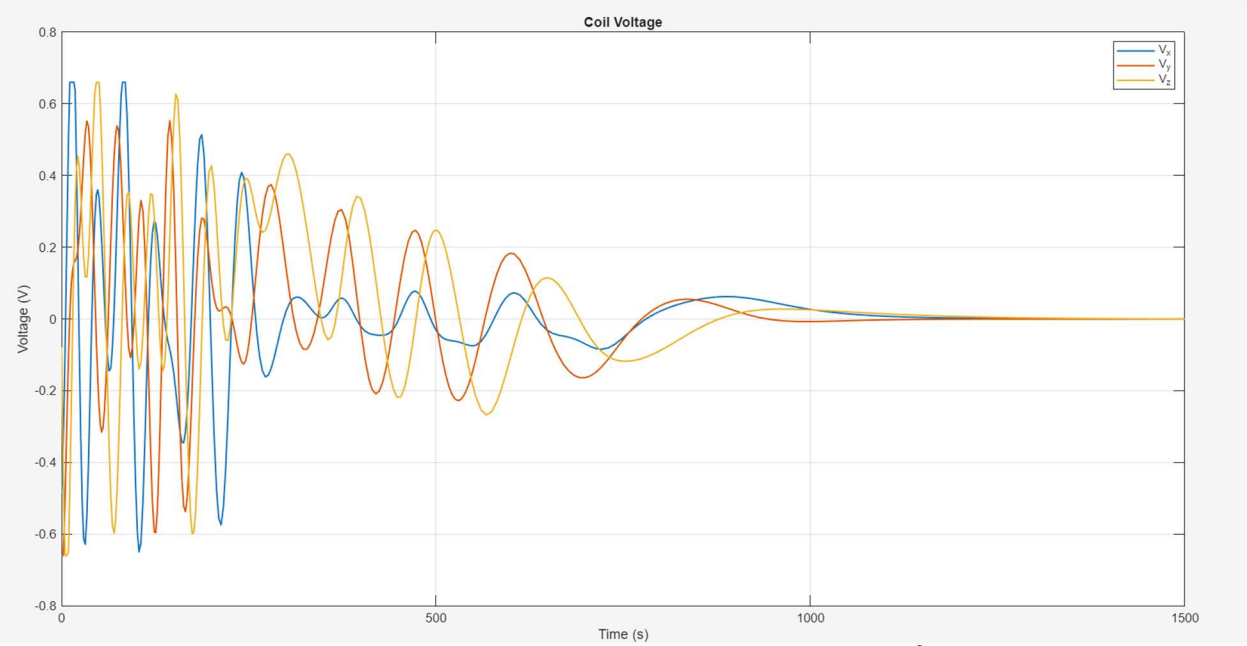


Figure 4.67 – Coil voltage coil area = 0.006 m^2

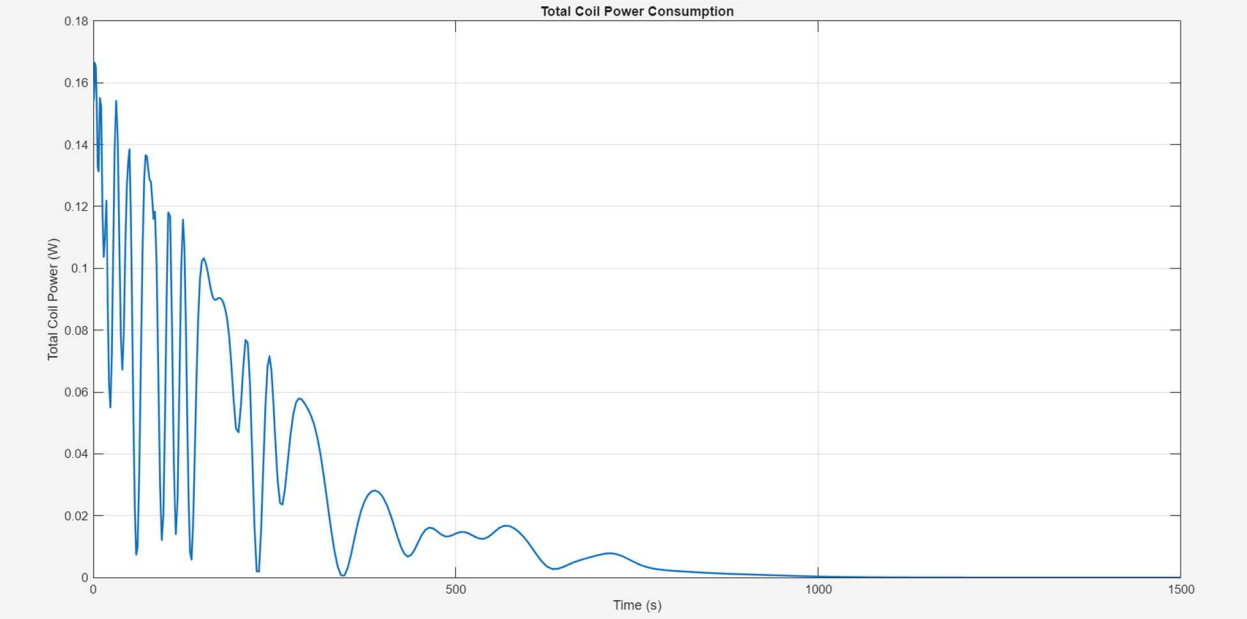


Figure 4.68 – Total coil power consumption coil area = 0.006 m^2

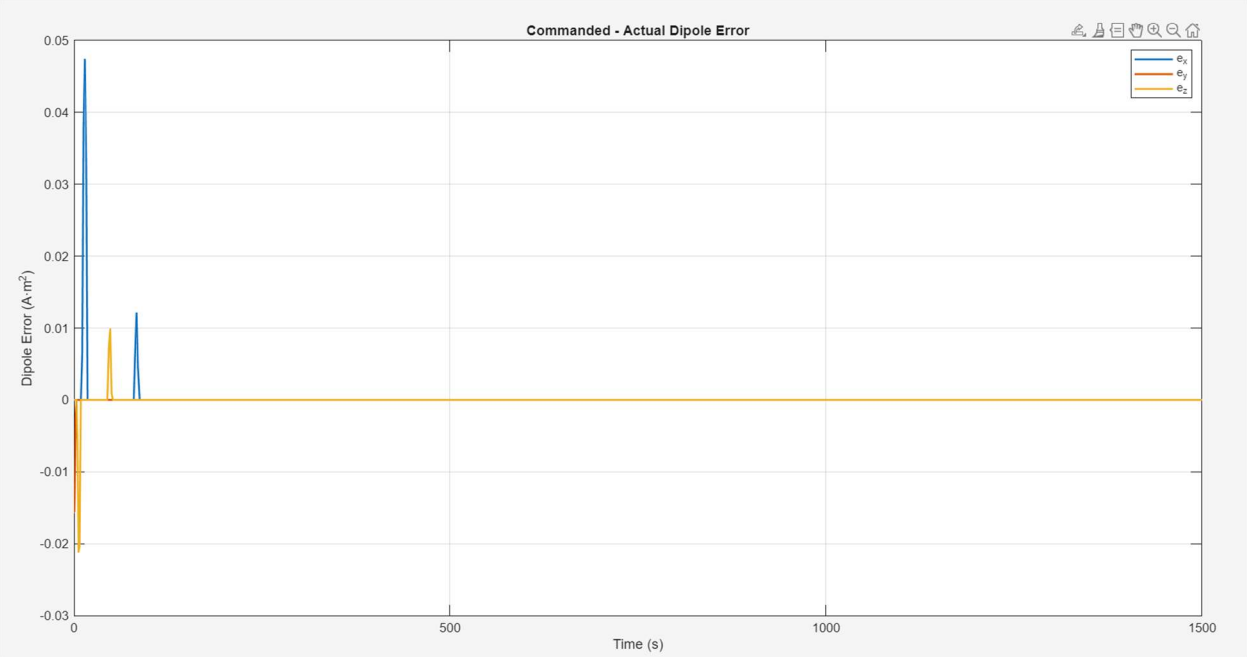


Figure 4.69 – Commanded vs actual dipole error coil area = 0.006 m^2

- **Coil Area = 0.008 m^2**

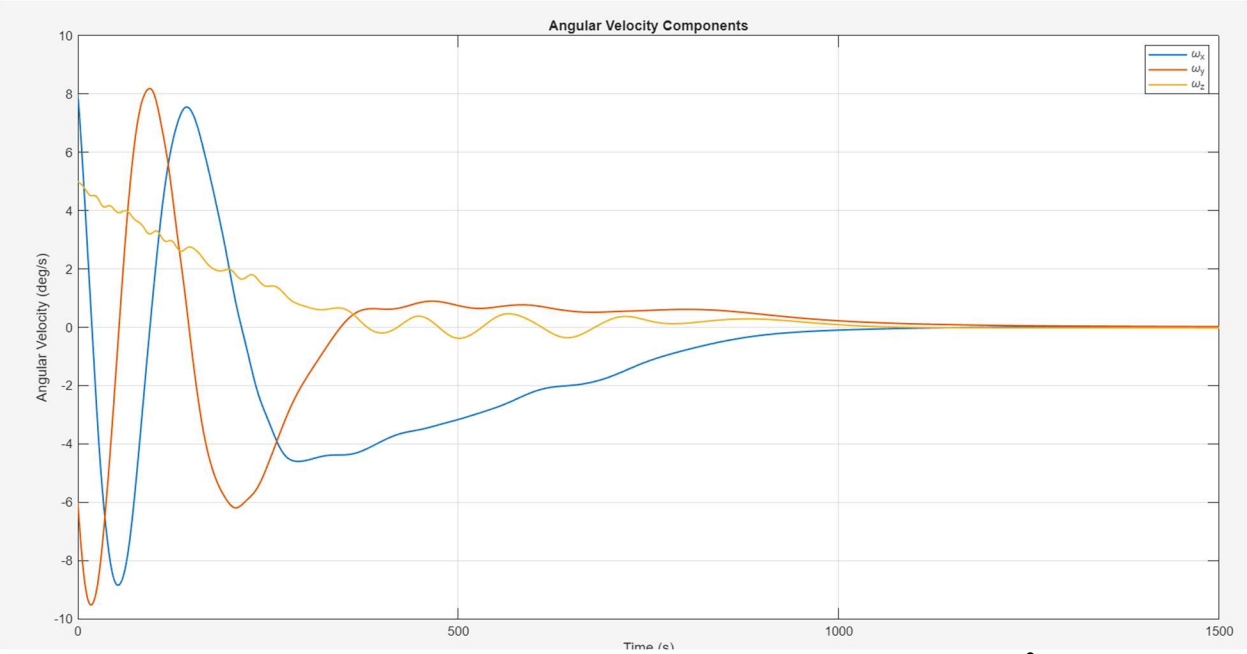


Figure 4.70 – Angular velocity components coil area = 0.008 m^2

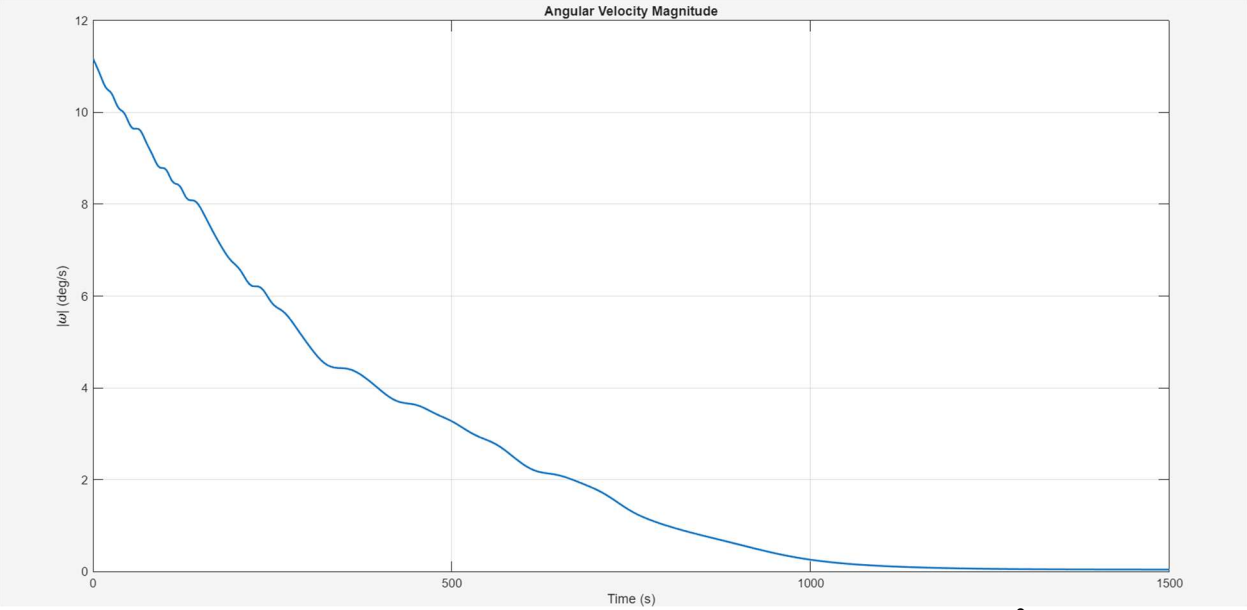


Figure 4.71 – Angular velocity magnitude coil area = 0.008 m^2

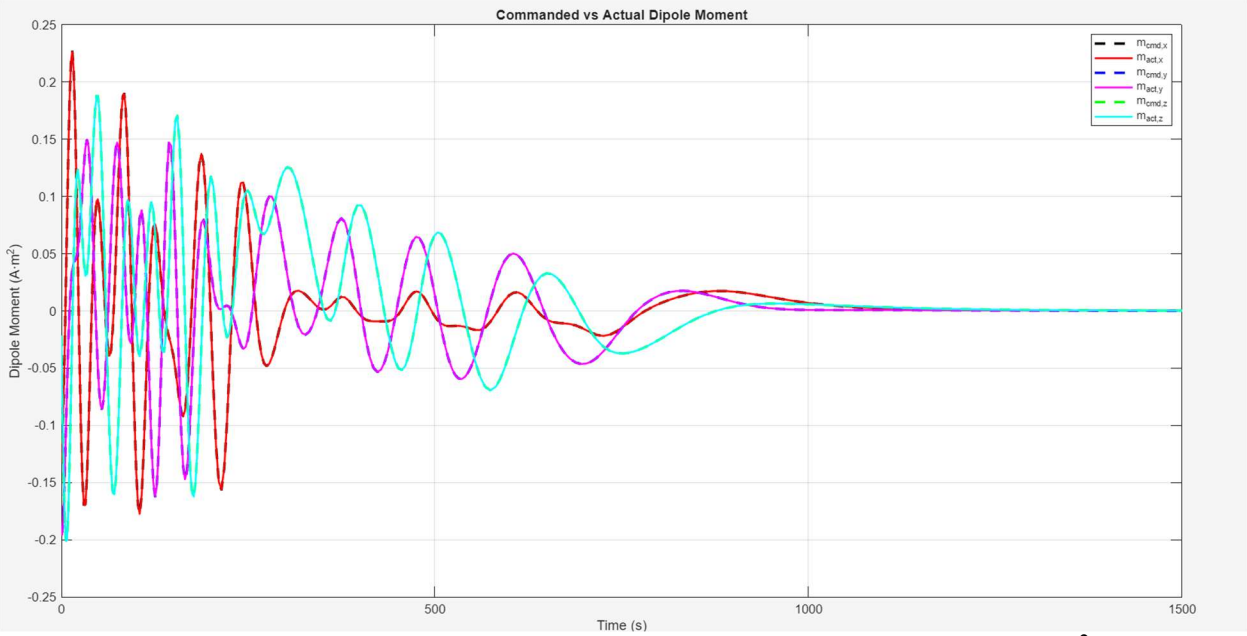


Figure 4.72 – Commanded vs actual dipole moment coil area = 0.008 m^2

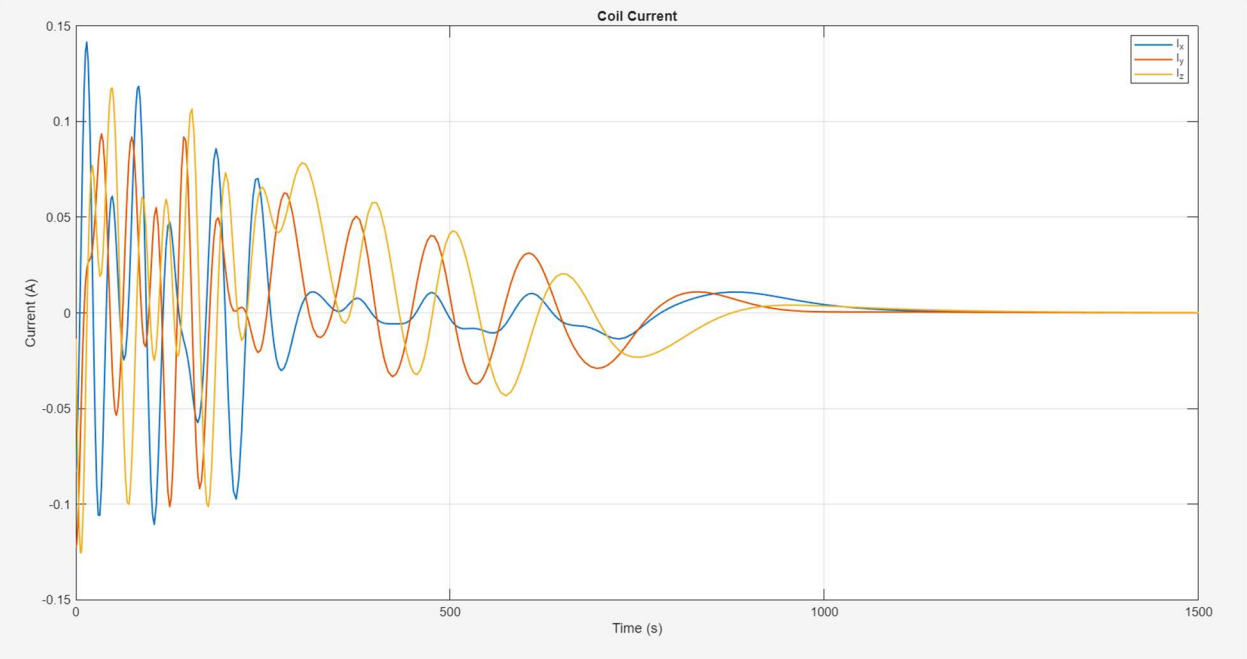


Figure 4.73 – Coil current coil area = 0.008 m^2

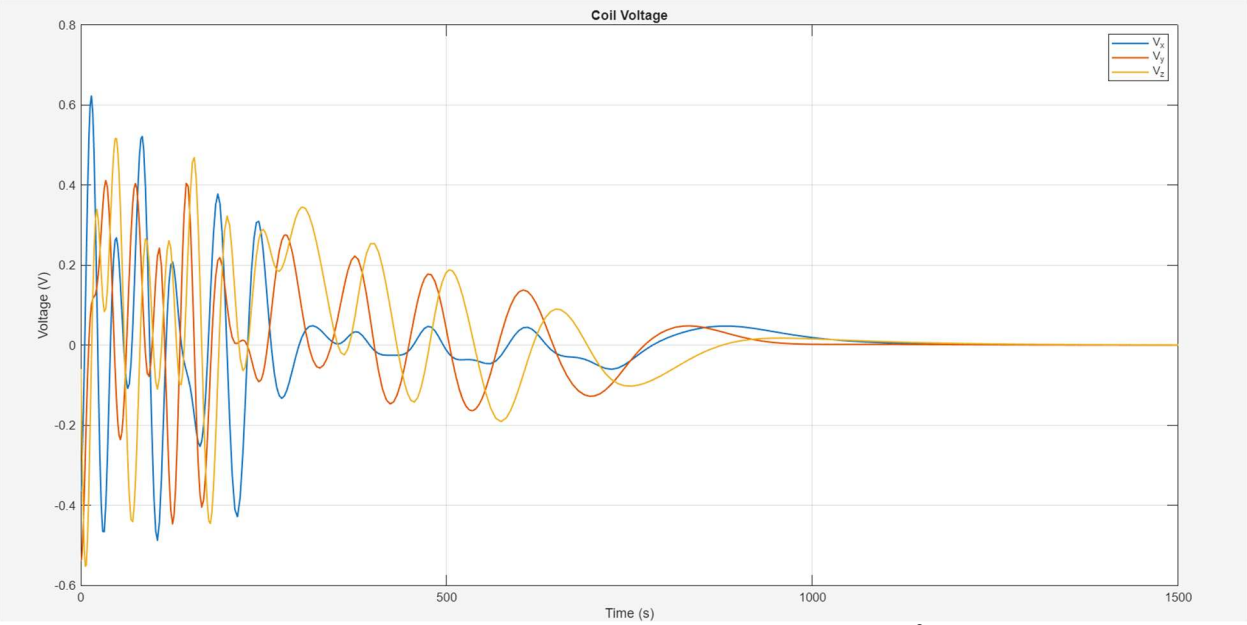


Figure 4.74 – Coil voltage coil area = 0.008 m^2

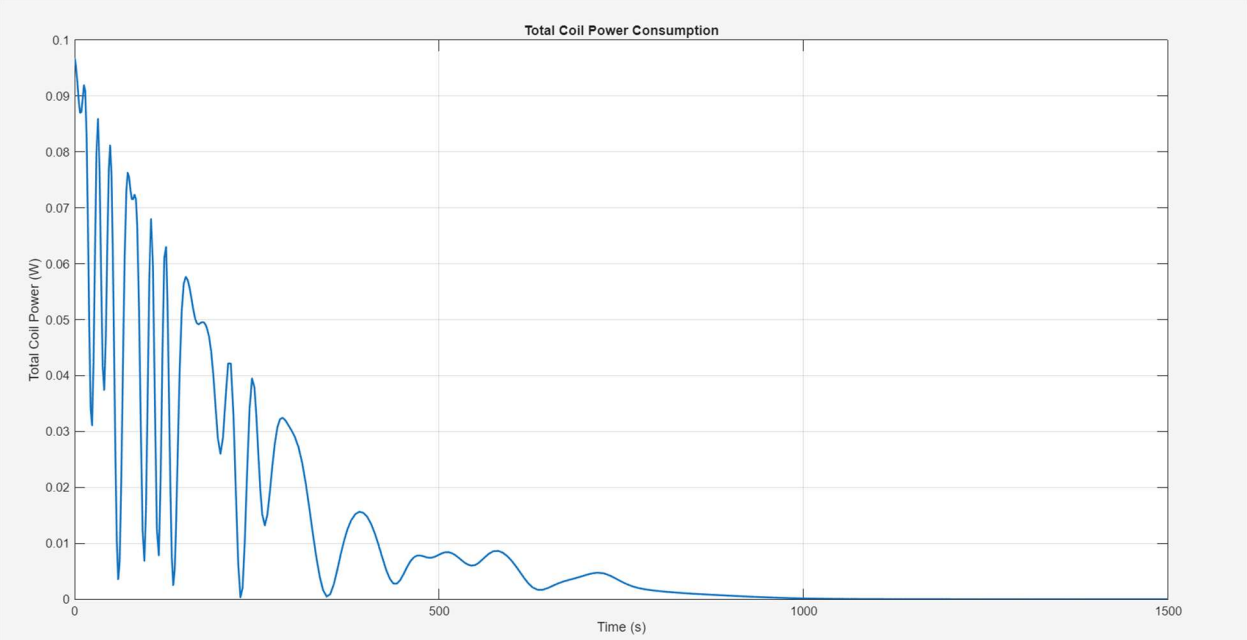


Figure 4.75 – Total coil power consumption coil area = 0.008 m^2

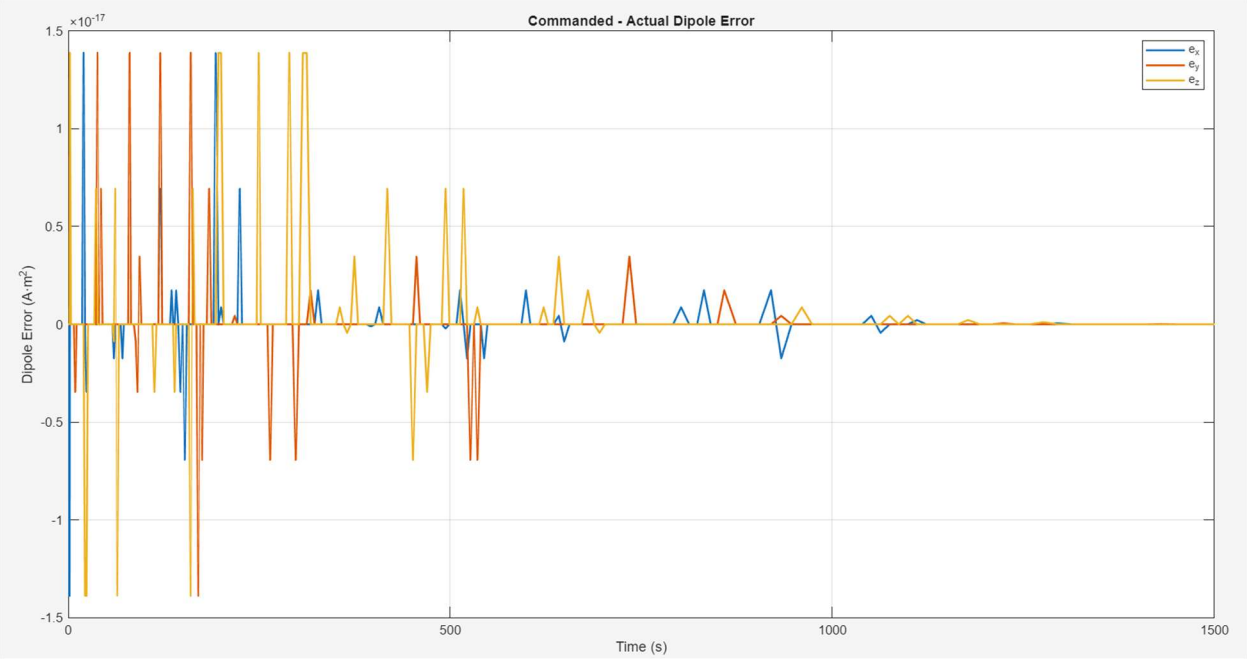


Figure 4.76 – Commanded vs actual dipole error coil area = 0.008 m^2

- **Coil Area = 0.01 m^2**

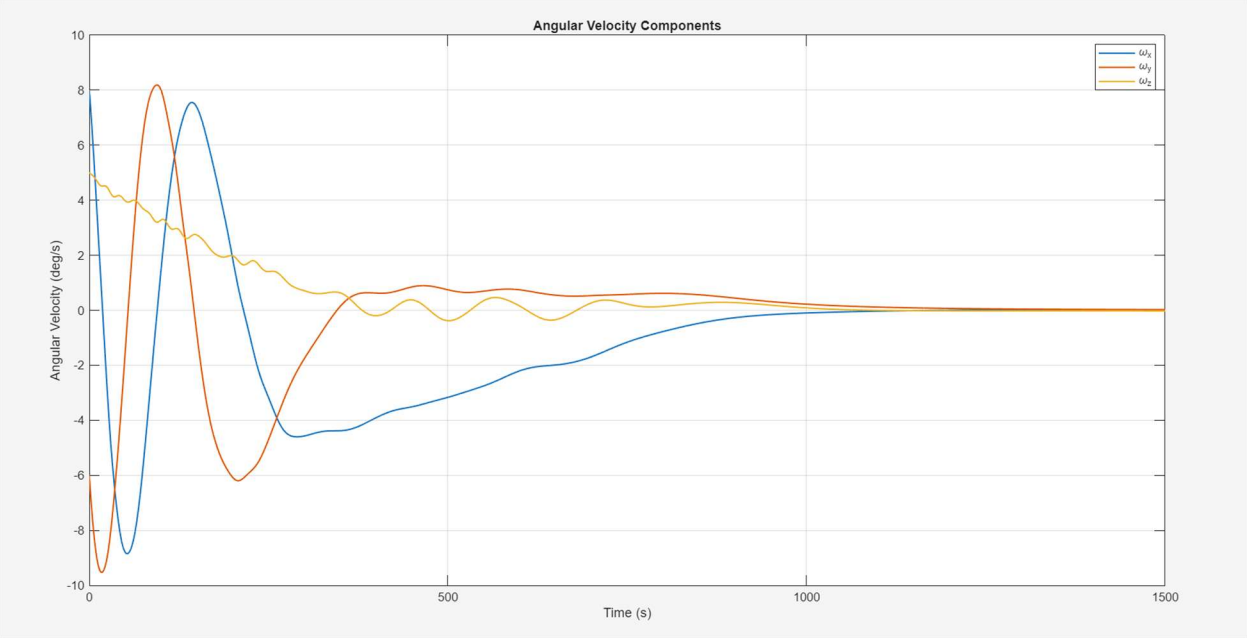


Figure 4.77 – Angular velocity components coil area = 0.01 m^2

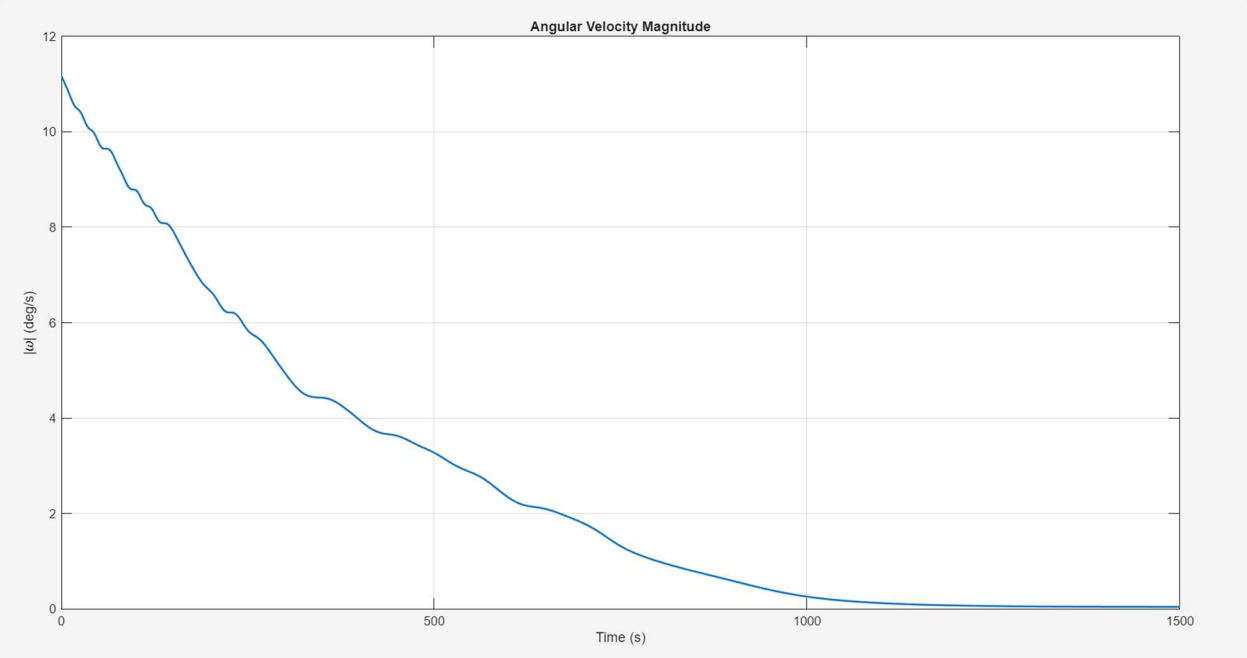


Figure 4.78 – Angular velocity magnitude coil area = 0.01 m^2

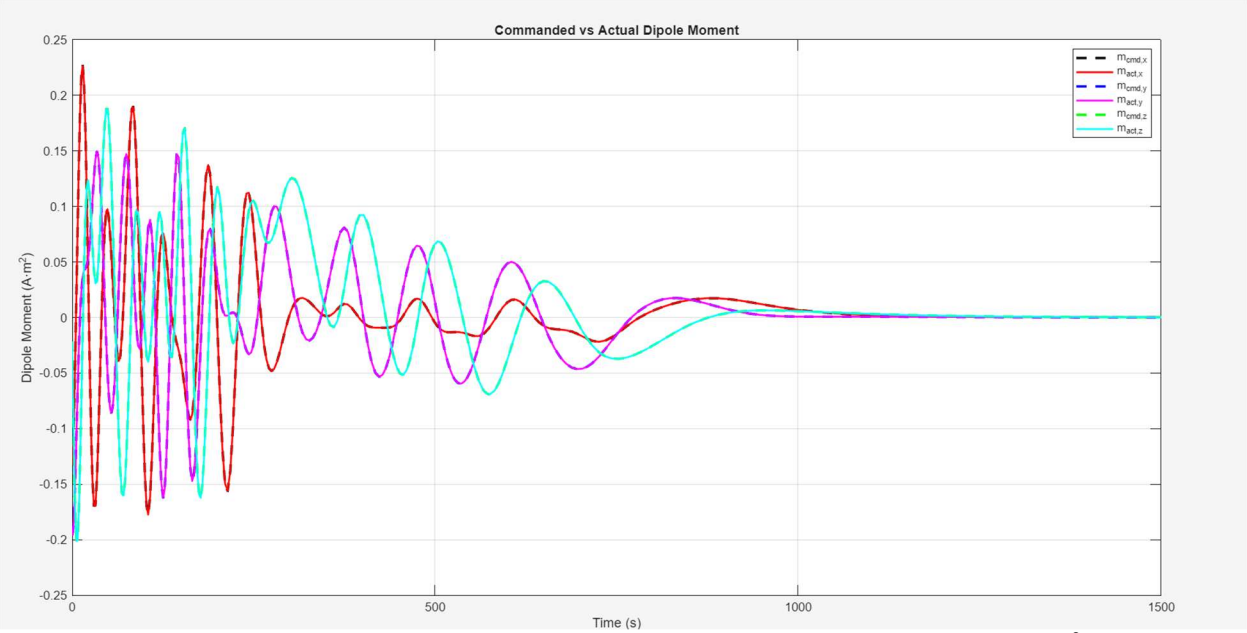


Figure 4.79 – Commanded vs actual dipole moment coil area = 0.01 m^2

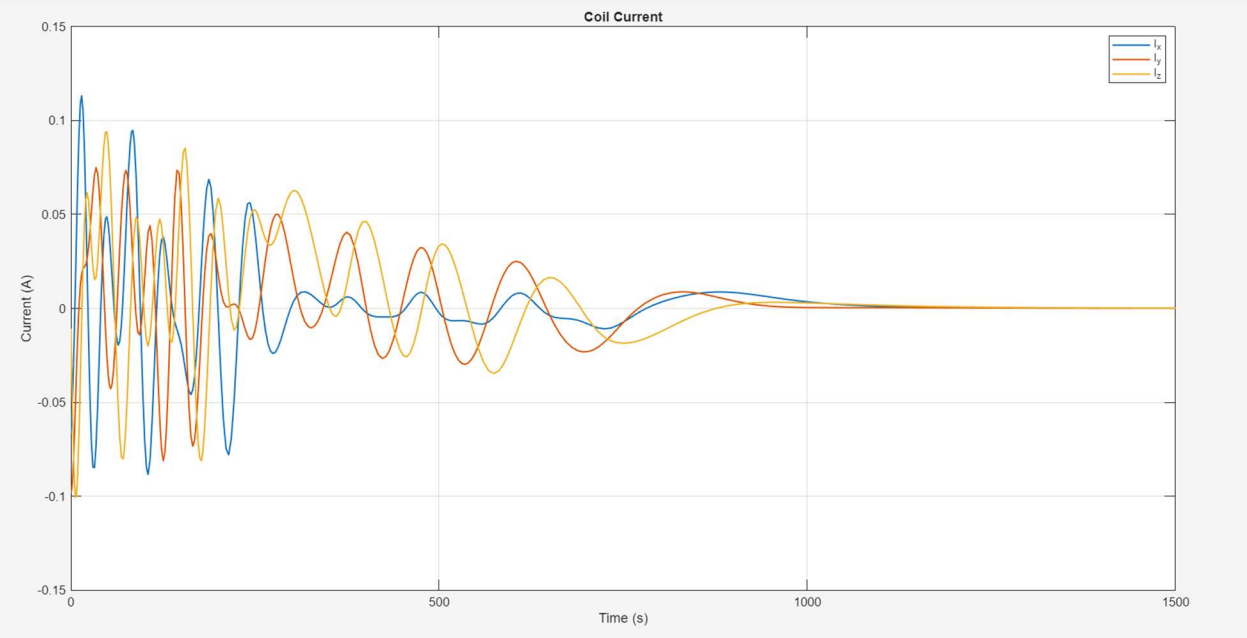


Figure 4.80 – Coil current coil area = 0.01 m^2

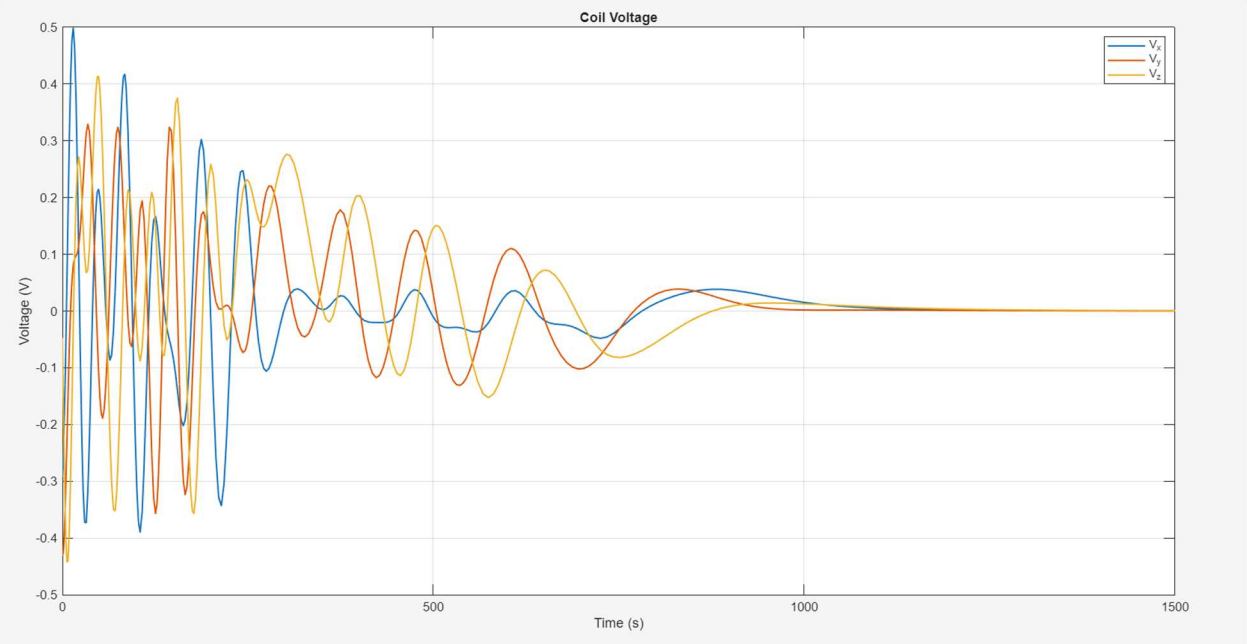


Figure 4.81 – Coil voltage coil area = 0.01 m^2

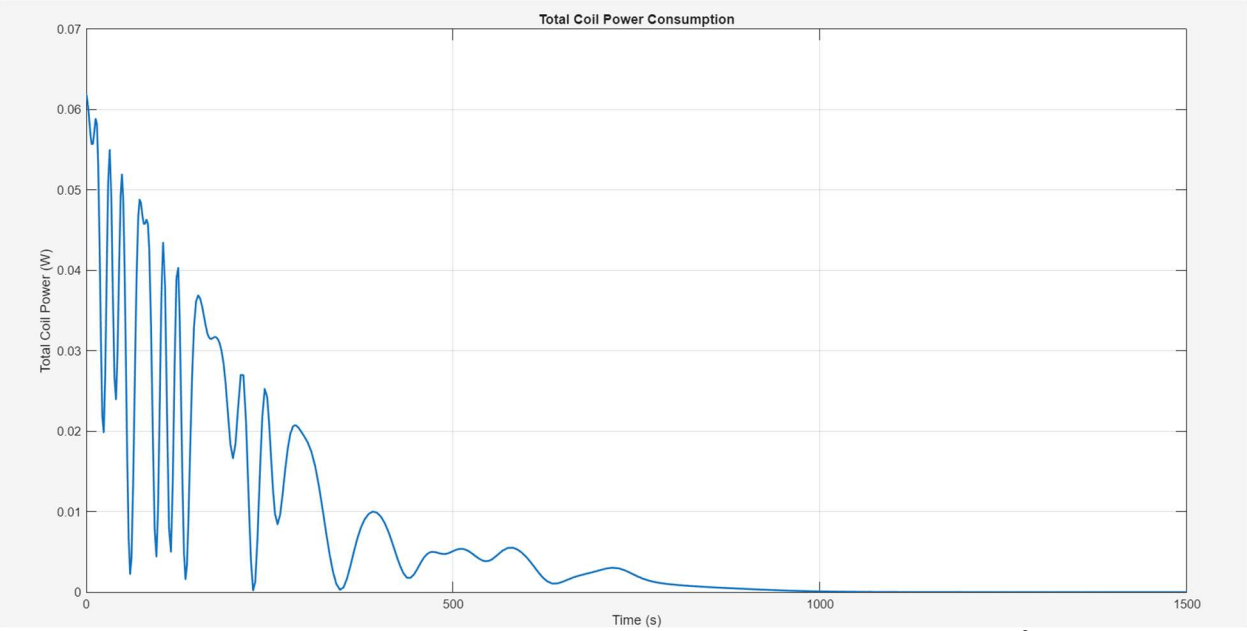


Figure 4.82 – Total coil power consumption coil area = 0.01 m^2

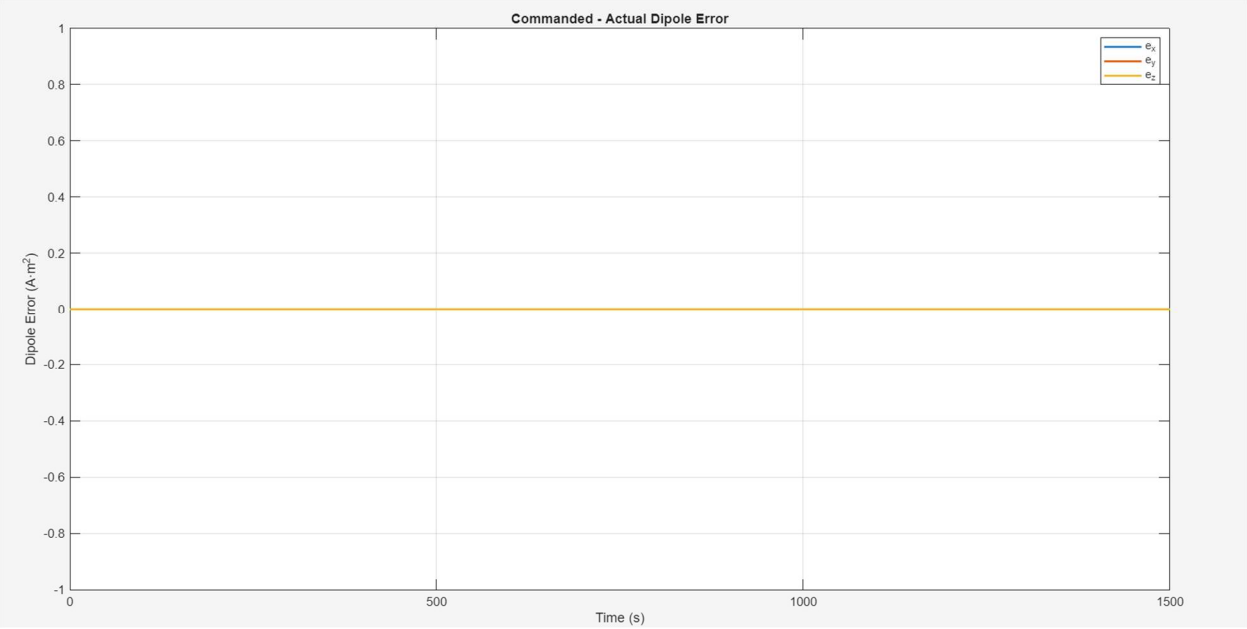


Figure 4.83 – Commanded vs actual dipole error coil area = 0.01 m^2

Quantitative numerical results are provided below for coil area sweep case study:

Table 4.6 – Quantitative numerical results of coil area sweep case study

Coil Area (m^2)	Detumble time to 0.50 deg/s (s)	Peak power (W)	Peak current (A)	Peak dipole (A·m²)	Peak Voltage (V)	Final $\|\omega\|$ (deg/s)
0.004	884.036	0.2598	[0.1500 0.1500 0.1500]	[0.1200 0.1200 0.1200]	[0.6600 0.6600 0.6600]	0.007
0.006	948.663	0.1664	[0.1500 0.1500 0.1500]	[0.1800 0.1800 0.1800]	[0.6600 0.6600 0.6600]	0.053
0.008	933.137	0.0968	[0.1417 0.1222 0.1257]	[0.2267 0.1956 0.2010]	[0.6233 0.5379 0.5529]	0.042
0.01	933.137	0.0620	[0.1133 0.0978	[0.2267 0.1956	[0.4987 0.4303	0.042

			0.1005]	0.2010]	0.4423]	

4.4.3 Current Limit Sweep

In this sub-study, the simulation was run for coil max current, I = 0.02, 0.05, 0.1, 0.15 A. Below are the set parameters for the plot results.

Table 4.7 – Fixed parameters for current limit sweep

B-dot controller gain, k	N turns	Coil resistance (Ohms)	Coil area (m^2)	Coil max voltage (V)
5e4	200	4.4	0.01	5

- **Max Current = 0.02 Amps**

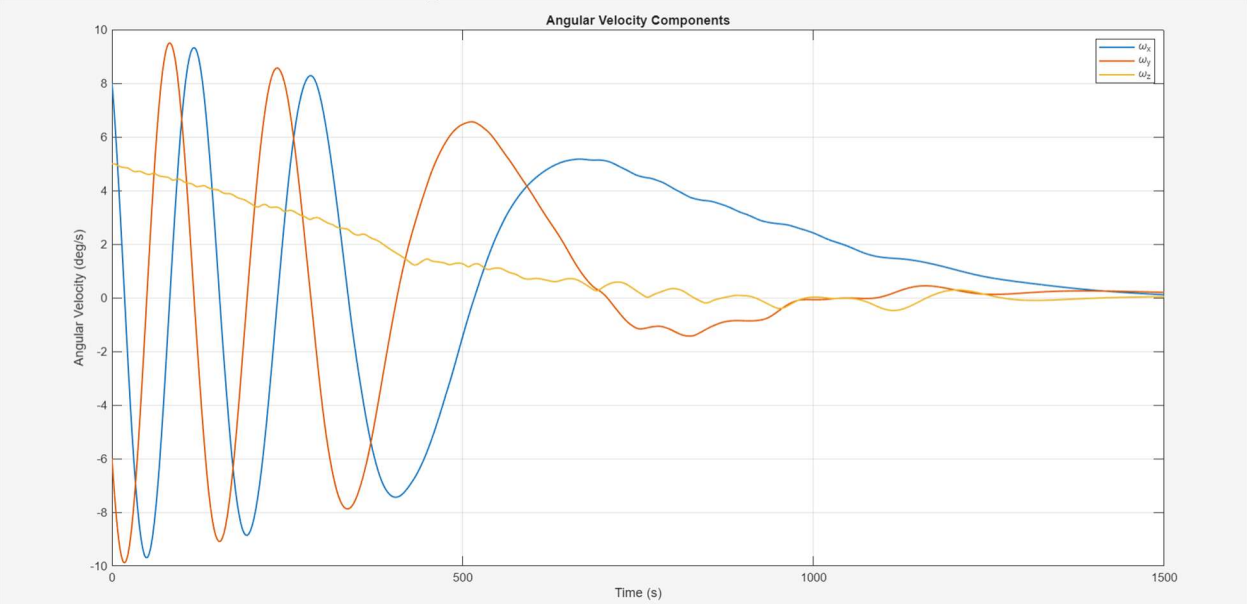


Figure 4.84 – Angular velocity components max current = 0.02 Amps

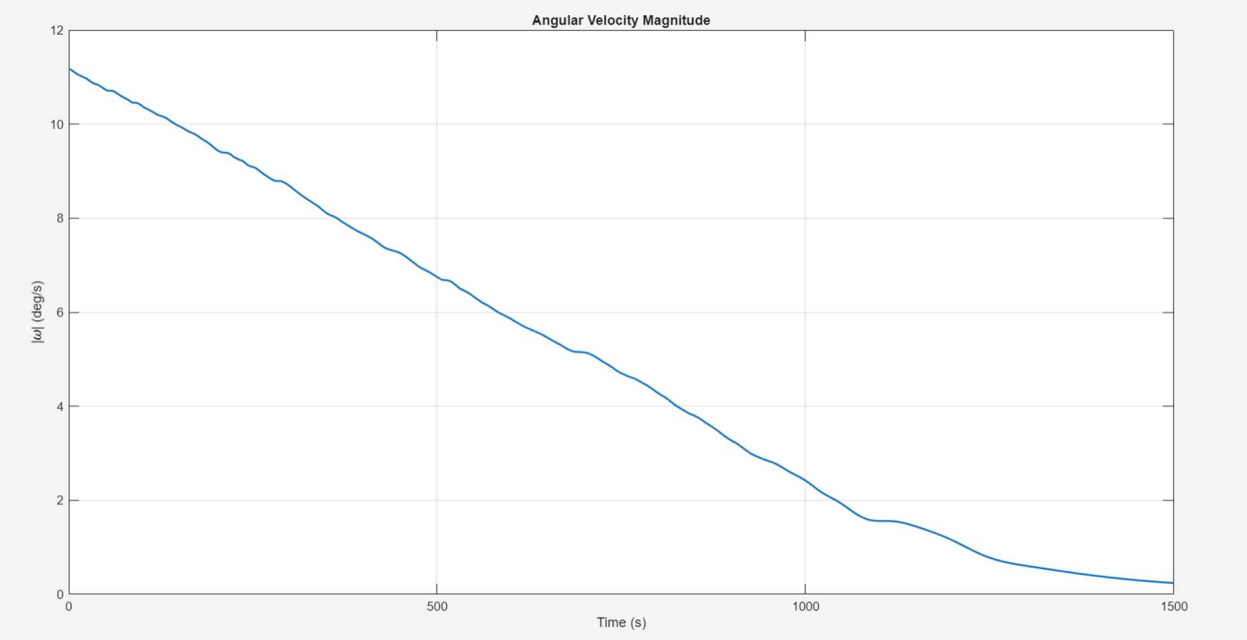


Figure 4.85 – Angular velocity magnitude max current = 0.02 Amps

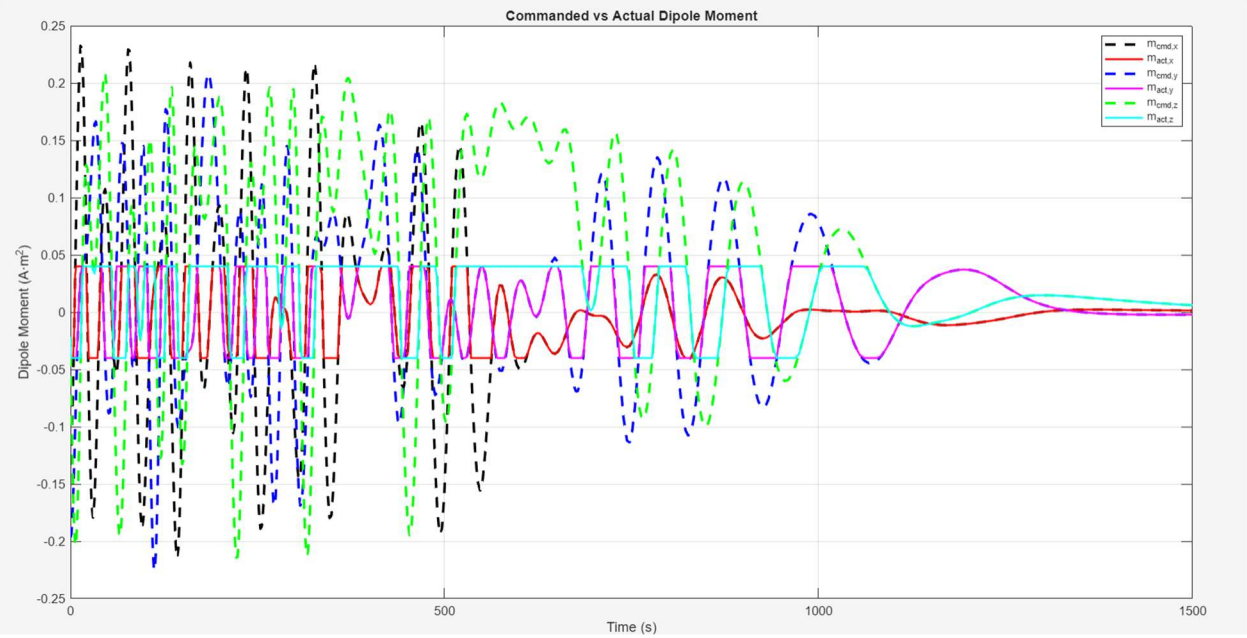


Figure 4.86 – Commanded vs actual dipole moment max current = 0.02 Amps

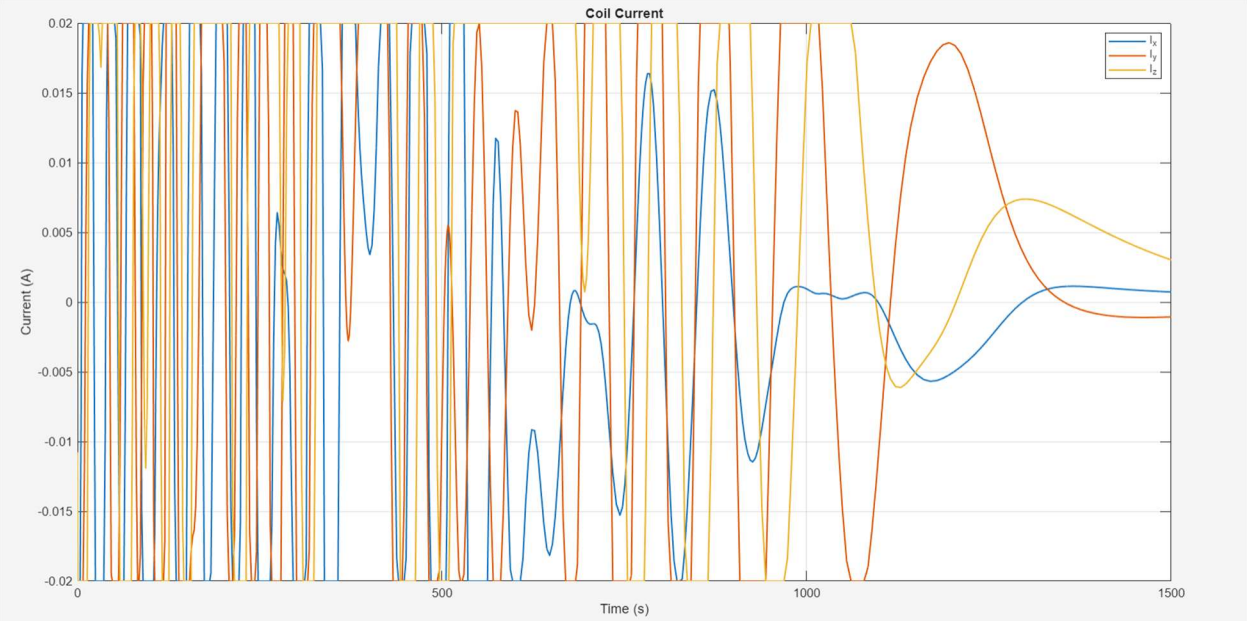


Figure 4.87 – Coil current max current = 0.02 Amps

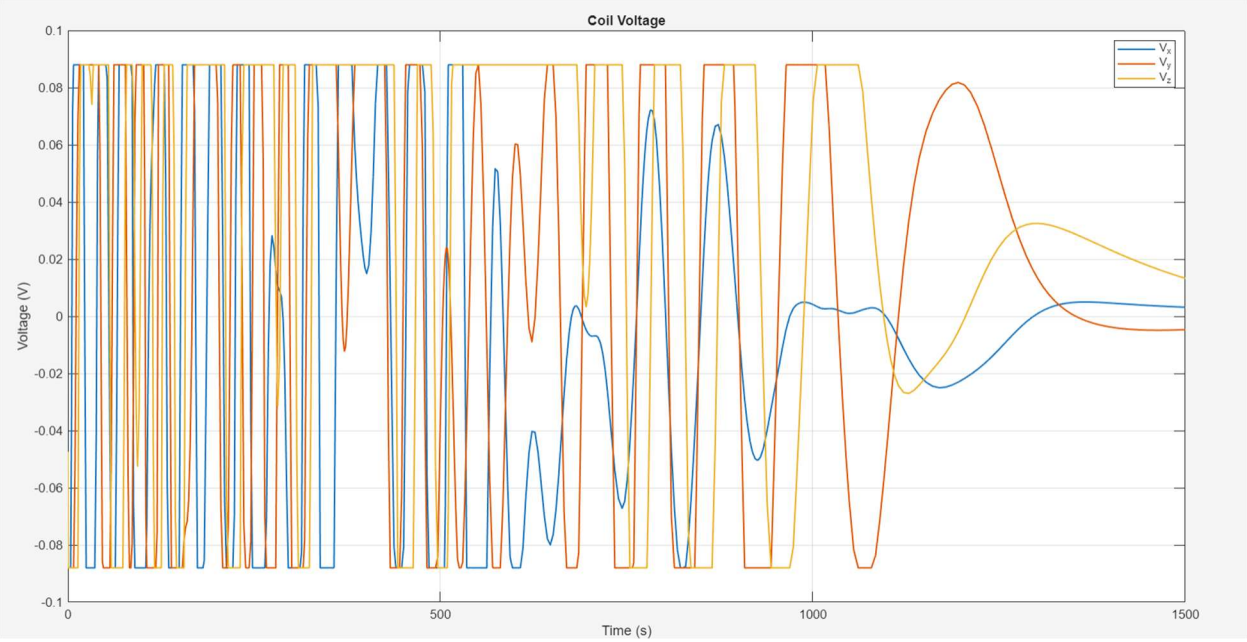


Figure 4.88 – Coil voltage max current = 0.02 Amps

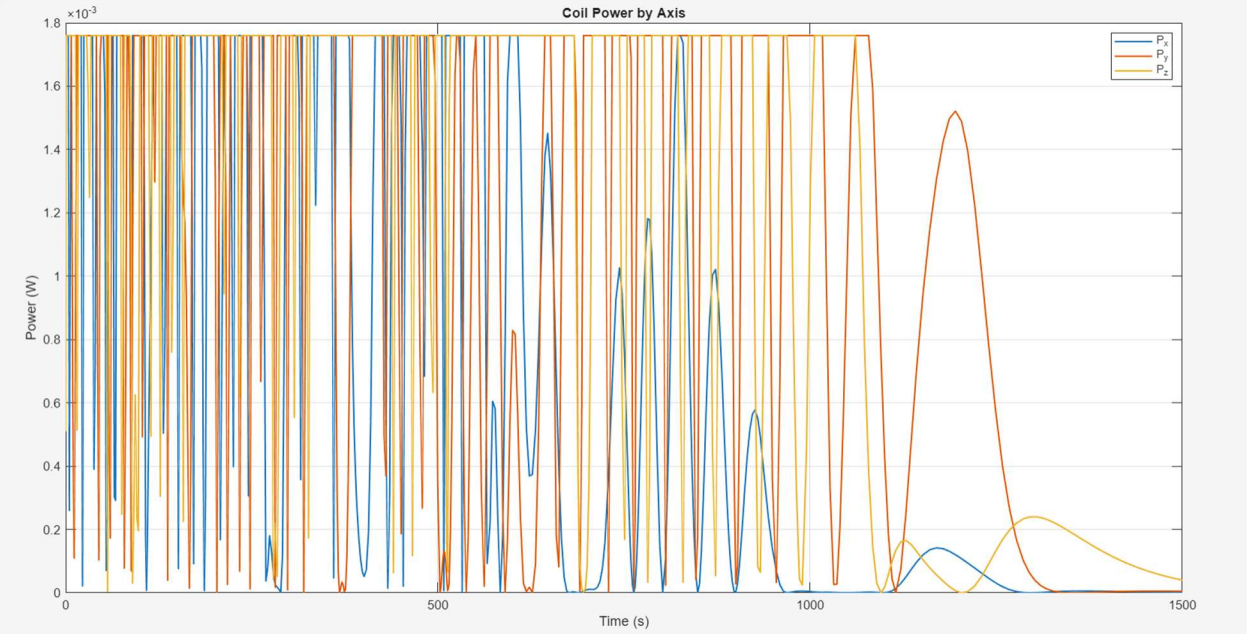


Figure 4.89 – Coil power consumption max current = 0.02 Amps

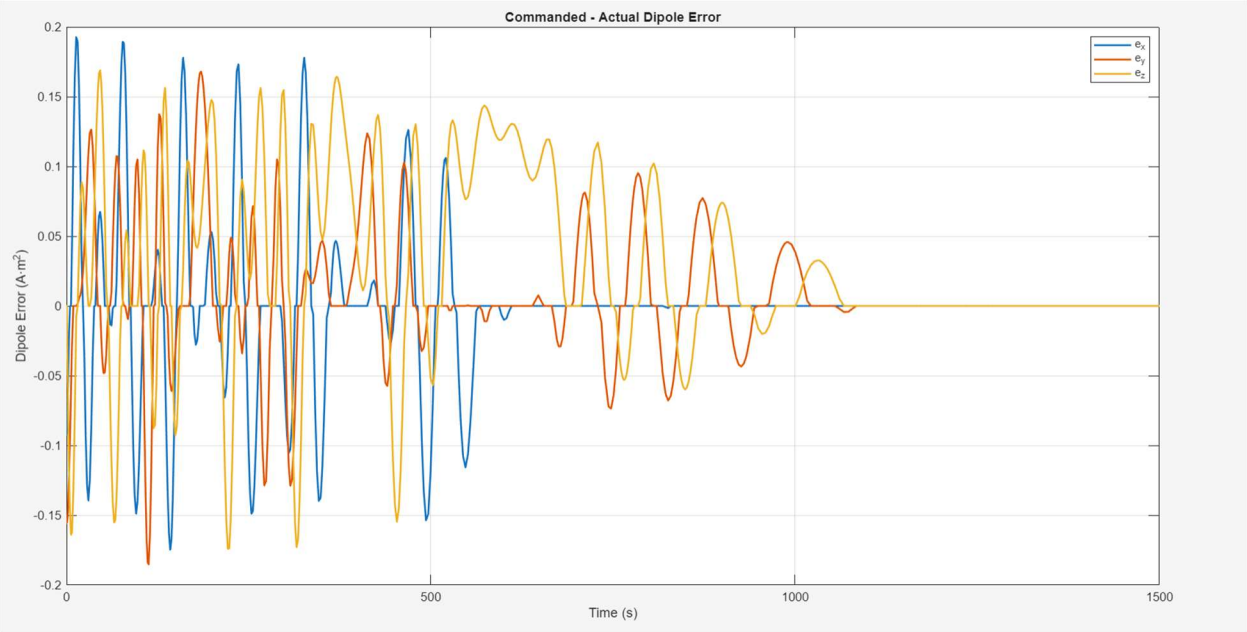


Figure 4.90 – Commanded vs actual dipole error max current = 0.02 Amps

- **Max Current = 0.05 Amps**

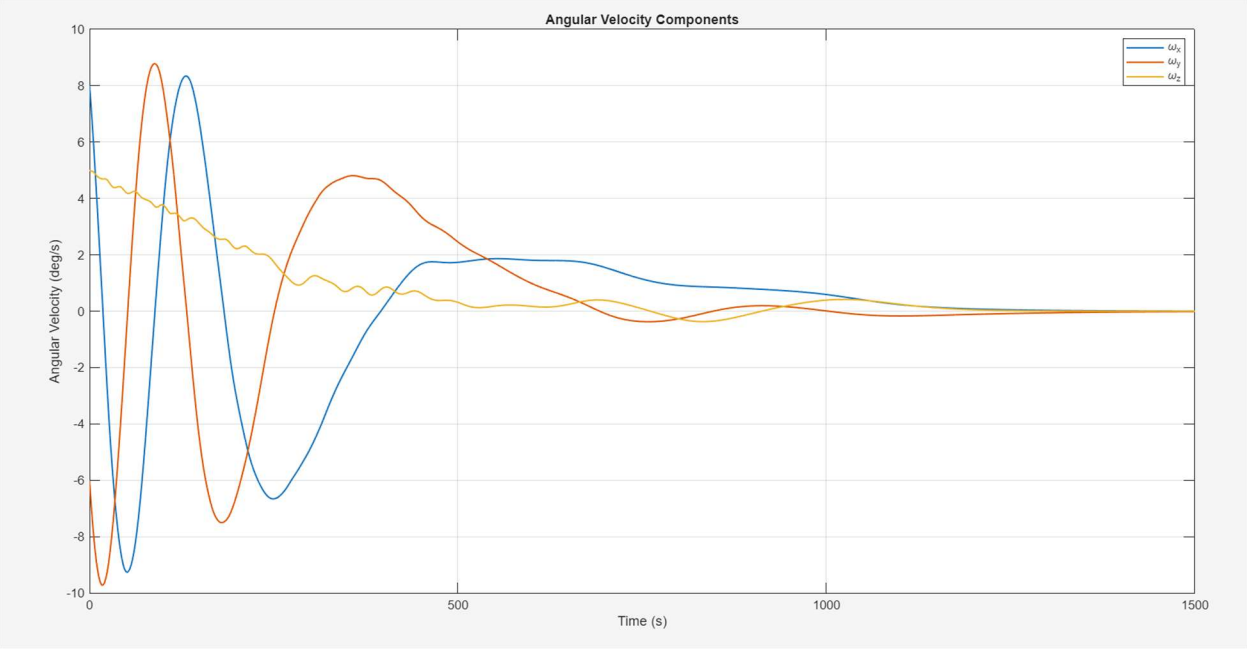


Figure 4.91 – Angular velocity components max current = 0.05 Amps

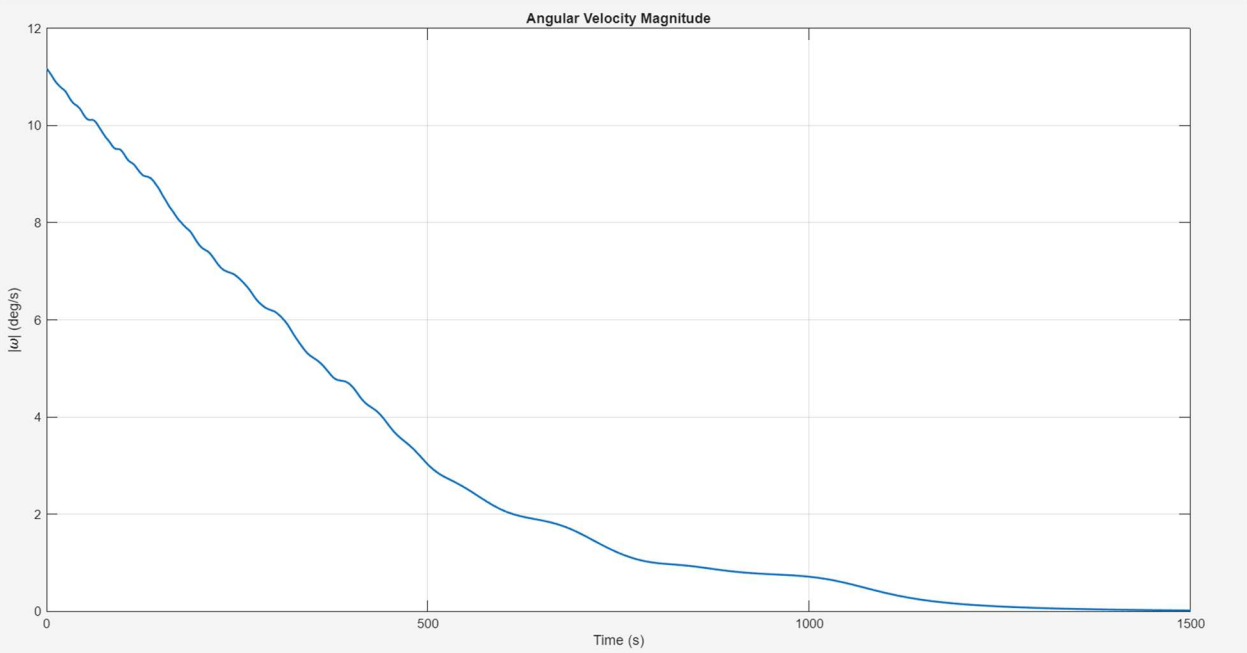


Figure 4.92 – Angular velocity magnitude max current = 0.05 Amps

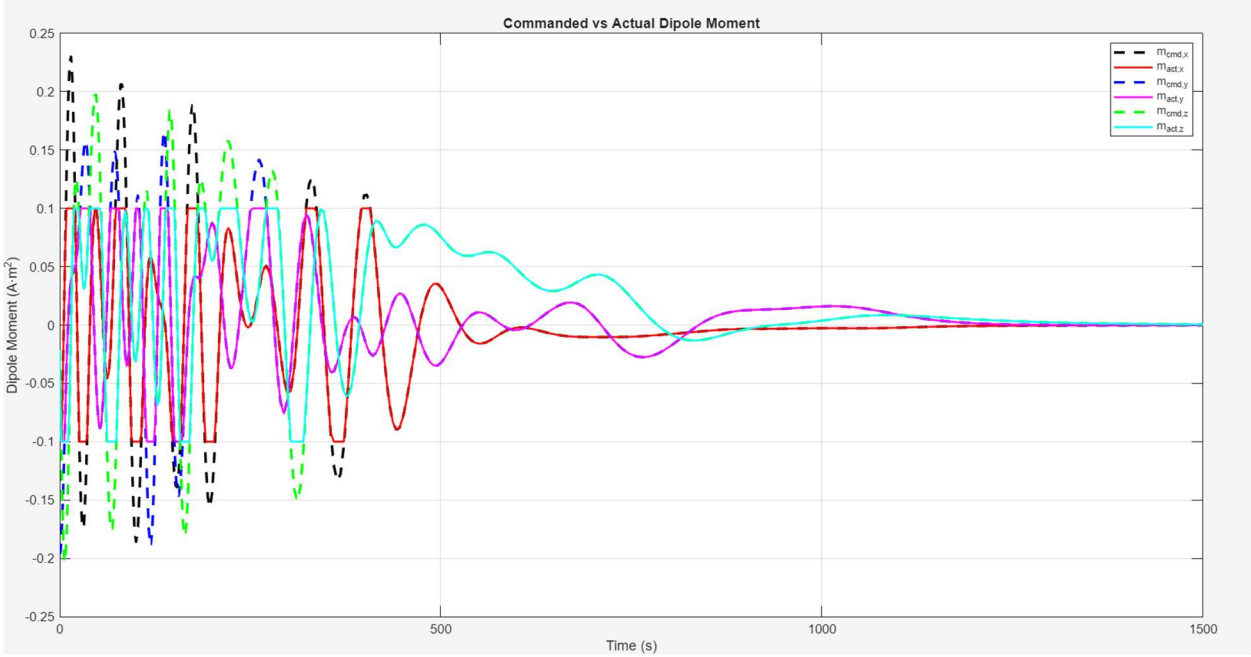


Figure 4.93 – Commanded vs actual dipole moment max current = 0.05 Amps

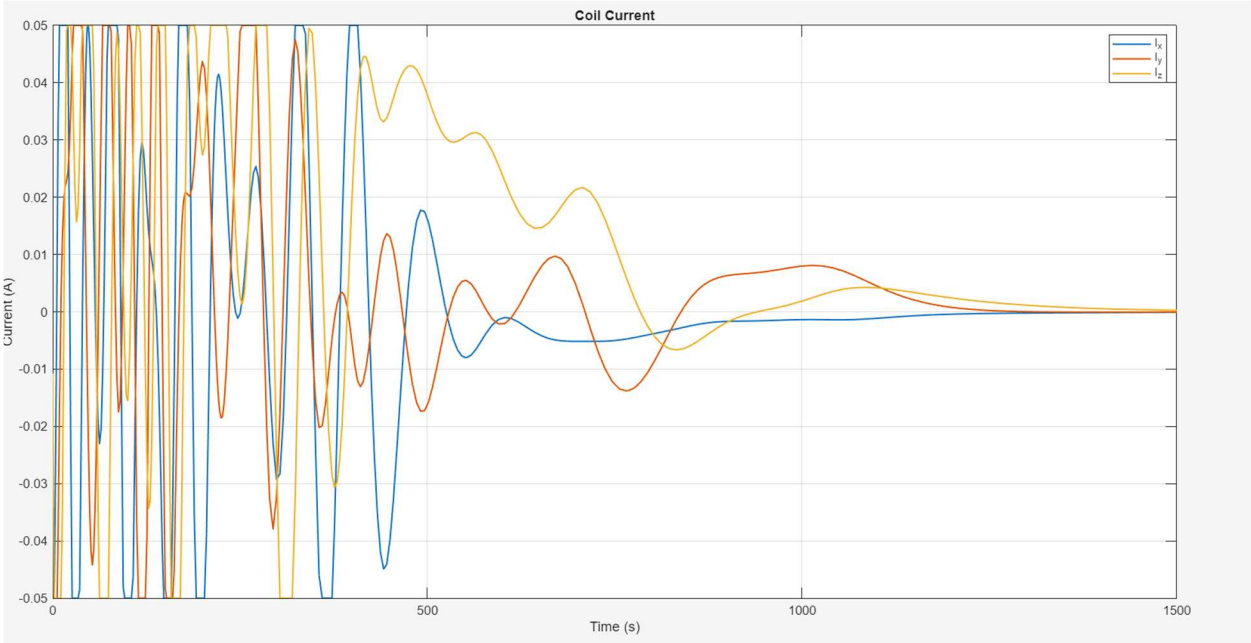


Figure 4.94 – Coil current max current = 0.05 Amps

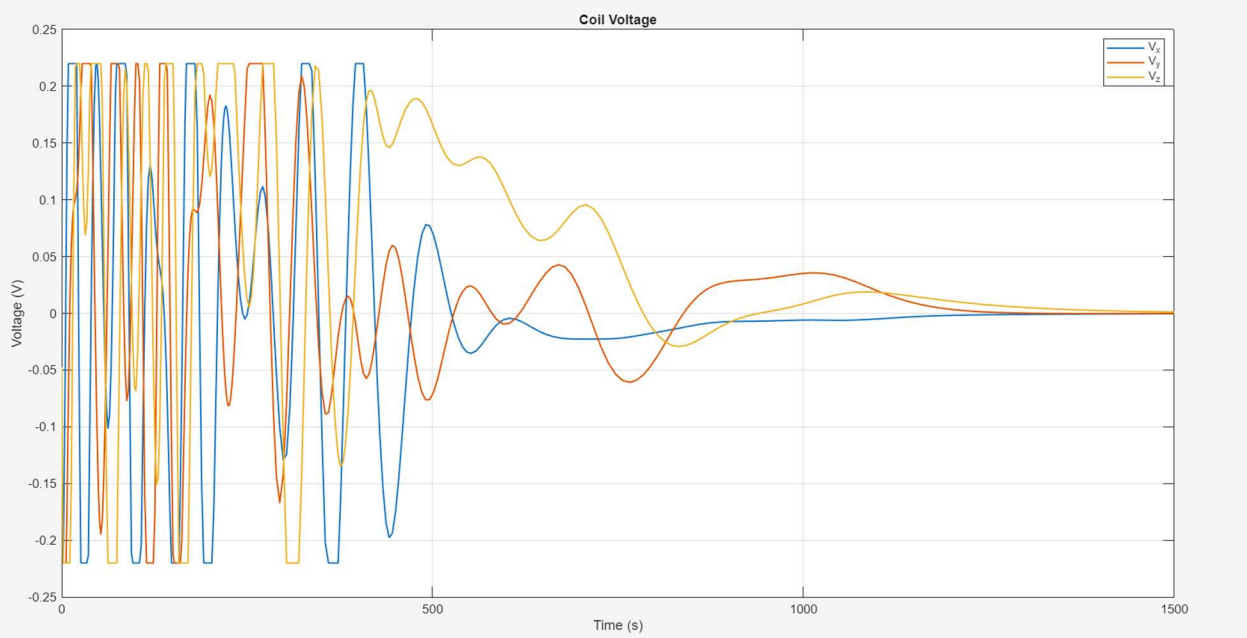


Figure 4.95 – Coil voltage max current = 0.05 Amps

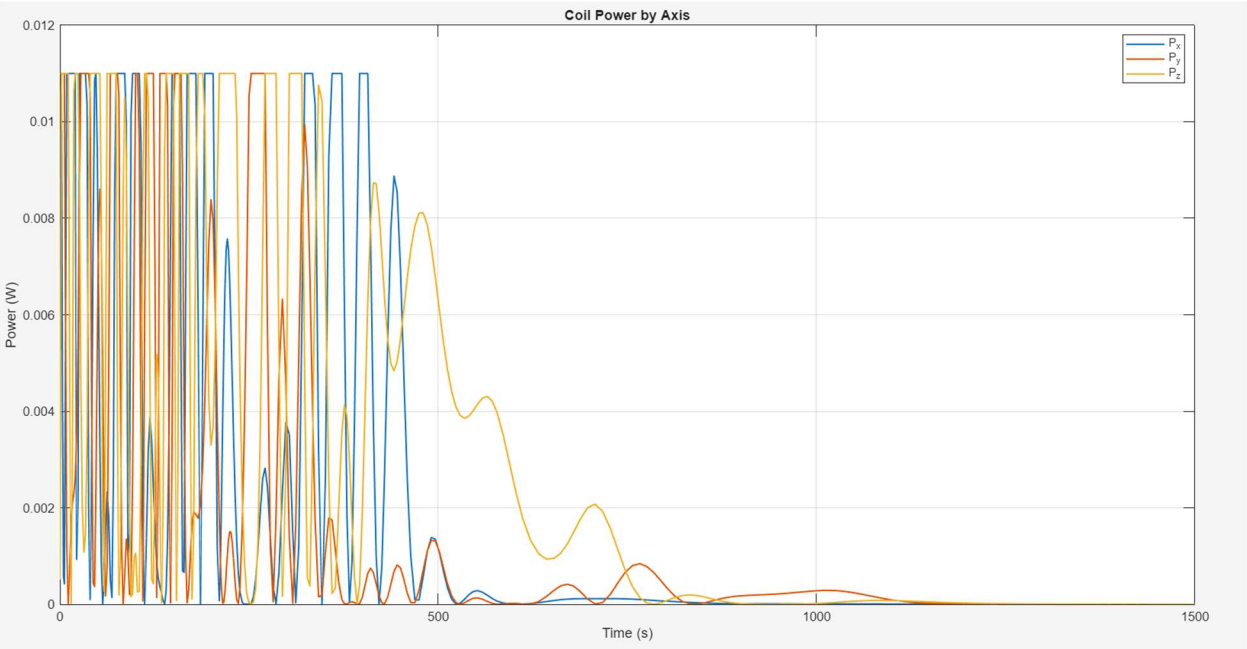


Figure 4.96 – Coil power consumption max current = 0.05 Amps

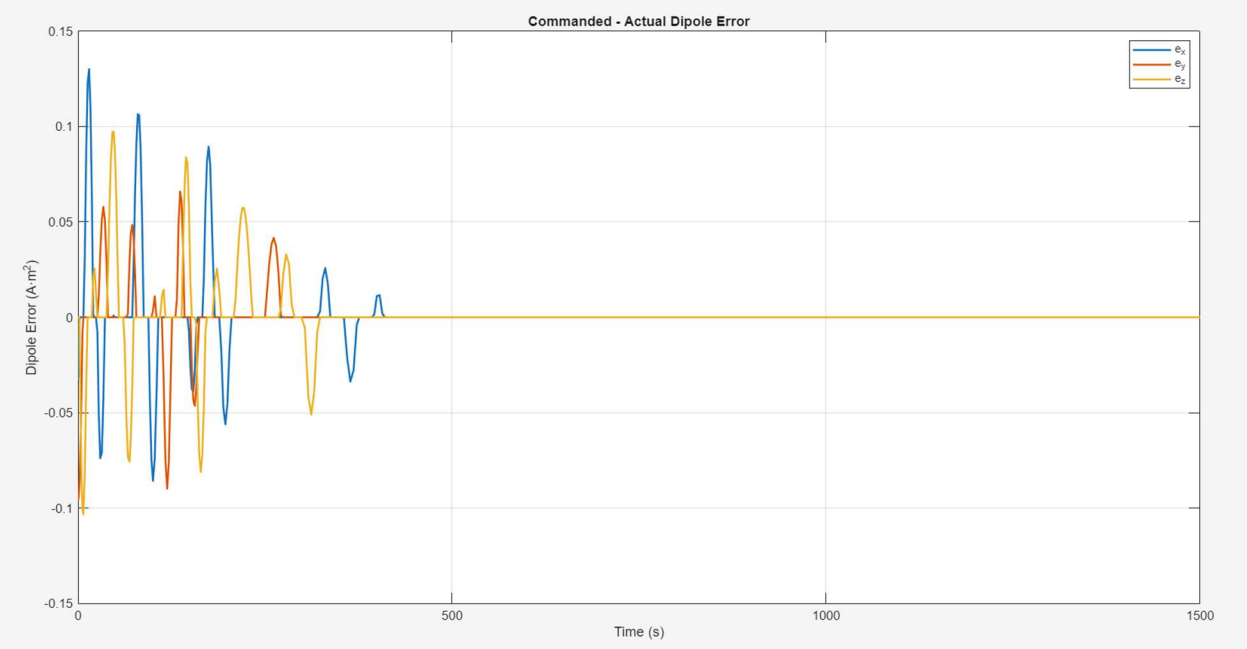


Figure 4.97 – Commanded vs actual dipole error max current = 0.05 Amps

- **Max Current = 0.1 Amps**

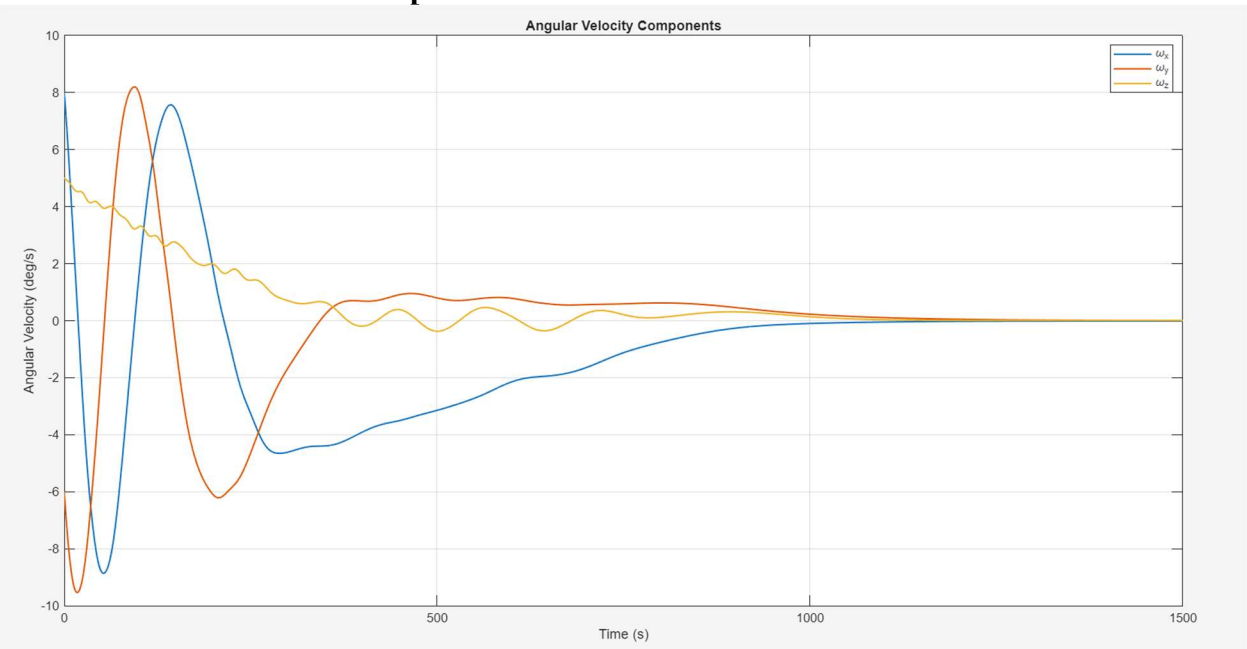


Figure 4.98 – Angular velocity components max current = 0.1 Amps

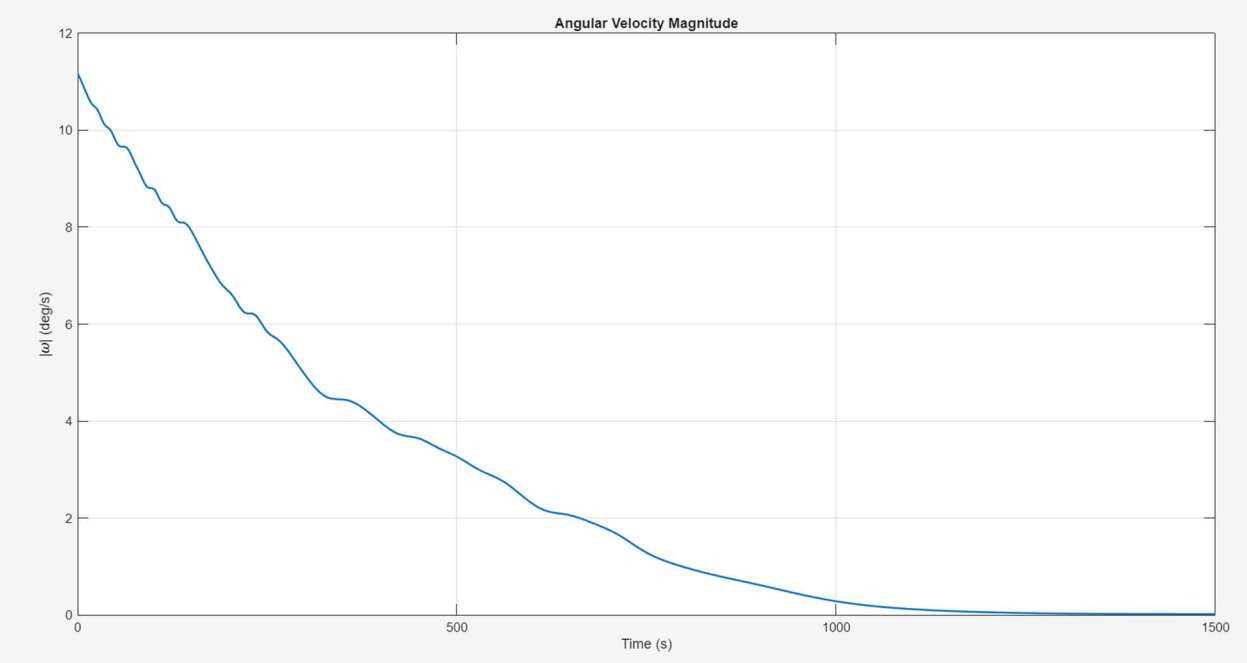


Figure 4.99 – Angular velocity magnitude max current = 0.1 Amps

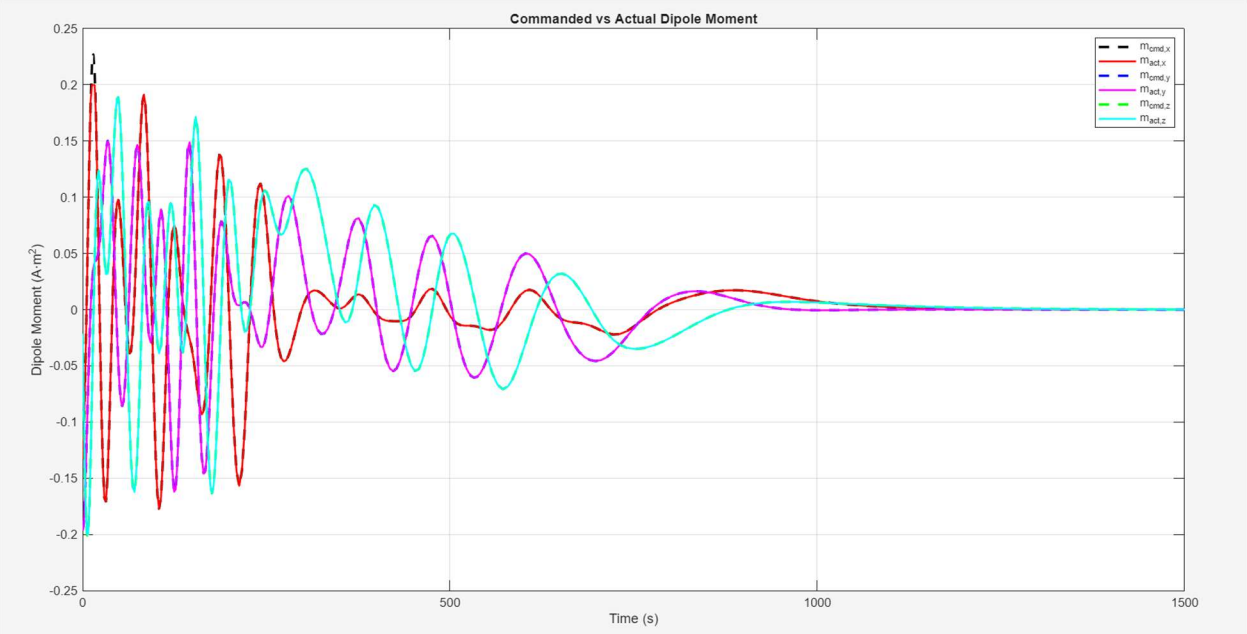


Figure 4.100 – Commanded vs actual dipole moment max current = 0.1 Amps

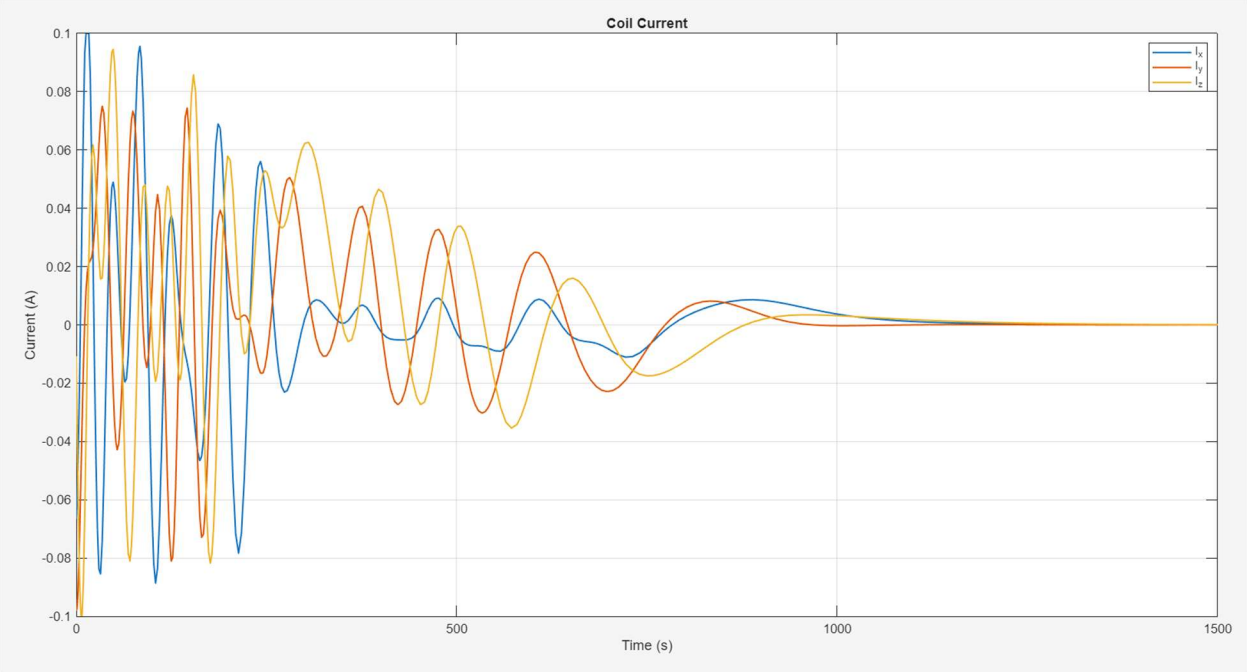


Figure 4.101 – Coil current max current = 0.1 Amps

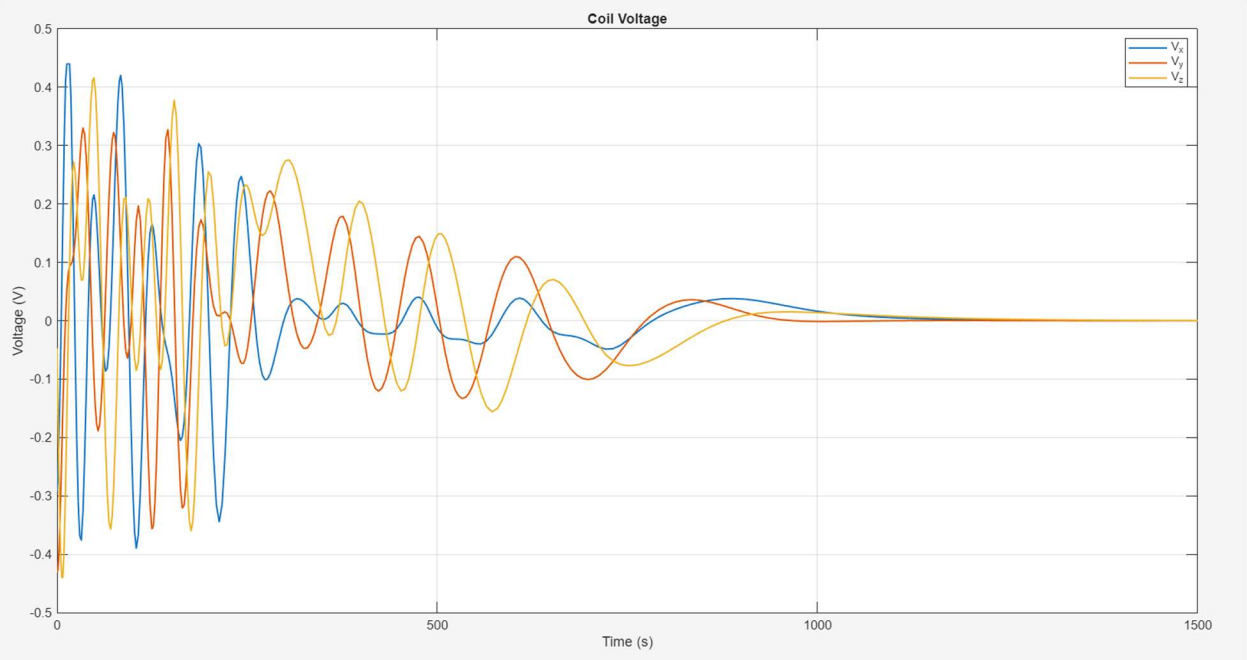


Figure 4.102 – Coil voltage max current = 0.1 Amps

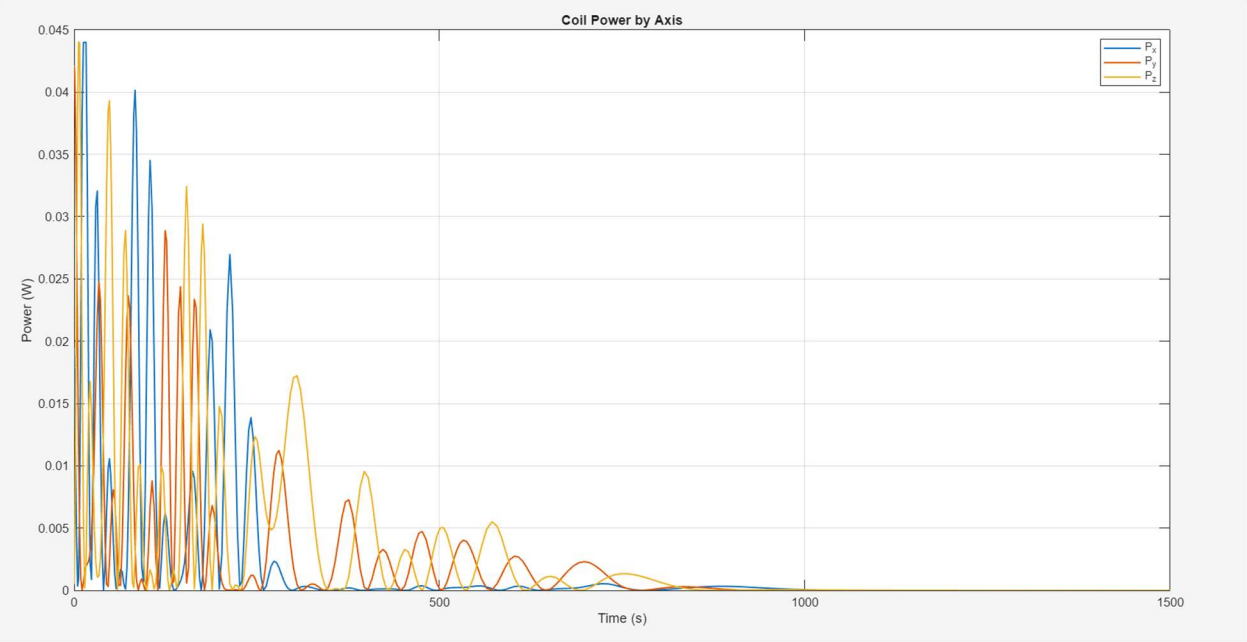


Figure 4.103 – Coil power consumption max current = 0.1 Amps

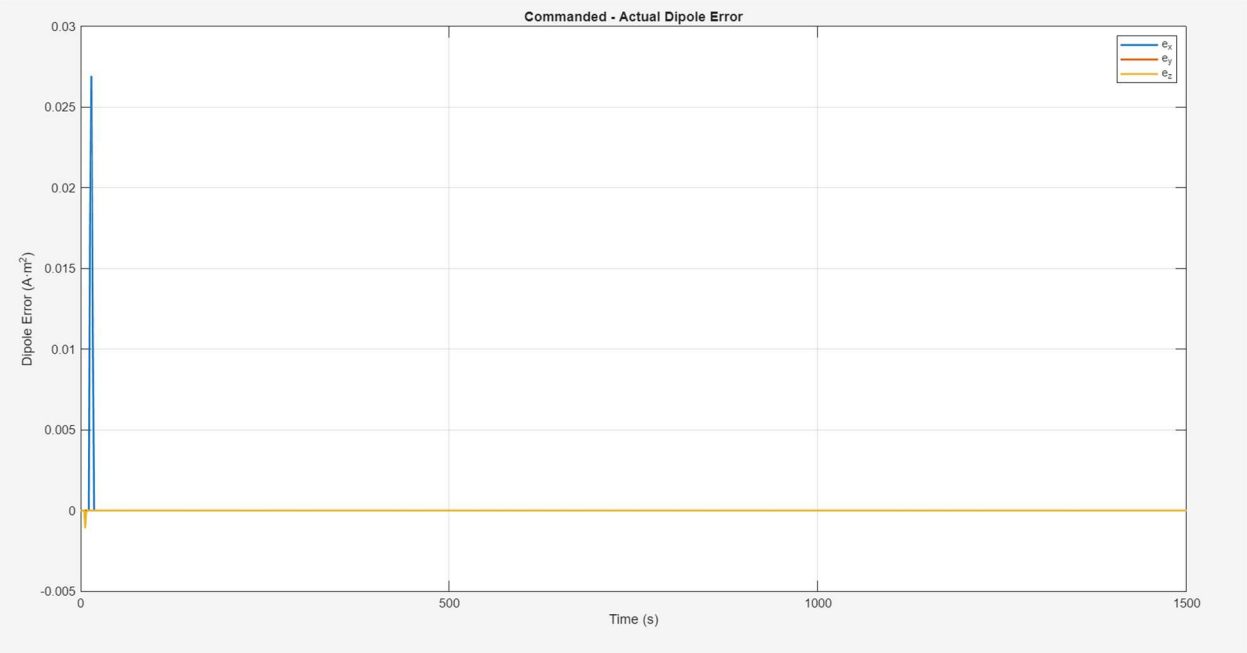


Figure 4.104 – Commanded vs actual dipole error max current = 0.1 Amps

- **Max Current = 0.15 Amps**

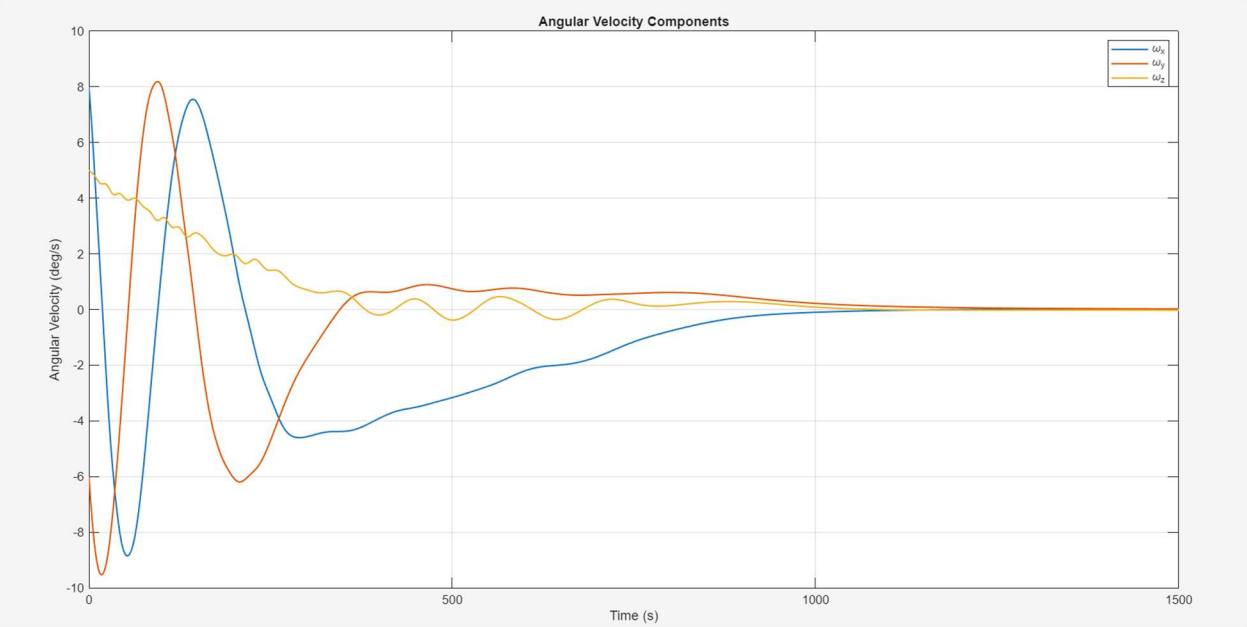


Figure 4.105 – Angular velocity components max current = 0.15 Amps

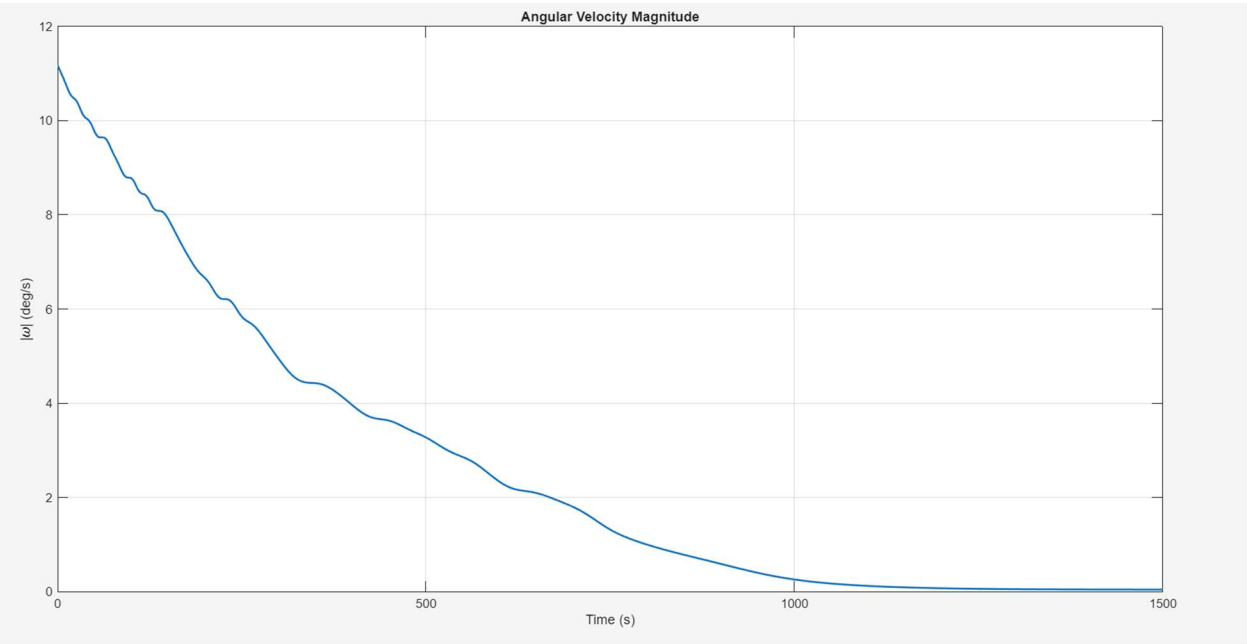


Figure 4.106 – Angular velocity magnitude max current = 0.15 Amps

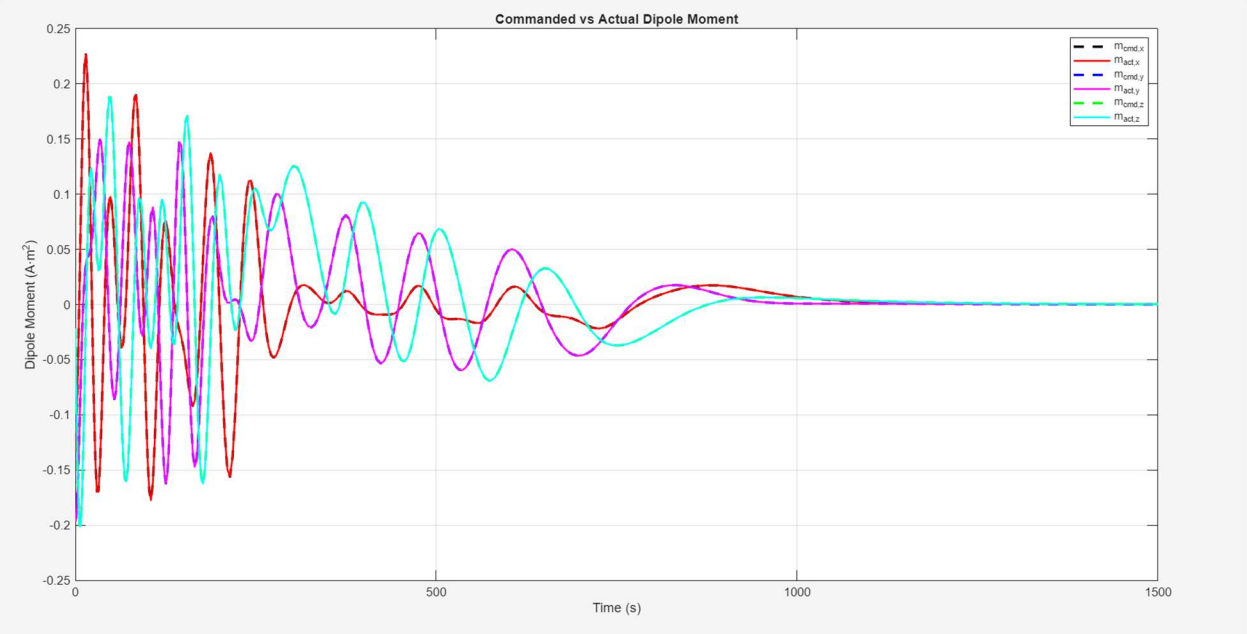


Figure 4.107 – Commanded vs actual dipole moment max current = 0.15 Amps

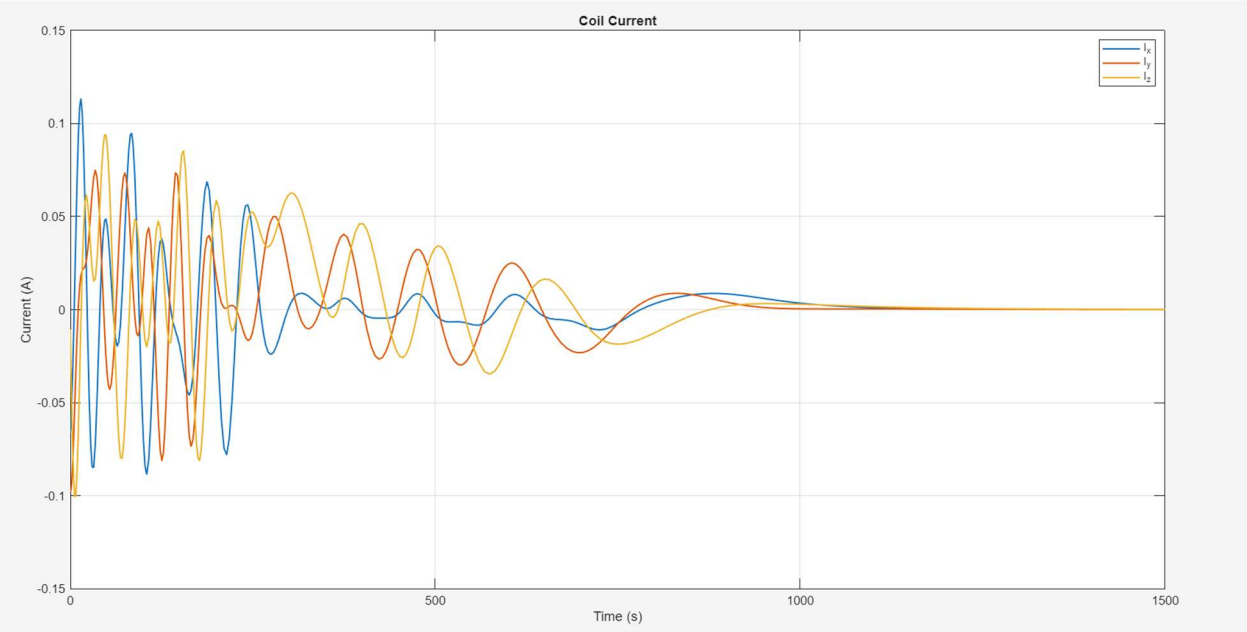


Figure 4.108 – Coil current max current = 0.15 Amps

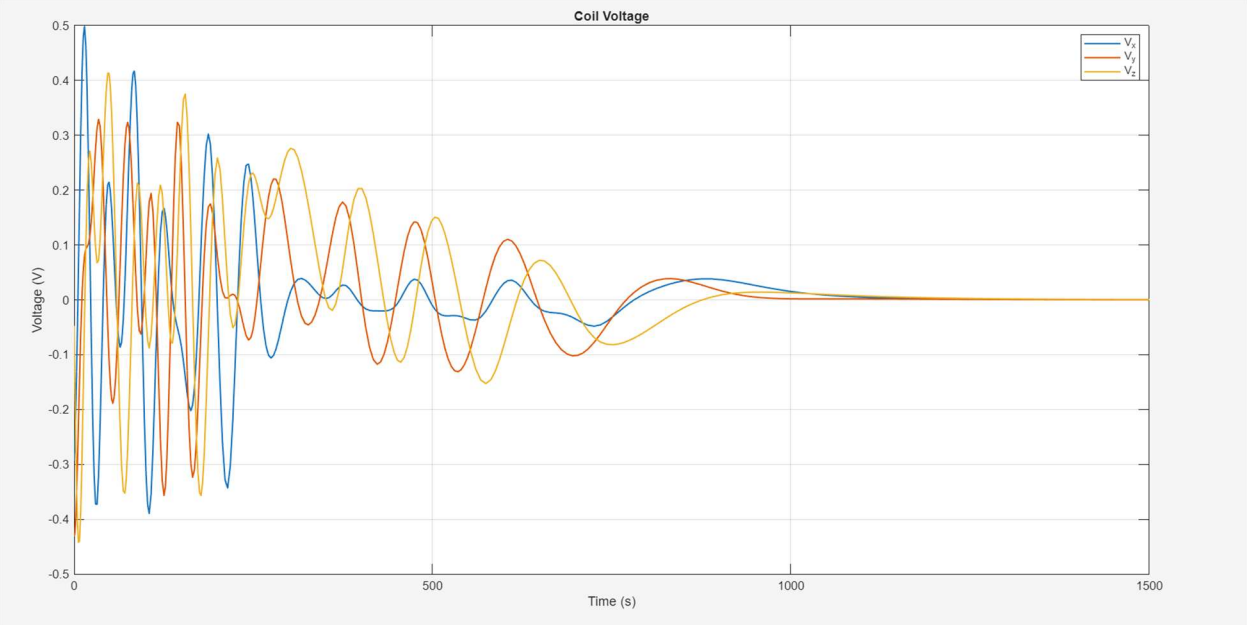


Figure 4.109 – Coil voltage max current = 0.15 Amps

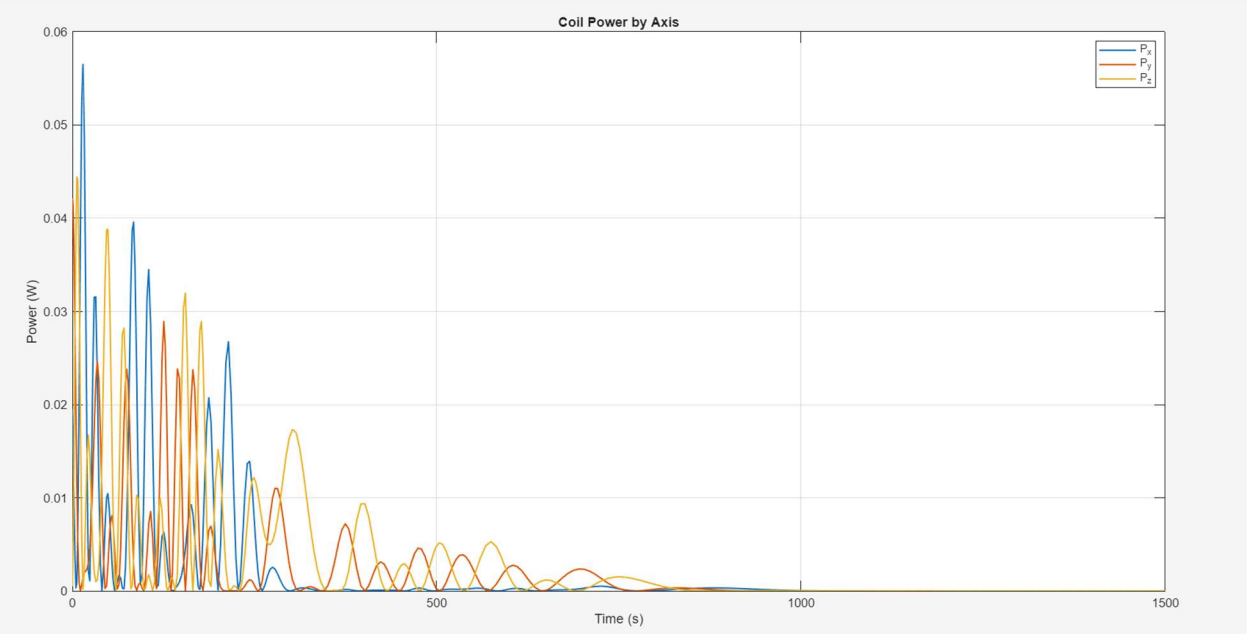


Figure 4.110 – Coil power consumption max current = 0.15 Amps

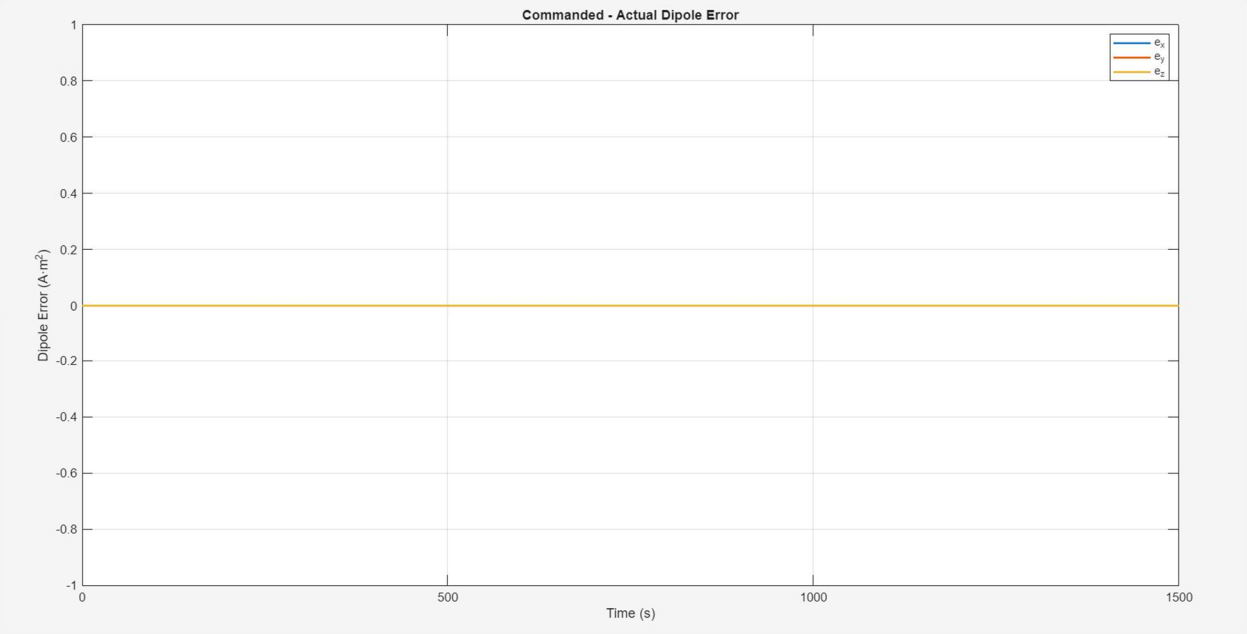


Figure 4.111 – Commanded vs actual dipole error max current = 0.15 Amps

Quantitative numerical results are provided below for current limit sweep case study:

Table 4.8 – Quantitative numerical results of current limit sweep case study

Max current (A)	Detumble time to 0.50 deg/s (s)	Peak power (W)	Peak current (A)	Peak dipole (A·m²)	Peak Voltage (V)	Final $\|\omega\|$ (deg/s)
0.02	1348.550	0.0053	[0.0200 0.0200 0.0200]	[0.0400 0.0400 0.0400]	[0.0880 0.0880 0.0880]	0.239
0.05	1069.187	0.0330	[0.0500 0.0500 0.0500]	[0.1000 0.1000 0.1000]	[0.2200 0.2200 0.2200]	0.016
0.1	936.385	0.0620	[0.1000 0.0978 0.1000]	[0.2000 0.1956 0.2000]	[0.4400 0.4303 0.4400]	0.018
0.15	933.137	0.0620	[0.1133 0.0978	[0.2267 0.1956	[0.4987 0.4303	0.042

			0.1005]	0.2010]	0.4423]	

4.4.4 Orbit Sensitivity Study

In this sub-study, the simulation was run various perigee and apogee values including the mission specific values of SpartanSAT as seen in Table 4.9. The set parameters for the plot results are provided in Table 4.10.

Table 4.9 – Perigee and apogee values for orbit sensitivity study

Case	Perigee (km)	Apogee (km)
Current Mission	416	425
Low LEO	300	300
Mid LEO	500	500
High LEO	900	900

Table 4.10 – Fixed parameters for orbit sensitivity study

B-dot controller gain, k	N turns	Coil resistance (Ohms)	Coil area (m^2)	Coil max current (A)	Coil max voltage (V)
5e4	200	4.4	0.01	0.15	5

- **Current Mission**

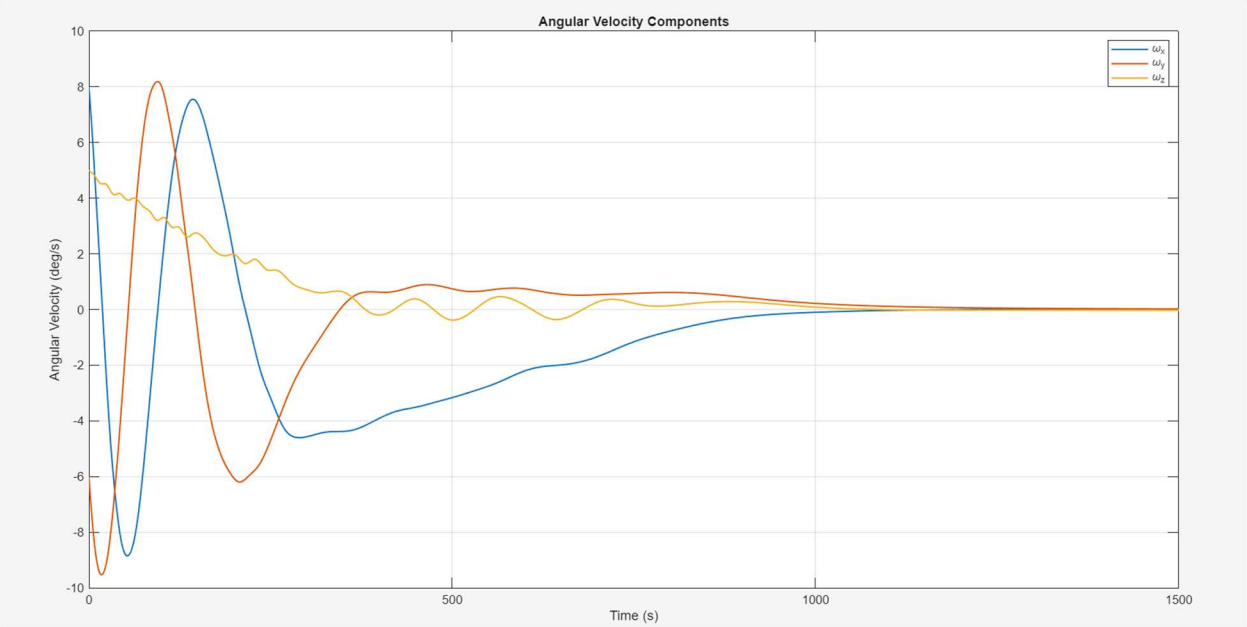


Figure 4.112 – Angular velocity components current mission

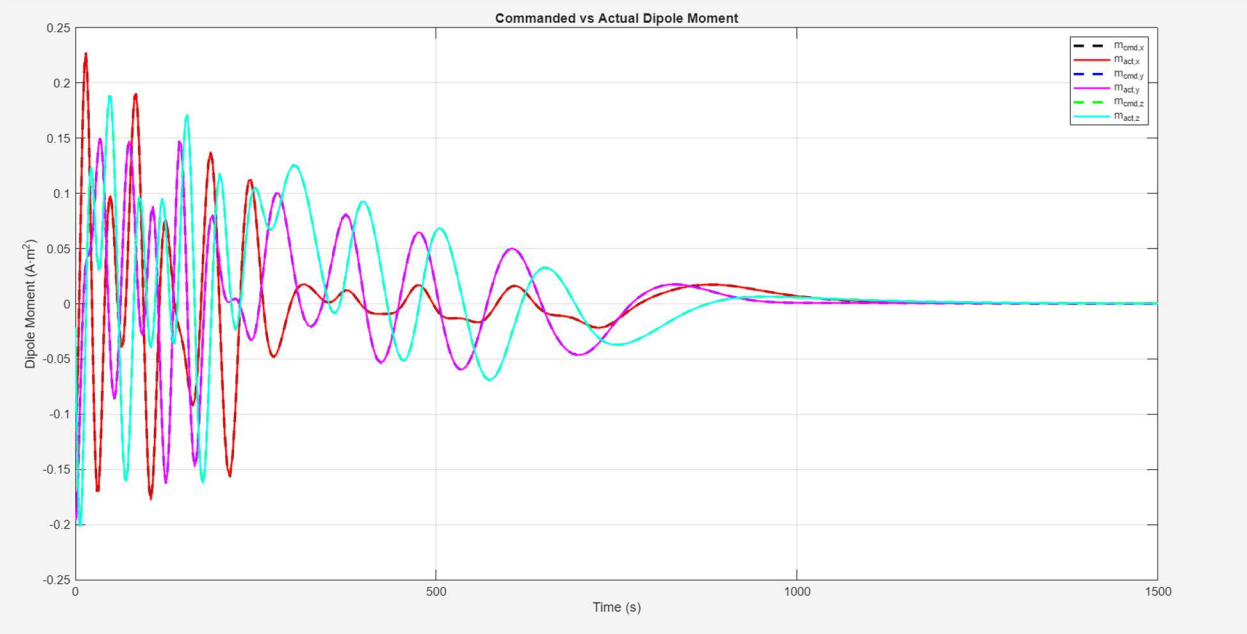


Figure 4.113 – Commanded vs actual dipole moment current mission

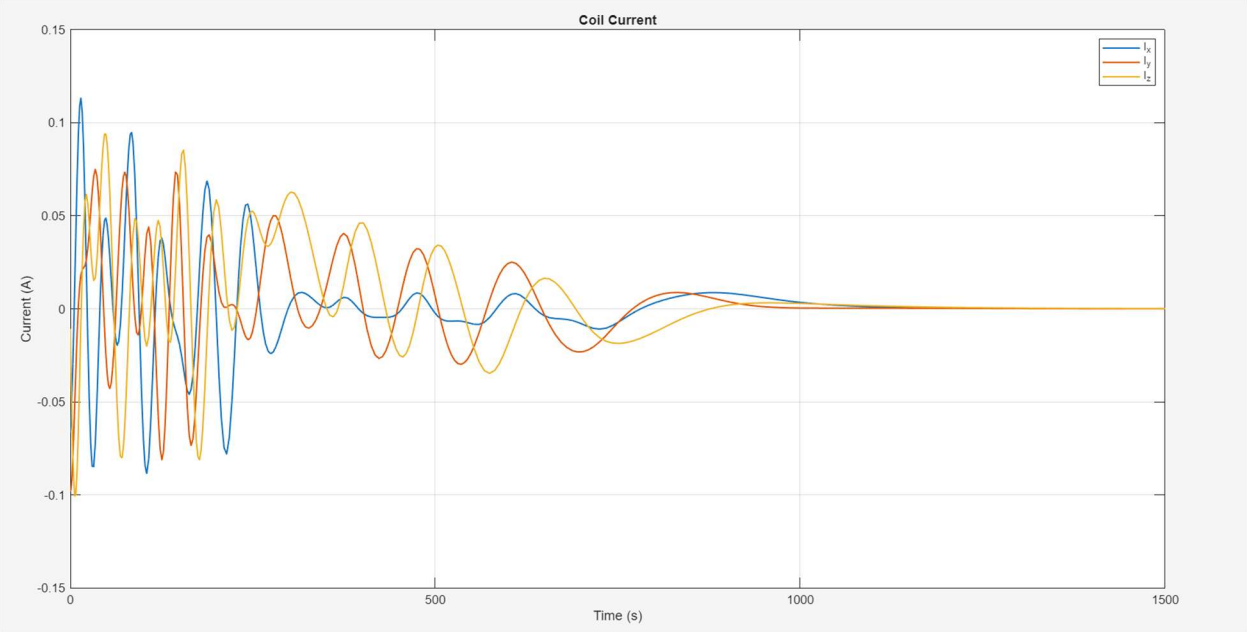


Figure 4.114 – Coil current current mission

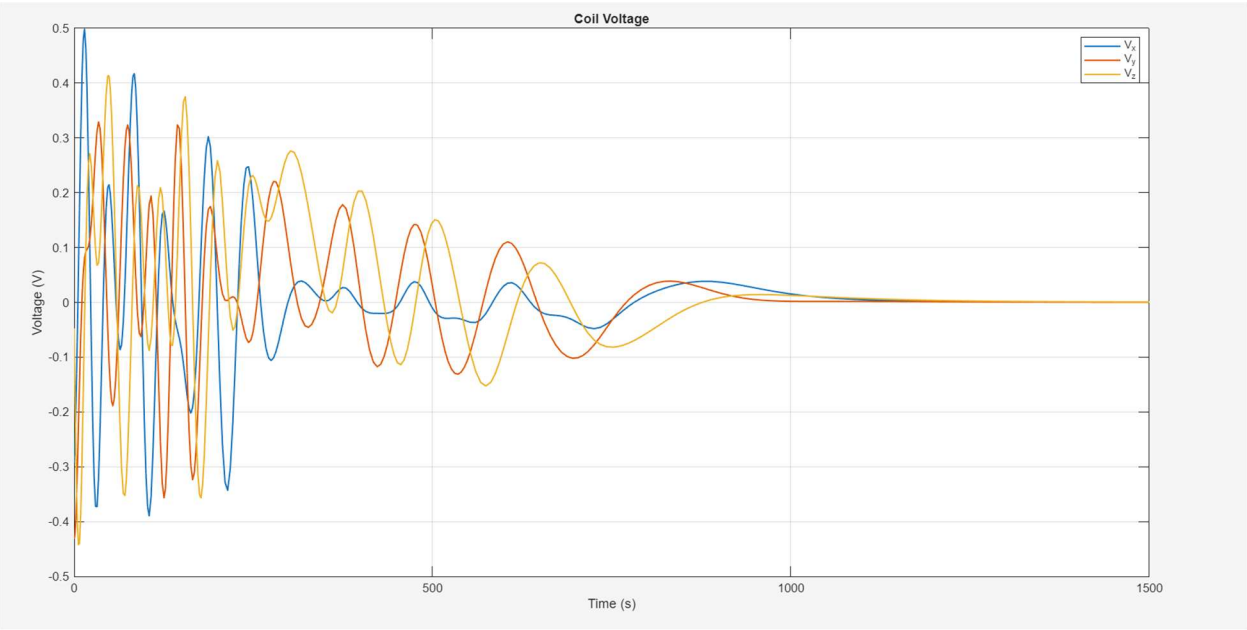


Figure 4.115 – Coil voltage current mission

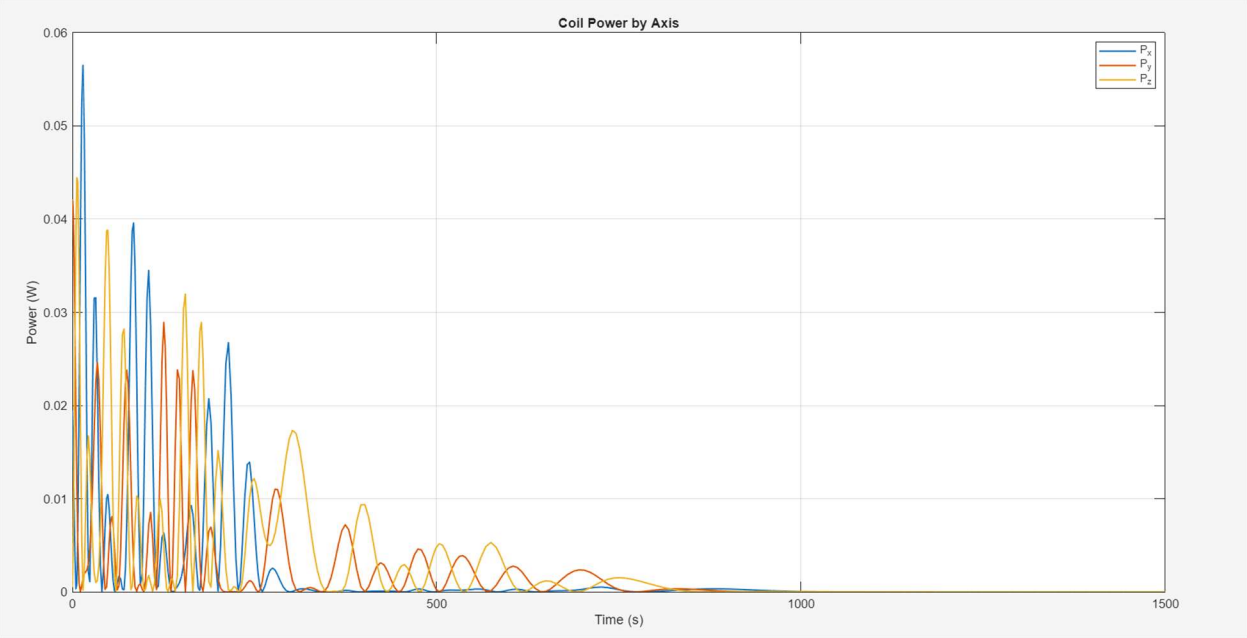


Figure 4.116 – Coil power current mission

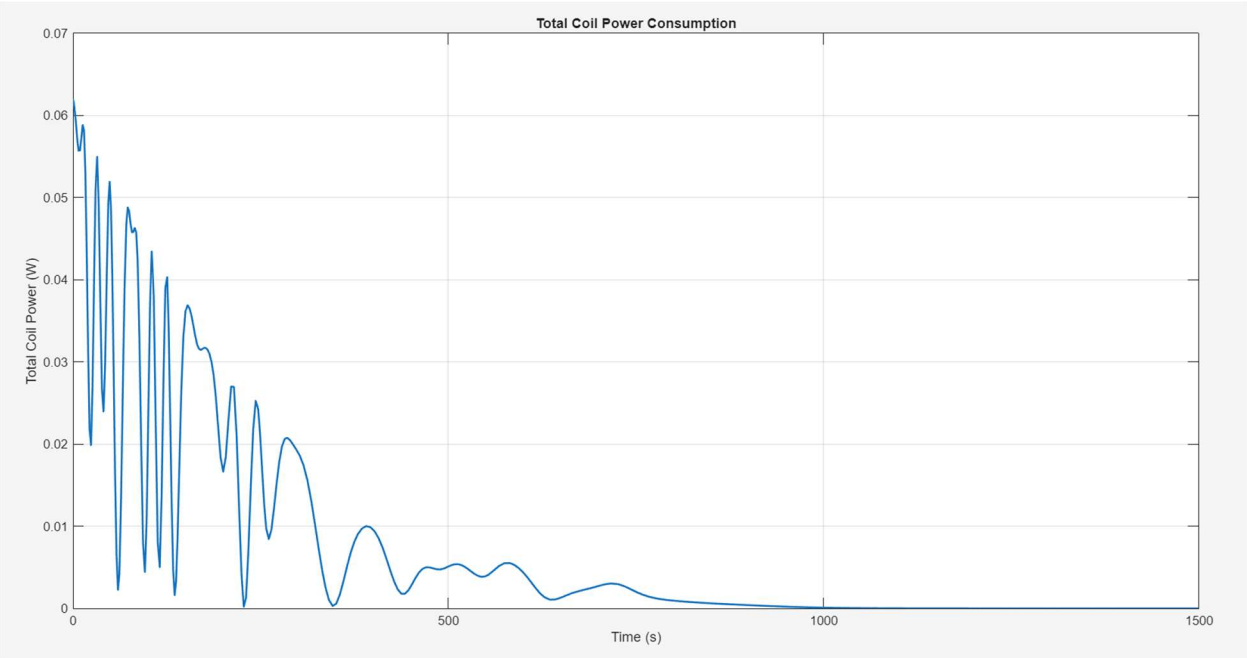


Figure 4.117 – Total coil power consumption current mission

- **Low LEO**

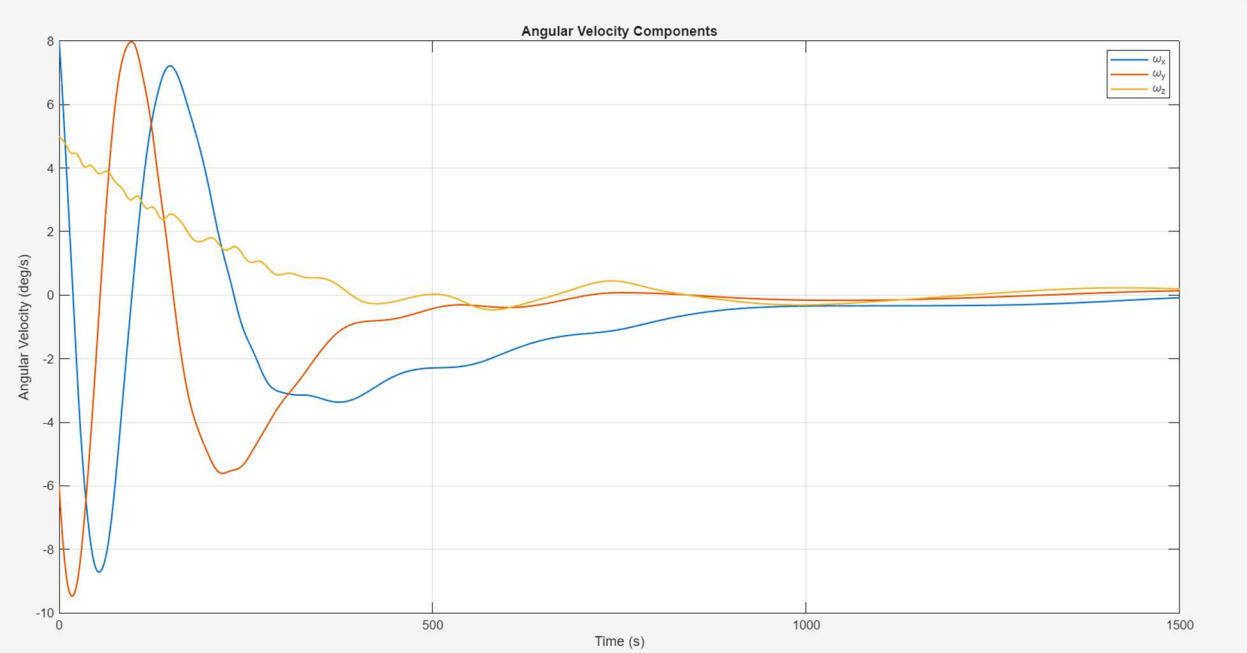


Figure 4.118 – Angular velocity components low LEO

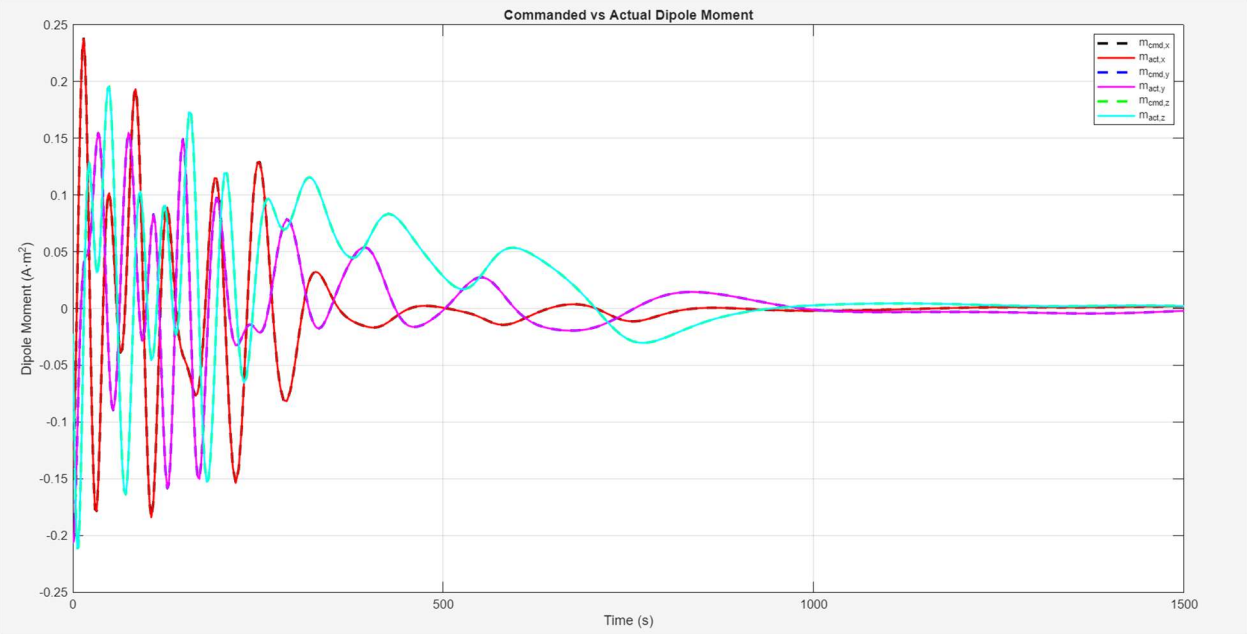


Figure 4.119 – Commanded vs actual dipole moment low LEO

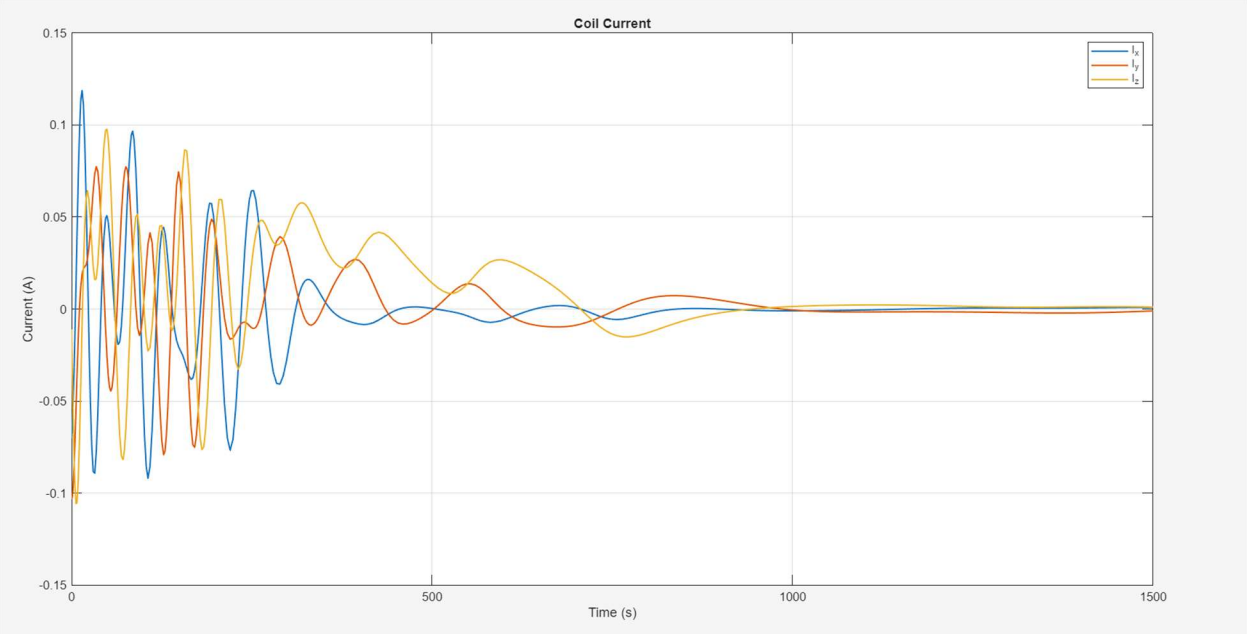


Figure 4.120 – Coil current low LEO

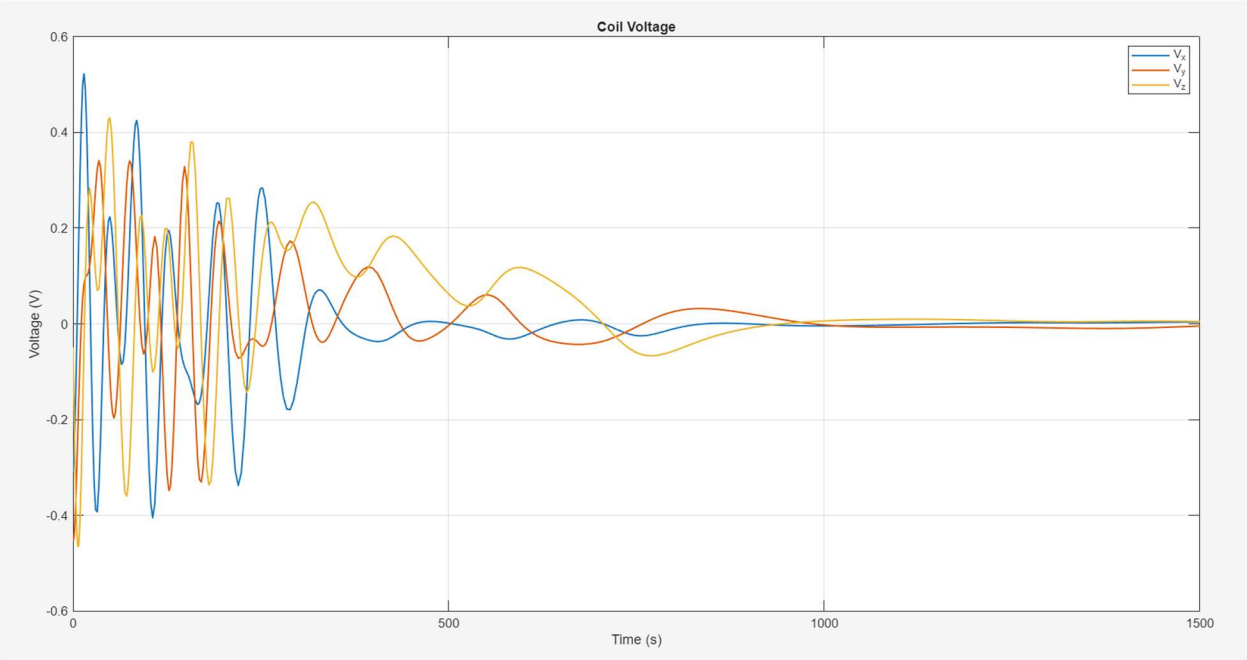


Figure 4.121 – Coil voltage low LEO

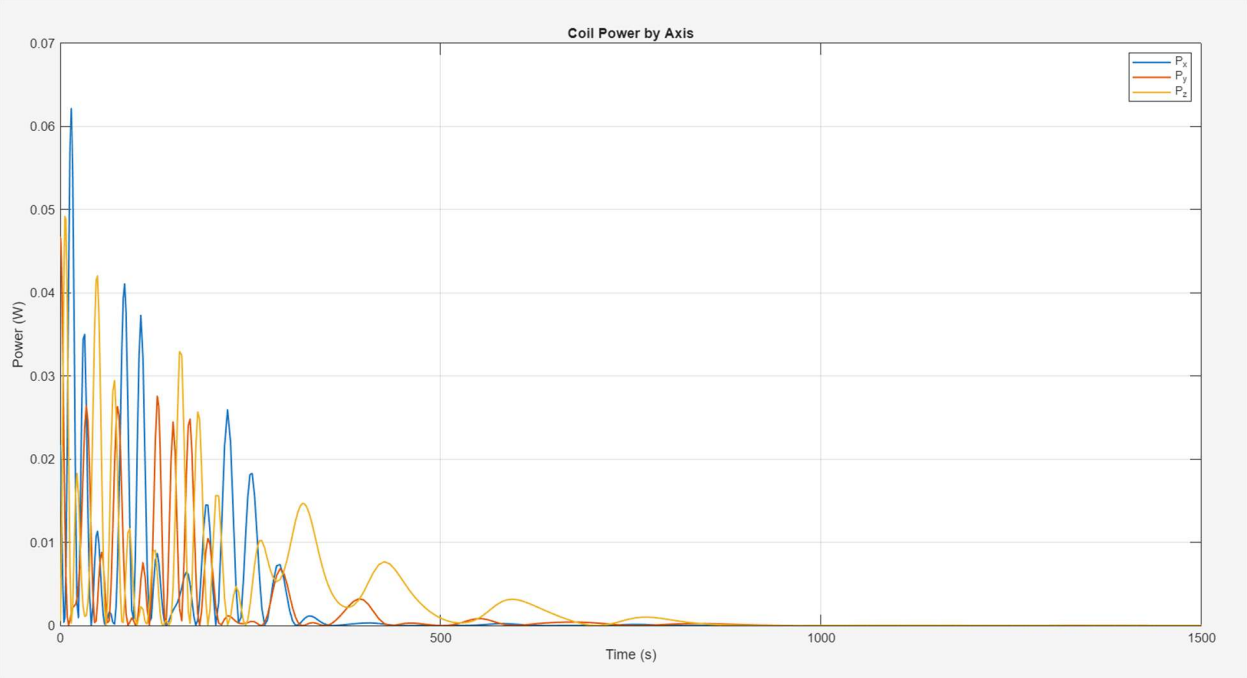


Figure 4.122 – Coil power low LEO

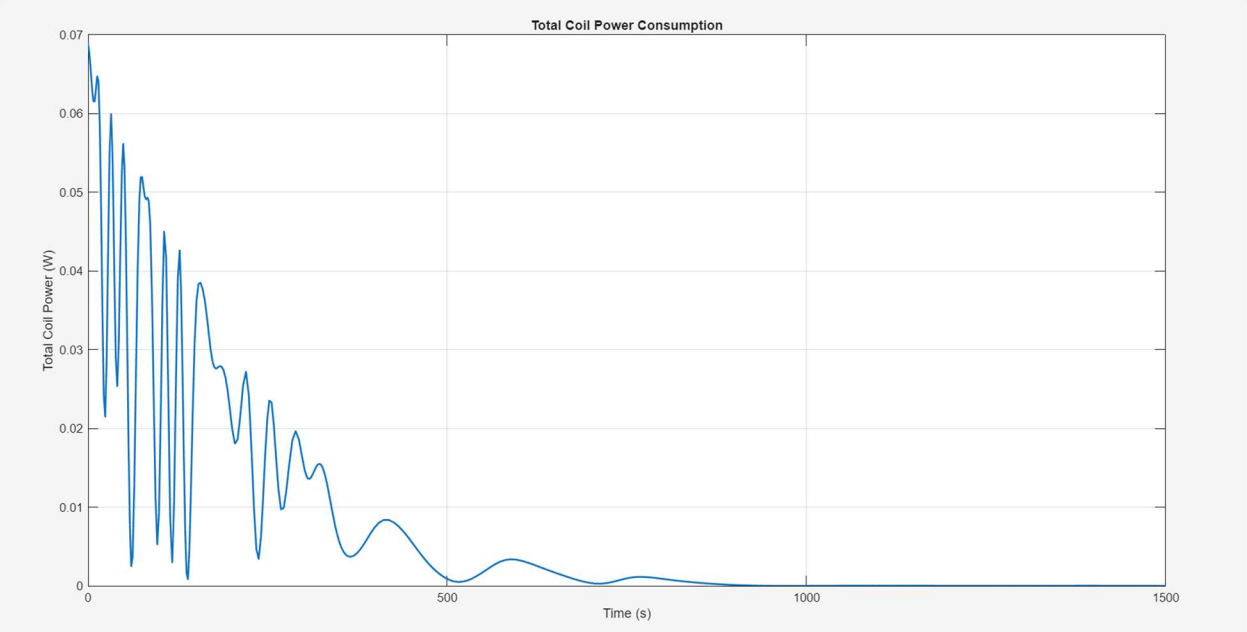


Figure 4.123 – Total coil power consumption low LEO

- **Mid LEO**

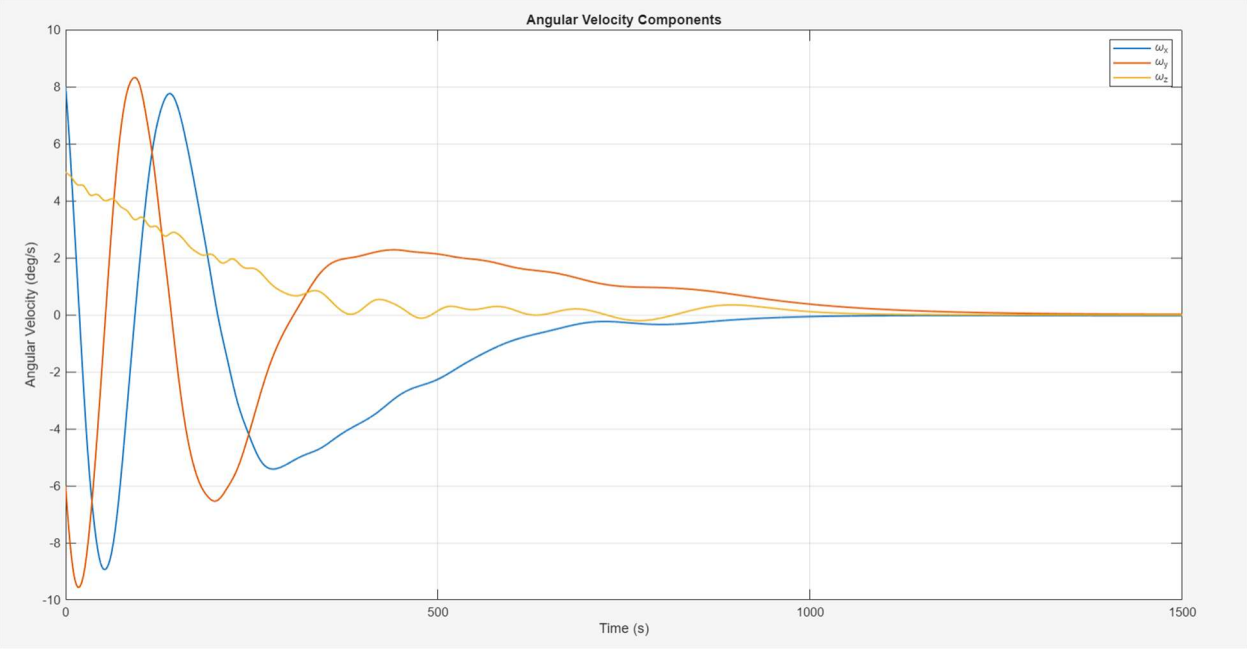


Figure 4.124 – Angular velocity components mid LEO

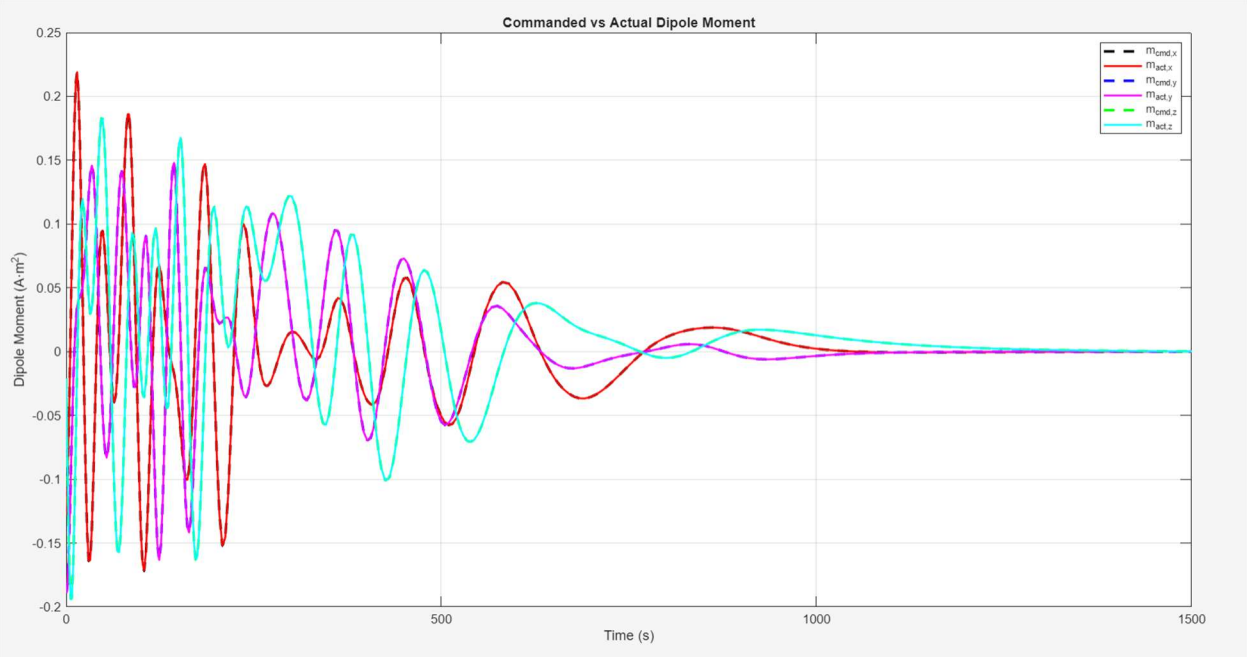


Figure 4.125 – Commanded vs actual dipole moment mid LEO

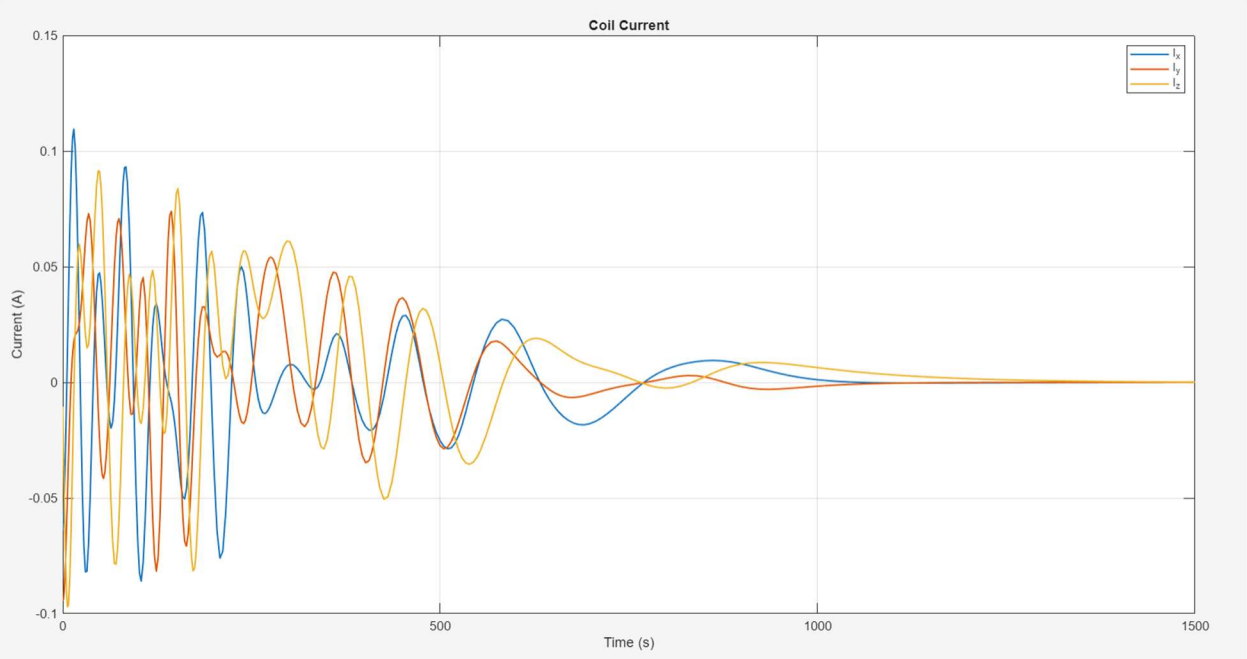


Figure 4.126 – Coil current mid LEO

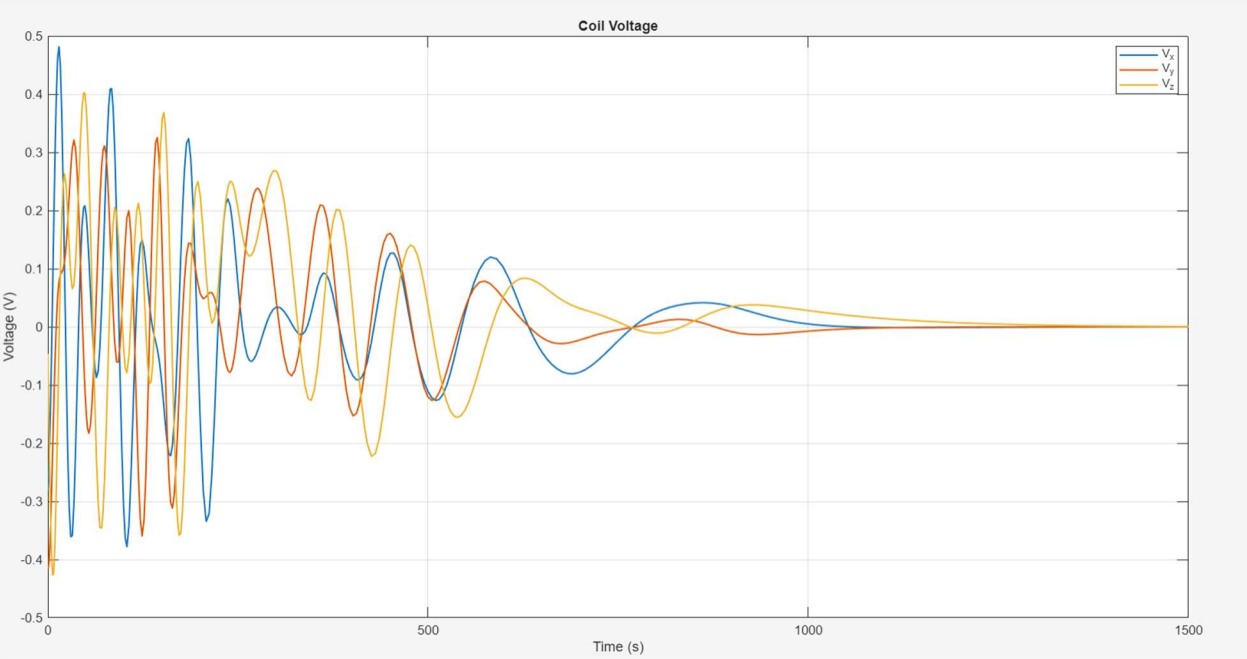


Figure 4.127 – Coil voltage mid LEO

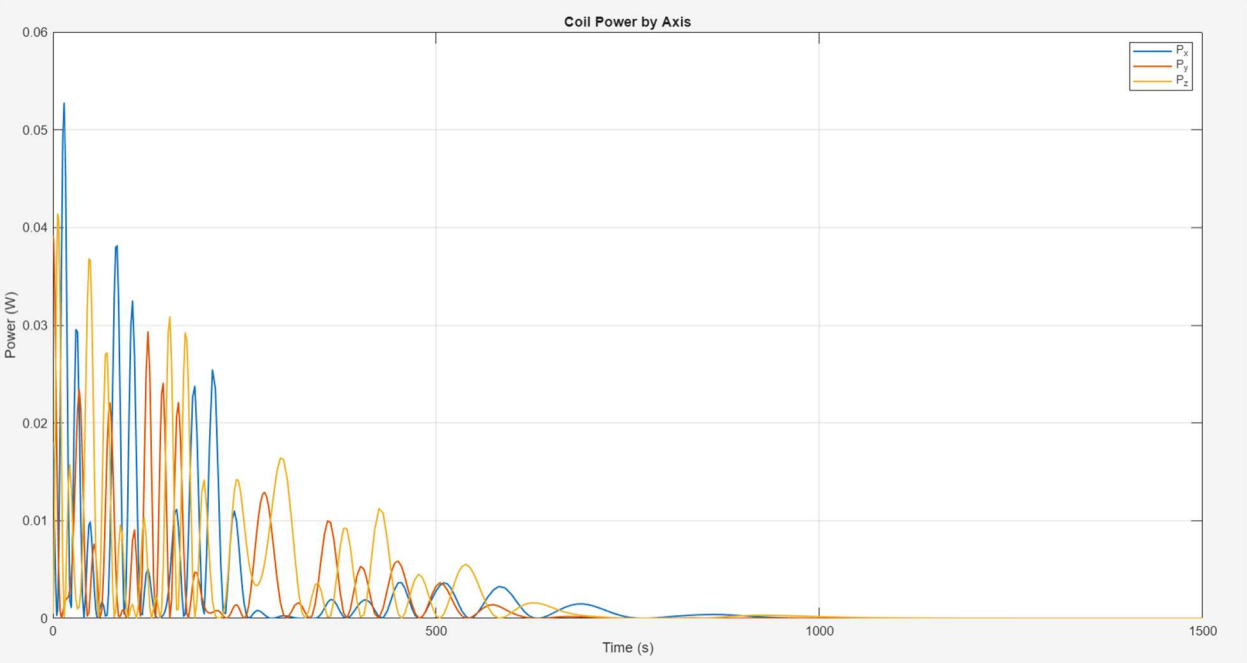


Figure 4.128 – Coil power mid LEO

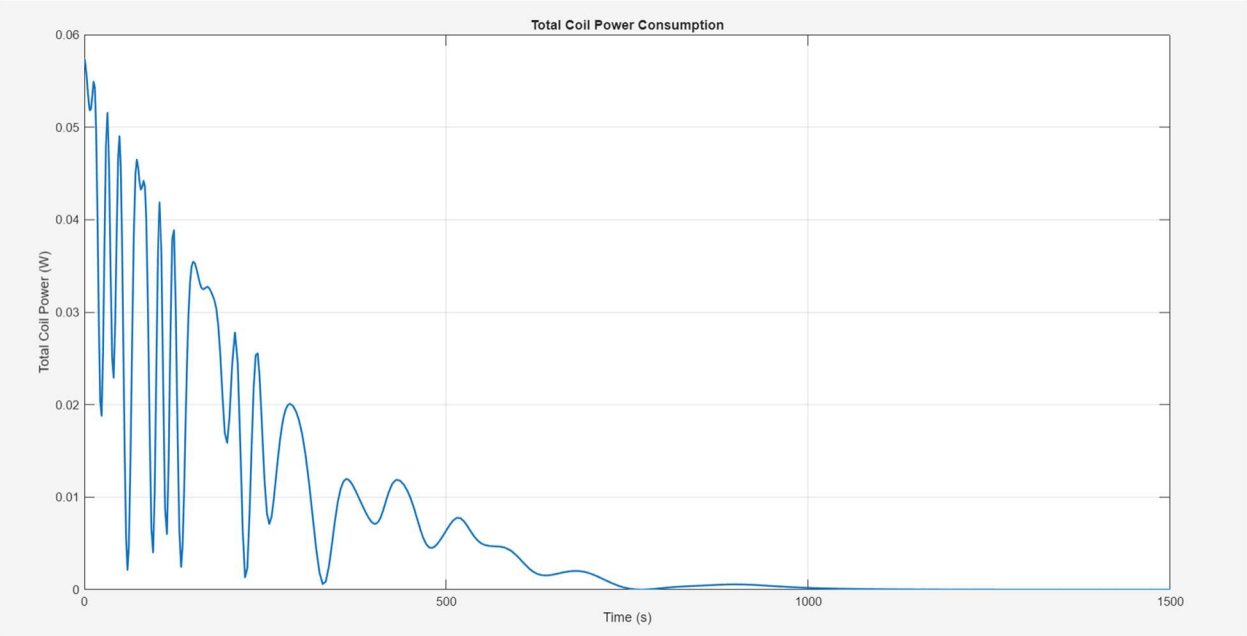


Figure 4.129 – Total coil power consumption mid LEO

- **High LEO**

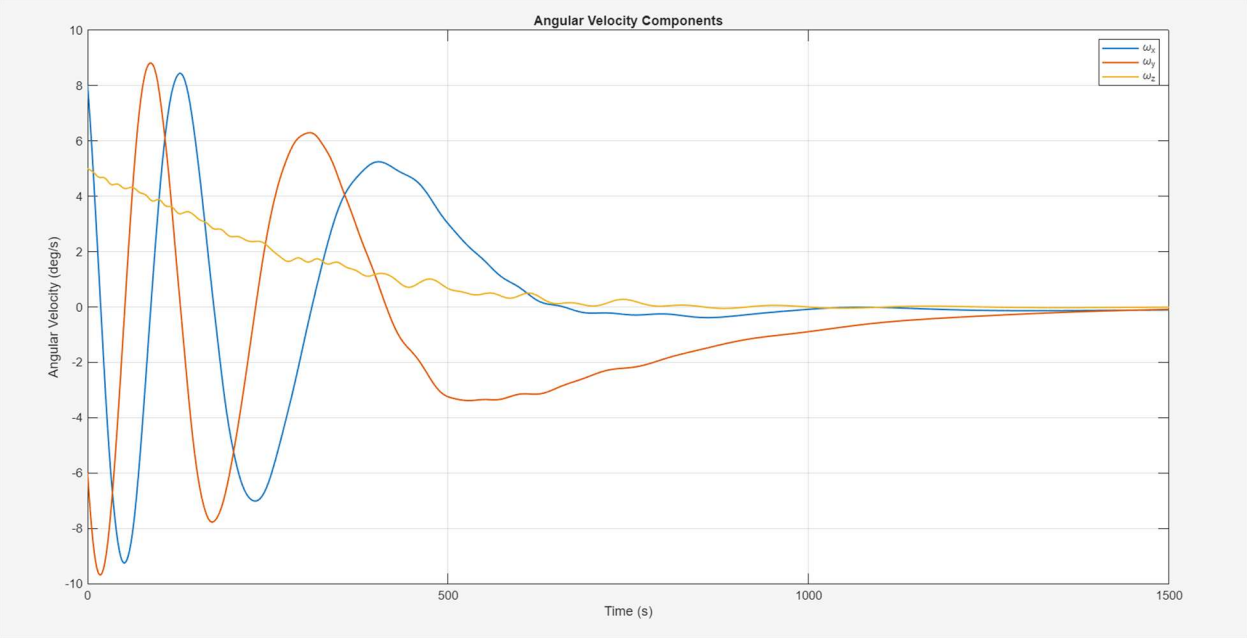


Figure 4.130 – Angular velocity components high LEO

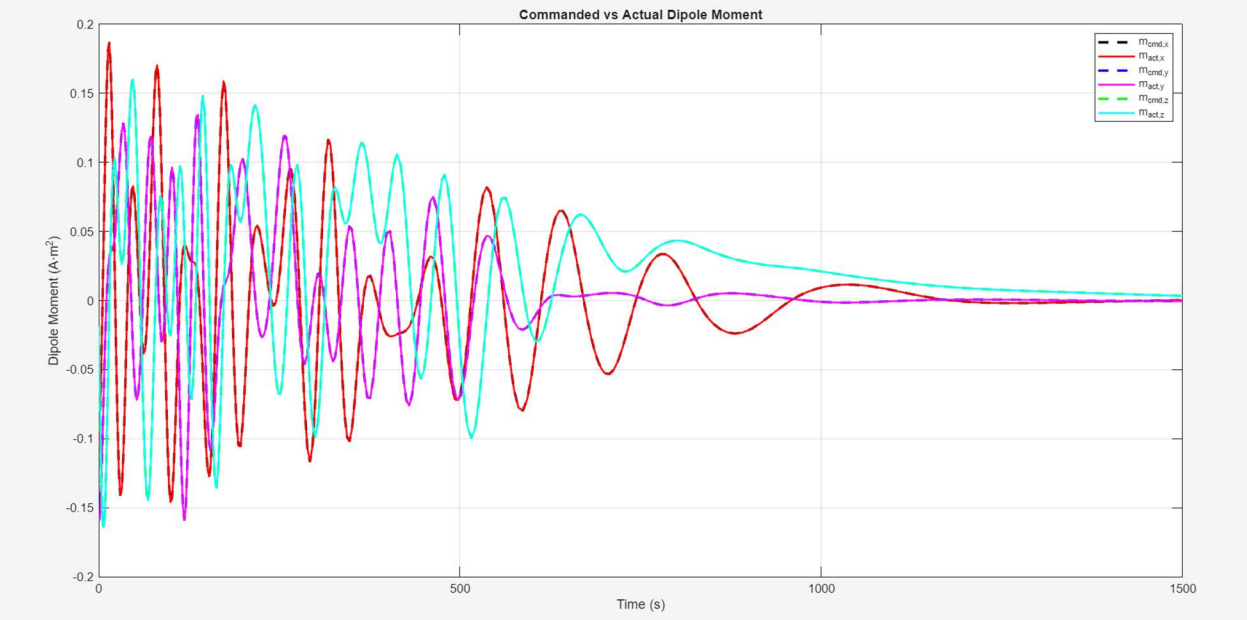


Figure 4.131 – Commanded vs actual dipole moment high LEO

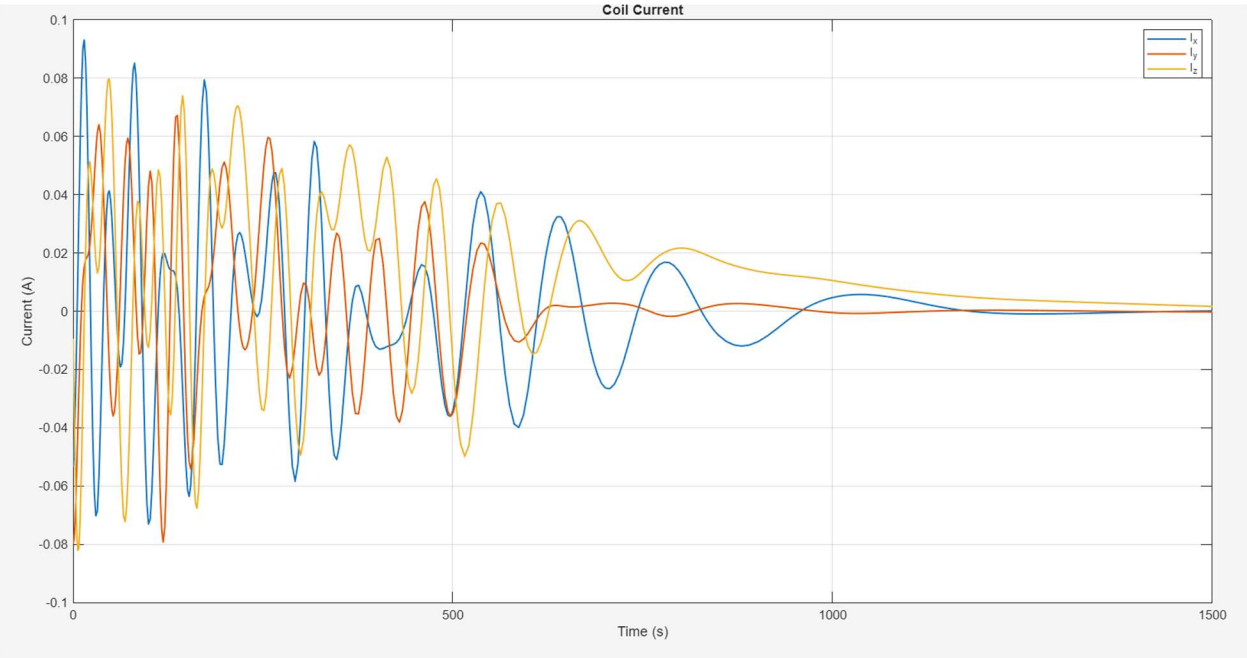


Figure 4.132 – Coil current high LEO

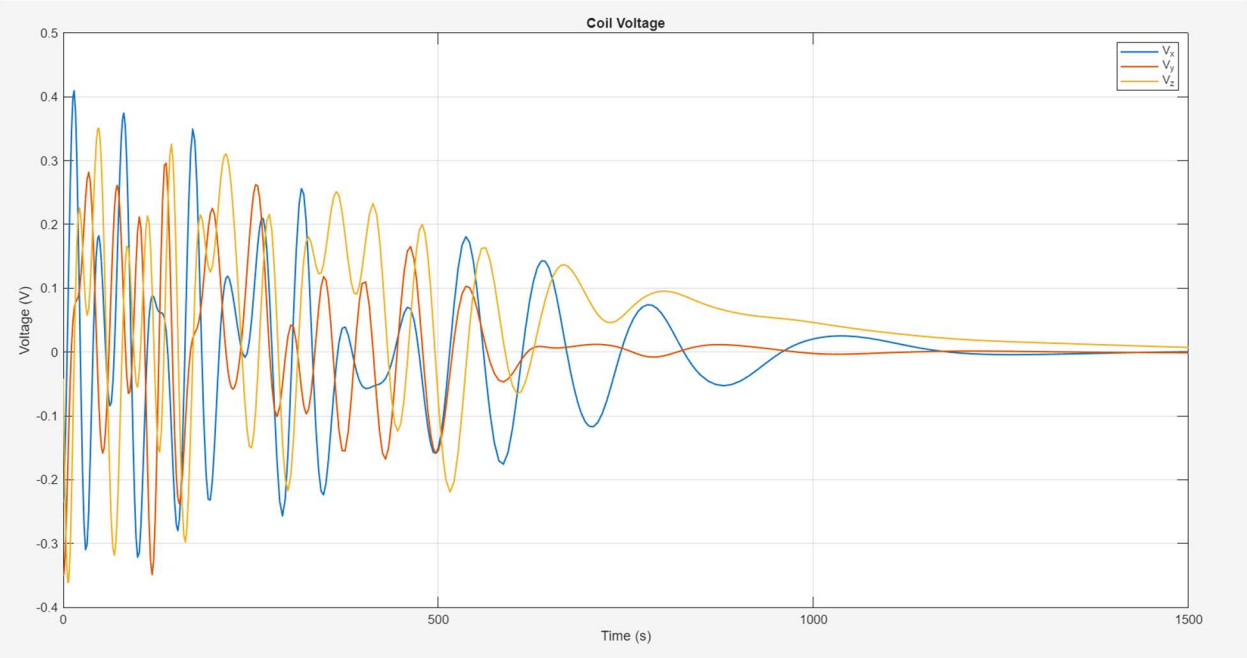


Figure 4.133 – Coil voltage high LEO

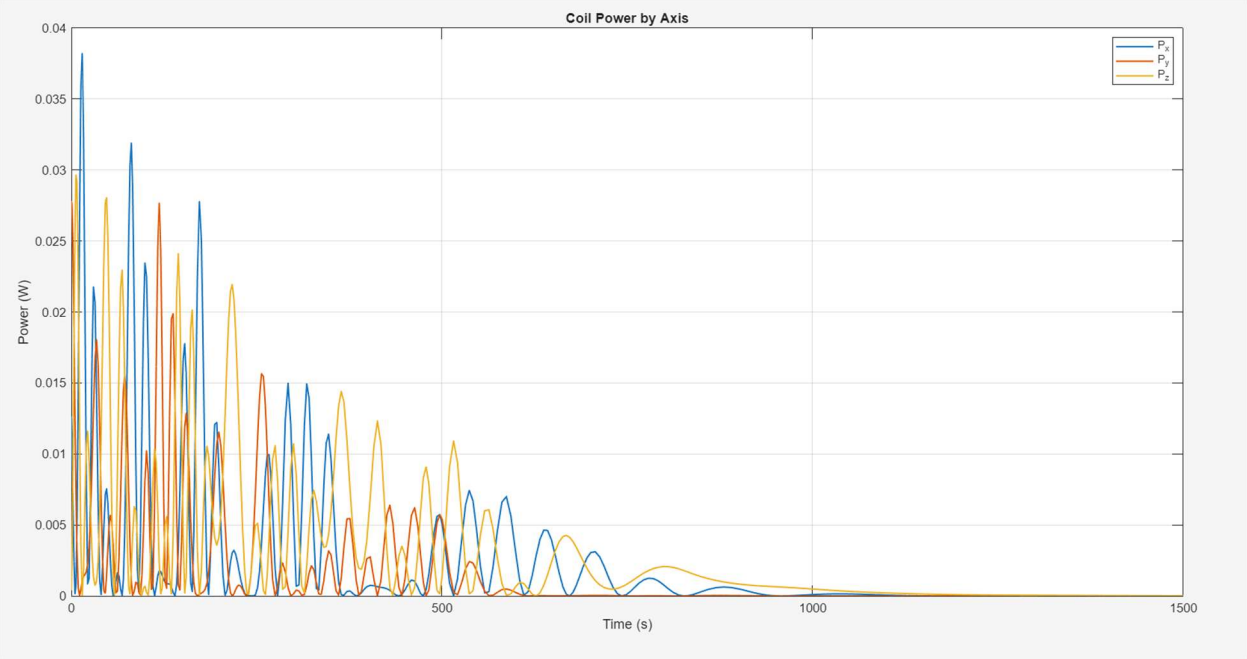


Figure 4.134 – Coil power high LEO

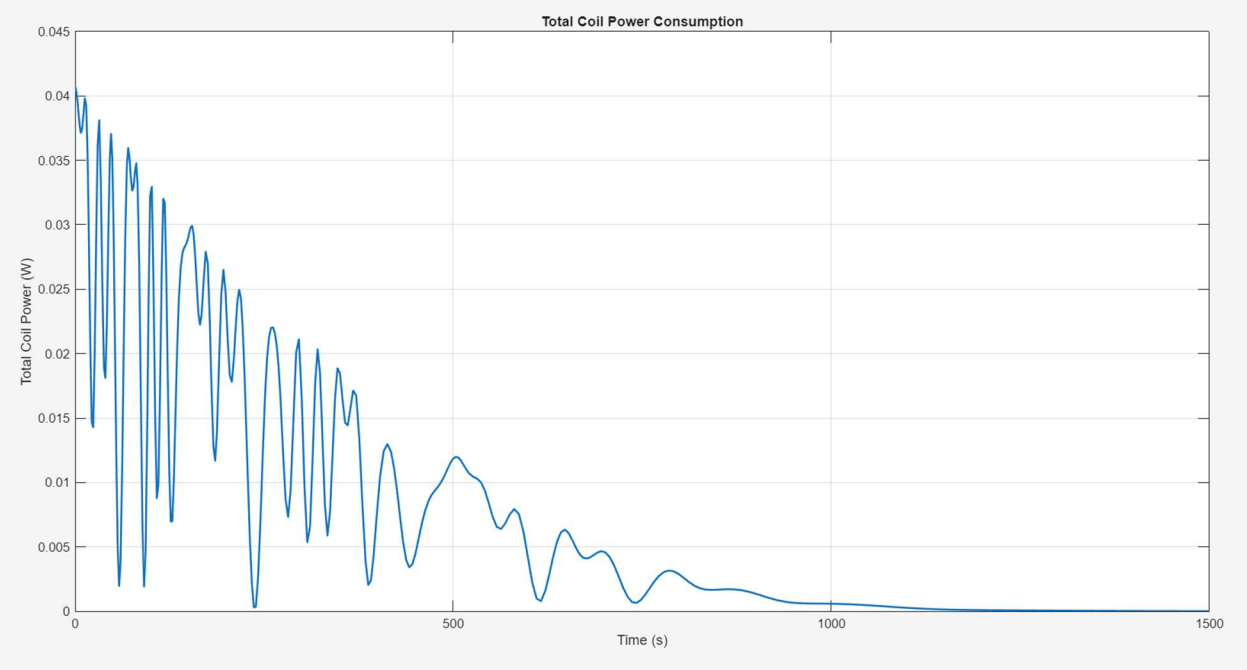


Figure 4.135 – Total coil power consumption high LEO

Quantitative numerical results are provided below for orbit sensitivity case study:

Table 4.11 – Quantitative numerical results of orbit sensitivity case study

Case	Detumble time to 0.50 deg/s (s)	Peak power (W)	Peak current (A)	Peak dipole (A·m²)	Peak Voltage (V)	Final $\|\omega\|$ (deg/s)
Current Mission	933.137	0.0620	[0.1133 0.0978 0.1005]	[0.2267 0.1956 0.2010]	[0.4987 0.4303 0.4423]	0.042
Low LEO	892.434	0.0689	[0.1189 0.1030 0.1057]	[0.2378 0.2060 0.2114]	[0.5231 0.4533 0.4651]	0.256
Mid LEO	974.075	0.0575	[0.1095 0.0942 0.0970]	[0.2190 0.1885 0.1939]	[0.4818 0.4146 0.4267]	0.039
High LEO	1141.371	0.0408	[0.0932 0.0794 0.0821]	[0.1864 0.1589 0.1642]	[0.4101 0.3495 0.3612]	0.139

5. Discussion

Based on the parametric case studies conducted, an optimal magnetorquer configuration can be identified by balancing detumbling performance, power consumption, and actuator feasibility.

From the number of turns sweep, it was observed that increasing the number of turns beyond $N = 200$ does not significantly reduce detumble time, which remains approximately 933 seconds. However, increasing Nsubstantially reduces the required current and power consumption. For example, increasing from $N = 200$ to $N = 800$ reduces peak power from 0.0620 W to 0.0039 W while maintaining identical detumble performance. This indicates that the system becomes control-limited rather than actuator-limited beyond this point. However, increasing the number of turns introduces practical constraints such as increased resistance, manufacturing complexity, and volume limitations. Therefore, a moderate value of $N = 200$–400 provides a practical balance between efficiency and feasibility.

The coil area sweep further supports this conclusion. While smaller coil areas (e.g., $A = 0.004$ m²) produce faster detumbling due to higher current utilization, they result in increased power consumption and actuator saturation. Larger coil areas reduce current demand but show diminishing returns in performance beyond $A = 0.008 - 0.01$ m². Thus, a coil area of $A = 0.01$ m² is selected as it provides stable performance with reduced electrical demand and aligns with the physical dimensions of a 2U CubeSat face that corresponds to SpartanSAT.

The current limit sweep revealed that actuator capability becomes insufficient below approximately 0.05 A, significantly increasing detumble time. Increasing the current limit beyond 0.1 A results in minimal performance improvement, indicating that the control system no longer requires additional actuator authority. Therefore, a current limit of $I_{max} = 0.1 - 0.15$ A is sufficient for effective detumbling.

Finally, the orbit sensitivity study demonstrated that lower altitude orbits provide stronger magnetic control authority due to increased geomagnetic field strength. The mission orbit of 416–425 km provides a favorable balance between performance and mission requirements, achieving detumbling in approximately 933 seconds. Higher altitude cases showed reduced performance, reinforcing that magnetorquer effectiveness decreases with altitude.

Overall, the optimal design is not defined by maximizing a single parameter, but rather by selecting a balanced configuration that minimizes power consumption while maintaining effective detumbling performance within mission constraints.

6. Conclusion and Future Work

Based on the simulation results and parametric trade studies, the following magnetorquer configuration is selected as the optimal design for the SpartanSAT mission given the current mission perigee and apogee:

- Number of turns: $N = 200$
- Coil area: $A = 0.01\text{m}^2$
- Maximum current: $I_{max} = 0.1$–0.15 A
- Coil resistance: $R = 4.4\ \Omega$
- Bus voltage: 5 V
- Controller gain: $k = 5 \times 10^4$

This configuration achieves detumbling from an initial angular velocity of approximately 11.18 deg/s (refer to eq. 4.5) to below 0.5 deg/s in approximately 933 seconds, while maintaining low power consumption (≈ 0.062 W peak) and operating within actuator limits. Increasing the number of turns or current capacity beyond these values does not significantly improve detumbling performance, confirming that the system is primarily control-limited rather than actuator-limited under nominal conditions. It is further important to note that this choice is based on current SpartanSAT magnetorquer specs and can change based on the delta in the design. The delta would require the change in MATLAB code provided in Appendix A as input of the simulation would change.

The selected design represents a balanced solution that satisfies mission requirements while minimizing electrical and structural complexity. It is also compatible with CubeSat form factor constraints, making it suitable for practical implementation.

While the current simulation provides a comprehensive first-order analysis, several areas can be expanded to improve model fidelity and system performance.

First, the inclusion of orbital mechanics assumptions, higher-order orbital perturbations, such as the Earth's oblateness, atmospheric drag, and solar radiation pressure, would allow for longer-duration and higher-fidelity simulations. These effects become increasingly important for extended mission timelines and precise orbit determination.

Second, the actuator model can be enhanced by incorporating coil inductance, current dynamics, and thermal effects. The present model assumes instantaneous current response and

does not account for heating, which may impose additional operational constraints in real hardware implementations.

Third, the control system can be extended beyond B-dot detumbling. This may involve integrating additional actuators such as reaction wheels or implementing advanced control strategies, including PID, LQR, or model predictive control, to achieve fine pointing accuracy required for payload operations.

Fourth, hardware validation through experimental testing, such as Helmholtz cage testing or hardware-in-the-loop simulations, would provide critical validation of the simulation results. This step is essential to ensure that the modeled performance translates accurately to real-world conditions.

Finally, future work may explore adaptive control strategies that account for variations in the geomagnetic field due to orbital changes, enabling improved performance across a wider range of mission scenarios.

References

[1] Mughal, M. R., Ali, H., Ali, A., Praks, J., and Reyneri, L. M., "Optimized Design and Thermal Analysis of Printed Magnetorquer for Attitude Control of Reconfigurable Nanosatellites," *IEEE Transactions on Aerospace and Electronic Systems*, Vol. 56, No. 1, Feb. 2020, pp. 736–747.

[2] Ali, H., ul Islam, Q., Mughal, M. R., Mahmood, R., Anjum, M. R., and Reyneri, L. M., "Design and Analysis of a Rectangular PCB Printed Magnetorquer for Nanosatellites," IEEE Journal on Miniaturization for Air and Space Systems, Vol. 2, No. 3, 2021, pp. 105–111

[3] Trégouët, J.-F., Arzelier, D., Peaucelle, D., Pittet, C., and Zaccarian, L., "Reaction Wheels Desaturation Using Magnetorquers and Static Input Allocation," *IEEE Transactions on Control Systems Technology*, Vol. 23, No. 2, Mar. 2015, pp. 525–539.

[4] Ali, H., Mughal, M. R., Praks, J., Reyneri, L. M., and ul Islam, Q., "Analysis and Design of Integrated Magnetorquer Coils for Attitude Control of Nanosatellites," Proc. of the 32nd Annual AIAA/USU Small Satellites Conference, Logan, UT, USA, August 4–9, 2018.

[5] Weston, S. V., Burkhard, C. D., Stupl, J. M., Ticknor, R. L., Yost, B. D., Austin, R. A., Galchenko, P., Newman, L. K., and Santos Soto, L., *State-of-the-Art Small Spacecraft Technology*, NASA Ames Research Center and NASA Goddard Space Flight Center, Moffett Field, CA, and Greenbelt, MD, Feb. 2025.

[6] Dildar, M. M. A., Ali, A., Ali, H., Khattak, M. S., and Pervez, F., "Embedded Magnetorquer Coil Design for Micro-Satellite," *Proceedings of the 3rd International Conference on Engineering and Emerging Technologies (ICEET)*, Superior University, Lahore, Pakistan, Apr. 7–8, 2016.

[7] Bellini, N., "Magnetic Actuators for Nanosatellite Attitude Control," Master's Thesis, Alma Mater Studiorum – Università di Bologna, Forlì, Italy, Oct. 9 2014

[8] Jovanovic, N., Riwanto, B., Niemelä, P., Mughal, M. R., and Praks, J., "Design of Magnetorquer-Based Attitude Control Subsystem for FORESAIL-1 Satellite," *IEEE Journal on Miniaturization for Air and Space Systems*, Vol. 2, No. 4, December 2021, Article No. 9468712

[9]A., Sedwick, R., Adams, C., Gettliffe, G. V., de Soria-Santacruz, M., Cohen, B., Smart, D., Bau tista, G., Perez, A., Lorenzini, E., Martinez-Sanchez, M., Miller, D. W., Porter, A., Schwartz, Z., a nd Wesenberg, R., "Magnetically Enabled Structures Using Interacting Coils," NASA TN HQ-E-DAA-TN63105 (Document No. 20190001165), National Aeronautics and Space Administration, November 12, 2018

[10] Sorensen, N. J., “Efficiency-Optimized Design of PCB-Integrated Magnetorquers for CubeSats,” IEEE Transactions on Aerospace and Electronic Systems, Vol. 57, No. 6, Dec. 2021, pp. 3623–3632.

[11]Weston, S. V., Burkhard, C. D., Stupl, J. M., Ticknor, R. L., Yost, B. D., Austin, R. A., Galchenko, P., Newman, L. K., Santos Soto, L., “State-of-the-Art Small Spacecraft Technology,” NASA TP–2025-0000142, National Aeronautics and Space Administration, February 2025.

[12] McGuire, M., Alexander, C., Burr, A., Hines, J., Kitts, C., “5.0 Guidance, Navigation, and Control,” in *State-of-the-Art of Small Spacecraft Technology*, Chapter 5, NASA, March 13 2025.

[13] Ali, A., Mughal, M. R., Ali, H., Reyneri, L. M., and Aman, M. N., "Design, Implementation, and Thermal Modeling of Embedded Reconfigurable Magnetorquer System for Nanosatellites," *IEEE Transactions on Aerospace and Electronic Systems*, Vol. 51, No. 4, Oct. 2015, pp. 2669–2679.

[14] Carletta, S., and Teofilatto, P., "Design and Numerical Validation of an Algorithm for the Detumbling and Angular Rate Determination of a CubeSat Using Only Three-Axis Magnetometer Data," *International Journal of Aerospace Engineering*, Vol. 2018, Article 9768475, 2018.

[15] Lovera, M., and Astolfi, A., "Spacecraft Attitude Control Using Magnetic Actuators," *Automatica*, Vol. 40, No. 8, 2004, pp. 1405–1414.

[16] Ava Avanzini, G., and Giulietti, F., "Magnetic Detumbling of a Rigid Spacecraft," *Journal of Guidance, Control, and Dynamics*, Vol. 35, No. 4, 2012, pp. 1326–1334.

[17] Schalkowsky, S. and Harris, M., *Spacecraft Magnetic Torques* (NASA SP-8018), National Aeronautics and Space Administration, Washington D.C., March 1969.

[18] Zhu, F., *A Guide to CubeSat Mission and Bus Design*, cloned version, August 2023.

[19] Ticona Coaquira, F.J., Wang, X., Vidaurre Torrez, K.W., Mamani Quiroga, M.J., Silva Plata, M.A., Luna Verdueta, G.A., Murillo Quispe, S.E., Auza Banegas, G.J., Antezana Lopez, F.P., Rojas, A. “Model-Based Design and Testbed for CubeSat Attitude Determination and Control System with Magnetic Actuation,” *Applied Sciences*, Vol. 14, Issue 14, Article 6065, July 2024.

[20] Polzin, K.A.; Hill, C.S. “Standard Practices for Usage of Inductive Magnetic Field Probes with Application to Electric Propulsion Testing,” NASA-Marshall Space Flight Center, NTRS Document 20140005775, 2014.

[21] Bensalah, M., *Attitude Stabilization of a CubeSat Using Fuzzy Logic Controller*, Master’s Thesis, Université Blida 1, Blida, Algeria, 2020.

[22] Andresen, B. Ø., Grøn, C., Knudsen, R. H., Nielsen, C., Sørensen, K. K., and Taagaard, D., *Attitude Control System for AAUSAT-II*, Aalborg University, Dept. of Electronic Systems, Aalborg, Denmark, May 2005.

Appendix A: MATLAB Code

A.1 main.m

```
% PARAMETERS
m = 2.66;
% Inertia matrix [kg*m^2]
Jx = (1/12)*m*(0.1^2 + 0.2^2);
Jy = (1/12)*m*(0.1^2 + 0.2^2);
Jz = (1/12)*m*(0.1^2 + 0.1^2);
J = diag([Jx Jy Jz]);
% Initial attitude quaternion [q0 q1 q2 q3]^T
q0 = [1; 0; 0; 0]; % spacecraft starts aligned with the inertial frame (no rotation)
% Initial angular velocity [rad/s]
omega0 = deg2rad([8; -6; 5]); % The initial angular velocity was assumed to represent a post-
deployment tumbling
% Initial state vector
x0 = [q0; omega0];
% Simulation time span [s]
tspan = [0 1500];
% B-dot controller gain
k = 5e4;
% k = 0;
coil = coil_parameters();
% RUN SIMULATION
[t, x] = ode45(@(t,x) spacecraft_dynamics(t, x, J, k, coil), tspan, x0);
% EXTRACT STATES
q_hist = x(:,1:4);
omega = x(:,5:7);
omega_mag = vecnorm(omega, 2, 2);
% STATE PLOTS
% Angular velocity components
figure;
plot(t, rad2deg(omega(:,1)), 'LineWidth', 1.2); hold on;
plot(t, rad2deg(omega(:,2)), 'LineWidth', 1.2);
plot(t, rad2deg(omega(:,3)), 'LineWidth', 1.2);
xlabel('Time (s)');
ylabel('Angular Velocity (deg/s)');
legend('\omega_x', '\omega_y', '\omega_z');
title('Angular Velocity Components');
grid on;
% Angular velocity magnitude
figure;
plot(t, rad2deg(omega_mag), 'LineWidth', 1.5);
xlabel('Time (s)');
ylabel('|\omega| (deg/s)');
title('Angular Velocity Magnitude');
grid on;
% Rotational kinetic energy
E = zeros(length(t),1);
for i = 1:length(t)
```

```
    w = omega(i,:)';
    E(i) = 0.5 * w' * J * w;
end
figure;
plot(t, E, 'LineWidth', 1.5);
xlabel('Time (s)');
ylabel('Rotational Kinetic Energy (J)');
title('Rotational Kinetic Energy');
grid on;
% COIL / ACTUATOR LOGGING
Npts = length(t);
m_cmd_hist    = zeros(Npts, 3);
m_actual_hist = zeros(Npts, 3);
I_hist        = zeros(Npts, 3);
V_hist        = zeros(Npts, 3);
P_hist        = zeros(Npts, 3);
B_body_hist   = zeros(Npts, 3);
for i = 1:Npts
    q = q_hist(i,:)';
    w = omega(i,:)';
    % Orbit position in ECI
    r_eci = orbit_position(t(i));
    % Magnetic field in ECI
    B_eci = earth_magnetic_field(r_eci, t(i));
    % Convert magnetic field to body frame
    R = quat_to_dcm(q);
    B_body = R' * B_eci;
    B_body_hist(i,:) = B_body';
    % Controller-commanded dipole
    m_cmd = bdot_controller(w, B_body, k, coil.m_max);
    % m_cmd = [0.1; 0; 0];   % open-loop fixed x-axis dipole
    % Actual coil response
    [m_actual, I_cmd, V_cmd, P_cmd] = coil_actuator_model(m_cmd, coil);
    m_cmd_hist(i,:)    = m_cmd';
    m_actual_hist(i,:) = m_actual';
    I_hist(i,:)        = I_cmd';
    V_hist(i,:)        = V_cmd';
    P_hist(i,:)        = P_cmd';
end
P_total = sum(P_hist, 2);
% COIL / ACTUATOR PLOTS
% Commanded vs actual dipole moment
figure;
% X-axis dipole
plot(t, m_cmd_hist(:,1), 'k--', 'LineWidth', 2); hold on;
plot(t, m_actual_hist(:,1), 'r-', 'LineWidth', 1.5);
% Y-axis dipole
plot(t, m_cmd_hist(:,2), 'b--', 'LineWidth', 2);
plot(t, m_actual_hist(:,2), 'm-', 'LineWidth', 1.5);
% Z-axis dipole
plot(t, m_cmd_hist(:,3), 'g--', 'LineWidth', 2);
plot(t, m_actual_hist(:,3), 'c-', 'LineWidth', 1.5);
xlabel('Time (s)');
ylabel('Dipole Moment (A·m^2)');
```

```
legend('m_{cmd,x}', 'm_{act,x}', ...
       'm_{cmd,y}', 'm_{act,y}', ...
       'm_{cmd,z}', 'm_{act,z}');
title('Commanded vs Actual Dipole Moment');
grid on;
% Coil current
figure;
plot(t, I_hist(:,1), 'LineWidth', 1.2); hold on;
plot(t, I_hist(:,2), 'LineWidth', 1.2);
plot(t, I_hist(:,3), 'LineWidth', 1.2);
xlabel('Time (s)');
ylabel('Current (A)');
legend('I_x', 'I_y', 'I_z');
title('Coil Current');
grid on;
% Coil voltage
figure;
plot(t, V_hist(:,1), 'LineWidth', 1.2); hold on;
plot(t, V_hist(:,2), 'LineWidth', 1.2);
plot(t, V_hist(:,3), 'LineWidth', 1.2);
xlabel('Time (s)');
ylabel('Voltage (V)');
legend('V_x', 'V_y', 'V_z');
title('Coil Voltage');
grid on;
% Coil power per axis
figure;
plot(t, P_hist(:,1), 'LineWidth', 1.2); hold on;
plot(t, P_hist(:,2), 'LineWidth', 1.2);
plot(t, P_hist(:,3), 'LineWidth', 1.2);
xlabel('Time (s)');
ylabel('Power (W)');
legend('P_x', 'P_y', 'P_z');
title('Coil Power by Axis');
grid on;
% Total coil power
figure;
plot(t, P_total, 'LineWidth', 1.5);
xlabel('Time (s)');
ylabel('Total Coil Power (W)');
title('Total Coil Power Consumption');
grid on;
% PERFORMANCE METRICS
omega0_deg = rad2deg(omega_mag(1));
omegaf_deg = rad2deg(omega_mag(end));
threshold_deg = 0.5;
idx_detumble = find(rad2deg(omega_mag) < threshold_deg, 1, 'first');
if isempty(idx_detumble)
    detumble_time = NaN;
else
    detumble_time = t(idx_detumble);
end
peak_power = max(P_total);
peak_current = max(abs(I_hist), [], 1);
```

```
peak_voltage = max(abs(V_hist), [], 1);
peak_dipole_actual = max(abs(m_actual_hist), [], 1);
fprintf('Initial angular speed: %.3f deg/s\n', omega0_deg);
fprintf('Final angular speed:   %.3f deg/s\n', omegaf_deg);
if isnan(detumble_time)
    fprintf('Detumble threshold of %.2f deg/s was not reached.\n', threshold_deg);
else
    fprintf('Detumble time to %.2f deg/s: %.3f s\n', threshold_deg, detumble_time);
end
fprintf('Peak total coil power: %.4f W\n', peak_power);
fprintf('Peak current [Ix Iy Iz]: [%.4f %.4f %.4f] A\n', ...
    peak_current(1), peak_current(2), peak_current(3));
fprintf('Peak voltage [Vx Vy Vz]: [%.4f %.4f %.4f] V\n', ...
    peak_voltage(1), peak_voltage(2), peak_voltage(3));
fprintf('Peak actual dipole [mx my mz]: [%.4f %.4f %.4f] A*m^2\n', ...
    peak_dipole_actual(1), peak_dipole_actual(2), peak_dipole_actual(3));
m_error = m_cmd_hist - m_actual_hist;
figure;
plot(t, m_error(:,1), 'LineWidth', 1.5); hold on;
plot(t, m_error(:,2), 'LineWidth', 1.5);
plot(t, m_error(:,3), 'LineWidth', 1.5);
xlabel('Time (s)');
ylabel('Dipole Error (A·m^2)');
legend('e_x','e_y','e_z');
title('Commanded - Actual Dipole Error');
grid on;
% ORBIT CHECK FOR THE ASSUMPTIONS VERIFICATION PART
r_hist = zeros(length(t),3);
for i = 1:length(t)
    r_hist(i,:) = orbit_position(t(i))';
end
figure;
plot3(r_hist(:,1), r_hist(:,2), r_hist(:,3), 'LineWidth', 1.5);
xlabel('x_{ECI} (m)');
ylabel('y_{ECI} (m)');
zlabel('z_{ECI} (m)');
title('Spacecraft Orbit in ECI');
grid on;
axis equal;
```

A.2 orbit_position.m

```
function r_eci = orbit_position(t)
% Earth constants
mu = 3.986004418e14;   % Earth's gravitational parameter [m^3/s^2]
Re = 6371e3;           % Earth radius [m]
% Mission orbital parameters
h_perigee = 500e3;     % perigee altitude [m]
h_apogee  = 500e3;     % apogee altitude [m]
i         = deg2rad(51.6);   % inclination [rad]
RAAN  = deg2rad(0);    % right ascension of ascending node [rad]
omega = deg2rad(0);    % argument of perigee [rad]
```

```
nu0   = deg2rad(0);    % initial true anomaly [rad]
% Convert altitudes to orbital radii
rp = Re + h_perigee;   % perigee radius [m]
ra = Re + h_apogee;    % apogee radius [m]
% Orbital elements
a = (rp + ra)/2; % semi-major axis [m]
e = (ra - rp)/(ra + rp); % eccentricity
p = a * (1 - e^2); % semi-latus rectum [m]
% Mean motion
n = sqrt(mu / a^3); % mean motion [rad/s]
% Propagate mean anomaly
M = n * t;
% Kepler's equation: M = E - e*sin(E)
E = kepler_solver(M, e);
% True anomaly from eccentric anomaly
nu = 2 * atan2( sqrt(1+e)*sin(E/2), sqrt(1-e)*cos(E/2) );
nu = nu0 + nu;
% Perifocal position
r_pf = (p / (1 + e*cos(nu))) * [cos(nu); sin(nu); 0];
% Rotation from perifocal frame to ECI
R3_RAAN = [ cos(RAAN) -sin(RAAN) 0;
            sin(RAAN)  cos(RAAN) 0;
            0          0         1];
R1_i = [ 1  0       0;
         0  cos(i) -sin(i);
         0  sin(i)  cos(i)];
R3_omega = [ cos(omega) -sin(omega) 0;
             sin(omega)  cos(omega) 0;
             0           0          1];
Q_pX = R3_RAAN * R1_i * R3_omega;
% ECI position
r_eci = Q_pX * r_pf;
end
% KEPLER SOLVER
function E = kepler_solver(M, e)
% Newton-Raphson
E = M;
for k = 1:20
    f = E - e*sin(E) - M;
    fp = 1 - e*cos(E);
    E = E - f/fp;
end
end
```

A.3 coil_parameters.m

```
function coil = coil_parameters()
coil.N = [200; 200; 200]; % turns
coil.A = [0.01; 0.01; 0.01]; % m^2
coil.R = [4.4; 4.4; 4.4]; % ohms
coil.I_max = [0.15; 0.15; 0.15]; % amps
coil.V_max = [5; 5; 5]; % volts
```

```
% Dipole limits
coil.m_max = coil.N .* coil.A .* coil.I_max;
end
```

A.4 spacecraft_dynamics.m

```
function xdot = spacecraft_dynamics(t, x, J, k, coil)
q = x(1:4);
omega = x(5:7);
q = q / norm(q);
% Orbit position in ECI
r_eci = orbit_position(t);
% Earth magnetic field in Earth centered inertial frame
B_eci = earth_magnetic_field(r_eci, t);
% Rotate into body frame
R = quat_to_dcm(q);
B_body = R' * B_eci;
m_cmd = bdot_controller(omega, B_body, k, coil.m_max);
% m_cmd = [0.1; 0; 0];   % fixed x-axis dipole [A*m^2] (open-loop)
% Coil actuator producing the actual dipole
[m_actual, ~, ~, ~] = coil_actuator_model(m_cmd, coil);
% Torque
tau = cross(m_actual, B_body);
% Angular dynamics
omega_dot = J \ (tau - cross(omega, J*omega));
% Quaternions
Omega = [0        -omega(1) -omega(2) -omega(3);
         omega(1)  0         omega(3) -omega(2);
         omega(2) -omega(3)  0         omega(1);
         omega(3)  omega(2) -omega(1)  0       ];
q_dot = 0.5 * Omega * q;
xdot = [q_dot; omega_dot];
end
```

A.5 bdot_controller.m

```
function m_cmd = bdot_controller(omega, B, k, ~)
m_cmd = k * cross(omega, B);
end
```

A.6 magnetorquer_torque.m

% Magnetic torque produced by magnetorquer

```
% Magnetic torque produced by magnetorquer
function tau = magnetorquer_torque(m, B)
```

```
tau = cross(m, B);
end
```

A.7 dipole_moment.m

```
% Magnetic dipole moment
function m = dipole_moment(N, I, A)
m = N * I * A;
end
```

A.8 earth_magnetic_field.m

```
% IGRF-based Earth magnetic field in ECI frame [T]
function B_eci = earth_magnetic_field(r_eci, t)
epochUTC = [2026 1 1 0 0 0];   % [Y M D h m s]
% Current UTC as numeric date vector
utc_dt = datetime(epochUTC) + seconds(t);
utc_vec = datevec(utc_dt);
% Convert ECI -> LLA
lla = eci2lla(r_eci.', utc_vec);   % [lat lon alt] = [deg deg m]
lat = lla(1);
lon = lla(2);
h   = lla(3);
dyear = decimal_year_local(utc_dt);
% XYZ = [North East Down]
B_ned_nT = igrfmagm(h, lat, lon, dyear, 14);
B_ned = B_ned_nT(:) * 1e-9;    % nT -> T
C_ned2ecef = ned2ecef_dcm_local(lat, lon);
B_ecef = C_ned2ecef * B_ned;
C_eci2ecef = dcmeci2ecef('IAU-2000/2006', utc_vec);
C_eci2ecef = C_eci2ecef(:,:,1);
B_eci = C_eci2ecef.' * B_ecef;
end
function dyear = decimal_year_local(utc_dt)
y0 = datetime(year(utc_dt),1,1,0,0,0);
y1 = datetime(year(utc_dt)+1,1,1,0,0,0);
dyear = year(utc_dt) + seconds(utc_dt - y0) / seconds(y1 - y0);
end


function C_ned2ecef = ned2ecef_dcm_local(lat_deg, lon_deg)

lat = deg2rad(lat_deg);
lon = deg2rad(lon_deg);
sLat = sin(lat);
cLat = cos(lat);
sLon = sin(lon);
cLon = cos(lon);

C_ned2ecef = [ -sLat*cLon, -sLon, -cLat*cLon;
```

```
                -sLat*sLon,  cLon, -cLat*sLon;
                 cLat,       0,    -sLat      ];
end
```

A.9 quat_to_dcm.m

```
function R = quat_to_dcm(q)
q = q / norm(q);
q0 = q(1);
q1 = q(2);
q2 = q(3);
q3 = q(4);
R = [1-2*(q2^2+q3^2),   2*(q1*q2+q0*q3),   2*(q1*q3-q0*q2);
     2*(q1*q2-q0*q3),   1-2*(q1^2+q3^2),   2*(q2*q3+q0*q1);
     2*(q1*q3+q0*q2),   2*(q2*q3-q0*q1),   1-2*(q1^2+q2^2)];
end
```

A. 10 coil_actuator_model.m

```
function [m_actual, I_cmd, V_cmd, P_cmd] = coil_actuator_model(m_cmd, coil)
% Convert desired dipole to required current
I_req = m_cmd ./ (coil.N .* coil.A);
% Saturate by current limits
I_cmd = max(min(I_req, coil.I_max), -coil.I_max);
% Compute voltage needed
V_req = I_cmd .* coil.R;
% voltage limits
overV = abs(V_req) > coil.V_max;
I_cmd(overV) = sign(I_cmd(overV)) .* (coil.V_max(overV) ./ coil.R(overV));
% Actual voltage after saturation
V_cmd = I_cmd .* coil.R;
% Actual dipole produced
m_actual = coil.N .* coil.A .* I_cmd;
% Coil power
P_cmd = I_cmd.^2 .* coil.R;
end
```